CO$_2$ Capture Using Ionic Liquids:
Thermodynamic Modeling and Molecular Dynamics Simulation

By

©Mahsa Aghaie Moghanjoghi

A thesis submitted to the school of Graduate Studies in partial fulfillment of the requirements for the degree of

Doctor of Philosophy

Faculty of Engineering and Applied Science
Memorial University of Newfoundland

May, 2020

St. John's, Newfoundland
Canada

Abstract

Global climate change is happening now, and the average temperature of Earth is rising. Several evidences show that one of the main reasons for global warming is the increased concentration of greenhouse gases (GHGs) in the atmosphere, particularly carbon dioxide (CO_2). CO_2 is mostly producing from burning fossil fuels. One of the effective strategies to reduce CO_2 emissions is implementing carbon capture in fossil fuel power plants. Current post-combustion carbon capture techniques typically employ amine-based solvents, such as monoethanolamine (MEA), for the absorption of CO_2. Although alkanol amines have an acceptable absorption capacity, their high vapor pressure, solvent loss during desorption, and high corrosion rate make amines absorption plants energy-intensive. In recent years, Ionic Liquids (ILs) have been emerged as promising alternative solvents for physisorption and chemisorption of acid gases due to their unique physiochemical properties, including negligible vapor pressure, high thermal stability, tunability, and being environmentally safe.

ILs require to be screened based on technical, economical, and environmental aspects. The main challenges of using ILs are increasing CO_2 capture capacity of ILs, and detailed understanding of the diffusivity of CO_2 in ILs, the effect of additives in solubility, selectivity features of ILs, phase behavior of gas-IL systems, and absorption mechanism. These challenges can be addressed using either experiment, thermodynamic modeling, and/or molecular simulations. In this study, the potential of the screened imidazolium-based ILs is investigated using thermodynamic modeling. The extended Peng–Robinson (PR) and Perturbed-Chain Statistical Associating Fluid Theory (PC-SAFT) EOSs are implemented to evaluate the solubility and selectivity of CO_2 in pure ILs and their mixture with water and toluene. The effects of water and toluene on solubility and viscosity of ILs are investigated.

Low concentrations of water (< 1 wt%) do not affect solubility; however, with increasing water concentration, the solubility of CO_2 is decreased. On the other hand, with increasing water content, the IL viscosity significantly decreases, which is in the favor of using viscous ILs for CO_2 separation.

In this thesis, Molecular Dynamics (MD) simulation is performed to determine the properties of ILs ([Bmim][BF$_4$] and [Bmim][Ac]), their structures, and molecular dynamics. A great agreement is noticed between the density and viscosity of the studied ILs from MD simulations and experimental data, indicating the accuracy of our simulation runs. This study also includes the effect of temperature and anion type on the structuring of ions and their self-diffusivities. Bulk systems of ILs and CO_2 are studied to evaluate the influence of temperature and types of ions on the diffusivity of CO_2 in the solvent as well as structural characteristics. A comprehensive analysis of the characteristics of the interface of IL/CO_2 is performed to explore species distribution, gas behavior at the interface, and molecule orientation. At the interface, CO_2 creates a dense layer which interrupts the association of cations and anions, leading to a decrease in the surface tension.

In addition, a comprehensive study on hydrophilic IL, 1-Butyl-3-methylimidazolium acetate or [Bmim][Ac], is conducted to evaluate the thermophysical properties, excess energy, structure, and dynamic characteristics of IL/Water and IL/Water/CO_2 systems, using MD simulation approach. The effect of water on radial distribution functions, coordination numbers, water clusters, hydrogen bonding, and diffusivity coefficients of the ions is assessed. The presence of water in IL mixture, even at high concentrations of water (>0.8 mole fraction), increases the diffusivity of cation, anion, water, and CO_2 molecules in the mixture due to

hydrophilicity of [Bmim][Ac] IL. MD simulations generate reliable and accurate results while dealing with systems including water, CO_2, and IL for carbon capture.

In this thesis, novel and robust computational approaches are also introduced to estimate the solubility of CO_2 in a large number of ILs within a wide range of temperatures and pressures. Four connectionist tools- Least Square Support Vector Machine (LSSVM), Decision Tree (DT), Random Forest (RF), and Multilinear Regression (MLR)- are employed to obtain CO_2 solubility in a variety of ILs based on thermodynamic properties and Quantitative Structure-Activity Relationship (QSPR) model. Among different types of descriptors, the most important input variables (e.g., Chi_G/D 3D and Homo/Lumo fraction (anion); SpMax_RG and Disps (cation)) are selected using Genetic Algorithm (GA)-MLR method. A great agreement between the predicted values and experimental measurements is attained while using RF and DT techniques developed based on descriptors and thermodynamics properties. The structural descriptors-based models are more accurate and robust than those built on critical properties.

Acknowledgments

I express my sincere appreciation to those who have given me an unconditional support and valuable advice and suggestions without them this dissertation would not been accomplished. This work could only have been accomplished by the mutual collaboration of many people. Firstly, I would like to express my sincere gratitude to my supervisor Dr. Sohrab Zendehboudi for his excellent support for my Ph.D. study, his patience, motivation, and enormous knowledge. His guidance helped me in all the time of research and writing of this thesis. He was truly a tremendous mentor for me. Furthermore, I would like to thank my colleagues in Reservoir Analysis and Energy & Environment Research Group who provided help and constructive feedback.

I gratefully acknowledge the support of Memorial University (NL, Canada), Equinor (formerly Statoil) Canada, Innovate NL, and the Natural Sciences and Engineering Research Council of Canada (NSERC) for their financial support.

Lastly, I would like to thank my parents, Ahmad and Azar; my siblings, Hamid and Majid for their faithful support, constant inspiration and motivation in all my endeavours. And most of all for my loving husband, Saeed, for supporting me throughout writing this thesis with his elegant presence, endless support and encouragement.

Table of Contents

List of Tables

List of Figures

xv

1. CHAPTER ONE

Introduction and Overview

1.1. Motivation

The dramatic climate change occurring around the world has been mostly attributed to accumulating CO_2 emissions in the atmosphere. CO_2 concentration increases mainly due to the use of fossil fuels. Although renewable energies are an appropriate alternative for fossil fuels, it is inevitable to remove fossil fuels due to their uses such as producing petroleum compounds and generating energy demands of the world. One of the methods to overcome climate change is retrofitting already operating fossil fuel power plants with Carbon Capture and Storage (CCS) systems. The primary idea of carbon capture is to separate CO_2 and acid gases (before emitting gases to the atmosphere) and then compress them for various utilizations such as underground storage and enhanced oil recovery. Carbon capture methods still require research and development to find a cost-effective, reliable, and safe technique.

CO_2 capture processes include three categories: post-combustion, oxy-combustion, and pre-combustion. The post-combustion carbon capture as the most promising and efficient method is currently implemented in some countries around the world. The most common applied post-combustion method is physically and/or chemically absorption and adsorption of CO_2. The captured CO_2 can be utilized in producing fuels (and chemicals), urea, carbonated beverages, polymers, and mineralization. Hence, absorption or adsorption of CO_2, while expensive, is profitable. The most commercialized solvents to capture CO_2 are amine-based solvents such as monoethanolamine (MEA). Amines are a popular choice of absorption due to high CO_2 absorption capacity, quick reaction with CO_2, and being relatively cheap. Besides these advantages, there are some drawbacks allied with them such as high vapor pressure, being corrosive, forming degradation products, and energy-intensive during the regeneration process. Thus, there is a need to find alternative techniques to overcome high energy consumption, high vapor pressure; the

alternatives should be also environmentally safe and non-corrosive. Ionic Liquids (ILs) have been recently proposed as a potential alternative solvent to amines. ILs are molten salts consisting of ions which are liquid at room temperatures. They have a very low vapor pressure, which makes them a safe absorbent without releasing to the atmosphere. An important feature of ILs is their tenability, means that their properties (e.g., density, viscosity, hydrophilicity, hydrophobicity, polar and quadrupole molecules affinity, and hydrogen bonding capability) can be tuned by varying the type of ions, and their structure by adding functionalized groups, to obtain a desirable solvent for various applications.

Numerous studies have evaluated the applications of ILs in selectively separating CO_2 with some promising outcomes based on preliminary results [3-5]. This research field still requires more experimental and modeling works on screening ILs, designing more efficient ILs, reducing the cost of synthesis, determining their properties in various mixtures, adjusting with more industrial applications, and further understanding of their detailed mechanism and dynamics of absorption. To accomplish the current knowledge gaps in this area, we propose studying CO_2 capture with ILs. The goals of this research are to characterize and assess the thermodynamic and molecular behaviors of CO_2 in IL and IL/Water mixtures to address some of the most fundamental challenges of the CO_2 absorption method.

1.2. Problem statement

The main technical obstacles for using ILs as an absorbent of CO_2 (in flue gases) in the real cases are as follows:

1. The solubility of CO_2 in some of ILs is studied; however, due to the large number of ILs, it is time-consuming and expensive to perform experiments on all the ILs for solubility

determination. Thermodynamic modeling is an appropriate method to characterize phase behavior of CO_2 and IL systems without conducting experimental tests at different operating conditions. There are challenges with selecting an appropriate EOS and mixing rules to be applicable for a wide range of ILs and complex systems such as IL/Water/CO_2 systems. Inappropriate models result in significant errors while predicting thermodynamic properties.

2. The primary concern associated with using ILs is their higher viscosity, compared to commercial solvents. The viscosity of ILs, which is vital in physisorption, can vary significantly by the type of cations and anions, the alkyl chain length of cation, and addition of other solvents such as water or other organic solvents. The properties and performance of ILs with a chemisorption mechanism strongly depend on the type of reaction happening between gas and solvent, the rate of reaction, and the diffusivity of CO_2 in the solvent. The magnitude of CO_2 diffusivity can be altered in ILs by additives and operating conditions. This challenge requires comprehensive studies.

3. Designing tunable ILs needs deep knowledge of transport phenomena mechanisms, chemical (and molecular) structures, and molecular dynamics of IL systems. The orientation of gases at the interface of ILs (and their mixtures) is still unclear. Molecular dynamics simulation can help to determine a considerable number of important thermodynamic and molecular properties. The influences of water, aggregation of molecules, operating conditions (temperature and pressure), structuring in bulk and interface, surface tension, and dynamics of CO_2 and ions can be investigated while dealing with pure ILs and their mixture with other solvents.

4. Fast and reliable deterministic (and screening) methods are required to study acid gases solubility in ILs, due to the high number of ILs, and expensive and laborious experiments. A robust and generalized model should be able to calculate the solubility of gases in ILs, and physiochemical properties with considering structural features of ILs.

In this thesis, we address the above concerns to facilitate the application of ILs in the absorption of gases at different processes and thermodynamic conditions.

1.3. Thesis structure

This thesis consists of seven chapters as follows:

Chapter 1 presents the motivation of the study, problem statement, and also provides the structure of the thesis.

Chapter 2 provides a comprehensive literature review on CO_2 capture using ILs method and fundamental concepts on absorption and properties (physical and chemical) which are required to evaluate the properties of ILs and their mixture with water, and interactions between species, and to design tunable ILs in the absorption processes. Chapter 2 is in the form of a review article that has been published in the Journal of Renewable and Sustainable Reviews.

Chapter 3 has been published in the Journal of Molecular Liquids. This chapter describes Vapor-Liquid Equilibrium (VLE) of the screened ILs, and IL/Water, and IL/Toluene systems; the accuracy performance of PR and PC-SAFT EOSs is also compared. It includes the solubility of CO_2 in ILs, the effect of water concentration on viscosity and solubility, and the selectivity of ILs in separating CO_2.

Chapter 4 has been published to the Journal of Molecular Liquids; it discusses the properties of pure [Bmim][BF$_4$] and [Bmim][Ac] ILs, CO$_2$ diffusivity in ILs, and structuring of different species in the mixture.

Chapter 5 has been accepted for publication in the Journal of Physical Chemistry B. It includes the influence of water on the diffusivity of ions and CO$_2$ in hydrophilic [bmim][Ac] IL. It evaluates the diffusivity coefficients, excess enthalpy, excess molar volume, and structuring order of species in the systems.

Chapter 6 introduces the developed smart models for the prediction of CO$_2$ solubility in ILs. It is prepared in the form of a manuscript that is now accepted for publication in the Journal of Fuel.

Chapter 7 contains a summary, conclusions, and recommendations for future work.

2. CHAPTER TWO

Literature Review (A Systematic Review on CO₂ Capture with Ionic Liquids: Current Status and Future Prospects)

Preface

A version of this chapter has been published in the Journal of Renewable and Sustainable Energy Reviews 96, 502-525 (2018). I am the primary author of this paper. Along with the co-authors, Sohrab Zendehboudi and Nima Rezaei. I carried out most of the literature review, data collection and the comparison of different carbon capture methods. I prepared the first draft of the manuscript and subsequently revised the manuscript based on the co-authors' feedback as well as the comments received from the peer-review process. The co-author, Nima Rezaei, helped in reviewing and revising the manuscript. The co-author, Sohrab Zendehboudi, contributed through providing the manuscript's outlines, comments on various parts of the manuscript, and technical points/critiques on previous works in the related field. Sohrab Zendehboudi also assisted in reviewing and revising the manuscript.

Abstract

Global warming due to the emission of greenhouse gases, especially carbon dioxide (CO_2), has a significant effect on climate change and has become a widespread concern in recent years. Carbon capture, utilization, and sequestration (CCUS) strategy appear to be effective to decrease the carbon dioxide level in the atmosphere. Despite great progress in this field, there are still major limitations in commercialized CO_2 capture methods through absorption processes. The high capital cost for CO_2 capture, low absorption and desorption rates (which requires large facilities), solvent loss due to evaporation, and the corrosive nature of the used solvents are the main limitations. Recently, CO_2 capture with ionic liquids (ILs) has appreciably attracted researchers' attention. The distinct properties of ILs such as negligible vapor pressure and their affinity towards CO_2 molecules make them a feasible alternative for currently available solvents including amines.

This chapter covers a brief of previous works on CO_2 capture, the description of CO_2 capture process using ILs, mechanisms of CO_2 capture with ILs at molecular and atomic levels, CO_2 and ILs properties, characterization of the CO_2/IL systems, impacts of operating and fluids conditions on CO_2 absorption capacity by ILs, and CO_2 solubility and selectivity in ILs. Moreover, the technical and economic aspects of the CO_2 capture with ILs, screening criteria for ILs/CO_2 systems, and important results obtained from previous studies will form the last parts of this chapter. This review offers a proper/systematic guideline that assists researchers and engineers to comprehensively understand and to effectively design the CO_2/ILs processes, focusing on thermodynamic and mass transfer aspects.

2.1. Introduction

It is believed that global warming mainly results from greenhouse gases (water vapor, carbon dioxide, methane, and nitrous oxide) which are trapping the heat in the Earth's atmosphere. Carbon dioxide (CO_2), which remains longer than other gases in the atmosphere, is more responsible for global warming and climate changes [6]. Carbon dioxide is naturally produced and consumed in the carbon cycle. As humans are currently consuming the long-buried carbons in the forms of fossil fuels and coal in significant amounts, excessive carbon is released in the atmosphere. On the other hand, the oceans (as a natural absorbent of CO_2) are not able to absorb all emitted carbon dioxide from the atmosphere [7].

Intergovernmental Panel on Climate Change (IPCC) report shows that about 79% of total CO_2 emissions come from fossil fuels and minerals that are being used for power generation [8]. Coal power plants (operated by natural gas and oil) with 60% of total CO_2 emissions have a great contribution to global warming [3,4]. Hence, removing the carbon dioxide from flue gases produced by power plants can effectively decrease the carbon level in the Earth's atmosphere. The production, processing, and utilization of fossil fuel sources such as oil, coal, and natural gases undoubtedly will continue. Thus, it seems necessary to use them as clean as feasible through employing effective strategies for carbon and other pollutants reduction. Carbon capture, utilization, and storage (CCUS) is an emerging method that helps to better manage CO_2 concentration through various techniques such as capturing carbon, sequestration, or/and turning it to useful chemicals [9, 10].

Carbon capture processes, in general, are divided into three main categories including pre-combustion, post-combustion, and oxy-combustion. In the post-combustion and oxy-combustion methods, the fuel is burned with air and oxygen, respectively. The heat released in these methods

is used to generate electricity. The main difference between the post-combustion and oxy-combustion processes is the composition of the flue-gas. In the latter technique, the flue-gas contains highly concentrated CO_2 which seems suitable for underground storage. However, in the post-combustion method, further stages/process units are required to capture the carbon from the flue-gas [11].

The pre-combustion method is associated with the integrated gasification combined cycle (IGCC). In the pre-combustion, the fuel is gasified to produce syngas [12]. The syngas, which contains CO and H_2, is utilized as a feed for the water-gas-shift reactors. In the presence of steam, CO is converted to CO_2 and H_2. CO_2 is then captured from the outlet stream and H_2 is combusted to generate the energy. Post-combustion is easier to be implemented as a retrofit option in the existing power plants, compared to the other two approaches [11]. In other words, pre-combustion and oxy-combustion methods can only be applied in new power plants [13].

As illustrated in Figure 2-1, the post-combustion carbon capture technique is divided into several main subcategories such as absorption, microbial (algal), adsorption, membrane, and cryogenics. Among these techniques, absorption is more popular and is widely employed in the commercial post-combustion CO_2 capture plants. In this method, the flue-gas in the tall columns or towers (known as absorbers) is in contact with the solvent which captures CO_2 from the flue-gas. The rate of CO_2 absorption with solvent is a crucial parameter in the chemical absorption processes. High absorption rate not only can reduce the capital costs of CO_2 capturing, but is also considered as an asset for an absorption process to be operated at the industrial scale [14, 15]. Figure 2-2 also illustrates a simple schematic of CO_2 absorption and desorption columns in a typical carbon capture plant.

Post-Combustion CO$_2$ Capture Methods

Absorption — Physical — Ionic Liquids (ILs); Purisol®; Rectisol®; Flour®; SELEXOL™

Absorption — Chemical — Amines; Mixed Amines; Potassium carbonate; Ammonia

Adsorption — Physical (packed bed) — Activated carbon; Zeolites; MOFs

Adsorption — Chemical (sorbents) — Amine-based; Potassium-based; Sodium-based; Lithium-based; Structured (novel)

Cryogenic

Membrane — Gas separation (PDMS, PPO); Gas absorption (PP); Ceramic-based

Microbial/Algal

Figure 2-1: Diagram of main carbon separation/capture methods in the post-combustion category (modified after [16]);[MOFs: metal-organic frameworks; PDMS: polydimethylsiloxane; PPO: polyphenyleneoxide; PP: polypropylene].
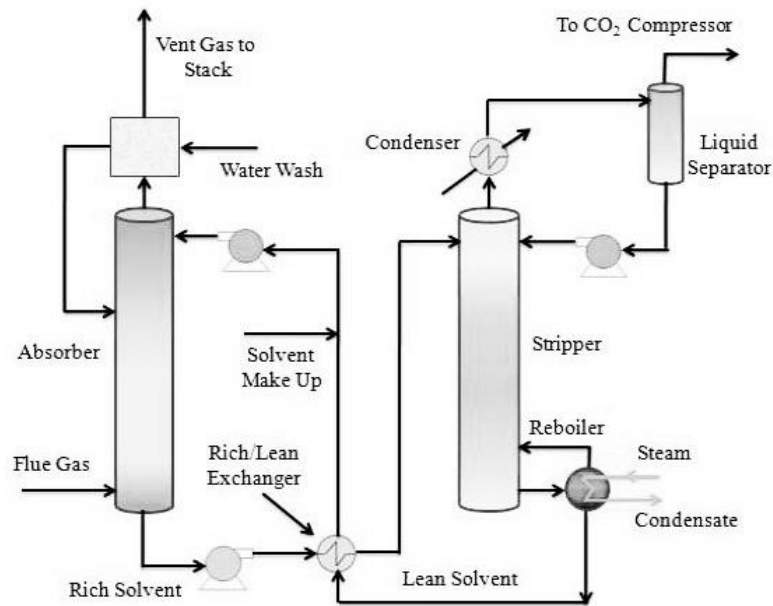
Figure 2-2: Schematic figure of absorption/desorption columns in a CO$_2$ capture process (modified after [17])Various solvents in the chemical absorption of CO$_2$ capture processes have been introduced [18].

Amines due to their high reactivity with CO$_2$ molecules, high thermal stability, and high absorption capacity are widely used as the absorbent for carbon capture operations [19]. Among all amine

31

groups, monoethanolamine (MEA), tertiary amines such as methyl diethanolamine (MDEA), and sterically hindered amines such as 2-amino-2-methyl-1-propanol (AMP) are the common absorbents for CO_2 capture systems [20]. Application of amines faces several drawbacks, including, high construction cost, high equipment corrosion rate, and amine degradation by SO_2, NO_2, and O_2 in the flue-gases which induces a high absorbent make-up rate and high energy consumption during high-temperature absorbent regeneration processes where large equipment are required [21]. These disadvantages are linked with the inherent properties of amines which have high vapor pressures, corrosive nature, and high energy contribution for regeneration [3]. Several research studies have been conducted to replace amines with superior solvents which have lower volatility, better thermal stability, lower corrosive characteristic, lower degradation rate, and lower regeneration cost [12-15]. Recently, Ionic Liquids (ILs) have been proposed as a potential replacement solvent for amines in the carbon capture processes [22]. The general properties of a majority of ILs are listed in Table 2-1 [23].

Table 2-1: General properties of ionic liquids [23].

Property	General characters
Salt ions	large cations and anions
Freezing temperature	$< 100°C$
Liquidous temperature	$> 200°C$
Thermal stability	high
Viscosity	< 100 cP, workable
Dielectric constant	< 30
Polarity	moderate
Specific conductivity	< 10 mS/cm, good
Vapor pressure	negligible
As a solvent	strong
As a catalyst	excellent (for organic reactions)

Strong ion-ion interactions for ILs (compared to other common intermolecular forces such as London forces and ion-dipole interactions in organic solvents) lead to negligible evaporation at the

ambient conditions [24]. Other appealing properties of ILs are their high thermal stability, large electrochemical window, and their ability to dissolve compounds with various polarities [25]. Furthermore, the physical and chemical properties of ILs can be adjusted by altering the cation and anion parts to make them suitable for particular applications [26]. From the environmental point of view, ILs are inflammable, non-volatile, and recyclable which make them environmentally friendly, compared to other chemicals such as amines [4, 27].

In a research work by Blanchard et al. [28] reported that CO_2 gas can be considerably dissolved into certain ILs. Since then, there is a growing interest in exploring and understanding the solubility of various gases in ILs [13, 22, 23].

A drawback of using ILs for CO_2 capture is their high viscosity due to their complex synthesis and purification processes. ILs have a higher viscosity, compared to conventional solvents [29]. This character makes them less suitable for industrial CO_2 capture since the rate, at which the CO_2 is absorbed by ILs, is much slower. Solvents that have a lower viscosity tend to be more favorable for this separation purpose as the pumping costs are lower and the mass transfer rates are normally higher [30]. According to Krupiczka et al. [31], the viscosity of ILs can be modified by using a proper combination of cations and anions. The cation has generally a lower impact on ILs properties than the anion. With increasing the alkyl chain of cations, the viscosity of ILs increases. The effect of anion on viscosity in imidazolium-based ILs is reported as [bmim][NTf$_2$] < [bmim][CF$_3$SO$_3$] < [bmim][BF$_4$] < [bmim][PF$_6$]. The viscosity of ILs also changes by adding a co-solvent. The effect of co-solvent in decreasing viscosity depends on the solvent polarity and the extent of dissociation of ILs into ions. Polar solvents such as water lower the viscosity more than nonpolar solvents, including, benzene and toluene.

Conventional ILs capture the carbon through a physical absorption mechanism. Although adjusting cations/anions in the ILs can enhance the solubility of CO_2 in conventional ILs, compared to the current commercial carbon capture technologies such as amine-based solvents, their CO_2 capture capacity is still low [32]. A comprehensive understanding of molecular structure/interactions and accurate determination of thermodynamic and physical characters such as solubility, vapor-liquid equilibria (VLE), liquid-liquid equilibria (LLE), selectivity, density, and viscosity are necessary to employ appropriate ILs in different applications/cases. To use ILs in gas separation processes, it is required to understand the phase behavior of ILs/gas systems. A well-developed methodology to obtain phase equilibrium conditions is thermodynamic modeling using appropriate equations of state (EOS). A large number of research works have focused on the solubility of gases in common imidazolium-based ILs with $[BF4]^-$ and $[PF_6]^-$ anions [26-28]. Karakastani et al. [33] predicted the solubility of CO_2 in some ILs through employing perturbed chain-statistical associating fluid theory (PC-SAFT) EOS where they considered the quadrupole interactions between CO_2 molecules, dipolar interactions between ionic liquid (IL) molecules, and the Lewis acid−base type of association between the IL and CO_2. They found a great agreement between the modeling results and experimental data at pressures 0-100 MPa. Shiftlet et al. [34, 35] utilized the most popular EOSs including Redlich–Kwong (RK), Soave-Redlich-Kwong (SRK), van der Waals (vdW), and Peng-Robinson (PR) with proper mixing rules for multi-component mixtures. They concluded that the experimental solubility data of CO_2, SO_2, CF_3-CFH_2, and NH_3 in ILs are well correlated with the cubic (modified) EOSs. Andrew et al. [36] examined Soft-SAFT EOS ability to estimate the solubility of CO_2 in $[C_n$-mim$][NTf_2]$ using one binary parameter, resulting in a good match with the experimental data. Chen et al. [11] checked the competence of PC-SAFT with and without associating parameters in determining the solubility of CO_2 in

imidazolium-based ILs where the temperature-dependent binary interaction parameters were taken into account. The results revealed that PC-SAFT can acceptably forecast the solubility so that the modeling results were very close to the experimental data. It was also found that PC-SAFT with the associating parameters describes VLE more precise, compared to that without the associating parameters.

The solubility of gases in ILs can be increased by extending the interface area of gas/ILs systems and by increasing the operating pressure. Maginn et al. [22] examined the solubility of nine different gases into [bmim][PF$_6$] IL and found out that water and CO_2 have strong interactions. CO_2 in ILs exhibits higher solubility, compared to solubility of ethylene, ethane, methane, carbon monoxide, hydrogen, and nitrogen in ILs. Argon and oxygen have also very low solubility in ILs. They also reported Henry's law constants of gases in ILs. The gas solubility can be explained based on the interactions of the molecules in terms of polarizability and dipole and quadrupole moments between the gas and solvent molecules. It should be noted that the mixing enthalpy and entropy can also indicate the strength of interactions between CO_2 and ILs. Yokozeki et al. [5] successfully correlated the experimental solubility of CO_2 in 18 ILs to fluids properties and operating conditions through using Redlich-Kwong equation of state (RK-EOS). In addition, they presented the data in terms of excess functions (excess Gibbs, G^E; excess enthalpy, H^E; and excess entropy S^E). Depending on the magnitudes of these excess functions, the CO_2 absorption might be a chemical or physical process.

The thermodynamic behaviors of CO_2/ILs systems such as physical and chemical properties, phase equilibrium of CO_2/ILs mixtures, and solubility and selectivity of CO_2 in ILs should be properly investigated. A suitable equation of state (EOS) and mixing rules are required to accurately model the thermodynamic behaviors of CO_2 and IL systems. A part of the common EOSs for research

investigations in this area are PR EOS, RK EOS [37], SRK EOS [38], Predictive Peng-Robinson EOS, Peng-Robinson-Stryjek-Vera EOS, Sanchez-Lacombe EOS [39], PC-SAFT EOS, extended PC-SAFT (PC-PSAFT) EOS, and truncated PC-PSAFT EOS [40]. The solubility of CO_2 in most of ILs are not determined yet since a majority of the previous studies have assessed the solubility of CO_2 in common imidazolium-based ILs [5,14,30]. Thus, modified versions of various EOSs need to be utilized to obtain the solubility of CO_2 in phosphonium, pyridinium, ammonium, and gauinidium-based ILs.

In this chapter, CO_2 capture using ILs is briefly described in terms of mechanisms, advantages, and disadvantages. The past research works in this research field are discussed and their main findings are reported. Comprehensive information on the properties and thermodynamic behaviors of CO_2, ILs, and CO_2/ILs systems are also provided. The last sections summarize the practical, economic, and theoretical aspects of CO_2 capture with ILs.

2.2. CO_2 emissions: sources and statistical data

Global greenhouse gas (GHG) emissions are mainly due to human activities, including fossil fuel burning, deforestation, and industrial processes. Among different sources of GHG emissions, the energy sector has the largest contribution [39,40]. The other shares come from agriculture, industrial processes, and solid biomass burning for the generation of heat and energy. Due to economic growth and population increase, the energy demand is increasing. Global total primary energy supply has increased by 150 % from 1971 to 2014 [39]. CO_2 has the largest share of anthropogenic GHG emissions. The growing world energy demand is mainly responsible for increasing CO_2 emissions. In 2014, global CO_2 emissions reached 32.4 Gt CO_2, of which 82 % comes from the energy sector, mainly due to the burning of fossil fuels. Among the fossil fuels, 34 % is from oil, 46 % from coal, 19 % from gas fuels, and the remaining 1 % has been resulted

from nuclear, hydro, geothermal, solar, wind, biofuels energies and waste [41]. Global GHG emissions from various sectors and world CO_2 emissions from fuel combustion are depicted in Figure 2-3: Schematic plot of (a) shares of global anthropogenic GHG emissions and (b) world CO_2 emissions from fuel combustion by sector in 2014 (modified after [42]) Electricity and heat generation, and transportation together are two major sectors, producing about two-thirds of the global CO_2 emissions from fuel combustion. A significant extent of the GHG emissions in heat and electricity generation is from coal, while road transportation is responsible for most of the CO_2 emissions in the transportation sector.
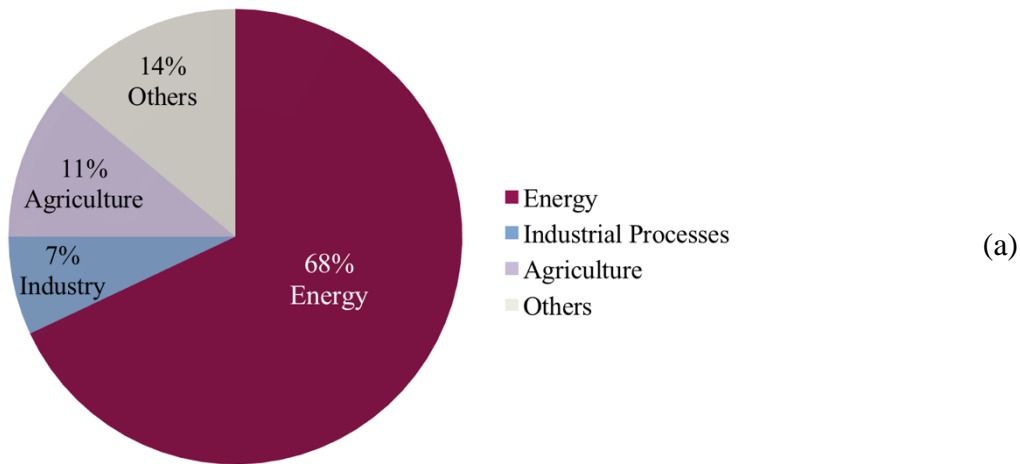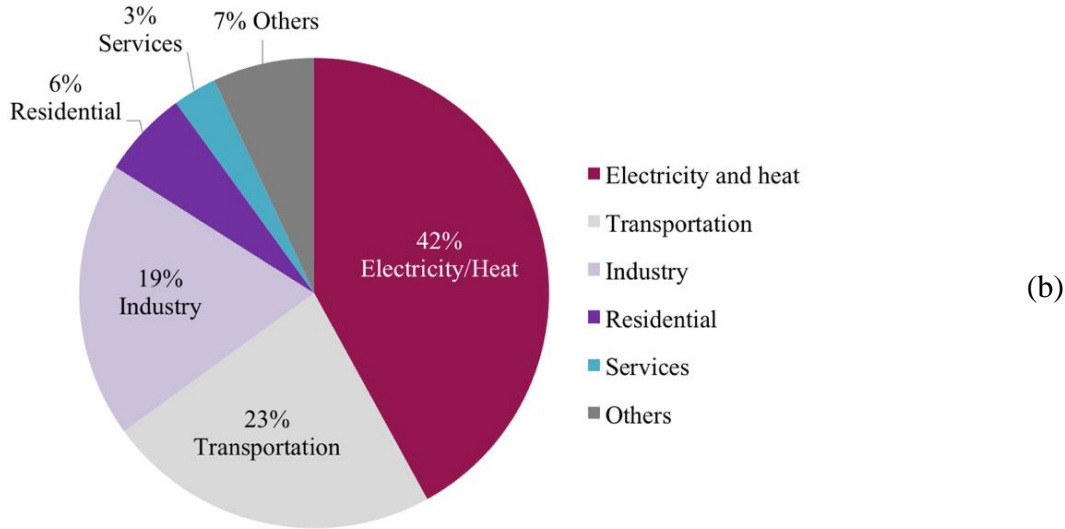
(a)

Figure 2-3: Schematic plot of (a) shares of global anthropogenic GHG emissions and (b) world CO_2 emissions from fuel combustion by sector in 2014 (modified after [42]).

In the atmosphere, the average volume concentration of CO_2 is about 385 ppm (or, 582 ppm by mass); the total mass of CO_2 in the atmosphere is therefore about 3.0×10^{15} kg [36,37]. The concentration of CO_2 varies by season, geographical region, and human-induced activities that produce carbon [43]. Figure 2-4 demonstrates the CO_2 emissions by sectors in the period of 1971 to 2014 [42, 44]. According to Figure 2-4, global carbon emissions from fossil fuels have been increased by about 90% since 1971. The carbon emissions from all sectors have exhibited a considerable increase from 1971 to 2014. In 2016, the annual rate of CO_2 emissions increased from 3.2 ppm at the beginning of 2016 to 3.6 ppm towards the end [45].

The total carbon dioxide emitted by region in 2014 is illustrated in Figure 2-5. China has the highest contribution to CO_2 emissions. It is clear that increasing the atmospheric carbon dioxide (CO_2) concentration will lead to an increase in CO_2 concentration in the ocean surface, because of the gas exchange between the air and oceans. Hence, the dissolved inorganic carbon (e.g.,

CO_2, HCO_3^-, and CO_3^{2-}) will be increased and subsequently, the pH of the ocean surface will decrease, resulting in ocean acidification [46].
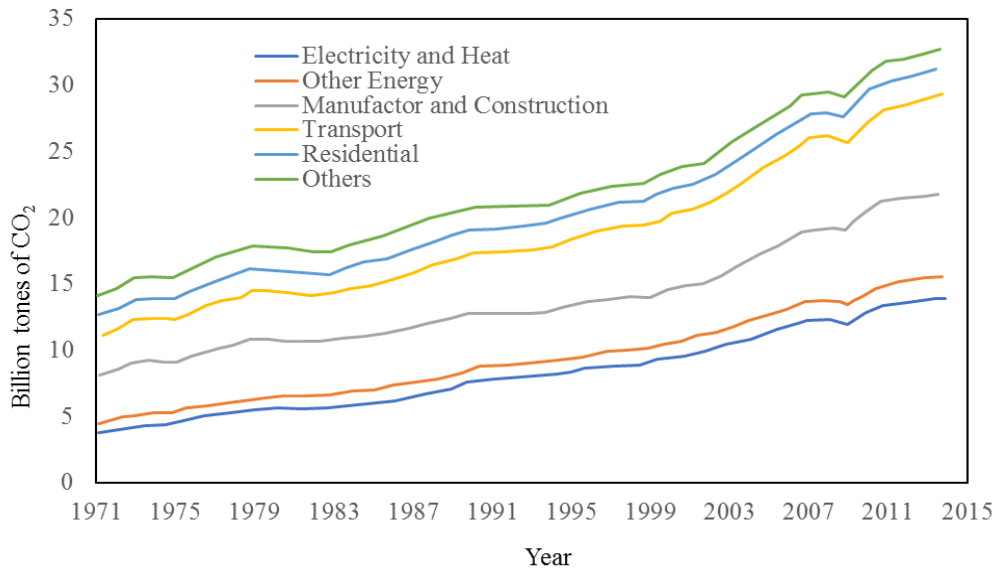
Figure 2-4: Global CO_2 emissions by sector in the period 1971-2014 (modified after [42, 44]).
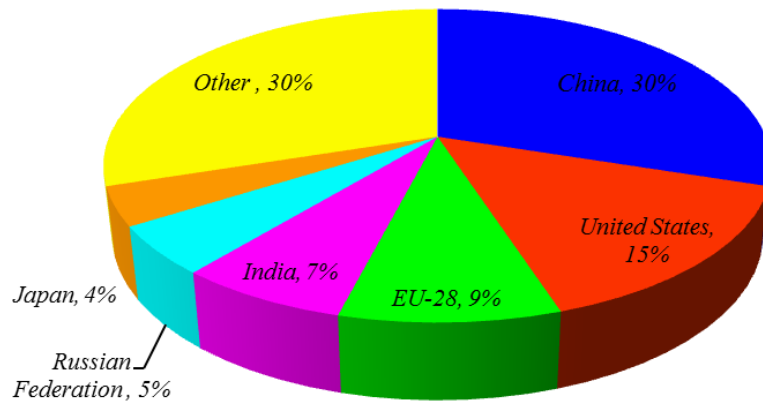
Figure 2-5: Regional distribution of 2014 global CO_2 emissions from fossil fuels combustion and industrial processes (modified after [47]).

2.3. CO₂ properties

CO$_2$ is an odorless and colorless gas at the atmospheric condition. This chemical component is relatively nontoxic, non-combustible, and soluble in water. Its molecular weight is 44.009 g/mol. The normal melting point of CO$_2$ is -56.5 °C and its solubility in water is 2.9 g/L at 25 °C [48]. CO$_2$ is also miscible with hydrocarbons and organic liquids at particular thermodynamic conditions [57,58]. The density of gas CO$_2$ is 1.976 g/l at 25 °C. Its vapor pressure and viscosity are 5720 kPa (56.5 atm) at 20 °C and 0.01503 cP at the atmospheric condition, respectively [49]. The surface tension of CO$_2$ is 0.0162 N/m at the melting point [58].

Viscosity: The viscosity of CO$_2$ in different conditions can be calculated using Equation (2-1), where it expresses $\eta(\rho,T)$ as a summation of three terms. The first term $\eta_0(T)$ is the dilute gas viscosity at a given temperature, $\Delta\eta(\rho,T)$ which is the excess viscosity which signifies the effect of density (or pressure) and $\Delta\eta_c(\rho,T)$ is the critical enhancement due to fluctuations near the critical point [50]. Equation 2-1) represents the above description in the mathematical form:

$$\eta(\rho,T) = \eta_0(T) + \Delta\eta(\rho,T) + \Delta\eta_c(\rho,T) \qquad\qquad \text{2-1)}$$

Fenghour et al. [51] proposed the following correlation to calculate the viscosity of carbon dioxide in dilute regions:

$$\eta_0(T) = \frac{1.00697 T^{1/2}}{\sigma_\eta^*(T^*)} \qquad\qquad \text{2-2)}$$

where $\eta_0(T)$ is the zero-density viscosity in $\mu Pa.s$, T is the temperature in Kelvin, and $\sigma_\mu^*(T^*)$ denotes the reduced effective cross-section, which is represented by the following empirical equation:

$$\ln \sigma_{\mu}^{*}(T^{*}) = \sum_{i=0}^{4} a_i (\ln T^{*})^i \qquad (2\text{-}3)$$

The reduced temperature (T^*) can be calculated using the following expression:

$$T^* = \frac{kT}{\varepsilon} \qquad (2\text{-}4)$$

where ε is the particle energy, k stands for the Boltzmann constant, and T represents the absolute

temperature ($\frac{\varepsilon}{k} = 251.196K$). A_i is a coefficient in Equation (2-3) which is listed in Table 2.2.

Table 2-2: Coefficients used in Equation (2-3) to obtain the viscosity of CO_2 at low density [51].

i	a_i
0	0.235156
1	-0.491266
2	5.211155×10^{-2}
3	5.347906×10^{-2}
4	-1.537102×10^{-2}

The excess viscosity describes the behavior of viscosity change with the density outside the critical

region as given by the following expression:

$$\Delta\mu(\rho,T) = \sum_{i=1}^{n} b_i(T)\rho^i \quad where \quad b_i = \sum_{j=1}^{m} \frac{d_{ij}}{T^{*(j-1)}} \qquad (2\text{-}5)$$

Where T^* stands for the reduced temperature as defined by Equation (2-5) and d_{ij} denotes a coefficient that is obtained through curve fitting of the excess viscosity experimental data versus the reduced temperature.

Vapor Pressure: The vapor pressure of CO_2 (P^{sat}) can be calculated using the Antoine equation as follows [50]:

$$\log P^{sat}(mmHg) = A - \frac{B}{C + T(^oC)} \tag{2-6}$$

where A, B, and C are the constants (For CO_2: A=9.8206, B=1347.790, and C=273.00) [52].

Thermodynamic Behavior and Critical Properties: Figure 2-6 presents the pressure-temperature diagram of CO_2. As depicted in Figure 2-6, the triple point represents the temperature and pressure of (-56.7 °C and 5.11 atm) that three phases can coexist at the thermodynamic equilibrium. The critical point also corresponds to 73.8 atm and 31.1 °C [51,52].
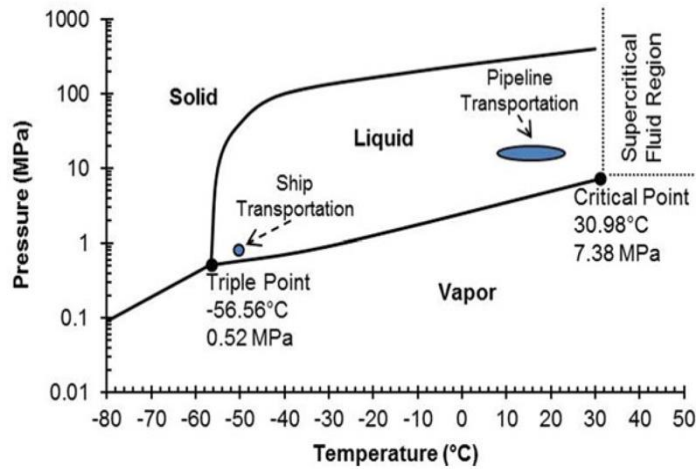
Figure 2-6: CO_2 phase diagram (reprinted with permission from [53]).

To reasonably forecast, the thermodynamic behavior of any component or mixture through Equations of States (EOSs), the critical properties and acentric factor of the component/mixture are required. The critical properties and acentric factor of CO_2 are listed in Table 2- [54].

Table 2-3: Critical properties of CO_2 [54].

Critical parameter	Designation/symbol	Value
Temperature	T_c (K)	304.2
Pressure	P_c (bar)	73.8
Volume	V_c (cm^3. mol^{-1})	94.0
Acentric factor	ω	0.2236

2.4. Ionic Liquids (ILs) characteristics

Based on the molecular structure, ILs are classified into proton-donating (protic ILs (PILs)) and nonproton-donating (aprotic ILs (AILs)) solvents. A general molecular configuration of common cations and anions of ILs is shown in Figure 2-7.
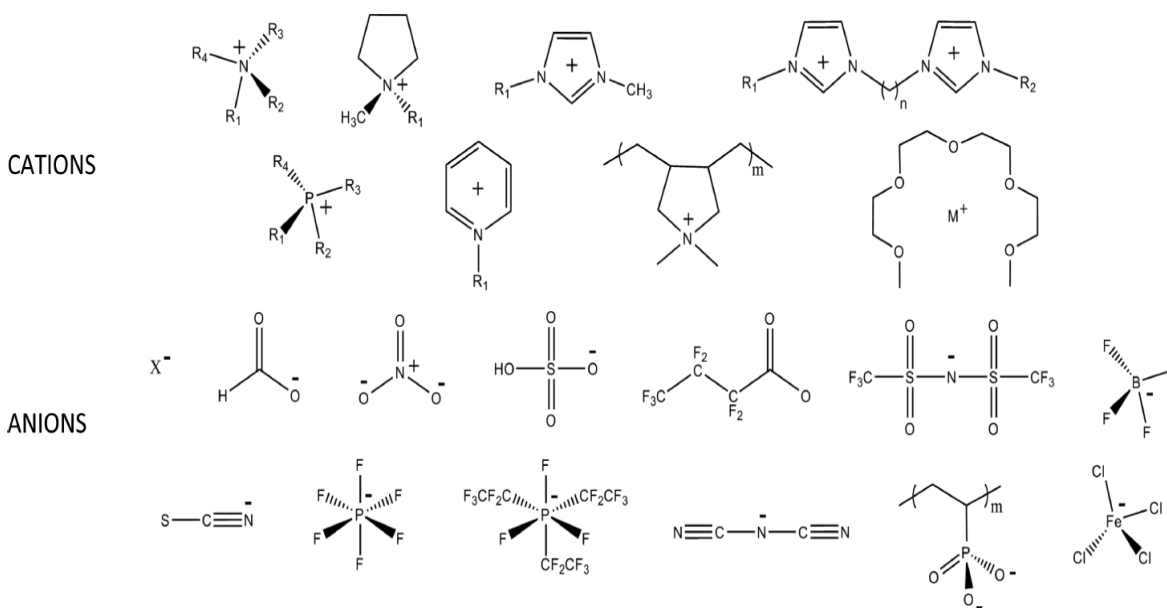
Figure 2-7: Structures of cations and anions of most common ionic liquids [55].

43

In Table 2-, the characteristics of ILs are listed and compared to the atomic, molecular, and molten salts. As clear from a comparison between the physical properties of different solvents, ILs due to their various structures and ions have different solvent properties, compared to the atomic salts; however, they are similar to the polar protic liquids and molten salts in terms of physical characteristics.

Table 2-4: A comparison between the physical properties of different solvents [55].

Parameter*	Solvent type				
	Atomic	**Molecular**	**Molten salt**	**Ionic liquid**	
				PIL	**AIL**
	Hg	**H₂O**	**NaCl**	**[CH₃CH₂NH₃][NO₃]**	**[C₄mim][PF₆]**
T_m (°C)	-38.8	0	801	12	10
T_b (°C)	356.7	100	1413	255	409
ρ (g/cm³)	13.53	0.997	1.539	1.21	1.366
μ (Pa.s)	1.526×10^{-3}	8.95×10^{-4}	12.5×10^{-4}	35.9×10^{-4}	36.9×10^{-4}
P^{sat} (Pa)	2.67	3173	12700	0.49	$<10^{-2}$
$D\times10^{-6}$ (cm²/s)	85	22.99	Na⁺: 80.1 Cl⁻: 63.5	[CH₃CH₂NH₃⁺]: 0.158 [NO₃⁻]: 0.151	[C₄mim⁺]: 1.5 [PF₆⁻]: 1.8
γ_{LV} (mN/m)	486.5	72.8	111.7	47.3	43.8
κ (S/cm)	10^5	5.5×10^{-4}	0.256	2.69×10^{-2}	1.4×10^{-3}

Cp (J/mol.K)	27.98	75.3	66.9	206	406

Density: ILs are denser than water, except pyrrolidinium dicyano-diamide and guanidinium with a density ranging from 0.9 g/cm^3 to 0.97 g/cm^3. As shown in Figure 2-8, the density of ILs declines while the number of carbons in the alkyl chain increases. Furthermore, the density of 1-methylimidazolium ILs decreases linearly with increasing temperature. An increase in the viscosity value of ILs is noticed by increasing the number of carbons in the alkyl group which exhibits a different trend, compared to the viscosity behavior for conventional organic solvents. The high viscosity of ILs is attributed to the van der Waals interactions and hydrogen bonding. Generally, the molecular interactions increase with alkyl lengthening and/or fluorination.

Luciana Tome et al. [56] showed that experimental density data of ILs are in good agreement with the Tait equation [57] for the density of liquids which is given below.

$$\rho = \frac{\rho(T, P = 0.1MPa)}{\left[1 - C\ln\frac{(B+P)}{(B+0.1)}\right]} \tag{2-7}$$

$$\rho(T, P = 0.1MPa) = a_1 + a_2 T + a_3 T^2 \tag{2-8}$$

$$B = b_1 + \frac{b_2}{T} \tag{2-9}$$

where a_1, a_2, and a_3 can be fitted to the experimental density data for different ILs versus temperature. C, b_1, and b_2 are also obtained if the density is plotted against temperature and pressure, using Equations (2-7) to (2-9).
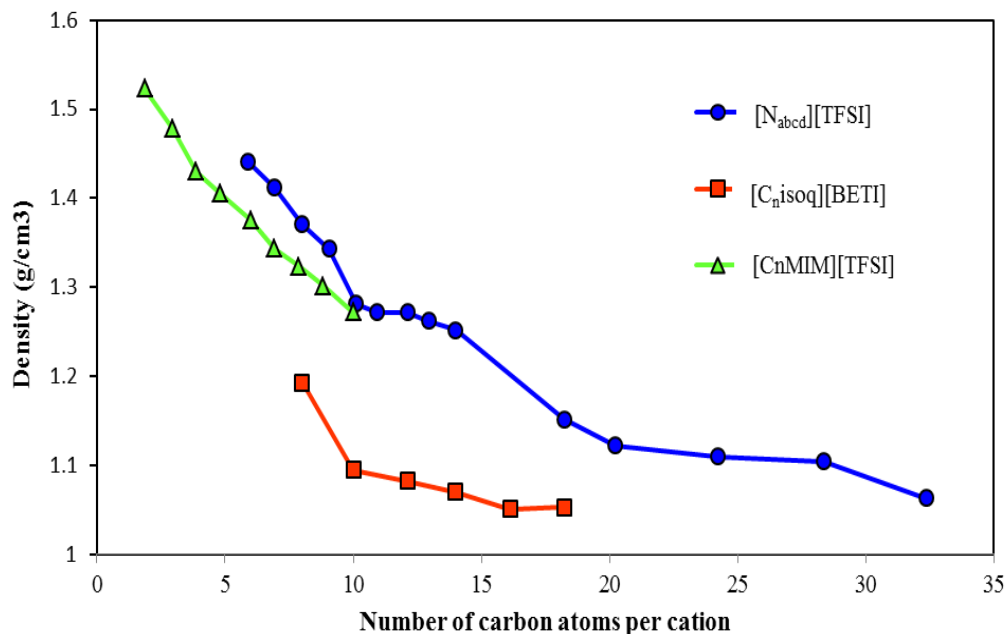
Figure 2-8: Density variation of ILs with number of carbons [25].

Viscosity: The empirical equation for the apparent dynamic viscosity (η in cP) of ILs to describe its temperature dependency is as follows [58]:

$$\eta = A e^{\varepsilon/RT} \tag{2-10}$$

where A represents a constant for a given liquid, ε is the activation energy for the viscous flow of liquid, T is the temperature in Kelvin, and R denotes the universal gas constant in J/(mol.K). Temperature and chemical additives strongly affect the viscosity of ILs. For instance, increasing temperature or/and adding organic solvents lead to a reduction in the viscosity.

The surface tension data of ILs is rare in the literature. It has been reported that ILs have a higher surface tension than conventional solvents (e.g., hexane with a surface tension of 1.8 Pa.cm); but, not as much as water (7.3 Pa.cm) [59]. For instance, the surface tensions of most imidazolium-based ILs at 298.15 K are in the range of 2.5 (Pa.cm) to 3.5 (Pa.cm).

Critical Properties: The critical properties of ILs are not readily available and should be estimated due to the decomposition phenomenon at temperatures near the boiling point. There are certain techniques/methods introduced by researchers to determine the critical properties of ILs. For instance, Valderrama and Robles [60] employed an extended group contribution method based on the concepts developed by Lydersen [61] and Joback and Reid [62] to obtain the critical properties, normal boiling point, and acentric factors of ILs. In this method, the only structure of the ILs and their molecular weights are required [63]. It is accurate enough to be used in the generalized correlations and methods based on equations of state. The absolute average deviation (AAD) of calculated and experimental liquid densities is 5 % to 6 % [63]. The critical properties and acentric factors for some common ILs are tabulated in Table 2-.

Table 2-5: The critical properties of common imidazolium-based ionic liquids [60, 64].

IL	IUPAC Name[*]	T_c (K)	P_c (bar)	V_c (cm³/mol)	ω
[bmim][PF$_6$]	1-*n*-butyl-3-methylimidazolium hexafluorophosphate	708.9	17.3	779.5	0.7553
[hmim][PF$_6$]	1-hexyl-3-methylimidazolium hexafluorophosphate	754.3	15.5	893.7	0.8352
[bmim][BF$_4$]	1-butyl-3-methylimidazolium tetrafluoroborate	623.3	20.4	672.0	0.8489

[hmim][BF₄]	1-hexyl-3-methylimidazolium tetrafluoroborat	679.1	17.9	786.2	0.9258
[N-bupy][BF₄]	*N*-butylpyridinium tetrafluoroborate	597.6	20.3	648.1	0.8307
[omim][Cl]	1-octyl-3-methylimidazolium chloride	860.1	20.3	814.2	0.6190
[emim][EtSO₄]	1-ethyl-3-methylimidazolium ethyl sulfate	1061.1	40.4	676.8	0.3368
[bmim][TfO]	1-butyl-3-methylimidazolium trifluoromethanesulfonate	1016.3	29.4	767.6	0.3677
[emim][TfO]	1-ethyl-3-methylimidazolium trifluoromethanesulfonate	985.2	35.8	653.4	0.2891
[bmim] [Nf₂T]	1-butyl-3-methylimidazolium trifluoromethanesulfonate	1265.0	27.6	1007.1	0.2656
[hmim] [Nf₂T]	1-hexyl-3-methylimidazolium trifluoromethanesulfonate	1287.3	23.9	1121.3	0.3539
[bmim] [Br]	1-butyl-3-methylimidazolium bromide	834.9	29.8	583.3	0.4891
[bmim] [dca]	1-butyl-3-methylimidazolium dicyanamid	1035.8	24.4	712.0	0.8419

*IUPAC is an acronym for International Union of Pure and Applied Chemistry

The group contribution method for the estimation of critical properties was developed by Lydersen [61]. In this approach, the critical properties of a compound are calculated based on the contribution of certain groups of atoms and the number of frequency of a group of atoms in a molecule, through the following expressions:

$$T_c = \frac{T_b}{A_L + \sum n_i \Delta T_{Li} - (\sum n_i \Delta T_{Li})^2} \tag{2-11}$$

$$P_c = \frac{M}{\left[C_L + \sum n_i \Delta P_{Li} \right]^2} \tag{2-12}$$

$$V_c = E_L + \sum n_i \Delta V_{Li} \tag{2-13}$$

in which, n_i stands for the number of times that a group appears in the molecule, T_b represents the normal boiling temperature, ΔT_{Li} denotes the contribution of group i to the critical temperature, ΔP_{Li} symbolizes the contribution of group i to the critical pressure, ΔV_{Li} is the contribution of group i to the critical volume, M is the molecular weight, and A_L, C_L, and E_L are the constants equal to

0.567, 0.34, and 40, respectively [61]. Equations (2-14) to (2-16) were also proposed by Joback and Reid [62] to determine the critical properties:

$$T_c = \frac{T_b}{A_J + \sum n_i \Delta T_{Ji} - (\sum n_i \Delta T_{Ji})^2}$$ (2-14)

$$P_c = \frac{1}{\left[C_J + D_J N - \sum n_i \Delta P_{Ji} \right]^2}$$ 2-15)

$$V_c = E_J + \sum n_i \Delta V_{Ji}$$ (2-16)

where N is the number of atoms in the molecule; A_J, B_J, C_J, D_J, and E_L represent the constants which are equal to 0.584, 0.965, 0.113, 0.0032, and 17.5, respectively [62].

The combination of Lydersen's method, Joback Reid method, and the technique proposed by Alvarez and Valderrama [65] was resulted in a proper strategy, called "modified Lydersen-Joback-Reid" method, as presented by the following equations:

$$T_b = 198.2 + \sum n_i \Delta T_{bMi}$$ (2-17)

$$T_c = \frac{T_b}{A_M + \sum n_i \Delta T_{Mi} - (\sum n_i \Delta T_{Mi})^2}$$ (2-18)

$$P_c = \frac{M}{\left[C_M + \sum n_i \Delta P_{Mi} \right]^2}$$ (2-19)

$$V_c = E_M + \sum n_i \Delta V_{Mi}$$ (2-20)

The constant parameters in Equations (2-18) to (2-20) are $A_M = 0.5703$, $B_M = 1.0121$, $C_M = 0.2573$, and $E_M = 6.75$ [58].

Valderrama et al. [60] extended the "modified Lydersen-Joback-Reid method" to ILs. Following

this strategy, the acentric factor is calculated using Equation (2-21):

$$\omega = \frac{(T_b - 43)(T_c - 43)}{(T_c - T_b)(0.7T_c - 43)} \log\left(\frac{P_c}{P_b}\right) - \frac{(T_c - 43)}{(T_c - T_b)} \log\left(\frac{P_c}{P_b}\right) + \log\left(\frac{P_c}{P_b}\right) - 1 \qquad (2\text{-}21)$$

Valderrama et al. [2] used the group contribution method with 44 defined groups and prepared the

most complete database for the critical properties of ILs.

Vapor Pressure: The vapor pressure of chemical components is required in many applications

such as separation, solvent selection, and design and operation of process equipment. According

to the literature, ILs have a negligible vapor pressure. There are a few models to predict the vapor

pressure of ILs.

The vapor pressure of ILs might be estimated through the equilibrium condition concept, implying

the same fugacity of components in both vapor and liquid phases [66].

The vapor pressure of ILs can also be calculated using the Antoine equation ($\log P^{Sat} = A - B/(T +$

C)) with water as a reference ($C = 43$). Valderrama and Sanga [64] suggested Equations (2-22)

and (2-23) to determine the two constants of A and B for twenty ILs, respectively:

$$A = \log\left[P_c(T_c - 43)(T_c - T_b)\right] \qquad (2\text{-}22)$$

$$B = \log\left[P_c(T_c - 43)\frac{(T_b - 43)}{(T_c - T_b)}\right] \qquad (2\text{-}23)$$

The values for vapor pressure are accurate based on the generalized correlations and EOSs [67].

Knudsen's strategy introduces another method to determine the vapor pressure of ILs. Knudson

equation for calculation of ILs vapor pressure is as follows [68]:

$$P^{sat} = \left(1 + \frac{kS}{S'\alpha}\right)\frac{\Delta m}{kS\tau}\sqrt{\frac{2\pi RT}{M}} \qquad (2\text{-}24)$$

where Δm stands for the mass loss during an elapsed time τ, S refers to the orifice area, k is the transmission coefficient, M signifies the molecular weight of a vapor, S' denotes the surface area of a liquid which is assumed to be equal to the cross-section area of a cell, and α represents the vaporization coefficient.

Vladimir et al. [69] measured the vapor pressure using the transpiration method and compared them with the values obtained from the Knudsen technique. They also introduced a relationship to calculate the saturated vapor pressure (P^{sat}) at different temperatures. The following equation is utilized to obtain vapor pressure [78]:

$$R\ln P^{sat} = a + \frac{b}{T} + \Delta_l^g C_p \ln\left(\frac{T}{T_0}\right) \qquad (2\text{-}25)$$

In Equation (2-25), T_0 is the reference temperature (298.15 K) and $\Delta_l^g C_p$ represents the difference between the heat capacities of gas and liquid phases [69].

Thermogravimetric analysis (TGA) is also a promising method for the rapid determination of vapor pressure. Equation (2-26) proposed by Langmuir can be used to calculate the vapor pressure based on the evaporation rate [70]:

$$\frac{dm}{dt} = \alpha\sqrt{\frac{M}{3\pi RT}}P^{sat} \qquad (2\text{-}26)$$

where dm/dt is the evaporation rate, α is the evaporation coefficient, M is the molecular weight of the vapor, and T and P^{sat} denote the temperature and vapor pressure, respectively. α depends on experimental conditions. Phang et al. [71] suggested a reference substance similar to the

experimental substance in terms of boiling and melting points and molecular structure so that α can be assumed constant. Thus, the vapor pressure of a substance S (as a sample) can be expressed by the following equation:

$$P_S^{sat} = \left(\frac{M_{ref}}{M_S}\right)^{0.5} \frac{\left(\frac{dm}{dt}\right)_S}{\left(\frac{dm}{dt}\right)_{ref}} \tag{2-27}$$

M_{ref} and M_S represent the molecular weight of the reference and sample, respectively. They concluded that the vapor pressures obtained through evaporation data are reliable where the TGA method is employed [72].

In general, the physical and thermodynamic properties of ILs including heat capacity, viscosity, density, solubility, excess enthalpies, and vapor-liquid equilibrium data of the water/CO_2/ILs mixtures are necessary to evaluate ILs for CO_2 capture and to design the absorption processes [73].

2.5. Characterization of CO₂/IL systems

Experimental Methods: It is vital to investigate the thermodynamic properties of the substances which are utilized in the CO_2 capture processes so that the appropriate equipment is chosen to attain the ultimate separation goal. There are several experimental methods developed by researchers and research centers to determine the thermodynamic properties of various ILs, CO_2, and their mixtures.

High-pressure phase equilibria experiments are traditionally classified as analytical systems when the composition is identified. They are referred to the synthetic systems if only the overall composition is known. Sub-classifications are based on the mobility of the sample. In the dynamic

systems, one or more phases are recirculated outside the equilibrium cell. However, in the static methods, the sample is agitated in a closed-cell. The volume of the cell can be constant or variable. A summary of common techniques for obtaining thermodynamic phase equilibria parameters is depicted in Figure 2-9.
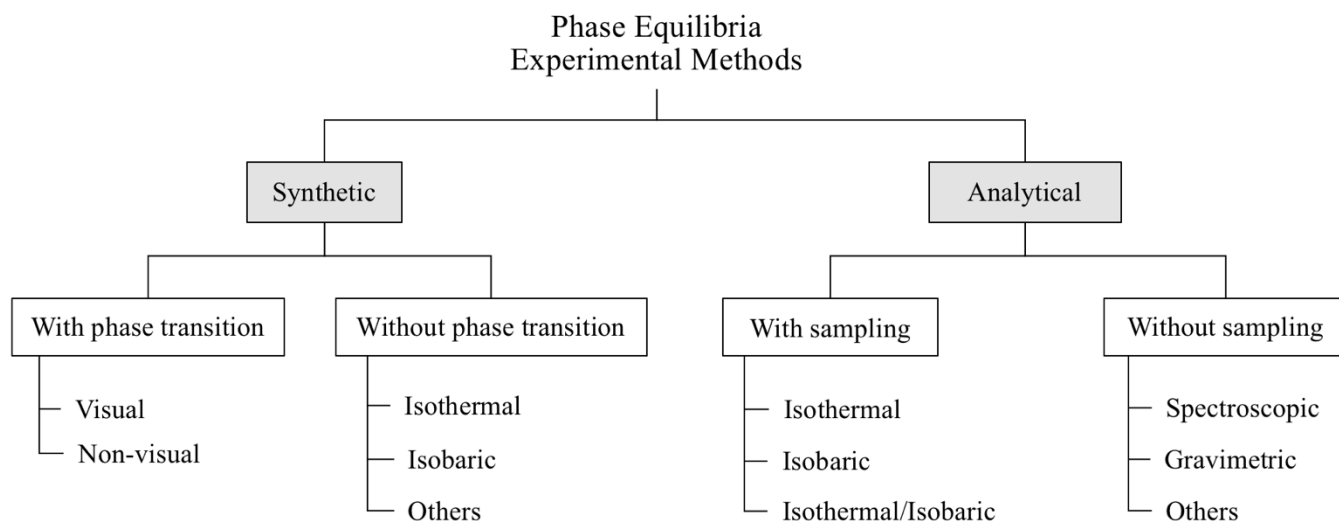
Figure 2-9: Experimental methods to obtain phase equilibria data (modified after [74]).

The common methods to determine the CO_2 solubility in an IL without sampling are the gravimetric analysis, pressure drop method, and gas chromatography. Gravimetric analysis is an analytical method that describes the quantitative determination of gas solubility through measuring the overall weight variation of a sample over the absorption process [3]. The schematic of the basic components of a gravimetric system is demonstrated in Figure 2-10(a). The pressure drop method is a synthetic technique. In this methodology, the system volume and temperature are held constant and the pressure difference is recorded during gas absorption [75]. A schematic of a pressure drop equipment is shown in Figure 2-10 (b). Since ILs have a negligible vapor pressure, the changes in pressure are assumed to be due to the gas absorption. Thus, the gas absorbed by the IL can be determined. Solubility data from a gas chromatography equipment can be achieved through employing a systematic procedure. The solvent (IL) is saturated with the solute (CO_2) and then

coated on a column. A non-absorbing carrier gas is directed into the column to extract CO_2 from the IL. The carrier gas is then analyzed in the gas chromatograph. This procedure determines the amount of absorbed CO_2 [75]. The pressure drop and synthetic methods are simpler than the gravimetric analysis and their results have higher sensitivity; but, their precision is lower [75].

(a)   (b)
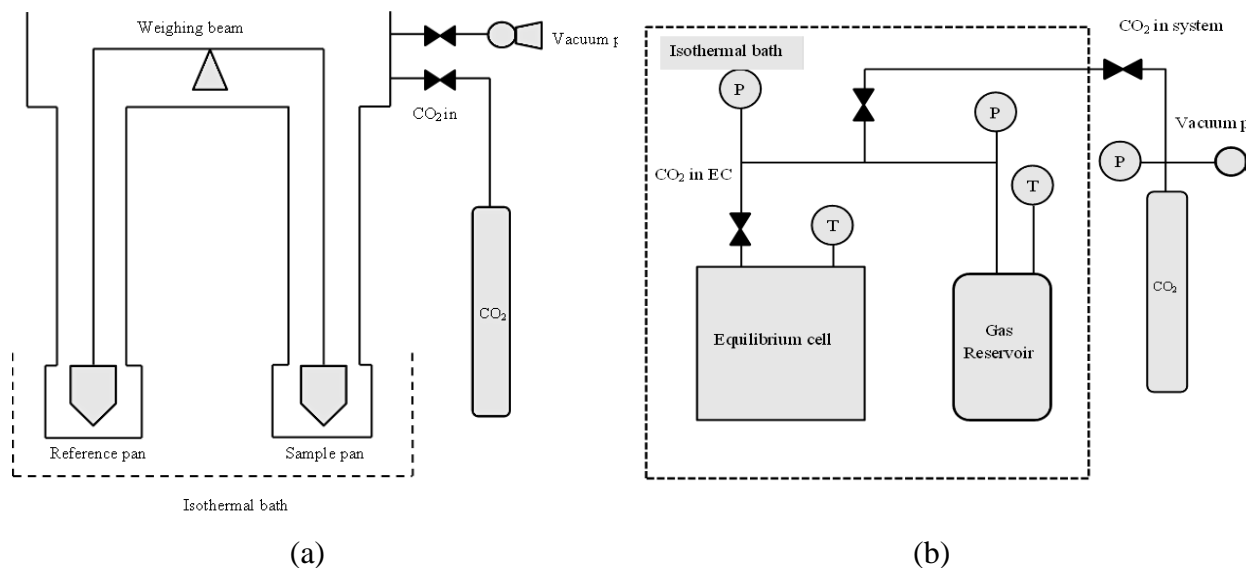
Figure 2-10: Schematics of (a) a simple gravimetric system, including basic components, and (b) diagram for pressure drop method [P and T correspond to the pressure and temperature sensors, correspondingly] (modified after [3]).

According to Blanchard, Gu, and Brennecke [76], a pycnometer with a known volume can be used to determine the density of each pure IL. The pycnometer is immersed in a constant-temperature bath and the amount of IL in the pycnometer is gravimetrically obtained where thermal equilibrium is maintained [77]. The density of ILs can also be measured using a density measuring module such as DMA 4500 (manufacturer: Anton Paar GmbH). Another method for the determination of IL density is with the aid of the proven oscillating U-tube principle that leads to a high accuracy [78].

Thermodynamic Modeling (Equations of State): It is important to study the vapor-liquid equilibrium (VLE) for the CO_2 capture processes to design and operate the separation stages [79] [54]. One of the most common approaches to correlate and predict phase equilibrium is using Equations of State (EOSs). According to Li [80], an EOS with a simple structure and reasonable accuracy are preferable, suggesting a cubic EOS is well suited to model phase equilibrium of multi-component systems. EOSs have been used to obtain the physical and thermodynamic characteristics of pure ILs and mixtures containing water, gases, and amines [63]. There are various EOSs; however, the most common EOSs are the cubic equations derived from van der Waals EOS. Among them, it has been proven that the Peng-Robinson (PR) EOS combines the simplicity and accuracy required for thermodynamic equilibrium calculations [54]. The well-known cubic EOSs are listed in Table 2-. Li [80] reported that there are four cubic EOSs which are widely used in oil and gas industries, including Peng-Robinson; Patel-Teja, Redlich-Kwong; and Soave-Redlich-Kwong.

Table 2-6: Summary of cubic EOSs widely used for VLE calculations [80].

EOS	Name	EOS or P = P(V,T)	Reference
vdW	van der Waals (1837)	$P = \dfrac{RT}{V-b} - \dfrac{a}{V^2}$	[81]
PR	Peng-Robinson (1976)	$P = \dfrac{RT}{V-b} - \dfrac{a}{V(V+b)+b(V-b)}$	[81]
PT	Patel-Teja (1982)	$P = \dfrac{RT}{V-b} - \dfrac{a(T)}{V(V+b)+c(V-b)}$	[82]
RK	Redlich-Kwong (1942)	$P = \dfrac{RT}{V-b} - \dfrac{a/T^{0.5}}{V(V+b)}$	[83]

SRK	Soave-Redlich-Kwong (1972)	$P = \dfrac{RT}{V+c-b} - \dfrac{a}{(V+c)(V+b+c)}$	[84]
PRSV	Peng–Robinson-Stryjek-Vera (1986)	$P = \dfrac{RT}{V-b} - \dfrac{a(T)}{(V+ub)(v+wb)}$	[85]

The Peng-Robinson (PR) EOS can be used with different mixing rules to model the VLE of mixtures so that it can accurately predict important parameters such as gas and liquid volumes and vapor pressure [80]. In many chemical and petroleum engineering cases, the results obtained from EOSs are well-matched with experimental data. Ren et al. [86] used the PR EOS with the van der Waals 2-parameter mixing rule to correlate VLE data for the CO_2-IL systems. A great agreement was attained between the experimental data and modeling outputs at all isotherms and pressures. However, Freitas et al. (2013) claimed that the combination of the van der Waals 2-parameter mixing rule and the PR EOS does not lead to acceptable VLE results for some multi-component systems [87]. Using a more complicated mixing rule such as the Wong-Sandler (WS) mixing rule was proposed for several multi-component mixtures. Based on Maia et al. [88], the PR EOS combined with the van der Waals and Wong-Sandler mixing rules is accurate at low pressures to model the VLE of binary systems; however, it does not offer reliable results at high pressures.

Another EOS, which is often addressed in the literature, is the Soave-Redlich-Kwong (SRK) EOS. According to Maia et al. [89], the PR EOS and SRK EOS can model the VLE data for most ternary systems with a total standard deviation of less than 0.03 and 0.04, respectively.

The general form of five-parameter EOSs is given below [90]:

$$P = \dfrac{RT}{V-b} + \dfrac{\theta(V-\mu)}{(V-b)(V^2+\delta V+\varepsilon)} \tag{2-28}$$

The parameters ε, θ, δ, and b might be constant or zero for a single component. They may depend on the composition of the mixture. These parameters are listed in Table 2-.

Table 2-7: Parameters of EOSs [90].

EOS	General EOS parameters			
	δ	ε	θ	μ
van der Waals (1890)	0	0	a	b
Redlich and Kwong (1949)	0	0	$a/(T_r^{0.5})$	b
Soave (1972)	b	0	$a\alpha(T)$	b
Peng and Robinson (1976)	$2b$	$-b^2$	$a\alpha(T)$	b
Patel and Teja (1982)	$b+c$	$-bc$	$a\alpha(T)$	b
Stryjek and Vera (1986)	$2b$	$-b^2$	$a\alpha(T)$	b

In all EOSs listed in Tables 2-6 and 2-7, parameter b is a positive constant and equal to μ. Parameters a and b are dependent on the critical properties of the component as expressed by the following equations:

$$a = a_c \, \alpha(T_r, \omega) \tag{2-29}$$

$$a_c = \frac{C_1 R T_c^2}{P_c} \tag{2-30}$$

$$b = \frac{C_2 R T_c}{P_c} \tag{2-31}$$

where the parameter α is a function of temperature and acentric factor.

C_1 and C_2 are the constants, depending on the type of EOS. C_1 is 0.0778 for Peng Robinson (PR) [81] and 0.0833 for Soave-Redlich- Kwong (SRK) [91]. C_2 is 0.4572 for PR and 0.4218 for SRK.

$\alpha(T_r, \omega)$ is a temperature-dependent parameter expressed in terms of the reduced temperature (T_r), as tabulated in Table 2-.

Table 2-8: Temperature-dependent parameter ($\alpha(T_r, \omega)$) for different EOSs [90].

Equation of state	$\alpha(T_r, \omega)$
van der Waals (1890)	1
Redlich and Kwong (1949)	$T_r^{-1/2}$

Soave (1972)	$[1+(0.48+1.574\omega-0.176\omega^2)(1-T_r^{1/2})]^2$
Peng and Robinson (1976)	$[1+(0.37646+1.5422\omega-0.2699\omega^2)(1-T_r^{1/2})]^2$
Patel and Teja (1982)	$(1+[1+(0.452413+1.38092\omega-0.295937\omega^2)(1-T_r^{1/2})]^2(1-T_r^{1/2}))^2$
Stryjek and Vera (1986)	$[1+(0.37889+1.48971\omega-0.0.171318\omega^2+0.019655\omega^3)$ $(1-T_r^{1/2})]^2+k_1(1-T_r)(0.7-T_r)$

Recently, some molecular-based models have been introduced which are more suitable for both complex and simple molecule structures. For instance, Chapman et al. [92] proposed the statistical associating fluid theory (SAFT) which uses a reference fluid that incorporates the chain length and molecular association. The reference fluid utilized in SAFT is simpler than the hard-sphere reference fluid used in most of EOSs. This EOS provides a useful thermodynamic basis through employing the chemical potential or fugacity concept to take into account the effects of molecular structure and interactions on the phase behavior and properties of fluids [11]. In late 1990, different versions of SAFT such as SAFT-VR (for potentials of variable attractive range),[93] Soft-SAFT (built from a reference Lennard-Jones fluid) [94, 95], and PC-SAFT (perturbed-chain SAFT) [96] have been developed for improving the accuracy of the reference fluid term. According to the literature, the perturbed-chain statistical associating fluid theory (PC-SAFT) is a suitable model to simulate the thermodynamic behaviors of pure ILs and binary systems of CO_2 and ILs.

The PC-SAFT equation is written in terms of Helmholtz free energy as the following:

$$\tilde{a}^{res} = \tilde{a}^{hc} + \tilde{a}^{disp} + \tilde{a}^{assoc} \tag{2-32}$$

in which, $\tilde{a}^{res}$ is the residual Helmholtz free energy of the system. The superscripts *hc*, *disp*, and *assoc* refer to a reference hard-chain contribution, a dispersion contribution, and an associating contribution, respectively. The following relationship also exists, according to PC-SAFT:

$$\tilde{a} = \frac{a}{RT} \qquad (2\text{-}33)$$

The binary interaction parameters are normally used to match the modeling results with the experimental data. In some cases, if the van der Waals 2-parameter mixing rules are incorporated in EOSs, modeling of VLE through EOS is not feasible. Based on the previous studies, the Wong-Sandler mixing rules are a proper choice while studying CO_2-IL systems [97]. Further information on the mixing rules is found in Appendix A1.

Pressure-Temperature-Composition Diagrams: To further understand the thermodynamic behaviors of CO_2/IL Systems, it seems necessary to plot pressure-temperature-composition diagrams through experimental and modeling methods so that researchers/engineers can specify the thermodynamic state of mixtures at the various process and thermodynamic conditions without conducting timely and difficult computational tasks.

In the literature, different models for obtaining VLE data with the aid of experimental data have been proposed. Generally, the Differential Evolution (DE) and Differential Evolution with Tabu List (DETL) show better performance than simulated annealing (SA), genetic algorithm (GA), and particle swarm optimization (PSO) [98]. The DE approach is based on the difference between two individuals and adding it to another individual and generating a new individual.

The pressure-temperature (P-T) diagram is depicted in Figure 2-11 for the CO_2/[omim][BF$_4$] system, based on the experimental data. The measured P-T data (isopleths) indicate the values at which the last tiny CO_2 bubble is completely dissolved in [omim][BF$_4$] at the equilibrium conditions [99]. A homogeneous liquid phase appears at higher pressures whereas, at lower pressures, gas and liquid phases co-exist: a CO_2-rich phase and a [omim][BF$_4$]-rich phase [99]. Gutkowski et al. [100] found no critical points for any of the measured isopleths. It was concluded

that the critical condition will not happen at temperatures below 363 K and pressures up to 100

MPa.
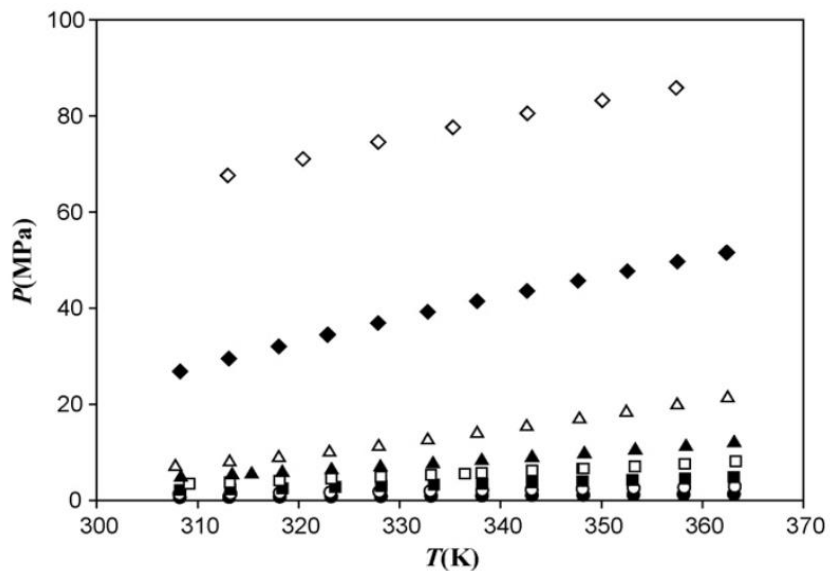
Figure 2-11: P-T diagram for the CO_2/[omim][BF$_4$] system at different isopleths for x_{CO_2}: ● 0.101, ○ 0.200, ■ 0.299, □ 0.412, ▲ 0.505, △ 0.602, ◆ 0.702, ◊ 0.752 [99].

Figure 2-12 shows a pressure-composition diagram for CO_2 in ten common imidazolium-based ILs where the pressure is plotted against the CO_2 mole fraction at 298 K [101].
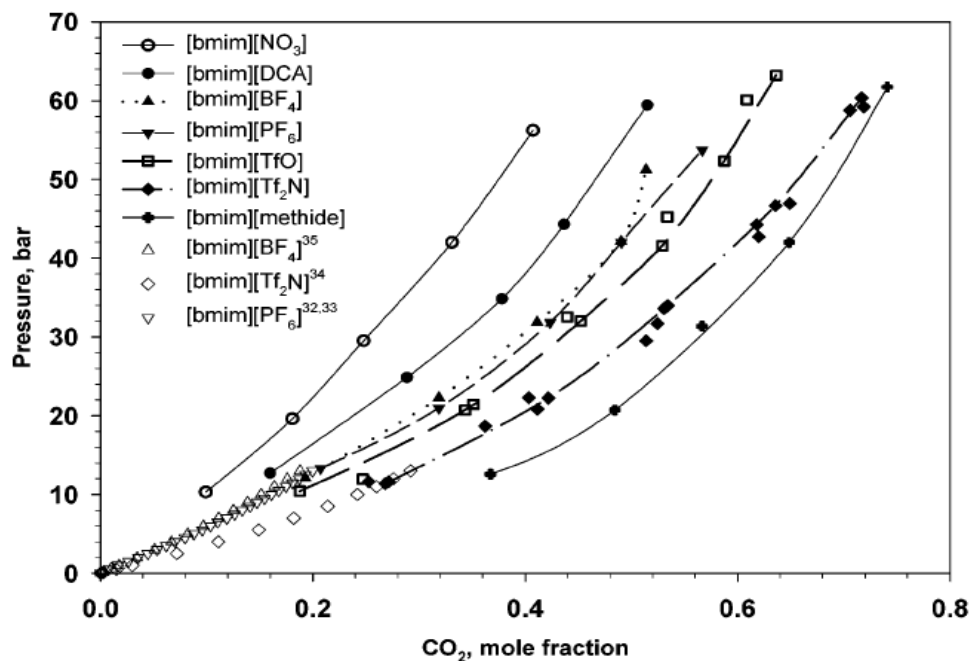
Figure 2-12: Effect of the anion and pressure on the solubility of CO_2 in [bmim] cation based ILs at a temperature of 298 K [101].

Another approach to attain appropriate and reliable properties of ILs and to experience high gas solubility of amines is using mixtures of ILs and amines. For example, Camper et al. [102] used two mixtures of alkanolamines, namely MEA and DEA with [Rmim][Tf₂N] ILs. Figure 2-13 demonstrates CO_2 uptake by two mixtures of ILs-amine. They observed that the absorption performance of the ILs-amine mixture is higher than pure amines and the desorption energy is lower. Furthermore, they do not exhibit the drawbacks of functionalized ILs.
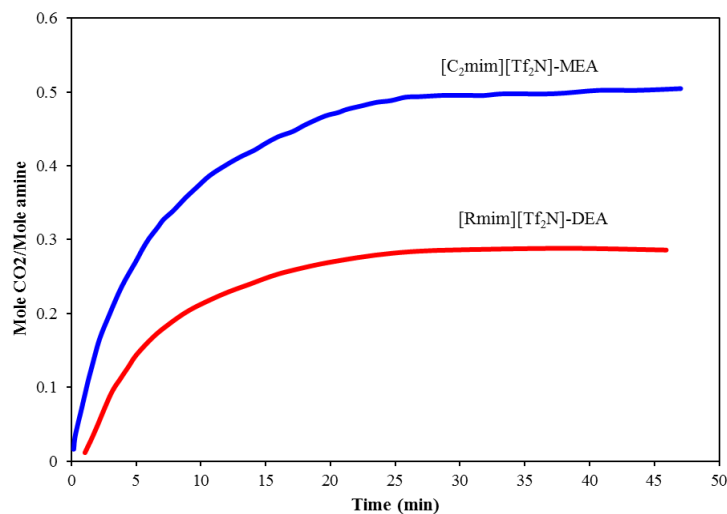
Figure 2-13: CO_2 uptake in equimolar solutions of [C_2mim][Tf_2N]-MEA and [Rmim][Tf_2N]-DEA (modified after [102]).

Optimization algorithms are an important element for properly controlling processes and developing mathematical models with optimal variables [103]. Algorithms simplify calculations and can be used to help researchers determine the VLE data. This is vital as pressure-temperature -composition diagrams can provide important thermodynamic data through a simple, straightforward, and understandable manner.

Particle swarm optimization (PSO) is an algorithm based on a social-psychological metaphor; a population of individuals (referred to particles) adapts by returning stochastically towards previously successful regions [104]. According to Lazzús [104], the PSO algorithm is appropriate to obtain the optimal values of important parameters involved in the VLE of binary systems containing supercritical fluids and ILs. Providing further information, the proposed PSO algorithm evaluates the binary interaction parameters with high accuracy. Lazzùs [104] compared the results obtained from the PSO and Levenberg-Marquart (LM) algorithms. It was found that the PSO

algorithm estimates VLE information of the system more accurately than LM. The flow diagram of the PSO algorithm to determine VLE data is shown in Figure 2-14.

Lazzus [105] also introduced a hybrid model including artificial neural network (ANN) and particle swarm optimization (PSO) for prediction of the thermodynamic properties.
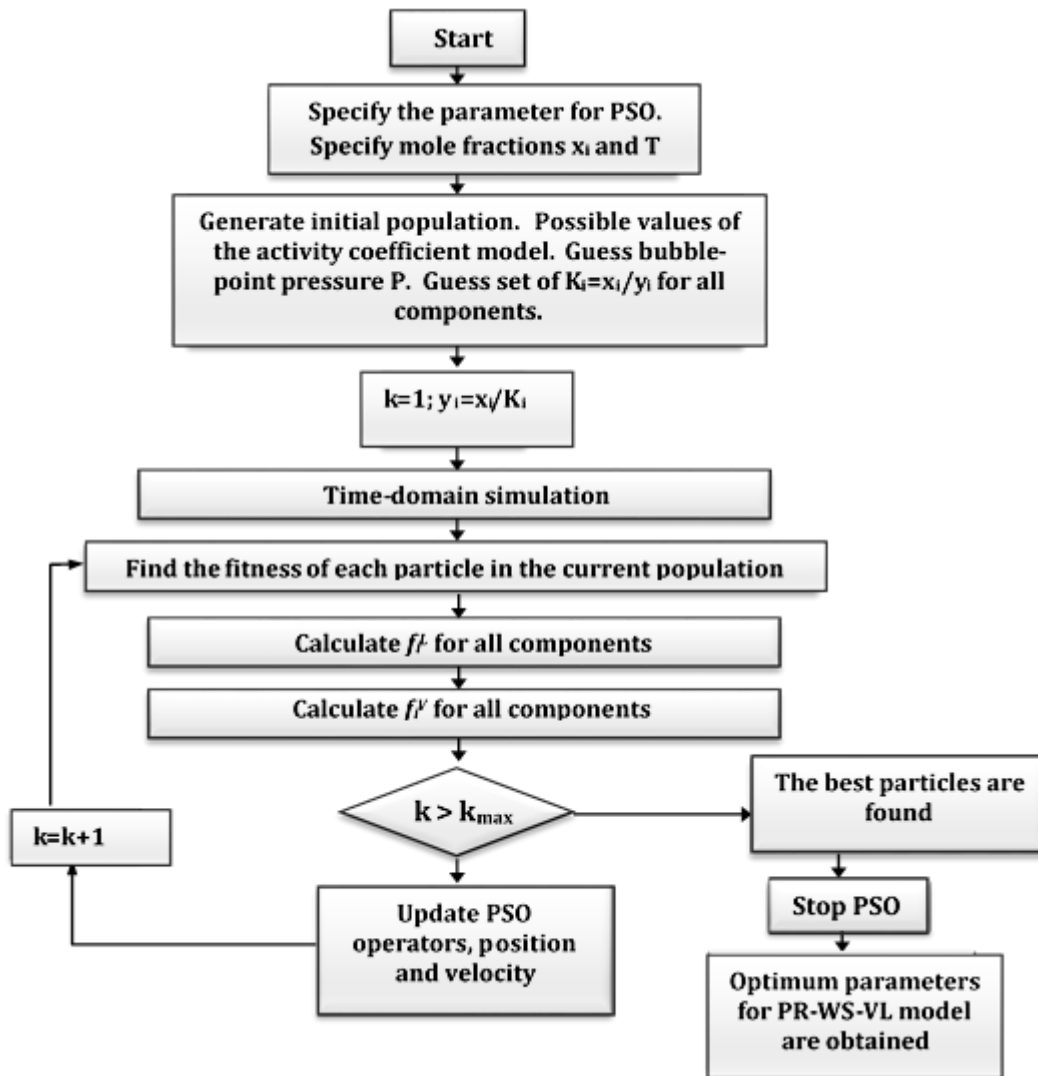
Figure 2-14: PSO algorithm diagram for vapor-liquid equilibrium modeling [104].

Experimental and Modelling Data for Thermodynamic Properties: There are advantages and disadvantages with both experimental and modeling approaches to forecasting the thermodynamic properties and behaviors of CO_2-IL systems. Experiments provide useful thermodynamic information. However, conducting experiments is costly and time-consuming. The cost associated with the experiments also limits the amount of ILs to be used in the tests. On the other hand, the modeling data are associated with some inherent errors due to assumptions, convergence, and solution method drawbacks [106]. Table 2-2, Table 2-3 and Table 2-4 represent the experimental CO_2 solubility data for imidazolium, phosphonium, pyridinium, pyrrolidinium, and functionalized ILs. It is important to compare experimental and modeling data to ensure that the appropriate model is chosen for the process and the model is accurate enough to predict the system's behaviors. Table 2- shows the absolute average deviations, in percentage, between the experimental and modeling data of the PC-SAFT EOS and PR EOS where Wong-Sandler/Van Laar (WS/VL) mixing rules and van der Waals (vdW) mixing rules are employed. These results show that the PR/WS/VL model predicts the high-pressure solubility of CO_2 in $[C_n\text{-mim}][Tf_2N]$ more accurate than PR/vdW model under pressures up to the supercritical region of CO_2 [97]. PC-SAFT EOS was used to compare the experimental solubility data of CO_2 in the imidazolium-based ILs. It was found that PC-SAFT EOS can estimate the solubility in a good agreement with experimental data [11]. PC-SAFT parameters can be determined using a correlation in terms of density and vapor pressure data of ILs. Hence, the parameters can be obtained without carrying out experiments. The binary interaction of ILs (as discussed before) is temperature dependant and increases linearly with temperature. The binary interaction can be obtained by curve-fitting of the experimental vapor-liquid equilibrium data, and a correlation can be determined using the group contribution method.

As shown in Table 2-, PC-SAFT EOS estimates the solubility of CO_2 in ILs with higher accuracy, compared to cubic EOSs.

In recent years, advanced EOS have been developed in the framework of statistical mechanics and have been proven promising due to their capability to accurately simulate complicated systems [104, 105]. Arguably, the most widely used EOSs in this context are the Statistical Associating Fluid Theory (SAFT) and the Perturbed Chain-SAFT (PC-SAFT) [107].

The SAFT and PC-SAFT EOSs were proposed to overcome the drawbacks of cubic EOSs, especially in estimating the density and compressibility factor of liquid phases. The cubic EOSs do not consider the effect of association and cross association of molecules on the phase equilibria. This will be an important feature in the IL-CO_2 systems. The PC-SAFT EOS incorporates the influence of molecular association on the volume and energy, and can potentially predict a more precise and reliable phase behavior when the association between the molecules becomes important. The SAFT parameters have physical significance, featuring diameter, number of segments, and segment-segment interactions [108]. Therefore, the SAFT EOSs consider the effect of molecular structure and interactions on the bulk properties and phase behavior, unlike the cubic EOSs that assume molecules as a hard-sphere [11].

Based on the experimental and modeling investigations available in the literature, the proper cubic EOSs to reasonably simulate the thermodynamic behaviors of CO_2-IL systems are also reported in this study (see Table 2-) where modifications on the mixing rules and interaction terms of the cubic EOSs have been made to attain a good agreement between the real data and modeling outputs [78].

As Equation (2-34) shows, AAD in Figure 2-9 stands for the average absolute deviation which represents the difference between the experimental and calculated target parameter(s).

$$AAD(\%) = \frac{100}{n_{pts}} \sum_{i=1}^{n_{pts}} \left| \frac{P_i^{sat,\exp} - P_i^{sat,cal}}{P_i^{sat,\exp}} \right| \qquad\qquad (2\text{-}34)$$

in which, n_{pts} represents the number of data points.

Table 2-9: Average absolute deviations of experimental and calculated data for equilibrium (saturation) pressure [11, 109].

Models	Ionic liquids	AAD (%)		
		303.15 K	**313.15 K**	**Average**
PR/WS/VL	[C₂-mim][Tf₂N]	4.5	4.1031	4.3015
	[C₄-mim][Tf₂N]	5.4092	3.91	4.6596
	[C₆-mim][Tf₂N]	5.8032	4.811	5.3071
	[C₈-mim][Tf₂N]	4.798	4.9773	4.8876
PR/VdW	[C₂-mim][Tf₂N]	12.0	13.5	12.75
	[C₄-mim][Tf₂N]	11.71	11.0	11.35
	[C₆-mim][Tf₂N]	9.7	9.6	9.65
	[C₈-mim][Tf₂N]	10.6	9.9	10.25
PC-SAFT	[C₂-mim][Tf₂N]	4.418	3.901	4.159
	[C₄-mim][Tf₂N]	4.934	6.920	5.927
	[C₆-mim][Tf₂N]	8.233	6.714	7.473
	[C₈-mim][Tf₂N]	8.056	9.171	8.613

Table 2-2: CO_2 solubility experimental data for imidazolium-based ionic liquids.

Ionic Liquid	T (K)	P (bar)	Max Solubility[*] (mol CO₂/mol IL)	H (bar)	References
[hmim][FEP],	283.15, 298.6 ,323.2	0.297-18.1	0.517	18.5	[110]
[bmpyrr][FEP],			0.498	20.3	
[ETT][FEP]			0.497	20.8	
[bmim][PF₆]	293-393	1-97	0.555	12	[111]
[bmim][PF6]	283-348	0.096-19.99	0.379	34	[112]
			0.364	38	
[bmim][BF4]					
([bmim][PF₆]	313.15, 323.15, 333.15	0.97-92	0.729	N/A	[76]
[C₈mim][PF₆]),			0.755		
[C₈mim][BF₄]),			0.513		

([bmim][NO$_3$]			0.708		
[emim][EtSO$_4$],			0.579		
[N-bupy][BF$_4$]			0.423		
[C$_2$-mim][Tf$_2$N]	301-344.4	10-43	0.761		[113]
[C$_4$-mim][Tf$_2$N]			0.803		
[C$_6$-mim][Tf$_2$N]			0.833		
[C$_8$-mim][Tf$_2$N]			0.845		
[bmim] [DCA]	298.15, 313.15, 333.15	1-120	0.55		[101]
[bmim] [NO$_3$]					
[bmim] [BF$_4$]			0.52		
[bmim] [PF$_6$]			0.64		
[bmim] [TfO]			0.64		
[bmim] [Tf$_2$N]			0.68		
[bmim] [methide]			0.76		
[bmim][NO$_3$]			0.44		

[*] Maximum solubility in the range of tested operating conditions.

Table 2-3: CO_2 solubility for phosphonium, pyridinium, and pyrrolidinium ionic liquids.

Ionic Liquid	T(K)	P(bar)	Max Solubility[*] (mol CO$_2$/mol IL)	H (bar)	References
[THTDP][NTf$_2$]	293.2-363.2	1.06-375	0.879	19.8	[114]
[THTDP][Cl]			0.8	18.9	
[N-bupy][BF$_4$]	313.15,323.15, 333.15	0.97-91.9	0.581		[76]
[P$_{(14)666}$][Cl]	303.15	1		36	[115]
[P$_{(14)666}$][DCA]			0.033	29	
[P$_{(14)666}$][Tf$_2$N]				37	
[P$_{(2)444}$][DEP]				59	
[P$_{(14)444}$][DBS]				29	
[N$_{(4)113}$][Tf$_2$N]				65	
[N$_{(6)113}$][Tf$_2$N]				53	
[N$_{(10)113}$][Tf$_2$N]				43	
[N$_{(4)111}$][Tf$_2$N]				61	
[N$_{(6)111}$][Tf$_2$N]				N/A	
[N$_{(10)111}$][Tf$_2$N]				44	
[N$_{(1)888}$][Tf$_2$N]			0.034	29	
[N$_{(6)222}$][Tf$_2$N]				60	
[hmpy][Tf$_2$N]	283	1-10	0.2	25.8	[116]

[*] Maximum solubility in the range of tested operating conditions.

Table 2-4 shows the CO_2 solubility for functionalized ionic liquids at two different temperatures and pressures. Providing further clarification on Table 2-4, the functionality of NH_2 -Cation means that the group of NH_2 is attached to a chemical group in the IL to form the cation part of the functionalized IL. NH_2 -Anion refers to the combination of the NH_2 group and a chemical branch in the IL structure to hold a negative charge, leading to the formation of the anion part of the functionalized IL.

Table 2-4: CO_2 solubility for functionalized ionic liquids.

Ionic Liquid	Functionality	P(bar)	T(K)	Max Solubility (mol CO_2/mol IL)	H (bar)	References
[P_{66614}][Ile]	NH_2 -Anion	0-1.5	295.15	0.5	26	[117]
[P_{66614}][Sar]	NH_2 -Anion			0.523	1000	
[P_{66614}][Gly]	NH_2 -Anion			0.574	5.5	
[P_{66614}][Pro]	NH_2 -Anion			0.56	1000	
[P_{66614}][Met]	NH_2 -Anion			0.568	18	
APMim[NTf_2]	NH_2 -Cation	0-10	303	0.26		[118]
APMim[DCA]	NH_2 -Cation			0.29		
APMim[BF_4]	NH_2 -Cation			0.33		
AEMPyrr[BF_4]	NH_2 -Cation			0.27		
MeImNet2[BF_4]	NR_3- -Cation			0.25		
Bmim[Tau]	NH_2 -Anion			0.44		
Bmim[Gly]	NH_2 -Anion			0.4		

Effect of ions on Thermodynamic Behaviors: ILs are composed solely of anions and cations. It implies that there are many different combinations of ions that can be used to tailor ILs for various purposes. According to the literature, certain anions and cations offer higher performance for CO_2 capture processes. Brennecke and Maginn [119] found from their research study that the types of cations and anions significantly affect the chemical, physical, and thermodynamic properties of ILs. For instance, the anion part of ILs has the greatest effect on the solubility. According to Freitas et al. [87], the solubility is strongly related to the energy of vaporization and molar volume. As

most of ILs have high energy of vaporization, ILs with larger anions have higher molar volumes, leading to greater CO_2 dissolution. It has been confirmed that the alkyl chain length of the cation has a major impact on the solubility of CO_2 in ILs. The alkyl group increases the dispersion forces of the cation for better interaction with CO_2, implying that growing the length of the alkyl chain leads to an increase in the CO_2 solubility [120].

The type of ions can also influence the melting point of the ILs. It was found that the melting point shows an ascending trend with increasing the chain length. When an IL contains a halide as an anion, the melting point is higher, compared to the cases having other anions [121].

The miscibility and hydrophobicity of ILs with water are also affected by the type of ions. For example, 1-alkyl-3-methylimidazolium hexafluorophosphate ILs are immiscible with water, while 1-alkyl-3-methylimidazolium nitrate ILs are completely miscible with water. Similarly, the hydrophobicity of an IL increases with increasing the chain length of the alkyl chain [122].

There is a correlation between the cation and the density where Uygur [90] concluded that the density of the IL lowers with increasing the alkyl chain length for the imidazolium cation case.

2.6. CO_2 solubility and selectivity

Flue-gas in practice contain various gases and impurities. Hence, the selectivity and solubility of CO_2 in ILs concerning various gases such as N_2, CH_4, H_2, and H_2S should be evaluated. In this section, the solubility of CO_2 in ILs and its selectivity in the presence of different gases will be discussed.

CO_2 Solubility in ILs: It has been found that anions have a higher impact, compared to cations, on the solubility of CO_2 in ILs [122]. The CO_2 solubility in ten distinct imidazolium-based ILs was evaluated by Sudhir et al. [99]. They observed that the highest and lowest CO_2 solubility can

be obtained in the ILs with fluoroalkyl groups in the anion part (e.g., [methide] and $[Tf_2N]^-$) and nonfluorinated inorganic anions (e.g., $[NO_3]^-$ and $[DCA]^-$), respectively. Their experiments also showed that the solubility strongly depends on the type of anions. However, in a smaller extent, the CO_2 solubility can be affected by the selection of alkyl groups on the cation part. In general, when the length of the alkyl chain increases from butyl to octyl, the CO_2 solubility increases [99]. Molecular simulations show that the imidazolium-based ILs have better performance in terms of CO_2 capture than phosphonium-based ILs, where the same cation and anion are in the structure of ILs. For instance, $[Tf_2N]^-$ is more efficient, compared to $[PF_6]^-$ [123]. Zhang et al. [108] used COSMO-RS and conducted a series of experiments to investigate CO_2 capture with ILs. They determined Henry's law constants of CO_2 with different combinations of cations and anions. Their results implied that [FEP] anion has the greatest CO_2 solubility. Their experiments on three different cations with [FEP] anion revealed that CO_2 is more soluble in [hmim][FEP] (imidazolium-based IL) than other ILs. Solubility and other properties including Henry's law constant, enthalpies, and entropies of nine gases dissolved in common imidazolium-based IL ([bmim][PF_6]) were studies where the pressure was up to 13 bar and three distinct temperatures (10, 25, and 50 °C) were examined. The experimental results showed that the highest and lowest solubilities in [bmim][PF_6] are obtained for carbon dioxide and oxygen, respectively. It was also concluded that [bmim][PF_6] (compared to common organic solvents) is not a very good solvent for reactions containing H_2, O_2, and CO (e.g., hydrogenation reactions, oxidation reactions, and hydroformylation reactions) for industrial purposes at extremely high pressures [19]. The solubility of CO_2 in ILs is an important factor to screen proper solvents and to design an efficient absorption system in CO_2 capture plants [123]. The solubility of gases in liquid solvents using Krichevsky-Kasarnovsky [124] equation is obtained as follows:

$$\ln\frac{f_2(T,P)}{x_2} = \ln H_2(P^{sat}) + \frac{V_2^{\infty}(P - P^{sat})}{RT}$$

(2-35)

where $f_2(T, P)$ represents the fugacity of gas solute in the gas phase at temperature T and pressure P; x_2 is the mole fraction of the gas dissolved in the liquid solvent; P^{sat} denotes the saturation or vapor pressure of the liquid solvents; V_2^{∞} refers to the partial molar volume of the gas at the infinite dilution of the liquid solvents; H_2 stands for Henry's law constant of the gas in the liquid solvents; R signifies the universal gas constant; T is the temperature of the system. The Krichevsky-Kasarnovsky equation is often used to obtain Henry's law constant from solubility data [124]. Thus, this equation is only limited to predicting the solubility of a gas in a liquid at low solubility conditions and should be avoided for the cases of CO_2 solubility in an IL with high magnitudes of solubility. It should be noted that Henry's law is valid only if the concentration of a component in the liquid phase is minor.

The fugacity of a pure gas can be determined using the following equation:

$$f_2(T,P) = \phi(T,P)P$$

(2-36)

in which, ϕ refers to the fugacity coefficient at pressure P and temperature T. This thermodynamic property can be obtained using various EOSs such as SRK and PR [38].

Maia et al. [89] claimed that all cubic-modified EOSs lead to almost the same accuracy while determining the solubility. In many cases, the Peng-Robinson (PR) and modified PR EOSs are appropriate EOSs to model the gas solubility. The PR EOS combined with the Wong-Sandler/UNIQUAC mixing rules can be used to estimate Henry's law constant, which provides the gas solubility in a liquid solvent when the gas concentration in the liquid phase is small. This strategy helps to obtain the limiting slope defined by Henry's law as the solubility approaches zero [125]. According to Carvalho et al. [114], this methodology results in uncertainty that considerably

affects the accuracy and reliability of the model outputs. Other models such as Predictive Peng-Robinson, Peng-Robinson-Stryjek-Vera, and Sanchez-Lacombe EOSs have been utilized to determine the gas solubility in ILs, exhibiting an error percentage of less than 9.0 % [39].

CO_2 Selectivity: Due to the presence of gases and impurities in the flue-gas, the selectivity of CO_2 in ILs appears to be vital in the carbon capture technique with ILs [127]. To systematically study the solubility of CO_2 in ILs, CO_2 selectivity in ILs needs to be investigated [128]. According to Zhang et al. [129], conventional ILs have greater CO_2 selectivity, compared to other gases (e.g., CO, H_2, and O_2) due to the large quadrupole moment of CO_2. Since there is a mixture of different gases in the flue-gas, this high CO_2 selectivity is interesting, implying that ILs absorb CO_2 easier than other gases. In general, the solubility of CO_2 in ILs is higher than N_2 and H_2. However, the solubility of H_2 and N_2 exhibits an increase with increasing temperature [33, 130]. In CO_2/H_2S systems, CO_2 selectivity is highly dependent on CO_2/H_2S feed ratio and CO_2 solubility is remarkably decreased in the presence of H_2S [36]. Mahinder Ramdin et al. [131] showed that the selectivity of CO_2/CH_4 in different phosphonium and imidazolium-based ILs significantly decreases with increasing temperature.

It seems necessary to optimize CO_2 selectivity in ILs in terms of gas composition and operating conditions. The selectivity generally increases the number of stages required for CO_2 capture processes and consequently the operating and capital costs. For instance, in the case of CO_2/H_2S /CH_4 systems at high temperatures, an additional step is required to separate H_2S and CH_4 from CO_2 [128].

2.7. CO_2 capture using ILs: performance and modifications

As discussed in the introduction, carbon capture processes, in general, are divided into three main categories including pre-combustion, post-combustion, and oxy-combustion. Among these

methods, the post-combustion is appropriate for retrofit plants and the industrialized absorption methods mainly employ post-combustion technology. The current solutions for the absorption method are amine-based solvents since they have a high CO_2 capacity. The practical applications of ILs for CO_2 capture depend on their effectiveness, compared to the amines. It is believed that ILs can be tailored to have a comparable CO_2 capacity without having the disadvantages associated with amine-based solvents.

Due to the volatility of amine-based solvents, the processes, which use this type of solvents, consume a high amount of energy during the solvent regeneration stage which leads to an extra cost to the entire CO_2 capture process. This cost can be significantly lowered or even eliminated through using ILs as the non-volatile solvents. The amine-based solvents are not environmentally friendly due to their volatility nature. They are unstable, resulting in producing dangerous toxic materials such as nitrosamines, nitramines, and amides. It should be noted that nitrosamines are of the most concern as they are carcinogenic and noxious to humans even at low concentrations [3]. ILs due to their negligibly low vapor pressure are considered non-volatile. It means that they do not vaporize and therefore do not contaminate the atmosphere. Therefore, solvent losses are negligible. Amines also participate in various parts of absorption processes and produce waste which can eventually corrode the equipment. However, ILs are not usually corrosive due to their high thermal and chemical stability. ILs are normally degraded at temperatures higher than 300 °C and only cause corrosion to equipment if there are impurities in the ILs [3].

Conventional ILs capture carbon through physical absorption mechanisms. Although adjusting cations/anions in the ILs can enhance the solubility of CO_2 in conventional ILs, their CO_2 capture capacity is still low in comparison with the current commercial carbon capture technologies such as amine-based solvents [32]. Indeed, there are strong chemical interactions between amine and

CO_2 ($-\Delta H$ = 80–130 kJ/mol) in the amine-based solvents which make amines favorable for CO_2

molecules. However, in the case of conventional ILs/ CO_2 systems, there are comparatively weak

forces ($-\Delta H$ = ~15 kJ/ mol) between ILs and CO_2 molecules [29]. Among alkanolamines as the

most common solvents for the absorption purpose, mono ethanol amine (MEA) is more efficient

than other amines. The order of absorption rate for amines is as following:

MEA>DEA>AMP>DIPA>MDEA [126]. Popular solvents for the physical absorption processes

are DEPG (Selexol process), methanol (Rectisol process), NMP or N-methyl-2-pyrrolidone

(Purisol process), Morphysorb process, and Propylene Carbonate (Flour process) [127]. A general

comparison between CO_2 capture processes through conventional ILs and the most commonly

used commercial solvents are provided in Table 2-5 [128].

Table 2-5: Comparison of properties of ILs with common solvents used for CO_2 capture [127-129].

Variable	Chemicals for CO_2 capture				
	Conventional ILs	Task-Specific ILs	MEA (30%wt)	DEPG	PC
Absorption type	Physical	Chemical	Chemical	Physical	Physical
Viscosity (cP)	20-2000	50-2000	18.98	5.8	3.0

Vapor pressure (bar) at 25°C	1.33e-9	1.33E-9	8.5E-4	9.73E-7	1.13E-4
ΔH_{abs} (kJ/mol CO_2) at 1bar and 40°C	~10- 20	~40-50	~85	~14.3	~15.9
CO_2 solubility (mol/mol) at 1bar and 20-40 °C	>2.51	1.6	50-85	3.63	3.41
Selectivity CO_2/CH_4	8-35		n/a	15	26
H_2S/CO_2	2-10		1-2	8.8	3.3
CO_2/H_2	50-150		n/a	77	126
CO_2/N_2	30-100		n/a	50	117
Cost	200 $/5 gr	400$/5gr	370 $/1L	80 $/1L	117 $/1L

As provided in Table 2-5, pure conventional ILs are not a promising option for the CO_2 capture processes. To overcome this drawback, task-specific or functionalized ILs with the ability of chemisorption rather than physisorption have been developed. In this type of ILs, suitable moieties such as amines are introduced in the conventional ILs [130]. In this property-modification process, CO_2 -philic functional groups are attached to ILs which can significantly increase the CO_2 capture capacity of ILs [131]. Task-specific ILs in the broad classification is divided into three groups including; cation-functionalized ILs, anion functionalized ILs, and dual amino-functionalized ILs. The experimental results show that the reaction mechanisms between the amine-functionalized IL and CO_2 are similar to the mechanisms between the organic amine and CO_2. The carbon capture capacity of task-specific ILs is also comparable to alkanolamines [9].

Complicated synthesis and purification steps, high viscosity which leads to slow CO_2 diffusion mass transfer, and high production cost are the main challenges to use functionalized ILs for CO_2 capture [132]. For instance, Camper et al. [102] concluded that the synthesis of amine-functionalized imidazolium-based ILs requires several steps, implying that the process is not economical compared to the absorption processes that utilize conventional solvents such as MEA. Therefore, to improve CO_2 capture capacity and to avoid these drawbacks, mixing ILs with other appropriate compounds such as water and amines are proposed. In this approach, solubility

increases due to the viscosity reduction of IL in the presence of water [128]. This mixture preserves the favorable properties of ILs for CO_2 capture and overcomes the inherent drawbacks of ILs including high viscosity and cost [133]. A mixture of alkanolamines such as MEA and an IL can also increase energy efficiency, absorption rate, and CO_2 absorption capacity [11]. There are some research studies in the literature, focusing on this challenging topic [102, 134-136]. Common IL-amine mixtures are MEA + 1-butyl-3-methylimidazolium tetrafluoroborate ([bmim][BF_4]) + H_2O and MEA + 1-(2-hydroxyethyl)-3-methylimidazolium ([hemim][DCA]) + H_2O. Xu et al. [137] conducted several experiments and found that the viscosity of two ILs, known as 1-(2-hydroxyethyl)-3-methyl-imidazolium dicyanamide ([C_2OHmim][DCA]) and 1-butyl-3-methylimidazolium ([Bmim][DCA]), which are 50 mPa.s and 7 mPa.s at 313.15 K respectively, lowers to 3.54 mPa.s through mixing with amine (MEA). According to another study carried out by Yang et al. [135], the viscosity of an IL-amine solution including [bmim][BF_4] (as an IL) is 3.54 mPa.s at 323 K, which is much lower than the viscosity of the conventional [bmim][BF_4] (e.g., 31.08 mPa s). The low viscosity of the IL-amine systems conveys the message that a higher mass transfer occurs where they are in contact with CO_2 such that more CO_2 is absorbed at a faster rate which is favourable for the CO_2 capture operations.

It should be noted that when the conventional amines are used for CO_2 capture, the energy consumption is fairly high which can be considerably decreased by utilizing an IL-amine system [102]. Based on the literature, when the content of ILs is 30 wt%, the energy consumption lowers by 27%, in contrast to the conventional MEA processes. However, if the concentration of ILs is lower than 10 wt%, the presence of ILs in aqueous 30 wt% MEA might decrease the required energy during the regeneration process without affecting the absorption efficiency/performance [137]. This increase in energy efficiency would be beneficial as it would cause a decrease in the

total costs of CO_2 capture processes. Table 2-6 summarizes various characters of three types of IL mixtures discussed in this section.

Table 2-6: Summary of advantages and disadvantages of three ionic liquid (IL) mixture systems [3].

Type	Advantages	Disadvantages
Conventional ILs (CILs)	• High CO_2 selectivity • Lower energy consumptions than conventional solvents	• High viscosity
Task-specific ILs	• Higher CO_2 storage capacity, compared to CILs (due to functional groups)	• Higher viscosities, compared to CILs • Complicated synthesis processes
IL-alkanolamine-water mixture	• Lower viscosities, compared to CILs • Higher CO_2 dissolution, compared to CILs	• Not environmentally friendly as pure ILs • Amine loss and energy consumption lower than amines but higher than CILs

Recently, a new generation of task-specific ILs such as super base and amino acid ILs with an equimolar CO_2 absorption capacity has been introduced. In the super basic task-specific ILs, the CO_2 molecule from C atom is bonded to the nitrogen atoms in the anionic part of ILs, as shown in Figure 2-15. Amino acids contain a carboxylic acid and an amino group which can be utilized as either an anion or a cation. Amino acid ILs have a promising carbon capture characteristic due to the presence of two functional groups, including carboxylic and amino groups. Furthermore, these ILs are more biodegradable, biocompatible, and easily producible in large scales with low cost [138]. The general reaction of amino acid IL production is illustrated in Figure 2-16 [139].
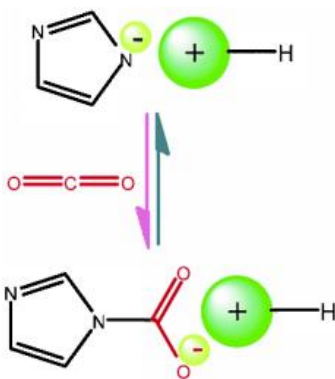
Figure 2-15: CO_2 absorption mechanism of super basic ILs [140].
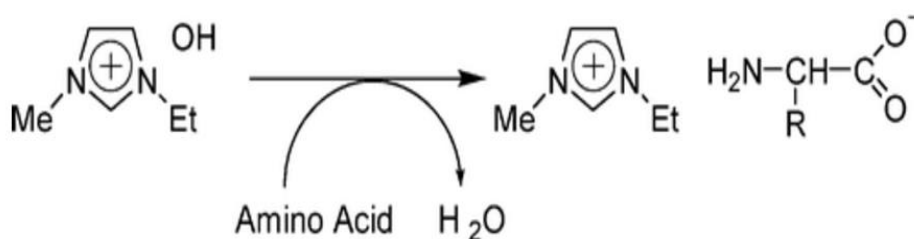
Figure 2-16: General reaction leading to production of amino acid IL [139].

Recently, deep eutectic solvents (DESs) have been introduced as a new class of ILs. They have most of the promising properties of ILs and they are economically comparable to the amines for CO_2 capture. DESs are synthesized by ammonium and phosphonium salts with different hydrogen bond donors (HBDs) such as urea. Some DESs offer a higher CO_2 solubility and a lower viscosity, compared to ILs. Moreover, functionalized DESs promote higher solubility for CO_2, compared to the conventional DESs [143,145,146]. It is important to note that CO_2 solubility in amine-based DESs such as ChCl-DEA is much higher than conventional DES and 30% (by weight) aqueous amines [141, 142].

2.8. Economic analysis of CO_2 capture using ionic liquids

Currently, ILs are not as commercially available as other solvents such as amine-based solvents. They are usually used at the lab scale which varies the industrial scale in terms of efficiency, operation, and cost. According to Waseem Arshad [143], there are several vendors such as Merck, Sigma Aldrich, DuPont, Fluka, Scionix, Chemada, and Degussa that provide ILs for various purposes; however, most of ILs are produced at the laboratory scales and their prices are in the range of $1/g-$10/g. The cost should be reduced by a factor of approximately 100 or greater to be comparable with that of the conventional solvents. Ramdin et al. [29] reported that the lab-scale cost of ILs is around $1000/kg, which is 100-1000 times more expensive, compared to the conventional solvents. This price is expected to drop by $40/kg to $100/kg according to the BASF company when ILs are produced at larger scales; however, it is still higher than the price of conventional solvents by a factor of 10-20 due to the complexity and cost of the synthesis and purification stages. The price of imidazolium-based, phosphonium based, pyridinium based, and tailored ILs are listed in Table 2-7. As shown in Table 2-7, the conventional ILs are cheaper than the functionalized ones. In general, the tailored ILs are at least five times more expensive than most conventional ILs. It is worth mentioning that all prices are based on the official website of Sigma Aldrich company, accessed June 2016 [144].

Protic ILs with their simple acid-base chemistry are used in industrial processes and have a low cost (<$1.23/kg) which is comparable to that of the organic solvents such as toluene and acetone [145]. Also, the cost for synthesizing ILs with hydrogen sulfate (as the anion group) through acid-base neutralization is comparable with that of the organic solvents such as acetone and ethyl acetate ($1.34/kg to $1.4 /kg). For example, the prices of triethylammonium hydrogen sulfate and 1-methylimidazolium hydrogen sulfate are $1.24/kg, and $2.96/kg to $5.88/kg, respectively [146].

Power plants include the costs for CO_2 capture from flue-gas (by amines) in the capital cost (CC) and operating costs (OC) [139]. Using ILs, some parts of the capital costs are less than those with amines. For example, in the desorption process, ILs will be recovered completely due to the low vapor pressure of the ILs. However, amines are volatile and some quantity of amines will be lost during the desorption process, leading to an increase in material and energy demands. Researchers found that using mixtures of ILs and amines, the energy consumption of the desorption stage lowers by more than 37%, compared to that with the amine solution [135].

Even though ILs are currently more expensive than the amines, their price is expected to be considerably decreased in the future. There are a large number of ILs available that can be synthesized in different ways. They have multiple-form markets such as use as a solvent and catalyst with application to reaction systems, separation systems, bio-refinery systems, energy storage, and GHG reducing media. These are great incentives for the commercialization of functional ILs with low costs. Some of the benefits of ILs, compared to the amines, in CO_2 capture are as follows [17]:

- Less energy is required for regeneration of diluted ILs to remove the absorbed CO_2, than amines due to their physical absorption mechanisms.
- There is a low chance of being involved in a reaction with impurities and low probability of corrosion occurrence in the equipment due to the high thermal and chemical stability ($>300\,°C$) of ILs.
- There is no loss in the gas stream during regeneration due to the low vapor pressure of ILs.
- There are high potentials to produce a task-specific IL with manipulating anions and cations due to the tunable nature of the ILs.

Table 2-7: Prices for imidazolium, phosphonium, pyridinium, and guanidium-based ILs and tailored ILs [144].

IL-based	Cation	Anion	Price (CAD$)	Quantity (g)
Imidazolium	1-Allyl-3-methylimidazolium	bis(trifluoromethylsulfonyl)imide	160	5
		bromide	151	5
		chloride	113	5
		dicyanamide	150	5
		iodide	225	5
	1-Benzyl-3-methylimidazolium	chloride	90	5
		hexafluorophosphate	105	5
		tetrafluoroborate	125	5
	1-Butyl-2,3-dimethylimidazolium	chloride	225	5
		hexafluorophosphate	83	5
		tetrafluoroborate	99.4 (>99%), 33(>97%)	5
	4-(3-Butyl-1-imidazolio)	butanesulfonate	303	5
	1-Butyl-3-methylimidazolium	acetate	331	5
		bis(trifluoromethylsulfonyl)imide	142	5
		bromide	71	5
		chloride	73	5
		dicyanamide	305	5
		hexafluoroantimonate	105	5
		hexafluorophosphate	90(>97%)	5
		hydrogen sulfate	149	5
		iodide	68	5
		tetrafluoroborate	45	5
	1,3-Dimethylimidazolium	dimethyl phosphate	46	5
		methyl sulfate	188	5
		tetrafluoroborate	43	5
	1-Ethyl-2,3-dimethylimidazolium	bis(pentafluoroethylsulfonyl)imide	339	5
		bis(trifluoromethylsulfonyl)imide	221	5
		chloride	40	5
		bromide	40	5
		dicyanamide	313	5
		tetrafluoroborate	275	5
		trifluoromethanesulfonate	103	5
	1-Hexyl-3-methylimidazolium	bis(trifluormethylsulfonyl)imide	185	5
		chloride	194	5
		hexafluorophosphate	87	5
	1-Methylimidazolium	Chloride	135	5

IL-based	Cation	Anion	Price (CAD$)	Quantity (g)
Phosphonium	Tetrabutylphosphonium	Methanesulfonate	84	5
		Tetrafluoroborate	338	5
		p-toluenesulfonate	122	5
		bis(trifluoromethylsulfonyl)amide	56	5
		bis(2,4,4-trimethylpentyl)phosphinate	27	5
	Trihexyltetradecylphosphonium	Bromide	90	5
		Chloride	25	5
		Decanoate	90	5
		Dicyanamide	33	5
	Triphenylphosphonio	propane-1-sulfonate	258	5
	Triphenylphosphonio	propane-1-sulfonic	963	50
Pyridinium	1-Butyl-3-methylpyridinium	bis(trifluormethylsulfonyl)imide	175	1
		Hexafluorophosphate	156	5
	1-Butyl-4-methylpyridinium	Iodide	59	5
		Tetrafluoroborate	110	5
	1-Butylpyridinium	Bromide	97	5
	1-(3-Cyanopropyl)pyridinium	Chloride	158	5
	1-Ethylpyridinium	Tetrafluoroborate	90	5
	3-Methyl-1-propylpyridinium	bis(trifluormethylsulfonyl)imide	183	1
Guanidinium	Guanidinium	iodide	82.50	5
	Guanidinium	chloride	97	5
	Guanidine	thiocyanate	120	100
	Guanidine	thiocyanate (solution)	107.50	50 ml
Tailored	1-(3-Cyanopropyl)-3-methylimidazolium	bis(trifluoromethylsulfonyl)amide	439	5
	1-(3-Cyanopropyl)-3-methylimidazolium	chloride	390	5

The separation cost consists of two parts including direct costs and indirect costs. The direct costs correspond to the costs of absorption and regeneration columns, lean/rich solvent heat exchangers, pumps, lean-solvent coolers, CO_2 compression unit, and other major equipment. The indirect costs include the general facilities, emergency, and owner's costs [147]. In addition, the Operating and Maintenance Expenses (OME) should be considered. The OME consists of operating labor,

maintenance costs, administrative and support labor costs, IL makeup, chemicals, solid waste treatment, power, and CO_2 transport and storage [147].

2.9. Screening of ionic liquids for CO_2 capture

Due to the tunability of ILs, room temperature ILs have 10^{18} possible structures [148]. This makes the selection of the best ILs for CO_2 capture difficult. However, particular factors should be considered to choose the most suitable ILs for CO_2 capture processes. These features include cost, the ability of the IL to absorb CO_2, how well the IL will work at ideal conditions, and selectivity of CO_2 in the presence of various gases by the IL. There are also other factors such as the toxicity and biodegradability of the ILs if it is planned to use ILs in large quantities.

Economic Prospect: As discussed before, ILs are currently expensive solvents. Their production processes are fairly difficult, which is a major obstacle while utilizing ILs for CO_2 capture at large scales. Many ILs are only available at the lab scales. Hence, it is not easy to estimate the total purchase cost if they are used in industrialized operations. The supplier Sigma-Aldrich is one of the ILs suppliers that provide the typical costs of a majority of ILs. It is clear that as the amount of the requested ILs increases, the price per gram drops significantly.

According to the prices listed for ILs by Sigma-Aldrich, the five best ILs in terms of economic aspect are: tributylmethylammonium chloride ([TBMA][Cl]); 1-butyl-3-methylimidazolium tetrafluoroborate ([bmim][BF$_4$]); trihexyl(tetradecyl)phosphonium bromide ([P$_{14,6,6,6}$][Br]); trihexyl(tetradecyl)phosphonium chloride ([P$_{14,6,6,6}$][Cl]); and 1-ethyl-1-methylpyrrolidinium bromide ([C$_2$Mpyrr][Br]). The prices of ILs at different scales are listed in Table 2-8.

Table 2-8: Prices for five potential ILs for CO_2 capture [144].

Ionic Liquid	Weight (g)	Price (CAD$)	Price per weight (CAD$/g)
[TBMA][Cl]	100	129	1.29
	500	595	1.19
[bmim][BF4]	100	180.5	1.81
	1000	108.5	1.09
[P14666] [Br]	50	107.5	3.25
[P14666] [Cl]	5	35.5	7.10
	50	112.5	2.25
[C2Mpyrr] [Br]	5	36.2	7.24
	50	136	2.72

Solubility and Selectivity Prospects: The CO_2 capture capacity of an IL is an important factor while choosing an IL for a CO_2 capture process. Researchers have studied many different ILs to determine what are the best in terms of their CO_2 solubility for the post-combustion CO_2 capture processes. It has been found that the anion of ILs has the greatest impact on the CO_2 capture capacity of ILs. According to the literature, the more fluorinated the anion is, the higher the CO_2 solubility is. It was also concluded that task-specific ionic liquids (TSILs) have a much greater CO_2 solubility than conventional ILs, since they are usually modified to absorb more CO_2.

Oliferenko et al. [149] provided a spreadsheet which lists many ILs and their corresponding Henry's law constants. Based on the data/information, the best ILs in terms of solubility are: 1-pentyl-3-methylimidazolium tris(nonafluorobutyl)trifluorophosphate ([p5mim][bFAP]); trihexyl(tetradecyl)phosphonium chloride ([P_{14666}][Cl]); 1-hexyl-3-methylimidazolium tris(heptafluoropropyl)trifluorophosphate ([hmim][pFAP]); trihexyl(tetradecyl)phosphonium bis(trifluoromethylsulfonyl)imide ([P_{14666}][Tf$_2$N]); and methyltrioctylammonium bis(trifluoromethylsulfonyl)imide ([N_{1888}][Tf$_2$N]). The Henry's law constants for these ILs are

presented in Table 2-9. It should be noted that the Henry's law constant represents the amount of CO_2 which is physically absorbed by an IL. In fact, it does not account for chemical absorption which can occur in TSILs.

The promising ILs in terms of selectivity of CO_2 and H_2S over other gases (e.g., methane) include BF_3, NO_3, and CH_3SO_4 anions and cations such as Tetrabutylammonium (N4111), Pentamethylguanidinium (pmg), and Tetramethylguanidinium (tmg) [150].

Maiti [151] concluded that ILs containing pentamethylpropylguanidinium [ppg] cation and [BF4], [FEP], and [PF_6] anions have higher CO_2 solubility. The solubility data are illustrated in Figure 2-17 and Figure 2-18. Thus, the functionalized-guanidinium cations show higher solubility than the imidazolium-based ILs [152]. Among anions, BF_4 and PF_6 are the best where the CO_2 solubility is the main selection criterion.

Table 2-9: Henry's law constant for potential ILs in terms of solubility [149].

Ionic Liquid	T (K)	Henry's law constant (bar)
[$p_5$mim][bFAP]	313	26.92
	303	22.44[*]
[hmim][pFAP]	313	28.84
	303	24.01[*]
[[P_{14666}][Cl]	303	23.99
[P_{14666}][Tf_2N]	303	26.30
[N_{1888}][Tf_2N]	303	38.18

[*] Linearly interpolated for comparison
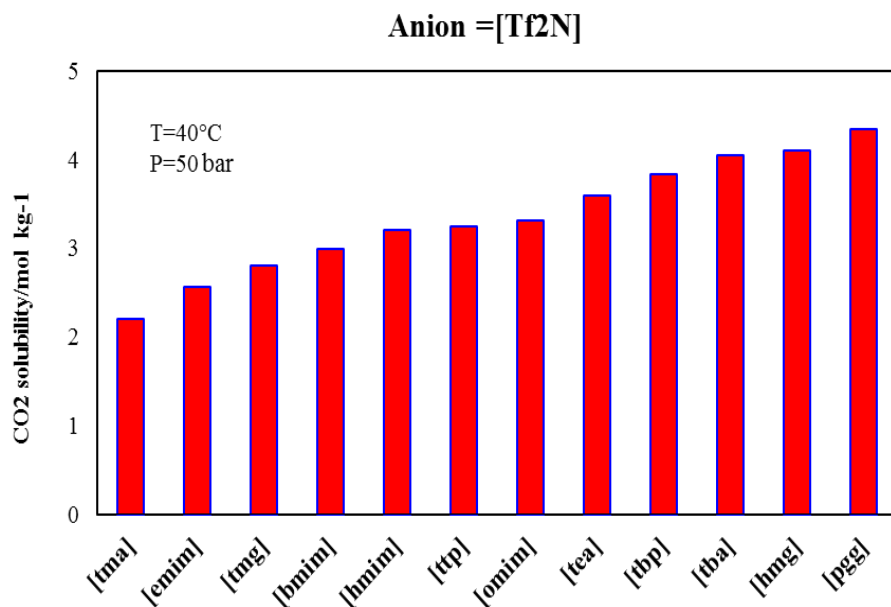
Figure 2-17: Calculated CO_2 solubility in various ILs having an anion of Tf_2N [151].
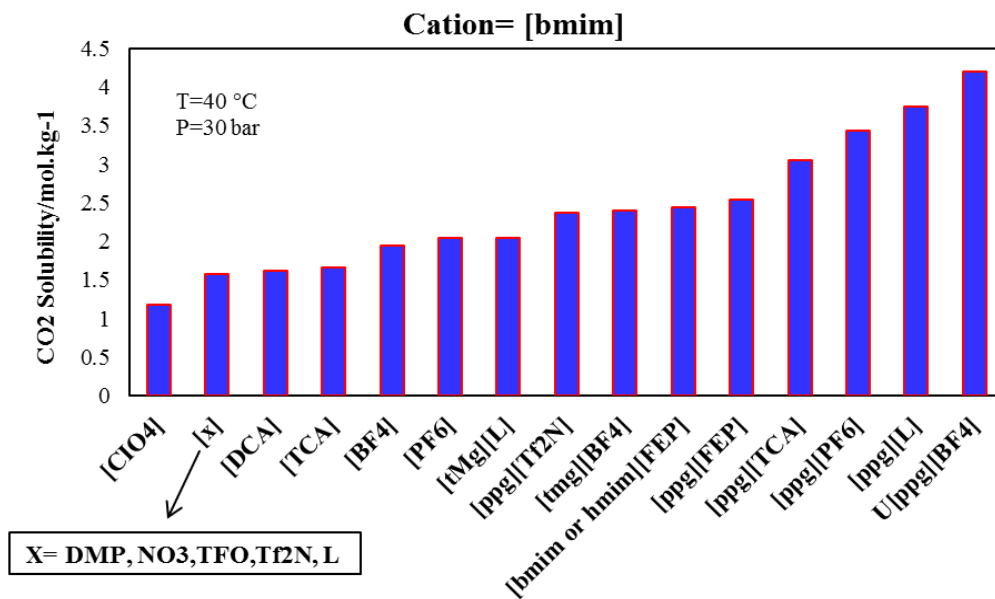
Figure 2-18: CO_2 solubility in different ILs having a cation of bmim [151].

Operational Condition Prospects: Since high pressure and low temperature operations facilitate

CO_2 absorption, the high pressure and low temperature conditions favor to absorb a high amount

of CO_2. However, this is not appropriate for post-combustion processes, because increasing the pressure will increase the operating costs. Therefore, it is necessary to employ ILs that can attain an acceptable solubility of >40 % at the moderate temperature range of 293-313.15 K and the moderate pressure range of 5-10 bar. Several researchers have studied important absorption and characterization aspects of the amine-functionalized ILs, since they exhibit higher CO_2 absorption capacities due to chemical absorption, compared to conventional ILs. A part of functionalized ILs used for CO_2 capture are trihexyl(tetradecyl)phosphonium glycinate ($[P_{14666}][Gly]$), isoleucinate ($[P_{14666}][Ile]$), 2-cyanopyrrolide ($[P_{14666}][2\text{-}CNpyr]$), 3-(trifluoromethyl) ($[P_{14666}][3\text{-}CF_3pyra]$), prolinate ($[P_{14666}][Pro]$), and methionate ($[P_{14666}][Met]$) [29, 117, 131]. These studies reveal that non-conventional ILs are able to absorb CO_2 in a 1:1 stoichiometry at 295 K under low pressure conditions.

2.10. Main technical and practical challenges

Although thermodynamic models are very useful to characterize CO_2 and IL systems, there are still major challenges in this area. Adequate knowledge is required to select appropriate EOSs and mixing rules for complex systems such as water/CO_2/IL. Inappropriate selection results in significant errors while predicting the thermodynamic characteristics [158,159].

The critical properties of CO_2 are available; however, finding the critical properties of the ILs is a challenging task, since they are decomposed at the normal boiling point. Hence, efficient methodologies need to be developed to accurately obtain the critical properties of ILs.

Thermodynamic models are often complex to be solved in phase equilibria for the determination of the corresponding parameters. There are computational and software tools that may assist researchers. However, most of these approaches are expensive, difficult, and time-consuming. This poses another major challenge while employing thermodynamic models.

The high viscosity of ILs, which leads to a decrease in the solubility of CO_2 in ILs, is one of the main challenges while utilizing ILs. There are some solutions to this challenge, which they need to be examined and investigated properly. One of the solutions is using a mixture of water and amines with ILs, in which the optimum composition and process conditions should be determined for these mixtures.

Another disadvantage of using ILs for CO_2 capture is the cost. ILs are more expensive, compared to amines. Although the price of ILs in the large scale (less than \$40/kg) can be much lower than the currently available lab scale price (~\$1000/kg), the cost is still 10 to 20 higher than the cost for conventional solvents [153]. Researchers need to find simple and economic synthesis solutions for CO_2 capture where the targeted solvent is an IL. To use ILs for the absorption method in large scales, appropriate system design and optimal operating conditions should be selected.

Recently, there have been new developments in CO_2 capture and utilization techniques such as the introduction of efficient solid/liquid/gas systems with high CO_2 capture efficiency, utilization of a single liquid absorber to simultaneously capture CO_2 and SO_2, hydrogen production through employing chemical looping technique for CO_2 capture, electrofuels production from CO_2, and use of CO_2 for algae culturing [160-164]. However, more systematic engineering and research activities need to be conducted to assess the viability of the new strategies in terms of practical implications and economic and environmental prospects.

2.11. Conclusions

CO_2 capture processes involve several challenges in terms of technical, economical, and environmental prospects. Novel options for removal of CO_2 from flue-gases including absorption with ionic liquids (ILs) have been proposed and investigated from thermodynamic, transport phenomena, and economic points of view. The CO_2 capture process using ILs is briefly explained

in this chapter where the absorption mechanisms and the main practical and economic advantages and advantages are highlighted. The physical and chemical characteristics and critical properties of CO_2 and ILs (and their mixtures) obtained from both experimental and modeling approaches are reported. The influences of important parameters such as type of anions and cations, ions length, IL volatility, and operating conditions on CO_2 solubility and selectivity are also discussed. The most appropriate equations of state (EOSs) to study the vapor-liquid equilibrium of CO_2/ILs systems are described in this work. In addition, the price of the most common ILs is reported as the economic analysis is very important in commercializing the IL-CO_2 absorption technique. The main conclusions are drawn as follows:

- The current CO_2 capture techniques mainly suffer from high capital and operating costs, solvent degradation, high solvent loss, corrosive nature of solvents, the toxicity of solvents, required large absorption equipment, and high energy consumption for solvent regeneration.

- Among EOSs, the results obtained by using PC-SAFT EOS showed great agreement with the experimental data at atmospheric and high pressures. Also, PR EOS results in good outputs where the Wong-Sandler/van Laar mixing rules are utilized.

- The functionalized ILs though are more suitable for absorption of CO_2, they are 2-4 times more expensive than conventional ILs.

- The best ILs in terms of technical and economic perspective are screened. Based on this investigation, it is concluded that Guanidinium cations and fluorine anions including [BF_4], [FEP], and [PF_6] are the best cation and anion, respectively as they exhibit high CO_2 solubility.

- To commercialize CO_2 capture technology with ILs, it is vital to find cheap but suitable IL/additive mixtures with relatively high solubility and selectivity where important mass transfer and thermodynamic prospects of CO_2/Water/IL/additive systems (diffusivity, mass transfer rate, vapor pressure, and equilibrium conditions) are well explored through experimental and modeling investigations.

- ILs as green solvents offer a promising CO_2 capture technique where an acceptable absorption rate can be attained if a proper ion or chemical is added to IL. In addition to engineering design aspects, their high viscosity, cost, availability, compatibility, and purity are the main challenges to developing appropriate absorption systems to capture CO_2 using ILs at an industrial scale.

Appendix A1: Mixing rules for equations of state

To use an EOS for mixtures, EOS constants should be obtained using mixing rules. Mixing rules include the binary interaction terms which represent the attractive and repulsive forces [154]. In general, the mixing rules are divided into two main categories including random and non-random mixing rules. The non-random mixing rules are used when the system contains asymmetric compounds such as water and methanol. The non-random mixing rules are represented by two terms; namely, conventional random mixing term and asymmetric term due to polarity.

The random mixing rules offer acceptable results in many practical cases. It is suggested that the mixing rules used in any EOS should attain the same form as that of the virial equation at conditions at which both equations are valid. The interactions between molecules in the multicomponent systems (the coefficients of virial equations) at low pressures are described at Table A1-1 [1].

The attractive (a_{ij}) and repulsive (b_{ij}) forces between molecules i and j in the EOS can be expressed by the simple geometric and arithmetic average, respectively, through the following equations [1]:

$$a_{ij} = (a_i a_j)^{1/2} \qquad (A1\text{-}1)$$

$$b_{ij} = (b_i + b_j)/2 \qquad (A1\text{-}2)$$

Considering the attractive term between two non-similar molecules, the following binary interaction parameter (k_{ij}) should be added, as well [1]:

$$a_{ij} = (a_i a_j)^{1/2}(1 - k_{ij}) \qquad (A1\text{-}3)$$

For the repulsive term, if there is a high concentration of CO_2 in the system, another binary interaction parameter for the repulsion term (K'_{ij}) should be used as follows:

$$b_{ij} = [(b_i + b_j)/2](1 - K'_{ij}) \qquad (A1\text{-}4)$$

where b_{ij} represents the coefficients due to interaction between molecules i and j.

Table A1-1: Different mixing rules for EOSs [1].

Mixing rule	Equation
van der Waals	$$a = \sum_i \sum_j x_i x_j (a_i . a_j)^{0.5}(1-k_{ij})$$ $$b = \sum_i \sum_j x_i x_j [(b_i + b_j)/2](1-k_{ij})$$
Wong-Sandler	$$b = \frac{RT \sum_i \sum_j x_i x_j (b - \frac{a}{RT})_{ij}}{RT - [\sum_i x_i (\frac{a_i}{a_j}) + \frac{G^E}{C}]}$$ $$a = b[\sum_i x_i (\frac{a_i}{a_j}) + \frac{G^E}{C}]$$
Huron-Vidal	$$a = b[\sum_i x_i (\frac{a_i}{a_j}) + \frac{G^E}{C}]$$
Mathias-Klotz-Prausnitz	$$a = \sum_{i=1}^{N} \sum_{j=1}^{N} x_i x_j \sqrt{a_i . a_j}(1-k_{ij})$$ $$+ \sum_{i=1}^{N} x_i (\sum_{j=1}^{N} x_j (\sqrt{a_i a_j I_{ji}})^{1/3})^3$$ $$b = \sum_i x_i b_i$$

Once the parameters a and b are determined, they can be used in EOSs.

NOMENCLATURES

Acronyms

AAD	average absolute deviation
AIL	aprotic ionic liquid
ANN	artificial neural network
CILs	conventional ionic liquids
CC	capital cost
CCS	carbon capture and storage
CCUS	carbon capture, utilization, and storage
DE	differential evolution
DESs	deep eutectic solvents
DETL	differential evolution with Tabu List
EOS	equation of state

GA	genetic algorithm
GHG	greenhouse gas
HBDs	hydrogen bond donors
IGCC	integrated gasification combined cycle
IL	ionic liquid
IPCC	intergovernmental panel on climate change
IUPAC	International Union of Pure and Applied Chemistry
LLE	liquid-liquid equilibria
LM	Levenberg-Marquart
MD	molecular dynamics
MOFs	metal-organic frameworks
NRTL	non-random two liquid equation of state
OC	operating cost
OME	operating and maintenance expenses
PC-SAFT	perturbed chain statistical association fluid theory
PILs	protic ILs
PR	Peng-Robinson equation of state
PT	Patel-Teja
PRSV	Peng-Robinson-Stryjek-Vera equation of state
PSO	particle swarm optimization
RK	Redlich-Kwong equation of state
SA	simulated annealing
SAFT	statistical association fluid theory
SRK	Soave-Redlich-Kwong equation of state
TGA	thermogravimetric analysis
TSIL	task-specific ionic liquid
vdW	van der Waals
VL	van Laar equation of state
VLE	vapor-liquid equilibria
WS	Wong-Sandler mixing rule

Chemicals

AMP	2-amino-2-methl-1-propanol
BF_4^-	tetra fluoroborate anion
[bmim][BF$_4$]	1-butyl-3-methylimidazolium tetrafluoroborate
[bmim] [Br]	1-butyl-3-methylimidazolium bromide
[bmim] [dca]	1-butyl-3-methylimidazolium dicyanamid
[bmim][NO$_3$]	1-butyl-3- methylimidazolium nitrate
[bmim][NTf$_2$]	1-butyl-3-methylimidazolium bis(trifluoromethylsulfonyl)imide
[bmim][CF$_3$SO$_3$]	1-butyl-3-methylimidazolium trifluoromethanesulfonate
[bmim][PF$_6$]	1-butyl-3-methylimidazolium hexafluorophosphate
[bmim][TfO]	1-butyl-3-methylimidazolium trifluoromethanesulfonate
Br^-	bromide anion
$CF_3\text{-}CFH_2CH_3SO_3^-$	methylsulfate anion
[CH$_3$CH$_2$NH$_3$][NO$_3$]	ethylammonium nitrate

CO_2	carbon dioxide
CO_3^{2-}	carbonate
$[C_2Mpyrr][Br]$	1-ethyl-1-methylpyrrolidinium bromide
$[C_nC_nMIM]^+$	1-alkyl-3-alkylimidazolium cation (n= carbon chain length)
$[C_nMIM]^+$	1-alkyl-3-methylimidazolium cation (n= carbon chain length)
$[C_2mim][NTf_2]$	1-ethyl-3-methylimidazolium bis(trifluoromethylsulfonyl)imide
$[emim][EtSO_4]$	1-ethyl-3-methylimidazolium ethyl sulfate
$[emim][TfO]$	1-ethyl-3-methylimidazolium trifluoromethanesulfonate
HCO_3^-	bicarbonate
Hg	mercury
hmg	hexamethylguanidinium
$[hmim][BF_4]$	1-hexyl-3-methylimidazolium tetrafluoroborat
$[hmim][Ntf_2]$	1-hexyl-3-methylimidazolium trifluoromethanesulfonate
$[hmim][PF_6]$	1-hexyl-3-methylimidazolium hexafluorophosphate
HSO_4^-	hydrogen sulfate anion
MDEA	methyl diethanolamine
MEA	monoethanolamine
$[N\text{-}bupy][BF_4]$	N-butylpyridinium tetrafluoroborate
$N(CN)^{2-}$	dicyanamide anion
N4111	tetrabutylammonium
NaCl	sodium chloride
$N_{n,n,n,n}^+$	tetraalkylammonium cation (n= carbon chain length)
NO_2	nitrogen dioxide
NPf^{2-}	bis(pentafluoroethylsulfonyl)imide anion
O_2	oxygen
OAc^-	acetate anion
omim	1-octyl-3-methyl imidazolium
$[omim][BF_4]$	1-methyl-3-octylimidazolium tetrafluoroborate
$[omim][Cl]$	1-octyl-3-methylimidazolium chloride
PDMS	polydimethylsiloxane
$[PF_6]^-$	hexafluorophosphate
pmg	pentamethylguanidinium
PP	polypropylene
ppg	pentamethylpropylguanidinium
PPO	polyphenyleneoxide
$[P_{14666}][2\text{-}CNpyr]$	trihexyl(tetradecyl)phosphonium 2-cyanopyrrolide
$[P_{14666}][3\text{-}CF_3pyra]$	trihexyl(tetradecyl)phosphonium 3-(trifluoromethyl) pyrazolide
$[P_{14666}][Br]$	trihexyl(tetradecyl)phosphonium bromide
$[P_{14666}][Cl]$	trihexyl(tetradecyl)phosphonium chloride
$[P_{14666}][Gly]$	trihexyl(tetradecyl)phosphonium glycinate
$[P_{14666}][Ile]$	trihexyl(tetradecyl)phosphonium isoleucinate
$P_{n,n,n,n}^+$	tetraalkylphosphonium cation (n= carbon chain length)
$[Py_{n,n}]^+$	1-alkyl-1-alkylpyrrolidinium cation (n= carbon chain length)
$[Rmim][Tf2N]$	1-alkyl-3-methylimidazolium (alkyl = methyl, butyl, octyl, and dodecyl) bis(trifluoromethylsulfonyl)imides

SCN$^-$	thiocyanate anion
SO$_2$	sulphur dioxide
tba	tetrabutylammonium
[TBMA][Cl]	tributylmethylammonium chloride
tbp	tetrabutylphosphonium
tea	tetraethylammonium
tma	tetramethylammonium
tmg	tetramethylguanidinium
ttp	trihexyl(tetradecyl)phosphonium

Variables/Parameters

A	Antoine constant in Equation (2-6); viscosity model coefficient in Equation (2-10)
A_J, A_L, A_M	critical temperature model constants in Equations (2-11), (2-14) and (2-18), respectively
a	constant in Equation (2-11); constant in vapor pressure model in Equation (2-25); energy parameter in Equations (2-33), (A2-1), (A2-7), (A2-8), and Table A2-1
$a_1, a_2, and\ a_3$	constants in dentistry-temperature correlation in Equation (2-8)
a_c	a constant in energy parameter in Equation (2-30)
$a_i, and\ a_j$	a coefficient in reduced effective cross section model in Equation (2-3); energy parameter for component i and j in Equations (A2-1), (A2-3), (A2-6), (A2-7), (A2-8), (A2-12), (A2-14) and Table A2-1
a_{ij}	attractive forces between molecules i and j in Equations (A2-3), (A2-12), (A2-14), and Table A2-1
$\tilde{a}$	Helmholtz free energy in Equations (2-32) and (2-33)
$\tilde{a}^{assoc}$	association contribution of Helmholtz free energy in Equation (2-32)
$\tilde{a}^{disp}$	dispersion contribution of Helmholtz free energy in Equation (2-32)
$\tilde{a}^{hc}$	hard chain molecules contribution of Helmholtz free energy in Equation (2-32)
B	coefficient of vapor pressure model in Equations (2-6) and (2-23); parameter in density model in Equations (2-7) and (2-9)
b	coefficient in vapor pressure model in Equation (25); volume parameter in Equations (2-28), (2-31), (A2-5), (A2-6), (A2-7), (A2-9) and in Tables 2-6, 2-7, and A2-1
$b_1\ and\ b_2$	parameters used in density model in Equation (2-9)
$b_i\ and\ b_j$	volume parameter for component i and j in Equations (A-2), (A2-4), (A2-5), (A2-9), (A2-13), (A2-15) and Table A2-1
b_{ij}	binary interaction coefficient of molecules i and j in Equations (A2-2), (A2-4), (A2-6), (A2-13), (A2-15) and Table A2-1

C	coefficient of vapor pressure model in Equation (2-6); coefficient in density model in Equation (2-7); parameter in Equations (A2-6), Equation (A2-7), and Table A2-1
C_J, C_L, C_M	critical pressure model constants in Equations (2-12), (2-15), and (2-19), respectively
C_p	specific heat capacity at constant pressure in Equation (2-25)
c	volume parameter in Tables 2-6 and 2-7
D_J	parameter in critical pressure model in Equation (2-15)
d_{ij}	parameter in viscosity-temperature model in Equation (2-5)
E_J, E_L, E_M	critical volume model constants in Equations (2-13), (2-16) and (2-20), respectively
f_2	fugacity of component 2 (solute) in Equations (2-35), (2-36), (A2-10), and (A2-11)
G^E	Gibbs excess free energy in Equations (A2-6), Equation (A2-7), and Table A2-1
H_2	enthalpy of component 2 (solute) in Equations (2-35) and (A2-10)
I_{ji}	binary interaction coefficient between molecules j and i in Equation (A2-8) and Table A2-1
k	transmission coefficient in Equation (2-24)
k_1	coefficient in energy parameter model in Table 2-8
k_{ij}	binary interaction coefficient in Equations (A2-1), (A2-3), (A2-4), (A2-7), (A2-14) and in Table A2-1
$K_{ij}{'}$	binary interaction coefficient in Equation (A2-15)
M	molecular weight in Equations (2-19), (2-24), and (2-26)
M_{ref}	molecular weight of reference in Equation (2-27)
M_S	molecular weight of reference in Equation (2-27)
m	mass in Equations (2-24) and (2-26)
m_{ref}	mass of reference in Equation (2-27)
m_S	mass of sample in Equation (2-27)
N	number of atoms in molecule in Equation (2-15)
n_i	number of occurrences of group i in Equations (2-11) – (2-20)
n_{pts}	number of data points in Equation (2-34)
P	pressure
P_b	bubble point pressure
P_c	critical pressure
P_{Ji}, P_{Li}, P_{Mi}	contributions of component i to critical pressure in Equations (2-12), (2-15), and (2-19), respectively
P^{sat}	saturation pressure
R	universal gas constant
S	orifice area in Equation (2-24)
S'	surface area to liquid in Equation (2-24)
T	temperature
T^*	reduced temperature in Equations (2-2) – (2-5)
T_b	boiling point temperature

T_c	critical temperature
T_{Ji}, T_{Li}, T_{Mi}	contributions of component i to critical temperature in Equations (2-12), (2-14), and (2-18), respectively
T_r	reduced temperature
t	time in Equations (2-26) and (2-27)
u	parameter in PRSV model in Table 2-6
V	volume
V_c	critical volume
V_{Ji}, V_{Li}, V_{Mi}	contributions of component i to critical volume in Equations (2-13), (2-16), and (2-20), respectively
v	parameter in PRSV model in Table 2-6
V_2^{∞}	partial molar volume of solute at infinite dilatation in Equations (2-35) and (A2-10)
w	parameter in PRSV model in Table 2-6
x_i and x_j	mole fraction of component i and j, respectively

Greek Letters

α	vaporization coefficient in Equations (2-24) and (2-26); energy parameter in Equation (2-29) and Table 2-7
Δ	change or difference
ϕ	fugacity coefficient
$\sigma_{\mu}^{*}(T^{*})$	reduced effective cross section in Equations (2-2) and (2-3)
δ	parameter in five parameter EOSs in Equation (2-28) and Table 2-7
ε	particle energy in Equation (2-4); activation energy in Equation (2-10); a parameter in five parameter EOS in Equation (2-28) and Table 2-7
η	apparent viscosity in Equation (2-10); a parameter in five parameter EOS in Equation (2-28) and Table 2-7
κ	conductivity in Table 2-4
ρ	density
τ	elapsed time in Equation (2-24)
ω	acentric factor

Subscripts and Superscripts

0	reference state, and dilute
*	reduced
∞	infinite dilution
assoc	association
b	boiling

c	critical
calc	calculation
disp	dispersion
E	excess
exp	experiment
hc	hard chain
LV	liquid-vapor
m	melting
r	reduced
ref	reference
res	residual
s	sample
sat	saturation

3. CHAPTER THREE

Assessment of carbon dioxide solubility in ionic liquid/toluene/water systems by extended PR and PC-SAFT EOSs: Carbon capture implication

Preface

A version of this chapter has been published in the Journal of Molecular Liquids 275, 323-337 (2018). I am the primary author of this paper. With the help and advice of the coauthors, Sohrab Zendehboudi and Nima Rezaei, I developed the conceptual thermodynamic model and designed the manuscript's structure. Most of the literature review, data collection, and the performance analysis of different methods were done by me as the first author. I prepared the first draft of the manuscript and subsequently revised the manuscript based on the co-authors' feedback and comments received from journal reviewers. The co-author, Sohrab Zendehboudi, helped in developing the method, results interpretation, and statistical analysis. The co-author, Sohrab Zendehboudi, also considerably contributed to entirely correcting the text in terms of technical and editorial aspects. Nima Rezaei reviewed and revised the manuscript.

Abstract

Recently, there has been a growing interest in CO_2 capture using Ionic Liquids (ILs). To determine the CO_2 absorption ability of ionic liquids and their selectivity in the presence of other gas mixtures, the solubility of ILs at various operating conditions and the influence of impurities such as water and toluene should be evaluated. The carbon capture capacity of ILs can be examined using various methods such as experiments, Equations of State (EOSs) modeling, and molecular-based modeling. In this research work, the extended Peng–Robinson (PR) and Perturbed-Chain Statistical Associating Fluid Theory (PC-SAFT) EOSs are utilized to evaluate the solubility and selectivity of CO_2 in ILs through comparing the modeling results with experimental data. PC-SAFT and PR parameters are determined by employing the experimental density data. Modeling results reveal that the solubility values estimated by PC-SAFT due to the association have lower deviation than PR EOS based on the magnitudes of Absolute Average Deviation (AAD %). The AAD (%) for [bmim][BF$_4$], [bmim][PF$_6$], [bmim][Tf$_2$N], [hmim][Tf$_2$N], [hmim][FAP], and [hmim][FAP] are calculated using PR EOS and PC-SAFT EOS in a range of 2-5.7% and 3-7.5%, respectively. Furthermore, ternary systems of CO_2/ILs/Water and CO_2/ILs/Toluene are modeled to determine the effect of water and toluene on the gas solubility in ILs and viscosity of ILs with PC-SAFT EOS. Based on the results, low concentrations of water (0.1 wt%) have a negligible effect on the CO_2 solubility in ILs. However, with increasing the water concentration, the solubility of water reduces significantly. On the other hand, the viscosity of ILs is reduced by increasing water concentration. Viscosity reduction in the hydrophilic ILs is significant. It is efficient to add water up to 10 wt% to hydrophilic ILs, with the implication of a decrease in the viscosity to an amount close to the viscosity of water and a decrease in solubility by 9%. Finally, the selectivity of [hmim][Tf$_2$N] in the separation of CO_2 and H_2S, SO_2, CH_4, and H_2 are reported. Based on the

results, [hmim][Tf$_2$N] is not appropriate for the separation of CO_2 from streams with a high concentration of H_2S and SO_2 gases.

3.1. Introduction

Ionic Liquids (ILs) are molten salts at temperatures below 100 ^{o}C. Their unique properties such as having a low vapor pressure (e.g., less than 10^{-8} bar [155]) and high thermal stability (473-673 K [156]) make them promising materials in different processes. Common ILs are those with cations based on imidazolium, phosphonium, pyridinium, ammonium, and guanidinium. The tunability of ILs is another attractive feature, enabling the design of engineered liquids for specific applications by selecting different cations, anions, and functionality. For instance, a specific IL can be tuned to promote desired viscosity, miscibility (in water), and reactivity with other compounds [116]. ILs are suitable substitutions for volatile organic solvents. They can be used as solvents for organic and polymer synthesis, biphasic separations (liquid-liquid extraction), and as a catalyst and catalyst support for reactions [157]. One of the important characteristics of ILs is their potential in separating gas from a mixture of gases. ILs have an exceptionally high solubility for some gases (such as CO_2 or/and H_2S). Hence, they can be regulated to selectively capture one gas from a mixture of gases [158]. Moreover, due to their unusual low vapor pressure, the solvent loss can be minimized. These characters give ILs great potential in capturing CO_2 from flue gases. As ILs do not contaminate the gas phase due to their non-volatility, the selectivity of gases is greater with ILs, compared to other solvents. The thermal stability of ILs also makes them suitable for high temperature applications.

Experimental measurements of CO_2 solubility in ILs are extensive in the literature, using gravimetric, isochoric saturation, synthetic, chromatography, and thermodynamic consistency tests [22, 29, 112, 159-168]. Aki et al. [101] investigated the solubility of CO_2 in 10 different

imidazolium-based ILs at temperature levels of 25 °C, 40 °C, and 60 °C and pressures up to 150 bar. They studied the effect of anion, cation alkyl chain length, and the addition of alkyl substituents (on the cation ring) on the solubility of CO_2 in ILs at high pressures. The experiments were conducted at the stoichiometric equilibrium condition. The ILs were charged into the cell which was kept at a constant temperature, using a water bath. A known amount of CO_2 was added to the cell, after stirring when they reached the equilibrium. The solubility of CO_2 in ILs was then measured. Shariati and Peters [169] conducted experiments based on the synthetic method (in this method, the composition of the mixture is known and temperature or pressure is adjusted until homogenous phase is achieved.) at high pressures in an autoclave cell for high concentrations of CO_2 and the Cailletet apparatus for lower concentrations of CO_2 in 1-hexyl-3-methylimidazolium hexafluorophosphate. Jacek Kumełan [170] conducted tests using a high-pressure view-cell technique based on the synthetic method for solubility of CO_2 in [hmim][Tf$_2$N]. Unfortunately, the experimental data are available in a narrow region of temperatures and pressures. To study the phase behavior of CO_2-ILs in a wider range of temperature and pressure, a thermodynamic model (or Equation of state) is required.

Lawien et al. [171] reported experimental results for the solubility and diffusivity of CO_2 in [C$_n$mim][TCM] ILs, using a magnetic suspension balance at pressures up to 2 MPa. They employed electrolyte Perturbed-Chain Statistical Associating Fluid Theory (ePC-SAFT) [172] EOS to model the system's behavior and verified it by the real data. Karakatsani et al. [33, 40] used the correlated density data at various temperatures to obtain the parameters of the truncated Perturbed Chain-Polar Statistical Associating Fluid Theory (tPC-PSAFT) [173] model. Using the correlated binary interaction from tuning solubility data, they determined the solubility of CO_2 and O_2 in [bmim][PF$_6$]. They reported an excellent agreement between the model and experimental

results. The tPC-PSAFT is suitable for systems with weakly dispersed and highly oriented polar interactions and short-range strong hydrogen bonding interactions. They modeled the ILs as highly polar and neutral ion pairs. Shiflett et al. [112, 174] generated the solubility data of CO_2 in three common ILs including, [bmim][PF$_6$], [bmim][BF$_4$], and [hmim][Tf$_2$N] through the gravimetric microbalance experiments over a temperature range of 283.15 K to 348.15 K and pressures up to 2.0 MPa. They simulated the phase equilibrium behavior by employing Redlich-Kwong (RK)[84] EOS. Shin et al. [175] reported the solubility of CO_2 in [Cn-mim][TfO] (for n =2, 4, 6, and 8) at pressures up to about 40 MPa and temperature levels of 303.85 K and 344.55 K, using Peng-Robinson (PR) EOS and van der Waals (vdW) mixing rules. Cavaliho et al. used PR EOS with Wong-Sandler mixing rule (PRWS EOS) to model the phase behavior of CO_2 and ILs ([bmim][Tf$_2$N] , [C$_5$-mim][Tf$_2$N], [THTDP][NTf$_2$], and [THTDP][Cl]) at temperatures up to 363 K and pressures up to 50 MPa [114, 176]. There are several modeling data for solubility of CO_2 in some ILs; however, they examined EOSs that is not as much accurate as PC-SAFT. In this work, we investigate the solubility of new ILs with PC-SAFT; the parameters are determined with high precision. The final solubility correlated data are more accurate and reliable than the data reported in the literature while comparing the Average Absolute Deviation (AAD %) results.

Fu et al. [177] studied the effect of water content from 0.0067 wt% to 1.6 wt% on the solubility of CO_2 in [bmim][PF$_6$]. They concluded that the deviation in solubility was not more than 15%. Most researchers only reported the effect of water on the solubility of gases in ILs without considering the effect of water content on the viscosity and solubility of CO_2 in ILs. In this research study, the effect of water on decreasing viscosity of ILs and solubility of CO_2 in the mixture of hydrophilic and hydrophobic ILs with water is evaluated.

SAFT based EOSs for CO_2 separation processes have not been studied and developed enough; however, they have shown accurate results for CO_2-ILs and CO_2-Amines systems. To the best of our knowledge, the PC-SAFT EOS has not been utilized in determining the solubility of CO_2 in some of the ILs, yet.

In this work, the solubility of CO_2 in different ILs is modeled using PR and PC-SAFT EOSs in broad ranges of temperature and pressure. The accuracy of PR and PC-SAFT EOSs in predicting the solubility of CO_2 in various ILs is compared. Then, the influence of water and toluene in the IL phase on the solubility of CO_2 in IL-water and IL-toluene mixtures and the IL mixture viscosities are investigated. Also, Henry's constant and the selectivity of CO_2 over other gases in [hmim][Tf$_2$N] IL are calculated. Finally, some concluding remarks are given in the last section.

3.2. Thermodynamic modeling

In this study, the Vaper-Liquid Equilibria (VLE) for the CO_2-IL system and Vapor-Liquid-Liquid Equilibria (VLLE) for the CO_2-IL-Water system are modeled by two thermodynamic models, namely: PRWS EOS (Peng-Robinson with Wong-Sandler mixing rules) and PC-SAFT (Perturbed Chain Statistical Associating Fluid Theory). The PRWS model serves as a reference to show the importance of association in the CO_2-IL system.

3.2.1. Peng-Robinson EOS

The Peng-Robinson EOS [81] is one of the appropriate cubic EOSs in the thermodynamics, which is defined as follows:

$$P = \frac{RT}{v-b} - \frac{a(T)}{v^2 + 2bv - b^2}$$

(3-1)

$$a(T) = 0.45724 \frac{R^2 T_c^2}{P_c} \alpha(T)$$

(3-2)

$$b = 0.07780 \frac{RT_c}{P_c} \tag{3-3}$$

where P_c and T_c are the critical pressure and critical temperature of pure compounds; V stands for the molar volume; a refers to the attraction parameter; b represents the hard-core or co-volume parameter [178]; and $\alpha(T)$ denotes the temperature-dependent term, which is expressed as follows:

$$\alpha(T) = [1 + (0.37464 + 1.54226\omega - 0.26992\omega^2)(1 - \sqrt{T_r})]^2 \tag{3-4}$$

where ω represents the acentric factor and T_r symbolizes the reduced temperature. PR EOS can be applied to mixtures by applying a suitable mixing rule. The most common mixing rules are the van der Waals mixing rules as given below:

$$a_m = \sum_{i=1}^{c} \sum_{j=1}^{c} x_i x_j a_{ij} \tag{3-5}$$

$$b_m = \sum_{i=1}^{c} \sum_{j=1}^{c} x_i x_j b_{ij} \tag{3-6}$$

where a_m and b_m signify the attraction and co-volume parameters of PR EOS for mixture, respectively; c is the number of components; x_i and x_j stand for the mole fractions of component i and j, respectively; a_{ij} and b_{ij} are the ij pair interaction parameters between molecules i and j which can be determined from a set of combining rules such as:

$$a_{ij} = (a_i a_j)^{1/2}(1 - k_{ij}) \tag{3-7}$$

$$b_{ij} = [(b_i + b_j)/2](1 - K'_{ij}) \tag{3-8}$$

where k_{ij} and K'_{ij} denote the binary interaction parameters. For cubic EOSs, using van der Waals mixing and combining rules, there are two problems. First, the predicted error for the liquid density of pure fluids and mixtures exceeds 5%. Second, for the system of molecules with the size or

chemical nature dissimilarity, the predictions may not be in a good agreement with real data. To overcome these problems, the modified mixing rules are introduced, among which Wong-Sandler [179] has been verified promising in estimating the liquid density [180]. The Wong-Sandler mixing rule combines the cubic EOS with excess free-energy (or liquid activity coefficient) models.

Wong Sandler [179] derived a general form of mixing rules first by combining the quadratic dependence of the second virial coefficient on composition and the relationship between the second virial coefficient and the parameters in a cubic EOS. The second equation in their mixing rules was derived by taking the limit of the excess Helmholtz free energy for a cubic EOS mixture at an infinite pressure. Helmholtz free energy is less pressure-dependent and can be approximated by excess Gibbs energy at low pressures where most experimental data are collected. The resultant mixing rules are the pressure independent, which satisfy the quadratic requirement:

$$B(T) = b - \frac{a}{RT} \tag{3-9}$$

in which, *a* and *b* denote the attraction and co-volume parameters of PR EOS. Since the composition dependence of the second virial coefficient is quadratic, the following relationships are obtained from the statistical mechanics:

$$b - \frac{a}{RT} = \sum\sum x_i x_j (b - \frac{a}{RT})_{ij} \tag{3-10}$$

$$b = \frac{RT\sum_i\sum_j x_i x_j \left(b - \frac{a}{RT}\right)_{ij}}{RT - \left[\sum_i x_i \left(\frac{a_i}{b_i}\right) + \frac{G^E}{C^*}\right]} \tag{3-11}$$

$$a = b\left[\frac{G^E}{C^*} + \sum x_i \frac{a_i}{b_i}\right] \qquad (3\text{-}12)$$

where x_i and x_j denote the composition of component i and j, and $C^* = 0.34657$ for the PR EOS.

The expression $(b - a/RT)_{ij}$, cross second virial coefficient, is given by the EOS as follows:

$$\left(b - \frac{a}{RT}\right)_{ij} = \left[\left(b_i - \frac{a_i}{RT}\right)\left(b_j - \frac{a_j}{RT}\right)\right]^{1/2}(1 - k_{ij}) \qquad (3\text{-}13)$$

or

$$\left(b - \frac{a}{RT}\right)_{ij} = \frac{1}{2}(b_i + b_j) - \frac{\sqrt{a_i a_j}}{RT}(1 - k_{ij}) \qquad (3\text{-}14)$$

In Equations (3-13) and (3-14), k_{ij} stands for the second virial coefficient binary interaction parameter. The values of the parameter are given in Appendix A2 for various CO_2/IL cases. This parameter has to be obtained experimentally near the conditions of interests. The experimental dependence of k_{ij} renders the WS model, not a fully predictive scheme.

Another relationship between a and b is defined by the excess Helmholtz free energy A^E for the liquid phase, as given below:

$$\lim_{p \to \infty}\left[\frac{A^E}{RT}\right] = \sigma(\alpha - \sum x_i \alpha_i) = \frac{A^E(x)}{RT} \qquad (3\text{-}15)$$

where σ is an EOS dependant constant and α represents the reduced attractive-term parameter, $\alpha = a/bRT$. The subscript i corresponds to pure component values of component i. Wong and Sandler assumed that A^E for liquid solutions is the same as G^E at low pressures, as shown below:

$$\frac{A^E_{\infty}(x)}{RT} = \frac{G^E(x)}{RT} \tag{3-16}$$

where A^E_{∞} signifies the excess Helmholtz free energy at the limit of infinite pressure and G^E is the excess Gibbs free energy.

3.2.2. PC-SAFT

The PC-SAFT EOS [181] can add the contribution of different terms to the residual Helmholtz free energy of the system, as listed below:

$$\tilde{a}^{res} = \tilde{a}^{hs} + \tilde{a}^{chain} + \tilde{a}^{disp} + \tilde{a}^{assoc} \tag{3-17}$$

where $\tilde{a}^{res}$ is the residual Helmholtz free energy of the system. The terms $\tilde{a}^{hs}$, $\tilde{a}^{chain}$, $\tilde{a}^{disp}$, and $\tilde{a}^{assoc}$ introduce the reference hard-sphere, chain (segment) formation, dispersion, and association contributions to the residual Helmholtz free energy, respectively. $\tilde{a}$ can be obtained from the following equation:

$$\tilde{a} = a/RT \tag{3-18}$$

where T is the absolute temperature and R represents the universal gas constant. The hard-sphere term in Equation (3-17) can be calculated using the Wertheim's theories [182] :

$$\frac{a^{hs}}{RT} = m\frac{4\eta - 3\eta^2}{(1-\eta)^2} \tag{3-19}$$

where m denotes the number of spherical segments per molecule and η stands for the reduced density, as defined below:

$$\eta = \tau\rho m v^0 \tag{3-20}$$

in which, v^0 is the segment molar volume of the fluid that can be expressed as follows:

$$v^0 = v^{00}(1 - C\exp(-\frac{3u}{kT}))^3 \qquad (3\text{-}21)$$

where u/k stands for the dispersive energy parameter per segment , v^{00} is the reference segment molar volume, and $C=0.12$ for all elements except for the hydrogen [183]. The chain formation and association contributions of Helmholtz free energy are calculated as follows [184]:

$$\frac{a^{chain}}{RT} = \sum_i x_i (1 - m_i)\rho[\frac{\partial \ln g_{ii}(d_{ii})^{hs}}{\partial \rho}]_{T,X_j} \qquad (3\text{-}22)$$

$$\frac{a^{assoc}}{RT} = \sum_i x_i \sum_\alpha \left[\sum_{A_{i\alpha}} (\ln X^{Ai\alpha} - \frac{X^{Ai\alpha}}{2}) + \frac{M_{i\alpha}}{2} \right] \qquad (3\text{-}23)$$

where,

$$[\frac{\partial \ln g_{ii}(d_{ii})^{hs}}{\partial \rho}]_{T,X_j} = \frac{i}{g_{ii}(d_{ii})^{hs}}[\frac{\xi_3}{(1-\xi_3)^2} + \frac{3}{2}\frac{d_{ii}\xi_2}{(1-\xi_3)^2}$$
$$+ \frac{3d_{ii}\xi_2}{(1-\xi_3)^3} + \frac{d_{ii}^2\xi_2^2}{(1-\xi_3)^3} + \frac{3d_{ii}^2\xi_2^2\xi_3}{2(1-\xi_3)^4}] \qquad (3\text{-}24)$$

in which, $M_{i\alpha}$ signifies the number of association sites of segment type α per molecule and X^A symbolizes the mole fraction of molecules not bonded at the association interaction site A. The summation is over all association sites on the molecule. The non-bonded fraction X^A is calculated from the following equation:

$$X^{Ai\alpha} = (1 + \rho\sum_j x_j \sum_\beta \sum_{B=1}^{M} \rho X^{Bj\beta}\Delta^{A_{i\alpha}B_{j\beta}})^{-1} \qquad (3\text{-}25)$$

where $\Delta^{A_{i\beta}B_{j\beta}}$ is the association strength which is introduced by the following expression:

$$\Delta^{A_{i\beta}B_{j\beta}} = g_{i\alpha i\beta}(d_{i\alpha i\beta})\kappa^{A_{i\alpha}B_{j\beta}}\sigma_{i\alpha i\beta}^3[\exp(\frac{\varepsilon^{A_{i\alpha}B_{j\beta}}}{kT}) - 1] \qquad (3\text{-}26)$$

where $\varepsilon^{A_{i\alpha}B_{j\beta}}$ is the association energy and $\kappa^{A_{i\alpha}B_{j\beta}}$ is the effective association volume between site A of molecule i and site B of molecule j.

The dispersion contribution to the Helmholtz free energy is given by the following equation [181]:

$$\frac{a^{disp}}{RT} = -2\pi\rho I_1(\eta,m)\sum_i\sum_j x_i x_j m_i m_j \sum_i\sum_j z_{i\alpha}z_{j\beta}(\frac{\varepsilon_{i\alpha j\beta}}{kT})\sigma_{i\alpha j\beta}{}^3 -$$

$$\pi\rho\overline{m}(1+Z^{hc}+\rho\frac{\partial Z^{hc}}{\partial\rho})^{-1}I_2(\eta,\overline{m})\sum_i\sum_j x_i x_j m_i m_j \sum_i\sum_j z_{i\alpha}z_{j\beta}(\frac{\varepsilon_{i\alpha j\beta}}{kT})\sigma_{i\alpha j\beta}{}^3 \qquad (3\text{-}27)$$

where $(1+Z^{hc}+\rho\frac{\partial Z^{hc}}{\partial\rho})^{-1}$, I_1 and I_2 integrals are given by the following relationships:

$$(1+Z^{hc}+\rho\frac{\partial Z^{hc}}{\partial\rho})^{-1} = (1+\overline{m}\frac{8\eta-2\eta^2}{(1-\eta)^4}+(1-\overline{m})\frac{20\eta-27\eta^2+12\eta^3-2\eta^4}{[(1-\eta)(2-\eta)]^2})^{-1} \qquad (3\text{-}28)$$

$$I_1(\eta,m) = \sum_{i=0}^{6} a_i(\overline{m})\eta^i \qquad (3\text{-}29)$$

$$I_2(\eta,m) = \sum_{i=0}^{6} b_i(\overline{m})\eta^i \qquad (3\text{-}30)$$

where the a_i and b_i coefficients are given below:

$$a_i(\overline{m}) = a_{0i} + \frac{\overline{m}-1}{\overline{m}}a_{1i} + \frac{\overline{m}-1}{\overline{m}}\frac{\overline{m}-2}{\overline{m}}a_{2i} \qquad (3\text{-}31)$$

$$b_i(\overline{m}) = b_{0i} + \frac{\overline{m}-1}{\overline{m}}b_{1i} + \frac{\overline{m}-1}{\overline{m}}\frac{\overline{m}-2}{\overline{m}}b_{2i} \qquad (3\text{-}32)$$

The model constants a_{0i}, a_{1i}, a_{2i}, b_{0i}, b_{1i}, and b_{2i} are reported in reference [181].

3.2.3. Modeling Algorithm and Assumptions

The solubility of CO_2 in ILs, using the PR and PC-SAFT EOSs, are obtained by applying the equilibrium condition at a constant temperature and pressure through the equality of fugacity of CO_2 (Component 1) in the gas phase ($\hat{f}_1^{gas}$) and ionic liquid phase ($\hat{f}_1^{IL}$) for the VLE system, as given below [181]:

$$\hat{f}_1^{gas} = \hat{f}_1^{IL} \qquad (3\text{-}33)$$

Using Equation (3-33) and conducting flash calculations with the PC-SAFT and PR EOSs, the solubility of CO_2 in different IL mixtures containing water and toluene are determined.

Figure 3-1 shows the computational procedure to calculate the solubility of gas components in the liquid phase. The main steps are as follows: (1) Enter pressure (P), temperature (T), and initial compositions of CO_2 and IL mixtures; (2) Guess the reduced density and K-values (distribution coefficients); (3) Input EOS parameters obtained from the density regression; (4) Obtain Z compressibility factor and fugacity coefficients for all components; (5) Determine the fugacity of each component in both phases; (6) Calculate the difference between the fugacity of the component in the phases (Δf_i^{vl}); (7) If the values of old and new pressures and magnitudes of fugacity of each component in both phases are equal, the correct extent of the solubility will be attained, otherwise, the reduced density and K-values should be updated; and (8) Determine the final pressure and solubility of gases in the liquid after the stop conditions are met.
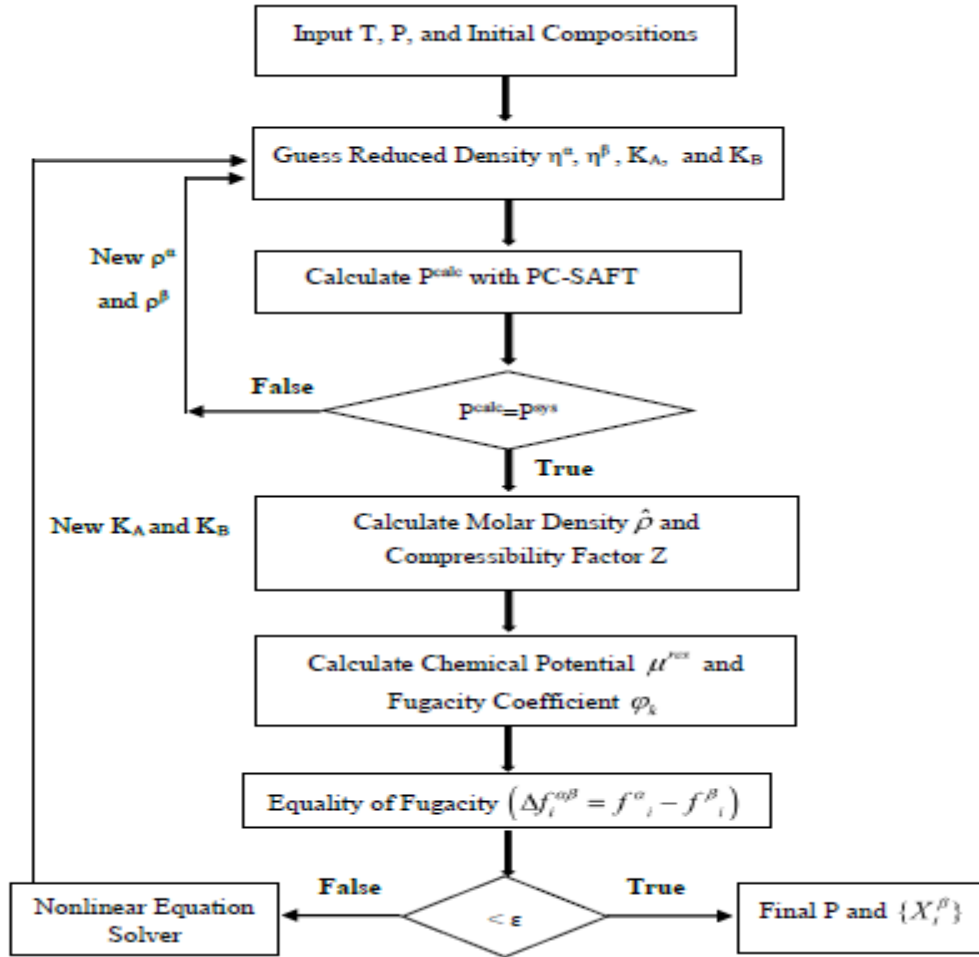
Figure 3-1: Flash algorithm to obtain solubility using EOSs such as PC-SAFT.

For three phases in equilibrium, the (VLLE) multi-flash calculations need to be performed. An isothermal flash with multiple phases is considered so that two functions/equations including a fraction of each phase in the equilibrium and stability of each phase are solved simultaneously. Minimization of Gibbs energy is implemented to solve these two functions.

In this modeling approach, ILs composed of cation and anions are considered as a single chain molecule with two associating sites.

Association or self-association occurs when complex formation due to the chemical forces act between like molecules and solvation. Cross association happens between unlike molecules. It is

important to define how molecules interact with each other using a number of association sites and their type (electron donor and/or electron acceptor) [185].

Associating molecules, which tend to form hydrogen bonds, and two association parameters are considered in the modeling. The first one is the association energy between sites A and B on molecule I and the second one is the effective association volume between sites A and B on the same molecule.

In this work, CO_2 gas is taken into account as a non-associating and also cross association between CO_2 and ILs is neglected. ILs are considered as associating molecules with the type of 2B. It implies that each IL molecule has one site type A as a donor site and one site type B as an acceptor site with a negative charge; only the donor-acceptor association bonding A-B type is allowed. In this case, the only non-zero interactions AB and BA are equivalent, as shown below [183]:

$$\Delta^{B_{i\alpha}A_{j\beta}} = \Delta^{A_{i\alpha}B_{j\beta}} \qquad (3\text{-}34)$$

which, Δ refers to the association strength. Thus, the mole fraction of molecules of type A and B will be equal, as follows:

$$X^{A_{i\alpha}} = X^{B_{i\alpha}} \qquad (3\text{-}35)$$

The proton donor can be one of the hydrogen atoms bonded to the carbons on the imidazolium ring. The proton acceptor can be any atoms of oxygen and fluorine in the anion [183].

3.3. Parameter estimation

The pure component parameters for PR EOS such as T_c and P_c are not available for all of the ionic liquids, but they can be determined from the group contribution method such as the modified Lyderson-Joback-Reid method [2]. The acentric factor ω for PR EOS can be calculated from the Ambrose-Walton corresponding-states method [186]. For the ILs used in this study, the parameters T_c, P_c, and ω are obtained based on the research work conducted by Valderrama et al. [2, 64]. The

binary interaction coefficients and activity coefficients are determined from fitting the experimental *P-xy* data for the CO_2-IL binary systems within the temperature range of interest. The optimized parameters are attained from minimizing the objective function which is the relative absolute error between the experimental and correlated solubility data for PR EOS. The objective function (OF) is defined as follows:

$$OF = \min \sum_{i}^{N} (\frac{P_i^{\exp} - P_i^{calc}}{P_i^{\exp}})^2 \qquad (3\text{-}36)$$

where $P_i^{\exp}$ is the experimental pressure, P_i^{calc} represents the calculated pressure from PR, and N stands for the number of data points.

The parameters of PC-SAFT EOS include the association and non-association parameters. Three non-association parameters include the segment number *m*, the segment diameter *σ*, and the segment energy parameter ε / k_B. The two association-based parameters are the association energy ε^{AB} and the association volume κ^{AB}. The PC-SAFT pure-component parameters for CO_2 are reported in the literature [173]. The non-association parameters for some ILs are also found in the literature [11]. The association parameters for the Lewis acid-base association between the CO_2 (Lewis acid) and the anion site on IL (Lewis base) can be estimated from the following equations [33]:

$$\frac{\varepsilon^{AB}}{k} \approx -\Delta H^{dissol} \qquad (3\text{-}37)$$

$$\kappa^{AB} \approx \exp(\frac{\Delta S^{dissol}}{R}) \qquad (3\text{-}38)$$

The values of the association energy (ε^{AB}/k) and association volume (κ^{AB}) are reported as 3540 K and 0.00225 for CO_2-IL system, respectively [11]. Values such as ε^{AB}/k=5000 K and κ^{AB} = 0.1 are also given in the open sources for the system of CO_2-IL, which exhibited accurate results for association parameters using the density correlation in some ILs [187]. Both values are adjusted for each IL and the best magnitudes are selected.

PC-SAFT parameters for pure ILs are obtained by fitting the pure component density data in a range of temperatures (260-370 K). The binary interaction coefficients are also calculated from fitting the VLE data for the CO_2-IL system. In the regression of density data for pure ILs to find the PC-SAFT parameters, it is noticed that the effect of the segment energy parameter is negligible, compared to other parameters. The segment number m and the segment diameter σ are found to have a considerable effect. It means that a slight change in these parameters leads to a significant variation in the estimation of density, using the fitted parameters. The references for the density data of studied ILs are listed in Table 3-1.

Table 3-1: Experimental information of pure-IL density data used for parameter fitting ($P \leq 1000$ bar).

ILs	T (K)	Ref
[BMIM][BF$_4$]	278–373	[188]
[BMIM][PF$_6$]	278–373	[188]
[BMIM][Tf$_2$N]	278-373	[189]
[hmim][Tf$_2$N]	273–413	[190]
[hmim][PF$_6$]	278–365	[191]
[hmim][FAP]	278-373	[192, 193]

In fitting the experimental data of pure IL density to the PC-SAFT EOS, the association parameters are considered constant. The values for these parameters are taken from the literature for the system of CO_2-IL [11, 194]. A better fit for [hmim][Tf$_2$N] is found with κ^{AB}=0.1 and (ε^{AB}/k)=5000 K as suggested by Ji et al. [187]. For [bmim][BF$_4$], [bmim][PF$_6$], [bmim][Tf$_2$N], [hmim][PF$_6$], and

[hmim][FAP] ILs, the association parameters are fitted with the association parameters as $\kappa^{AB} =$ 0.00225 and (ε^{AB}/k)=3540 K.

The objective function, which is used for the density data regression, is the maximum-likelihood function using the Britt-Luecke algorithm [195]. PC-SAFT parameters of pure ILs are obtained by fitting the calculated density data of ILs to the experimental density data.

The optimal parameters of PC-SAFT that are determined for various ILs (used in this work) are presented in Table 3-2. Absolute Average Deviation Percentage (AAD %) is used as a measure of model accuracy, as shown below:

$$AAD(\%) = (\frac{100}{N})\sum_{i=1}^{N}(\frac{\rho_i^{\exp} - \rho_i^{calc}}{\rho_i^{\exp}})$$ (3-39)

where $\rho_i^{\exp}$ is experimental density; ρ_i^{calc} is the calculated density; N denotes the number of data points. Figure 3-2 compares the PC-SAFT and experimental results to forecast pure IL ([hmim][Tf$_2$N]) density with temperature. For brevity, we do not show the results for other ILs here; they are presented in Appendix A2. The resultant density-temperature diagram shows that the density is well correlated within the range of temperature. The magnitudes of AAD (%) achieved in estimating the density of pure ILs are tabulated in Table 3-2: Optimized PC-SAFT parameters used for different ILs. These values are in the order of 0.01% which shows a great agreement between the PC-SAFT predictions and experimental density data.
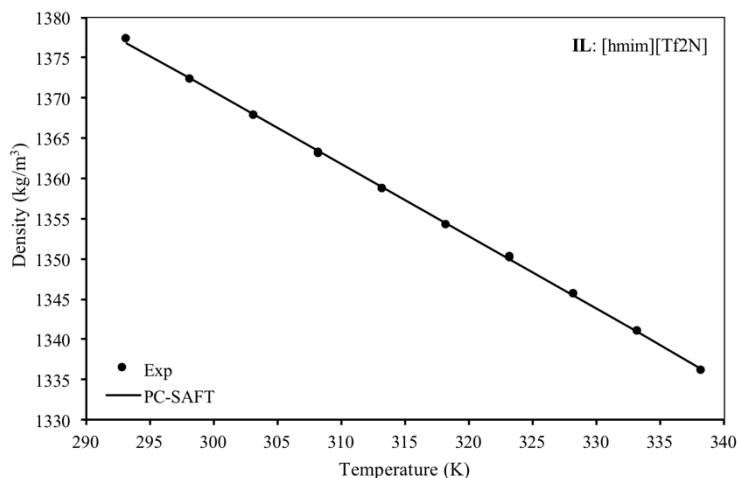
Figure 3-2: Comparison of the density of pure [hmim][Tf$_2$N] with temperature, using experimental data [190] (scatter points) and PC-SAFT EOS (solid line).

Table 3-2: Optimized PC-SAFT parameters used for different ILs.

IL	Mw (g/mol)	PC-SAFT parameters					Absolute Deviation (%)			No. data
		m	σ (A)	ε/k (K)	κ^{AB}	ε^{AB}/k (K)	min	average	max	
[bmim][BF$_4$]	226	2.2969	5.037	483.53	0.00225	3450	0.00017	0.0056	0.0190	22
[bmim][PF$_6$]	284	2.2820	5.201	456.29	0.00225	3450	0.00027	0.0080	0.0150	22
[bmim][Tf$_2$N]	419	2.7150	5.451	350.50	0.00225	3450	0.00046	0.0044	0.0140	28
[hmim][Tf$_2$N]	447	11.000	3.342	305.25	0.10000	5000	0.00120	0.0141	0.0350	18
[hmim][PF$_6$]	312	2.5500	5.301	487.13	0.00225	3450	0.00240	0.0152	0.0250	18
[hmim][FAP]	239	4.4060	5.145	357.91	0.00225	3450	0.00096	0.0140	0.0410	21

The Heat capacities of [hmim][Tf$_2$N], [hmim][PF$_6$], and [hmim][FAP] at different temperatures and pressures are reported in [196], [197], and [198], respectively. The binary interaction coefficients between ILs and CO$_2$ are also presented in Appendix A2.

3.4. Results and discussion

3.4.1. The solubility of CO₂ in pure Ionic Liquids (ILs)

The solubility of CO_2 in [bmim][BF$_4$], [bmim][PF$_6$], and [bmim][Tf$_2$N] at 298 K, 313 K, and 333 K are modeled, using PR and PC-SAFT EOSs in a broad pressure range of 1–100 bar. The average absolute deviation percentage, AAD (%), between the calculated and experimental equilibrium pressure data is calculated at different temperatures for various CO_2-IL systems. The results are shown in Table 3-3.

Table 3-3: Calculated AAD (%) for the solubility of CO_2 in ILs based on PR and PC-SAFT EOSs.

EOS	IL	AAD (%)			Data Ref.
		298 K	313 K	333 K	
PR	[bmim][BF$_4$]	3.630	5.806	4.699	[101, 161]
	[bmim][PF$_6$]	3.164	5.700	4.510	[112]
	[bmim][Tf$_2$N]	6.473	7.513	6.710	[199]
PC-SAFT	[bmim][BF$_4$]	2.013	4.163	2.827	[101, 161]
	[bmim][PF$_6$]	3.010	4.300	5.420	[112]
	[bmim][Tf$_2$N]	5.710	5.730	5.120	[199]

Based on AAD (%) for PR and PC-SAFT EOSs presented in Table 3-, the PC-SAFT estimates the solubility with more accuracy for all ILs, compared to the PR. The SAFT EOS considers the effect of molecular structure and interactions on the bulk properties and phase behavior, while the PR EOS assumes molecules to behave as hard spheres. The SAFT parameters have the physical significance, featuring the diameter of a segment, the number of segments in a chain, and the segment-segment van der Waals interactions [108]. Furthermore, the PC-SAFT EOS incorporates the influence of molecular association on the volume and energy, which can potentially predict a more precise and reliable phase behavior when the association between the molecules becomes important.

Since PC-SAFT modeling had accurate results compared to PR, the rest of the solubility predictions in this study are done with PC-SAFT EOS. In this section, three ILs with relatively high CO_2 solubility have chosen to study. The solubility of CO_2 in [hmim][Tf$_2$N], [hmim][PF$_6$], and [hmim][FAP] at temperatures of 298.15 K, 313.15 K, and 333.15 K (common temperatures for experiments in the literature) and a broad range of pressure (1–100 bar) is determined using PC-SAFT. The solubility results (*P-x*) diagram is given in terms of mole fraction (x_{CO2}) in the liquid phase for different isotherms. For each isotherm, the maximum pressure is chosen around the bubble point pressure of the mixture. The temperature-dependent binary interaction coefficient is tuned by fitting to the experimental VLE data for the binary systems of CO_2-IL. Figure 3-3 depicts the solubility values for [hmim][PF$_6$], [hmim][Tf$_2$N], and [hmim][FAP] at wide range of pressure. The modeling results are also compared with the experimental data in Figure 3-3, exhibiting an excellent agreement between the experimental data of solubility and those estimated from the PC-SAFT model. However, at higher pressures and temperature, some deviations in both systems, particularly at 313 K are observed. As it is expected, the solubility of CO_2 in IL increases with increasing pressure and decreases with increasing temperature. The AAD (%) values for each IL at various temperatures are reported in Table 3-, showing that the modeling outputs are in great agreement with the experimental data of the solubility for the CO_2-IL systems.
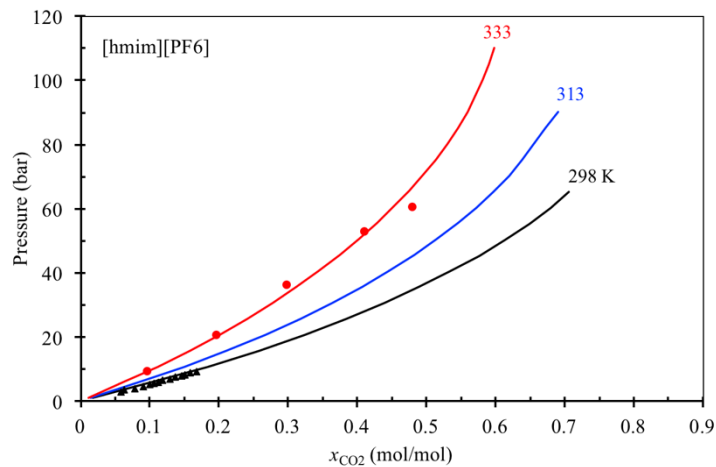
(a)
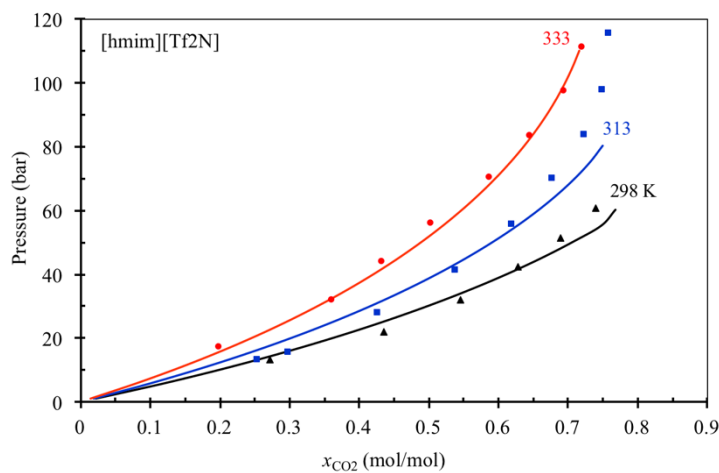
(b)
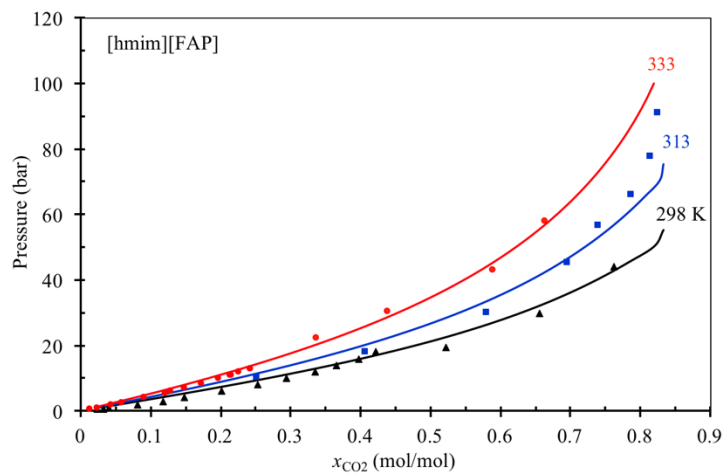
(c)

Figure 3-3: Solubility of CO_2 in different ILs at 298 K, 313 K, and 333 K for (a) [hmim][PF$_6$] (scatter data from [169, 200]) , (b) [hmim][Tf$_2$N] (scatter data from [101]), and (c) [hmim][FAP]

(scatter data from [110, 201, 202]). Solid lines show the PC-SAFT predictions and scatter points are taken from the experiments.

Table 3-4: Calculated AAD (%) achieved in estimating CO_2 solubility in ILs with PC-SAFT for [hmim][Tf$_2$N], [hmim][PF$_6$], and [hmim][FAP] at various temperatures.

IL	AAD (%)			Data Ref.
	298 K	**313 K**	**333 K**	
[hmim][PF$_6$]	5.26	-	2.97	[169, 200]
[hmim][Tf$_2$N]	3.52	2.29	1.20	[101]
[hmim][FAP]	1.70	2.08	4.45	[110, 201, 202]

3.4.2. The solubility of CO$_2$ in Mixtures of ILs and Water

Adding other solvents to ILs is performed for two main purposes: 1) to reduce the viscosity of ILs by using a less viscous solvent such as water, and 2) to decrease the overall cost. In this section, the solubility of CO_2 in ILs + water and ILs + toluene systems are investigated and compared to that in pure ILs. The solubility of CO_2 in hydrophilic IL, [bmim][Ac], and two hydrophobic ILs including [hmim][Tf$_2$N] and [hmim][FAP] at different water contents (0.1, 1.0, and 10 wt%) and various temperatures and pressures are investigated. In general, the hydrophobicity of the ILs increases with increasing the alkyl cation chain length [191, 203]. Figure 3-4 demonstrates the influence of water content in the liquid medium on the solubility of CO_2 at 298 K, 313 K, and 323 K for [hmim][FAP], being used as the IL. According to Figure 3-4, the presence of water at low concentrations (e.g., <1 wt%) does not have a significant impact on the solubility of CO_2 when compared to the case, using pure IL ([hmim][FAP) at the same temperature and pressure. However, at a higher water content, the solubility of CO_2 is lowered considerably. When the concentration of water reaches 10 wt%, there is a substantial decrease (by about 45%) in the solubility of CO_2 in IL+W solution (IL and water mixture), compared to the solubility of CO_2 in pure IL at 298 K. On the other hand, the mixture viscosity decreases with increasing the water content, as shown in

Table 3-. To evaluate the solubility of CO_2 in the mixture of ILs and water, the Vapor-Liquid-Liquid Equilibrium (VLLE) is performed. There are two liquid phases; the first phase is mostly water at which a minor amount of CO_2 (e.g., 3×10^{-5} mole/mole) is dissolved in, and the second phase is mainly IL where most of the CO_2 is dissolved in this phase.
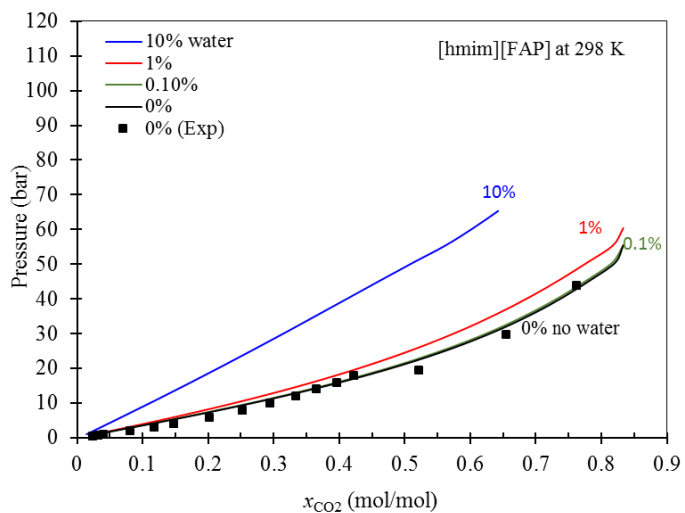
(a)
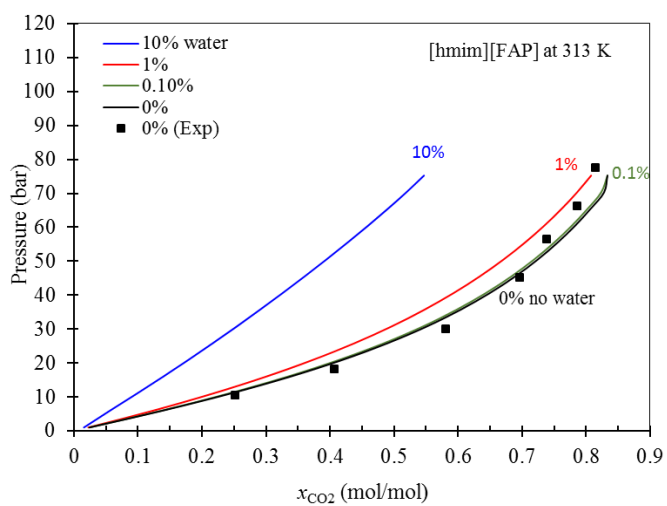
(b)
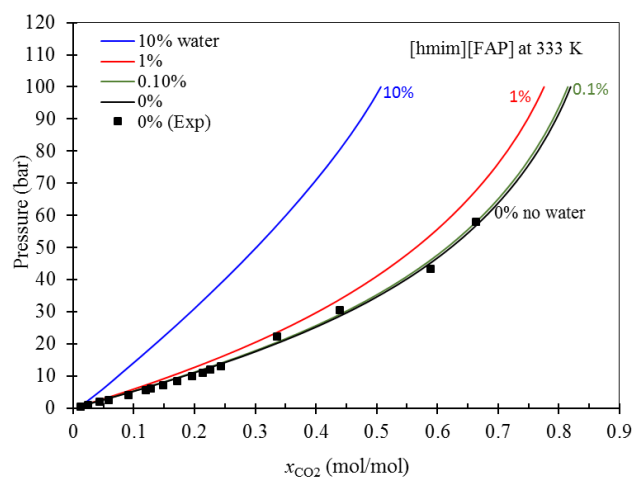
(c)

Figure 3-4: Effect of water content on the solubility of CO_2 in [hmim][FAP] at (a) 298 K, (b) 313 K, and (c) 333 K.

With increasing the concentration of water from 0 to 10 wt% the viscosity of the system decreases from 88.49 to 56.01 cP at temperature and pressure of 298 K and 20 bar. Adding water to reduce the viscosity of hydrophobic ILs is not the best solution since it decreases the solubility of CO_2 significantly. Similarly, we investigate the effect of water content on the solubility of CO_2 in [hmim][Tf$_2$N] mixture with water in Figure 3-5 and in [bmim][Ac] mixture with water in Figure 3-6.

The temperature dependency of the viscosity for pure liquids is expressed by the Vogel-Tammann-Fulcher equation, where various mixing rules can be applied for the mixtures [204].

The mixing rule used to determine the viscosity of the mixture of ILs and water is based on the Katti and Chaudhri mixing law as shown below [205]:

$$\log(v\,\eta) = x_1 \log(v_1\,\eta_1) + (1-x_1)\log(v_2\,\eta_2) + \frac{\Delta G^{*E}}{RT} \qquad (3\text{-}40)$$

where v denotes the molar volume; η symbolizes the absolute viscosity of the mixture; η_1 and η_2 stand for the viscosity of component 1 and component 2, respectively; x_1 represents the mole fraction of component 1; R is the universal gas constant; T introduces the absolute temperature, and ΔG^{*E} is the excess molar Gibbs energy of activation. If a mixture does not deviate considerably from the ideal mixture model, $\Delta G^{*E} = 0$.

There is another equation, based on a similar hypothesis, called the "ideal" Grunberg and Nissan mixing law [206]. The corresponding equation is given by the following expression:

$$\log(\eta) = x_1 \log(\eta_1) + (1-x_1)\log(\eta_2) \qquad (3\text{-}41)$$

Equation (3-39) is also suitable for systems which do not exhibit large deviations from the ideal mixture model.

It is found that the organic solutes including water and toluene studied in this work alter the viscosity of the IL (η_{IL}) by the following exponential equation:

$$\eta = \eta_{IL}\exp(-x_s/a) \tag{3-42}$$

where η and η_{IL} represent the viscosity of the mixture and the viscosity of the pure ionic liquid, respectively; x_s signifies the mole fraction of the organic solutes; and a is a constant with a value of 0.231 ± 0.003 for [hmim][Tf$_2$N] and [hmim][FAP] and 0.022 ± 0.011 for [bmim][Ac]. This confirms the findings attained by Seddon et al. [207]. Therefore, the viscosity of a mixture can be estimated as a function of the concentration of the dissolved compounds, independent of their polarity [208].

Table 3-5: Solubility of CO_2 in IL+W mixtures and the viscosity of IL and IL+W mixtures at various levels of water contents.

Parameter	T (K)	IL	IL+W mixture (wt% of W)					
			0	0.1 %	1 %	2 %	5 %	10 %
Viscosity† (cP)	298	[hmim][Tf$_2$N]	69.48	69.18	66.54	63.71	55.95	45.05
		[hmim][FAP]	88.49	88.09	84.54	80.76	70.40	56.01
		[bmim][Ac]	416	389	225.86	135.5	44.08	14.34
	313	[hmim][Tf$_2$N]	36.86	36.72	35.42	34.02	30.17	24.69
		[hmim][FAP]	43.64	43.61	43.59	43.53	43.36	43.02
		[bmim][Ac]	139.86	131.96	81.92	56.53	19.73	7.41
	333	[hmim][Tf$_2$N]	18.88	18.6	18.2	17.54	15.7	13.066
		[hmim][FAP]	20.72	20.71	20.70	20.66	20.60	20.47
		[bmim][Ac]	47.64	45.30	30.04	20.45	8.78	3.77
Solubility of $CO_2^†$ (mol/mol)	298	[hmim][Tf$_2$N]	0.394	0.361	0.318	0.297	0.247	0.219
		[hmim][FAP]	0.478	0.473	0.429	0.390	0.304	0.215
		[bmim][Ac]	0.456	0.45	0.436	0.429	0.419	0.41
	313	[hmim][Tf$_2$N]	0.315	0.297	0.256	0.247	0.203	0.172
		[hmim][FAP]	0.417	0.412	0.37	0.31	0.272	0.177
		[bmim][Ac]	0.424	0.421	0.405	0.391	0.378	0.363
	333	[hmim][Tf$_2$N]	0.251	0.239	0.208	0.197	0.163	0.131
		[hmim][FAP]	0.344	0.339	0.304	0.281	0.235	0.14
	323	[bmim][Ac]	0.389	0.388	0.378	0.367	0.334	0.318

† At P=20 bar

The result for adding water into the moderately hydrophobic IL [hmim][Tf$_2$N] reveals that at a low concentration of water (0.1 wt%) there is no effect on the solubility of CO_2 similar to the case for [hmim][FAP]. However, by increasing the concentration of water in [hmim][Tf$_2$N] to 10 wt%, the solubility of CO_2 is reduced by about 20 % at 298 K and 20 bar, as demonstrated in Figure 3-5 (and also Table 3-). The reduction in the solubility of CO_2 in [hmim][Tf$_2$N] by adding 10 wt% water is less than that with [hmim][FAP]. The influence of water on the IL+W mixture viscosity shows the same trend as that with the strongly hydrophobic IL. Also, at a higher temperature and pressure, the reduction in the solubility is more pronounced. By increasing the concentration of water from 0 to 10 wt%, the mixture viscosity ([hmim][Tf$_2$N] and water) declines from 69.48 to 45.2 cP at a temperature and pressure of 298 K and 20 bar, respectively. Hence, water with low concentrations such as 0.1 wt% case can be employed as a suitable additive to decrease the viscosity of hydrophilic ILs that has a minimal effect on the solubility at lower concentrations. The optimum amount of water in the IL+W mixture depends on the composition of the IL systems.

As shown in Table 3-, the viscosity of IL+W mixture decreases and the solubility of CO_2 in the mixture of IL+W also decreases with increasing the water content. The optimum amount of water needs to be obtained by considering the thermodynamic characteristics (solubility and selectivity), transport properties (rate of mass transfer), unit operations (number of equilibrium stages), process design (equipment sizing), and energy requirement (for pumping based on the viscosity). For instance, in the case of [hmim][Tf$_2$N] at 298 K and 20 bar, there is less than 2 % reduction in the viscosity by adding 10 wt% water, while the solubility lowers by about 20%. A careful optimization process requires the contribution of water content to a reduction in the capital and operating costs (due to viscosity reduction and an increase in dissolution rate) to be evaluated.

Figure 3-6 illustrates the effect of water content in the IL on the solubility of CO_2 at temperatures 298 K, 313 K, and 333 K within a pressure range of up to 30 bar with [bmim][Ac], which is a hydrophilic IL. As clear from Figure 3-6, at low water concentrations (e.g., 0.1 wt%), water content does not exhibit an appreciable influence on the solubility of CO_2. With increasing the concentration of water to 10 wt%, the solubility of CO_2 is reduced by about 9 % at 298 K and 20 bar. The effect of water concentration on IL+W mixture viscosity implies that by increasing the concentration of water from 0 to 10 wt%, the viscosity of the mixture lowers dramatically from 416 to 14.5 cP at a temperature and a pressure of 298 K and 20 bar. Thus, water can be considered as a viable additive to hydrophilic ILs for CO_2 separation, as a significant viscosity reduction is experienced without sacrificing solubility. This helps to lower the pressure drop in the CO_2 capture process that will affect the amount of energy requirement and GHG emissions.

Although with the addition of water to the IL, the solubility decreases (slightly), the rate of CO_2 mass transfer in the IL+W mixture will be increased as it is proportional to the inverse of viscosity. Therefore, it will contribute to a decrease in the capital cost due to smaller process equipment as a result of shorter processing time.
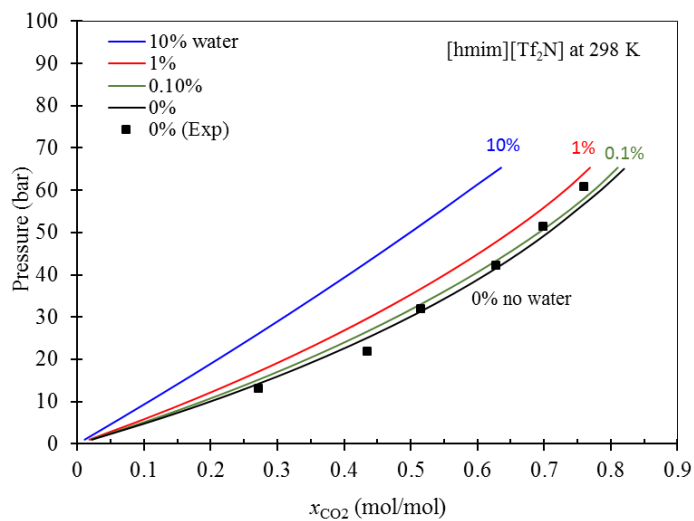
(a)
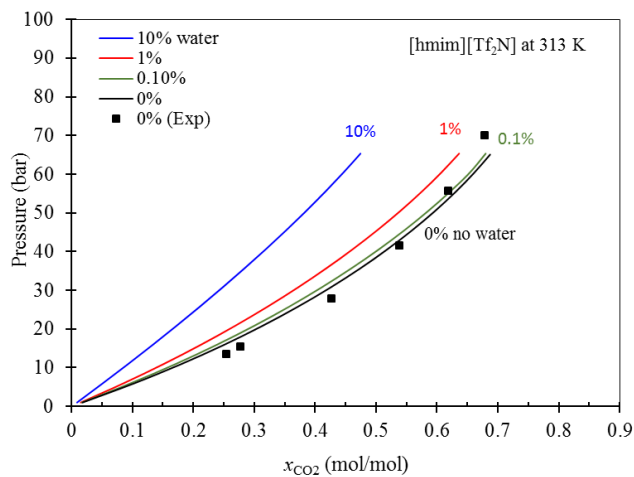
(b)
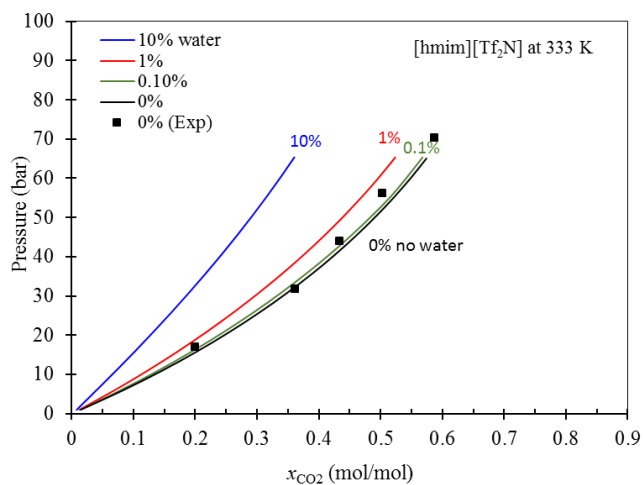
(c)

Figure 3-5: Effect of water content on the solubility of CO_2 in [hmim][Tf$_2$N] at (a) 298 K, (b) 313 K, and (c) 333 K.
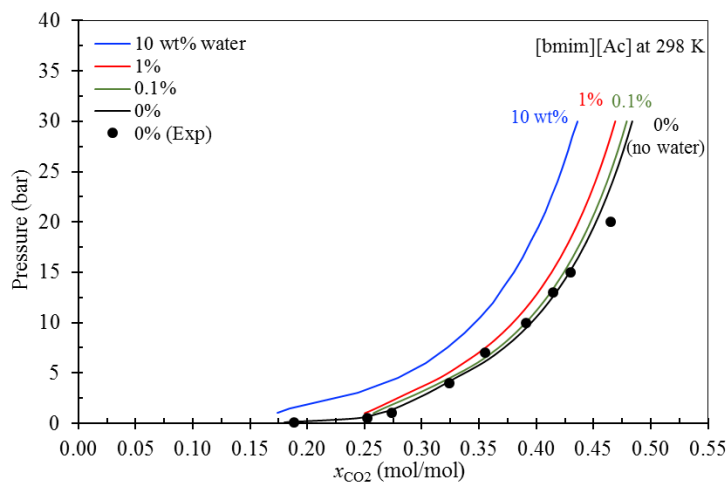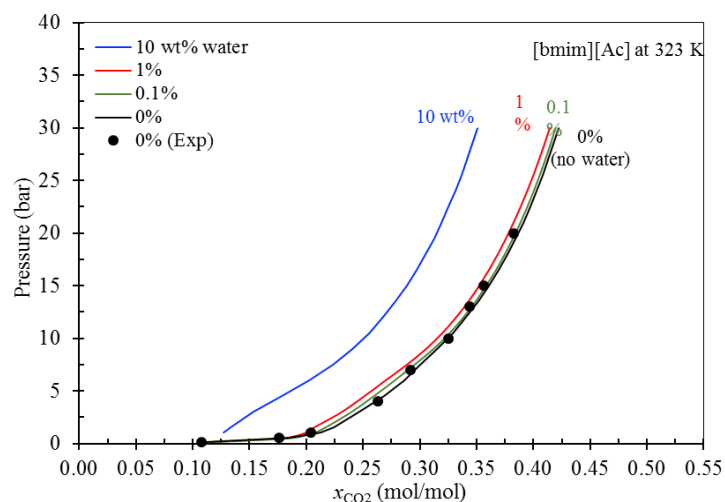
Figure 3-6: Effect of water content on the solubility of CO_2 in [bmim][Ac] at (a) 298 K, and (b) 323 K.

The effect of water on the solubility of CO_2 in mixtures of IL with water is also explored by plotting the ratio of solubility in IL with and without water as a function of solubility in pure IL (without water). This is shown for [hmim][FAP] (in Figure 3-7(a)), [hmim][Tf$_2$N] (in Figure 3-7 (b)), and [bmim][Ac] (in Figure 3-7(c)). The solubility behavior is interesting. For Figure 3-7 (a) and (b), the solubility values are compiled for different temperatures (298, 313, and 333 K) and pressure

(up to 100 bar) conditions. In Figure 3-7(c), the ranges of operating conditions for the solubility are temperatures of 298 and 323 K and pressures up to 30 bar.
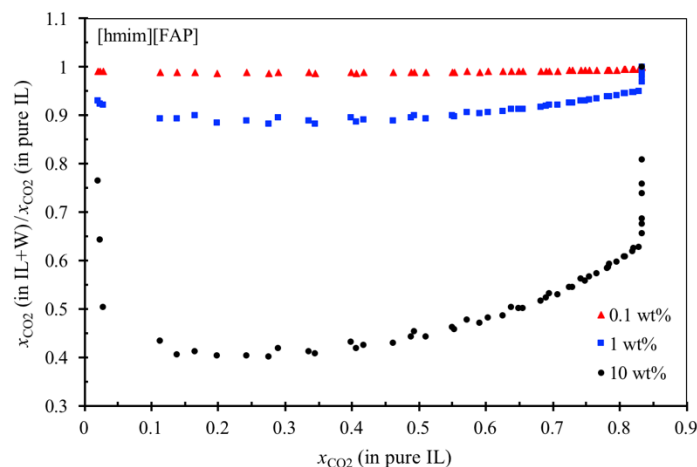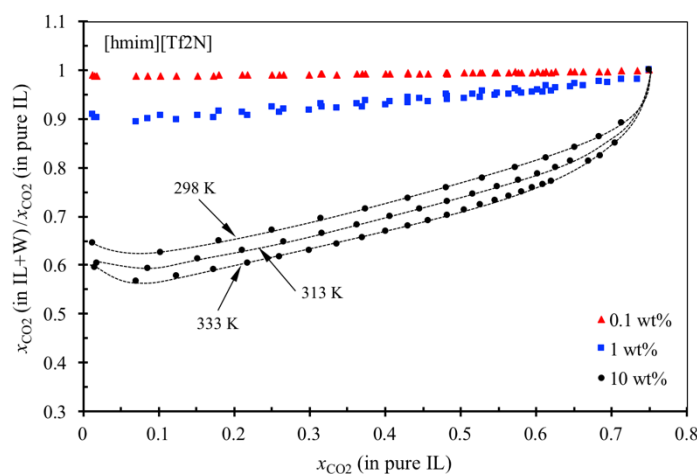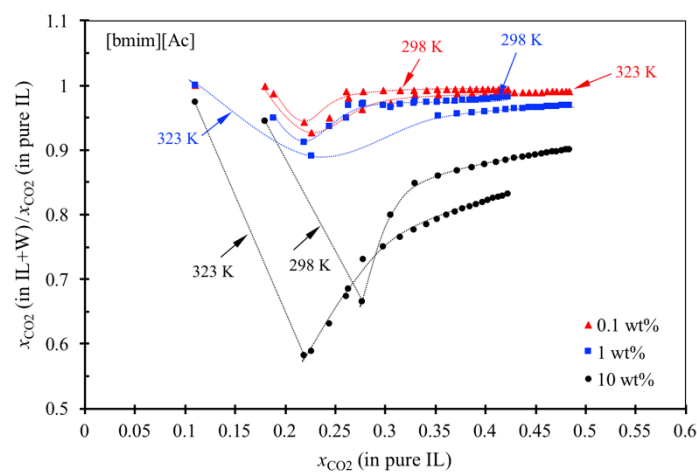
Figure 3-7: The effect of water content on the solubility of CO_2 in mixtures of IL with water, using PC-SAFT EOS for (a) [hmim][FAP], (b) [hmim][Tf$_2$N], and (c) [bmim][Ac]. In panels (a) and (b), temperatures of 298, 313, and 333 K and the pressure range 1-100 bar are used; while in panel (c) temperatures 298 and 323 K; and pressure range 1-30 bar are utilized.

Figure 3-7 depicts that there is a minimum in the ratio of solubility in IL+W mixtures and that in the pure ILs, which appears at a lower solubility limit (0.1-0.3 mol/mol). This will occur at higher temperatures and lower pressures. Among the three ILs shown in Figure 3-7, [hmim][FAP] and [hmim][Tf$_2$N] are hydrophobic and [bmim][Ac] is hydrophilic. Moreover, [hmim][FAP] is more hydrophobic than [hmim][Tf$_2$N]. Based on Figure 3-7, it is concluded that the effect of water content is different for hydrophobic and hydrophilic IL cases. The extent of hydrophobicity also affects the contribution/role of water (as an additive to the IL) to the solubility of CO_2. Comparing Figure 3-7 panels (a) and (b) conveys the message that the performance of IL in CO_2 capture process is not affected by the water content at concentration 0.1 wt%. By adding 1% water, a negative effect on the solubility for most of the solubility range is noticed and there is no strong correlation between the performance and temperature. However, by adding 10 wt% water, there is a significant reduction in the solubility of CO_2 in IL+W mixture, compared to that in the pure IL. Moreover, we observe a minimum performance compared to the baseline, which occurs at an equivalent solubility in pure IL at 0.1 mol/mol for [hmim][FAP] and about 0.2 for [hmim][Tf$_2$N]. This minimum performance (in terms of solubility) is experienced at 0.25 mol/mol for [bmim][Ac]. Therefore, there is a shift in the minimum solubility towards higher solubility values with lowering the hydrophobicity characteristic. Also, the ratio of solubility in IL+W mixture to that in pure IL at 10 wt% water is not correlated with temperature for the most hydrophobic IL ([hmim][FAP]), while there is a significant correlation to temperature for the other two ILs (in Figure 3-7 (b) and (c)) for which, the performance decreases due to an increase in the temperature. A shift in the location of the minimum concentration towards lower solubility values (with respect to the solubility in pure IL) is also observed. The drop in the solubility of CO_2 as a result of the water presence is much more predominant for the hydrophilic IL ([hmim][Ac]); however, it affects

a narrower range of solubility, beyond which the solubility is not much different than the pure IL (without water). This analysis (as described in Figure 3-7(c)) suggests that the addition of a fixed amount of water to the IL will not significantly alter the performance of IL+W mixture beyond the solubility value of 0.3 mol/mol. This will provide screening criteria on operating temperatures and pressures, which are suitable for CO_2 capture.

3.4.3. The solubility of CO_2 in Mixtures of ILs and Toluene

Toluene can be added to ILs to decrease their viscosity and make them more suitable for high-temperature carbon capture systems. To study the influence of toluene (T) content on the viscosity and vapor pressure of IL+T mixture and the solubility of CO_2 in IL+T mixture, [hmim][Tf_2N] is utilized. The toluene content in the IL+T mixture in the range of 0-100 % is investigated as listed in Table 3-. Through adding toluene, the viscosity of the mixture reduces. In this research work, the effect of adding toluene on the vapor pressure of IL+T mixtures is also determined. Based on the results, the vapor pressure of the mixture is similar to the vapor pressure of toluene (as a volatile component). Even by adding only 1 mol % toluene to the ionic liquid, the vapor pressure of the mixture will be 0.0011 bar, which is much higher than the vapor pressure of pure IL. Hence, the effect of ILs in reducing the volatility of toluene is not applicable. The solubility of CO_2 in pure [hmim][Tf_2N] is higher than that in pure toluene. Hence, to decrease the cost of using ILs and lower the viscosity, we can add some toluene into the system at lower temperatures. The optimum amount of added toluene should be determined. At 298 K and 20 bar, the solubility of CO_2 in the mixture is reported in Table 3-. It appears that having up to 8.1 wt% of toluene in the IL+T mixture is acceptable. However, adding more than 30 mole% toluene causes an increase in the volatility of the mixture close to the volatility of the toluene. Due to this addition, solubility will be also

declined by more than 6.3%. The validity of the model is tested by comparing the experimental data in the literature with those from the PC-SAFT model. As demonstrated in Figure 3-8, the solubility predictions from PC-SAFT EOS show a great match with the real data for the solubility of CO_2 in pure IL ([hmim][Tf$_2$N]), pure toluene, and mixtures of [hmim][Tf$_2$N] + toluene. However, the solubility values estimated by the PC-SAFT model deviate from the experimental data for pure IL at higher pressures (e.g., >40 bar).

Table 3-6: Viscosity, vapor pressure, and solubility of CO_2 in IL+T mixtures for [hmim][Tf$_2$N].

Parameter	% Toluene (T) in IL+T mixture (mol%)						
	0% (0 wt%)	**1%** (0.2 wt%)	**10%** (1.1 wt%)	**30%** (8.1 wt%)	**50%** (17 wt%)	**70%** (32.4 wt%)	**100%** (100 wt%)
Viscosity (cP)	69.48	68.79	62.37	46.92	30.45	14.48	0.554
$P^{sat\,*}$ (bar)	6×10^{-17}	0.0011	0.0109	0.0288	0.0399	0.042	0.0366
Solubility* (mol/mol)	0.394	0.39	0.386	0.369	0.351	0.328	0.25

* At T=298 K and P=20 bar
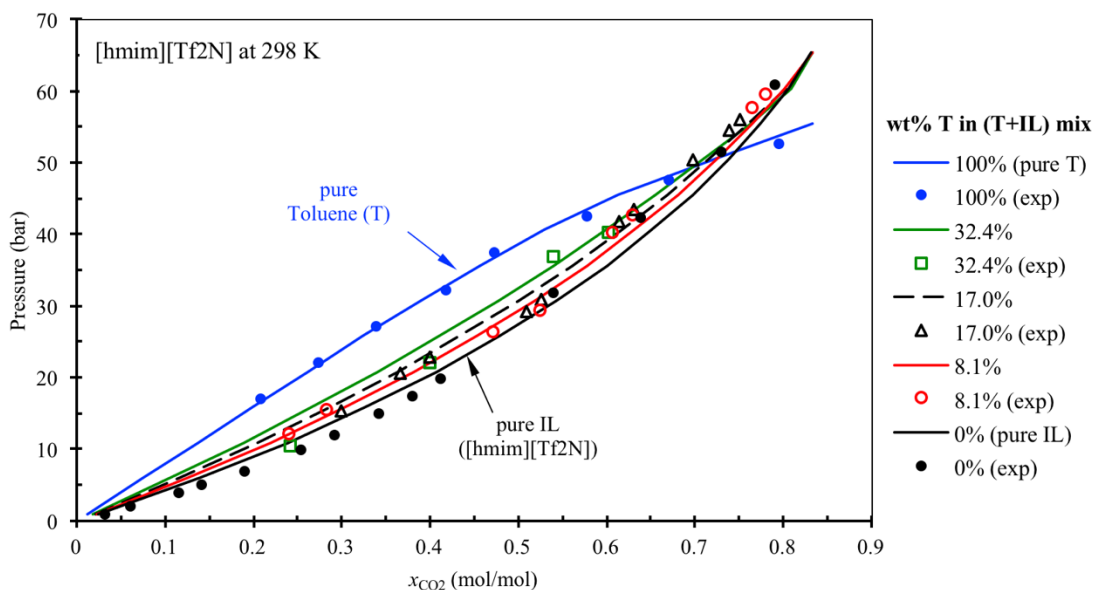
Figure 3-8: Solubility of CO_2 in pure IL ([hmim][Tf$_2$N]) [101, 209], pure toluene [210], and their mixtures [211]. Scatter points show the experimental values and the solid lines represent PC-SAFT model results,

using the parameters listed in Table 3-2, and $k_{ij}=$ -0.01 for [hmim][Tf$_2$N]+CO$_2$ and $k_{ij}=$ 0.105 for toluene+CO$_2$ at 298 K.

According to Figure 3-8, it is clear that IL has a higher solubility at the same pressure (at 298 K). Toluene exhibits a good solubility in [hmim][Tf$_2$N]. With the addition of toluene to the IL, the solubility decreases slightly while the viscosity is significantly reduced. This reduction in the viscosity is expected to lower the dissolution rate of CO$_2$ and also the energy input for the processing/transferring of IL. The effect of toluene on the solubility of CO$_2$ in the IL+T mixture is also depicted in Figure 3-9 as the ratio of solubility in the IL with and without toluene versus the CO$_2$ solubility in pure IL (without toluene). Figure 3-9 illustrates a different trend, compared to the behavior of water as an additive, as seen in Figure 3-7. In this research investigation, a monotonic increase in the performance of toluene as an additive is observed at higher levels of solubility, compared to the CO$_2$ solubility in pure IL as the baseline. In other words, the negative effect of toluene as an additive on the solubility of CO$_2$ is less pronounced at higher solubility values (higher pressures and lower temperatures). Moreover, with increasing the toluene concentration, the solubility of CO$_2$ is decreased, which is expected. However, this difference becomes less at a greater range of CO$_2$ solubility (in pure IL).
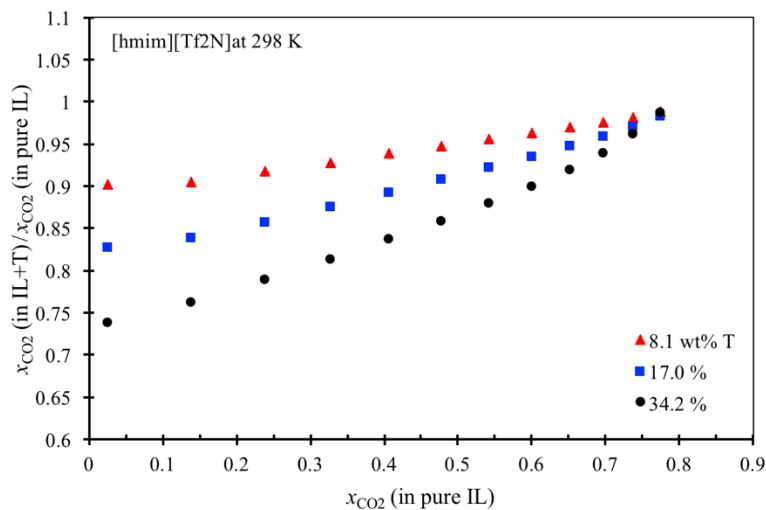
Figure 3-9: Influence of toluene (T) on the solubility of CO_2 in mixtures of [hmim][Tf$_2$N] and toluene at a temperature 298 K and a pressure range 1-100 bar, using PC-SAFT EOS.

The effect of an additive (water or toluene) on the solubility of the IL-additive mixture is illustrated in Figure 3-10. It implies that the solubility behavior for W (water) as an additive to the hydrophobic IL and the solubility behavior of toluene (T) in the hydrophilic IL follow a similar trend while adding water to the hydrophilic IL shows significantly different behavior. There is a substantial decrease in the solubility of hydrophilic IL ([bmim][Ac] mixture with increasing the water concentration upon the addition of water. At about 10 w% water content, the solubility of IL in the mixture is about 0.05 of that without the water phase. This IL has the highest viscosity among the studied cases. At 298 K, its viscosity is about 416 cP, which decreases to about 14 cP by adding 10 wt% water.
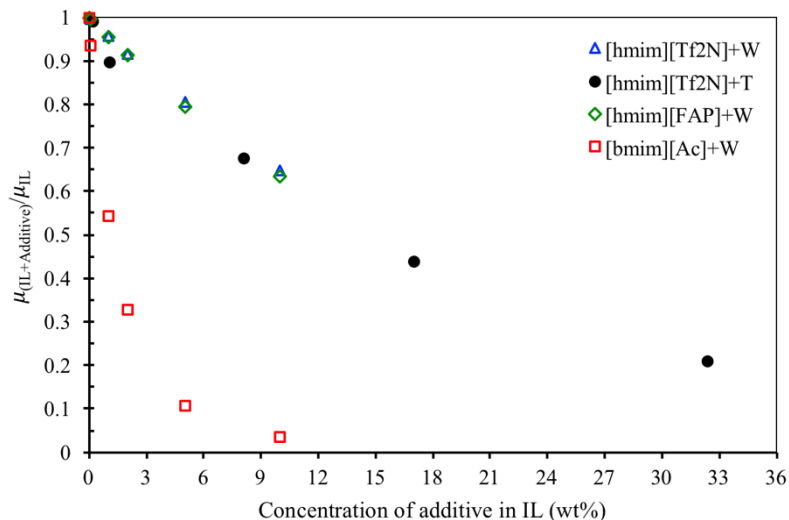
Figure 3-10: Effect of additives (water (W) or/and toluene(T)) on the viscosity of IL-additive mixture for [hmim][Tf₂N], [hmim][FAP], and [hmim][Ac] at 298 K.

3.4.4. Selectivity

To assess the solvent's ability in gas separation, the selectivity of gases into the solvent should be examined. The selectivity can be calculated from Henry's constant of various gases. Henry's constant relates the fugacity of CO_2 in the vapor phase to the molality of CO_2 in the liquid phase, which is represented by the following expression:

$$H_{CO_2}(T) = \lim_{P \to 0} \left[\frac{f_{CO_2}(T,P)}{m_{CO_2}/m^0} \right] \qquad (3\text{-}43)$$

where $m^0=1$ mol/kg, $f_{CO_2}(T,P)$ denotes the fugacity of CO_2 in the vapor phase and m_{CO_2} stands for the molality of CO_2 in the liquid phase.

The PC-SAFT EOS is used to compute Henry's constant as the pressure approaches zero. The PC-SAFT parameters for various gases are reported in Table 3- based on the literature. The magnitudes of Henry's constant at different temperatures for [hmim][Tf₂N] are listed in

Table 3-. Henry's law constants for CO_2, H_2S, and SO_2 are intensely lower than other gases, which is due to the higher solubility of CO_2, H_2S, and SO_2. Using Henry's constants of all gases, the gas selectivity can be calculated as the ratio of Henry's constants of two gases, as written below:

$$S_{CO_2/gas} = \frac{H_{gas}}{H_{CO_2}}$$
(3-44)

The results of the selectivity of gases are displayed in

Table 3-8: Henry's constant (bar) for CO_2, CH_4, H_2, H_2S, and SO_2 in [hmim][Tf$_2$N], estimated through using PC-SAFT EOS at various temperatures. [hmim][Tf$_2$N] has high selectivity for CO_2 separation from H_2 and CH_4, which is due to the very low solubility of H_2 and CH_4 in [hmim][Tf$_2$N]. Hence, carbon dioxide capture from gaseous streams containing these gases is recommended where the IL is employed. On the other hand, due to the low selectivity of CO_2 concerning H_2S and SO_2, [hmim][Tf$_2$N] is not appropriate for separation of CO_2 from the stream with a high concentration of H_2S and SO_2 gases. This is in agreement that H_2S and SO_2 have a high solubility and low Henry's constant in [hmim][Tf$_2$N]. However, the low values of selectivity show that the solvent can be used to remove these acid gases from the gaseous effluents and leave the CO_2 in the gas phase without contaminants.

It is worth noting that the Henry's constant is not a suitable measure for the selectivity evaluation when the extent of solubility is at high to moderate level.

Table 3-7: PC-SAFT parameters for different gases used in the selectivity study phase [212].

Gas	PC-SAFT parameters				
	m	σ (A)	ε/k (K)	κ^{AB}	ε^{AB}/k (K)
CO_2	2.604	2.550	151.04	-	-
CO_2(4C)	2.228	2.731	157.25	0.0287	307.41
CH_4	1.000	3.704	150.03	-	-
H_2S	1.630	3.075	230.35	0.00689	273.55
N_2	1.205	3.313	90.96	-	-

SO_2	2.444	2.680	228.30	-	-
H_2	0.487	4.240	33.85	-	-

Table 3-8: Henry's constant (bar) for CO_2, CH_4, H_2, H_2S, and SO_2 in [hmim][Tf$_2$N], estimated through using PC-SAFT EOS at various temperatures.

Gas	T (K)	Henry's constant H (bar)			Ref.
		PC-SAFT	**Experiment**	**% Abs Error**	
CO_2	293	19.11	12.44+0.024	53.62	[101, 170]
	298	20.20	18.91	6.82	
	303	21.35	-	n/a	
	313	26.57	23.64	12.39	
	333	33.80	28.56+0.029	18.34	
H_2S	303	17.67	17.4 ± 0.01	1.55	[213]
	313	21.52	21.7 ± 0.01	0.83	
	323	26.19	26.2 ± 0.07	0.04	
	333	34.06	33.7 ± 0.03	1.07	
H_2	293	886.74	863±0.7	2.75	[214]
	333	704.77	701±0.6	0.54	
SO_2	298	1.64	1.64±0.01	0.00	[116]
	313	2.62	2.29±0.02	14.41	
	333	4.36	4.09±0.06	6.60	
CH_4	298	328.33	329±23	0.20	[116]
	313	380.34	380±31	0.09	
	333	360.09	359±28	0.30	

Table 3-9: Selectivity of CO_2 over H_2S, H_2, SO_2, and CH_4, using [hmim][Tf$_2$N] through thermodynamic modeling with PC-SAFT EOS.

T (K)	Selectivity (S)			
	CO_2/H_2S	CO_2/H_2	CO_2/SO_2	CO_2/CH_4
293	n/a	46.40188	n/a	n/a
298	n/a	n/a	0.08119	16.2540
303	0.82764	n/a	n/a	n/a
313	0.80994	n/a	0.09861	14.3146
333	1.00769	20.85118	0.12899	10.6536

Since various gases are present in real flue gases, it appears to be inevitable to study the solubility of each gas in the presence of other gases. In this research work, the selectivity of CO_2 over other gases is determined. Based on the modeling results, it is not easy to separate CO_2, SO_2, and H_2S from flue gas in one single separation stage. Variations of gas selectivity in recycling ILs to use in

139

the regeneration operation of ILs should be analyzed carefully. Energy consumption of the desorption column needs to be considered while using the CO_2 capture methods in pilot-scale applications.

In general, the model presented in this research investigation can simulate the solubility of the common gas mixtures in quantitative agreement with the available experimental data.

3.5. Conclusions

In this research work, the reliability and accuracy of PC-SAFT and PR EOSs to forecast the solubility of CO_2 in ILs are investigated over practical ranges of temperature, pressure, and composition. The influences of adding water and toluene on the carbon capture capacity of ILs are thermodynamically modeled using PC-SAFT EOS. The main conclusion drawn based on the modeling outputs are listed below:

- PC-SAFT EOS is more accurate and applicable than PR while predicting the CO_2 solubility in ILs. This precision comes from the characteristic/nature of SAFT EOSs where they take into account the effect of molecular structure and interactions on the bulk properties and phase behavior, unlike the cubic EOSs that assume molecules as a hard-sphere.

- PC-SAFT EOS estimates the solubility of CO_2 in the mixtures of IL + water with great accuracy. Water can decrease the viscosity of ILs, however, its effect on the solubility of CO_2 in the ILs is different for the cases of hydrophilic and hydrophobic ILs. The hydrophobic IL shows more solubility reduction in the presence of water, compared to hydrophilic ILs.

- ILs with high hydrophilicity such as [bmim][Ac] are miscible with water so that it leads to a decrease in the viscosity of the mixture of [bmim][Ac] and water significantly, although

140

the solubility of CO_2 in the mixture of [bmim][Ac]+Water is not decreased as much as hydrophobic ILs.

- The solubility of CO_2 in the mixtures of IL + toluene is also modeled by utilizing PC-SAFT with high accuracy. The presence of toluene with small concentrations (e.g., 0.002 wt%) can increase the vapor pressure of the ILs, which is not favorable for using a mixture of toluene and ILs. However, adding up to 0.081wt % toluene to [hmim][Tf$_2$N] does not exhibit a remarkable negative effect on the solubility of CO_2. Since toluene is much cheaper than ILs, employing mixtures of toluene and ILs is still an option to be considered in potential CO_2 capture operations.

- CO_2 separation in the presence of other gases is studied in terms of selectivity. The Henry's constant and selectivity of CO_2 with CH_4, H_2, H_2S, and SO_2 gases are estimated. CO_2 separation can be achieved in the presence of CH_4 and H_2, while H_2S and SO_2 are absorbed favorably and CO_2 remains in the gas phase.

Appendix A2

Density data for different ILs correlated with PC-SAFT EOS are compared with the experimental data available in the literature. Figure A2-1 represents a very good match between the experimental and correlated data.
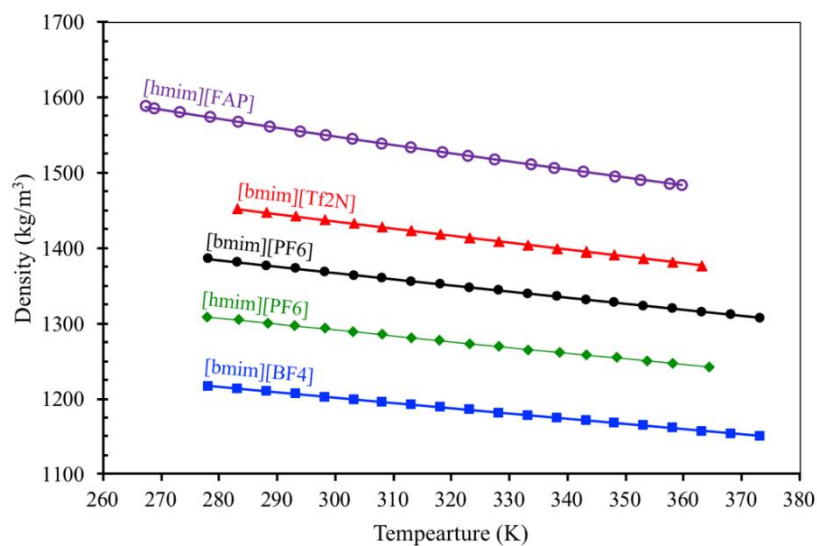
Figure A2-1: Density of a variety of pure ILs versus temperature and comparison of predictions and experimental data. The scatter points and solid lines represent the real data and PC-SAFT EOS results, respectively.

Table A2-1 lists the magnitudes of the binary interactions of CO_2 and ILs (k_{ij}) at different temperatures where various ILs are utilized.

Table A2-1: Binary interactions of CO_2 and IL systems (k_{ij}) versus temperature for different ILs used in this research work.

IL	T (K)		
	298	**313**	**333**
[bmim][BF$_4$]	-0.016	-0.014	-0.011
[bmim][PF$_6$]	0.080	0.090	0.100
[bmim][Tf$_2$N]	-0.031	-0.028	-0.025
[hmim][PF$_6$]	0.199	0.220	0.240
[hmim][FAP]	0.175	0.179	0.182
[hmim][Tf$_2$N]	0.010	0.015	0.019
[bmim][Ac]	-0.19	-0.15	-0.12

NOMENCLATURES

Variables/Parameters	Description
A_∞^E	Helmholtz excess free energy at the limit of infinite pressure
G^E	Gibbs excess free energy
$\hat{f}_1^{gas}$	Fugacity of comp-1 (solute) in the gas phase
$\hat{f}_1^{IL}$	Fugacity of comp-1 (solute) in the IL id phase
$\Delta^{B_{i\alpha}A_{j\beta}}$	Association strength
$X^{A_{i\alpha}}$	Mole fraction of molecules bonded at interaction site A
g_{ii}	Site-site radial distribution function
ε/k	Segment energy parameter
a	Attraction parameters of PR EOS
a^{assoc}	Helmholtz free energy of the association reference contribution
a^{chain}	Helmholtz free energy of the hard-chain reference contribution
a^{disp}	Helmholtz free energy of the dispersion reference contribution
a^{hs}	Helmholtz free energy of the hard-sphere reference contribution
b	Co-volume parameters of PR EOS
d	Segment diameter
H	Henry's constant
I	Integral
k	Boltzmann constant
K'_{ij}	Binary interaction coefficient parameter
k_{ij}	Binary interaction parameter for the attractive parameter
m	Number of segments
P_C	Critical pressure
P^{sat}	Vapor pressure
R	Universal gas constant
T_b	Boiling point
T_C	Critical temperature
V	Molar volume
x	Mole fraction
Z	Compressibility factor
Z^{assoc}	Association contribution to the compressibility factor
Z^{chain}	Hard chain contribution to the compressibility factor
Z^{disp}	Dispersion contribution to the compressibility factor
Z^{hs}	Hard sphere contribution to the compressibility factor

Chemical Formula	
[bmim][Ac]	1-Butyl-3-methylimidazolium acetate
[bmim][BF$_4$]	1-Butyl-3-methylimidazolium tetrafluoroborate
[bmim][PF$_6$]	1-Butyl-3-methylimidazolium hexafluorophosphate
[bmim][Tf$_2$N]	1-Butyl-3-methylimidazolium bis(trifluoromethylsulfonyl)imide
[FAP]	tris(pentafluoroalkyl)-trifluorophosphate
[hmim][FAP]	1-hexyl-3-methylimidazolium tris (pentafluoroethyl) trifluoro phosphate
[hmim][PF$_6$]	1-Hexyl-3-methylimidazolium hexafluorophosphate

[hmim][Tf$_2$N]	1-hexyl-3-methylimidazolium bis(trifluoromethylsulfonyl)imide
[THTDP][Cl])	trihexyltetradecylphosphonium chloride
[THTDP][NTf$_2$]	trihexyltetradecylphosphonium bis(trifluoromethylsulfonyl)imide
CH$_4$	Methane
CO$_2$	Carbon dioxide
H$_2$	Hydrogen
H$_2$S	Hydrogen sulfide
SO$_2$	Sulphur dioxide

Acronyms

AAD	Average absolute deviation
CCS	Carbon capture and storage
EOS	Equation of state
IL	Ionic liquid
PC-SAFT	Perturbed chain statistical associating fluid theory
PR	Peng-Robinson EOS
VLE	Vapor liquid equilibria
VLLE	Vapor liquid liquid equilibria
WS	Wong Sandler

Greek Letters

ε^{AB}	Association energy
μ	Viscosity
γ	Surface tension
κ	Conductivity
κ^{AB}	Association volume
ρ	Density
σ	Viscosity, and also the diameter of the segment
ω	Acentric factor
η	Viscosity

4. CHAPTER FOUR

New Insights into Bulk and Interface Properties of [Bmim][Ac]/[Bmim][BF$_4$]

Ionic Liquid/CO$_2$ Systems- Molecular Dynamics Simulation Approach

Preface

A version of this chapter has been published in the Journal of Molecular Liquids, 113497 (2020). I am the primary author of this paper. Sohrab Zendehboudi provided me with valuable tips/guidelines to conduct the MD simulations and inferring results. I prepared the first draft of the manuscript and then revised the manuscript based on the co-authors' feedback. The co-author Sohrab Zendehboudi also helped in model development, creating a proper manuscript structure, and revising all parts of the manuscript. The co-author, Nima Rezaei, provided comments on various sections of the manuscript.

Abstract

Ionic liquids (ILs) show great potential for CO_2 separation. In this research, we perform molecular dynamics (MD) simulations to explore vital transport and thermodynamic behaviors of CO_2 in the bulk and interface of [Bmim][Ac] and [Bmim][BF$_4$] ILs. Physiochemical properties of pure ILs are calculated, and structural properties such as radial distribution function (RDF) and self-diffusivity of cations and anions are determined at various conditions. A great agreement between the experimental and calculated properties is achieved. Diffusion coefficients obtained for cations and anions of the ILs are in the range of $(3\text{-}34\ )\times10^{-12}$ m^2/s. The cations have a higher diffusivity than the anions. In the bulk systems of ILs and CO_2, the structuring of CO_2 around the cation and anion and comparing volume expansion of the bulk system with that of pure ILs imply that the anion has an important effect on CO_2 absorption. With the addition of CO_2 to ILs, their volume expansion is relatively smaller, compared to other organic solvents. The diffusion coefficient of CO_2 in ILs varies from 1×10^{-10} to 3×10^{-10} m^2/s, depending on temperature, CO_2 concentration, and mixture viscosity. At the interface, the cation and anion association density increases. Due to CO_2 diffusion, CO_2 creates a dense layer at the interface that interrupts the association of the cation and anion, leading to a reduction in the surface tension. MD simulations show that the diffusion of CO_2 in the bulk occurs slowly. This study can be beneficial in designing appropriate ILs for various energy and environment applications at different processes and thermodynamic conditions.

4.1. Introduction

Greenhouse gases (GHGs) emissions into the atmosphere are the main reason for global warming. The combustion of fossil fuels produces CO_2 (as a GHG) that can be used as a precursor in the synthesis of other chemicals (e.g., urea and methanol) [215]. Therefore, the separation of CO_2 from

other flue gases has a significant role in reducing the GHG impacts on climate change while making it available for utilization and sequestration. Absorption of CO_2 using solvents is the most commercialized method for CO_2 capture. Alkanolamine solutions have shown satisfactory CO_2 absorption capacity; however, they pose drawbacks such as low vapor pressure, solvent loss during desorption, and high corrosion rate [216].

In recent years, ionic liquids (ILs) have been emerged as promising alternative solvents for physisorption and chemisorption of the acid gases due to their unique physicochemical characteristics; they feature negligible vapor pressure, high thermal stability, the proper capability to be engineered (task-specific), and environmentally friendly characteristic. The main shortcoming of the ILs is their high viscosity. The solubility of CO_2 in a variety of ILs has been examined experimentally [217] and theoretically [218, 219]. Recently, we proposed a technical and economic screening of various ILs with applications to capturing CO_2 from other gases [158]. We found fluorinated anions, including $[BF_4]^-$, $[FEP]^-$, and $[PF_6]^-$, to provide the highest solubility of CO_2 with the imidazolium-based ILs. In another research study by Aghaie et al. [220], it was concluded that an equation of state with associating terms (such as perturbed-chain statistical associating fluid theory (PC-SAFT)) can accurately estimate the CO_2 solubility in different ILs when compared to the experimental data [218]. Zhang et al. [217] screened Henry's constants for CO_2 with 409 different ILs, using COSMO-RS (conductor-like screening model for reactive solvents) method at 298 K; they also conducted experiments using selected effective ILs; their finding reveals that the $[FEP]^-$ anion exhibits a higher CO_2 solubility among the examined ILs. They suggested using molecular dynamics (MD) simulations to further understand the absorption performance of the ILs at the molecular level. Phase equilibria thermodynamic models are generally used to forecast the vapor-liquid equilibrium of CO_2/IL systems [219]. Although the

147

experimental and analytical models help researchers and engineers to screen suitable ILs for absorption and to predict some physical and chemical properties, they lack generalization. Also, the experimental runs/tests are relatively costly and time-consuming to obtain equilibrium data points. It seems difficult to use appropriate correlations and models to determine various properties of the IL/CO_2 systems without a molecular-level understanding of the CO_2 absorption mechanisms in ILs.

Due to the economic burden of experimental works and a large number of anion-cation combinations of the ILs, the MD simulation technique can be used as a powerful tool to study the physical properties, solubility, and interactions between the molecules of CO_2 and ILs. Also, MD helps to better understand the nature of solvation in ILs and to obtain the liquid phase properties based on the chemical structures. Research studies have been performed to determine the pure ILs' properties with MD [221-223]. According to a study by Koddermann et al. [224], very good agreement was observed between the simulation results and experimental data for the heat of vaporization, viscosity, and nuclear magnetic resonance (NMR) rotational correlation times for [$C_n$mim][NTf_2] where their own parametrized force-fields were utilized. They refined the force-field developed by Lopes and coworkers [225] in such a way that simulation data agree with experimental densities, self-diffusion coefficients for anions and cations of studied IL, and NMR rotational correlation times for the cations. The ILs properties can be obtained from MD simulations, using various force-field parameters, which are imperative for the determination of the molecular interactions of ILs. The MD is also employed to investigate the molecular phenomena, occurring in the bulk and interface of ILs and gases using different force-fields, computational algorithms, and run times [226-228]. The interactions between the anions and CO_2

play a dominant role in the absorption of gases, based on MD simulation and density functional theory (DFT) [223].

Three different types of non-polarizable force-fields, including all-atom, united atom (UA), and coarse-grained (CG) are introduced for ILs [229]. The CG reduces computational time by removing details; UA accelerates the calculations by reducing the number of degree of freedom; all-atom force-field explicitly represents the aliphatic hydrogen atoms [229]. Maginn studied molecular behaviors (and dynamics) of ILs using mostly the all-atom force field. Compared to other force-fields, the all-atom model can capture the particular interactions in IL+CO_2 systems with more details [230]. The ILs molecular simulation is complicated by its slow dynamics (compared to other liquids), dynamic heterogeneity, and long-range order in the liquid phase [230]. Sprenger et al. [229] showed that general Amber force-filed can accurately predict the thermodynamic and transport properties of different ILs. The all-atom optimized potentials with liquid simulations (OPLS-AA) force-field parameters were developed and validated for combinations of [Rmim]$^+$ cations and different anions of ILs with high precision in predicting properties of ILs [231].

The self-diffusivity of ILs, excess molar volume of CO_2-ILs systems, CO_2 solubility, and CO_2 absorption mechanisms in a mixture of gases are reported in the literature [224, 232-235]. There are some limitations and drawbacks with previous MD simulations for bulk ILs and mixture systems. A majority of studies have focused on imidazolium cations and PF_6 and Nf_2T anions [236]. A validated force-field parametrization of ILs is still needed to be extended for including other combinations of the cations and anions; the force-fields are required to obtain physical properties, structure, hydrogen bonding, and intra-molecular interactions of pure ILs and their mixtures with other solvents. An adequate understanding of the mechanisms that govern the high

solubility and selectivity of CO_2 in some ILs needs further elaborations, using MD simulations. Most of the previous molecular simulation studies of gas dissolution in ILs have been conducted at equilibrium condition, using Monte Carlo; this methodology lacks information on the dynamics of ILs. To the best of our knowledge, only a few research studies focus on transport properties of gases in the IL bulk and at the gas-IL interface. In addition, there are only a few systematic MD simulation studies to estimate the chemical and physical properties of IL mixtures. In the current research, the characteristics of pure ILs and gas-IL systems are determined, using MD simulations where an optimal force-field is selected. A comprehensive investigation of molecules interactions, structures, coordination around other molecules, probability of positioning in the mixture, diffusivity, volume expansion upon mixing (swelling), and interfacial behaviors is included in this study. The outcomes can assist to effectively design (and operate) separation processes with IL through a more reliable and cost-effective manner.

In this work, we use the all-atom force-field OPLS-AA [231] in the MD simulations in systems of CO_2 with two promising ILs, namely, [Bmim][BF$_4$] and [Bmim][Ac]. In the first phase, pure ILs physical properties (e.g., density and shear viscosity) and structural properties (e.g., radial distribution functions (RDF) and self-diffusivities) are studied. In the bulk systems, we investigate the effects of CO_2 presence on the viscosity and volume expansion of the IL-CO_2 mixtures, RDF, the coordination number of absorption, and diffusivity of CO_2 in the ILs. Finally, the interfacial behavior of the CO_2-IL systems is analyzed in terms of the number density profile along simulation box length, distribution and the molecular orientation of gas around the IL cations and anions, interaction energy, and interfacial tension.

This chapter is organized as follows: After the introduction, a brief theory of molecular dynamics simulation, force-field, viscosity, diffusivity, and radial distribution functions are provided in

150

Section 4.2. In Section 4.3, a brief description of the simulation methodology, input parameters, and cell configuration are presented. Section 4.4 includes the results and discussions in three subsections, including the simulation results for pure ILs, bulk systems of CO_2/IL, and the interfacial characteristics. Finally, the main findings of the study are highlighted in Section 4.5 (conclusions).

4.2. Theory on computational approach

The molecular dynamics (MD) approach is a powerful tool for understanding the physicochemical properties and structures of the molecules and mixtures. MD can also provide detailed information on the molecule dynamics and interactions between molecules. Thus, the MD simulation can provide the properties of the systems at a lower cost, compared to laboratory tests. Another importance of the molecular simulation is that potentials used in the simulations can be altered by a user so that the contribution of each term in the potentials can be examined/studied for further understanding of molecules interactions [237]. The force field parameters have an important impact on the accuracy of the MD results while predicting physiochemical and dynamic properties.

MD simulation requires a set of initial coordinates and velocities of particles (molecules) in the system which normally appears in the form of simulation cell with specific dimensions. Then, it calculates the forces between non-bonded and bonded interactions and the summation of various contributions to the total potential energy of the system. The configuration of each particle is updated, using the integration of Newton's equations of motion through the Verlet algorithm [238]. It is necessary to control the temperature and pressure of the system due to drift, occurring in the equilibration stage. The drift is a result of force truncation and integration errors, and also heating as a result of external or frictional forces. The simulation outputs are the temperature, pressure, positions, velocities, and different contributions of energy.

151

4.2.1. Force-Field Parameters

The standard form of force-filed (U) includes the intramolecular interactions such as bond stretching ($U_{stretch}$), angle bending (U_{bend}), dihedral torsion ($U_{torsion}$), and the non-bonded interactions, including Lennard-Jones (U_{LJ}), and Coulomb interactions ($U_{Coulomb}$) as shown below:

$$U = U_{stretch} + U_{bend} + U_{torsion} + U_{LJ} + U_{Coulomb} \tag{4-1}$$

The functional forms of the above potentials for the OPLS-AA force-field [239] used in this work are listed below [240]:

$$U_{stretch} = \sum_{ij}^{bonds} \frac{k_{r,ij}}{2}(r_{ij} - r_{0,ij})^2 \tag{4-2}$$

$$U_{bend} = \sum_{ij}^{angles} \frac{k_{\theta,ij}}{2}(\theta_{ij} - \theta_{0,ijk})^2 \tag{4-3}$$

$$U_{torsion} = \sum_{ij}^{dihedrals} \sum_{m=1}^{4} \frac{v_{m,ijkl}}{2}[1 + (-1)^m \cos(m\varphi_{ijkl})] \tag{4-4}$$

$$U_{LJ} = \sum_{i} \sum_{j \neq i} 4\varepsilon_{ij}[(\frac{\sigma_{ij}}{r_{ij}})^{12} - (\frac{\sigma_{ij}}{r_{ij}})^6] \tag{4-5}$$

$$U_{Coulomb} = \sum_{i} \sum_{j \neq i} \frac{1}{4\pi\varepsilon_{ij}} \frac{q_i q_j}{r_{ij}} \tag{4-6}$$

where r_{0ij}, $\theta_{0,ijk}$, and $\varphi_{0,ijkl}$ are the initial bond length, angle, and dihedral angle, respectively. Other parameters are the force constant (k), Fourier coefficients (V), partial atomic charges (q), Lennard-Jones potential radii (σ), and potential well depths (ε). Repulsive and dispersive terms are described by the Lennard-Jones 12-6 potentials. The electrostatic interactions are introduced by the Coulomb potential term. These two potentials act between sites in different molecules and sites within the same molecules.

4.2.2. Viscosity Calculation

The shear viscosity of each IL can be calculated using the Green-Kubo relationship [241, 242], as the integral over time of the pressure tensor autocorrelation function:

$$\eta = \frac{V}{k_B T} \lim_{t \to \infty} \int_0^t \left\langle P_{\alpha\beta}(0) P_{\alpha\beta}(t) \right\rangle dt \tag{4-7}$$

In Equation (4-7), V symbolizes the volume of the system; T is the temperature; k_B resembles the Boltzmann constant. The brackets show that the pressure tensors are averaged over time. $P_{\alpha\beta}$ denotes the pressure tensor of the $\alpha\beta$ element. To attain more reliable results, the viscosity is determined by taking the average over three independent terms of the pressure tensor components, namely, P_{xy}, P_{yz} and P_{xz}. To calculate viscosity, the canonical ensemble (NVT) is employed as the Green-Kubo equation is defined for a constant-volume system.

4.2.3. Diffusivity Calculation

The dynamic properties of the ILs in the liquid phase can be calculated in terms of mean square displacement (MSD) of the ion center of mass, as expressed below:

$$MSD = \frac{1}{N} \left\langle \sum_{i=1}^{N} \left| r_i^c(t) - r_i^c(0) \right|^2 \right\rangle = \Delta \left| r(t) \right|^2 \tag{4-8}$$

The diffusivity is obtained by the MSDs averaged with time through the Einstein correlation: [243]

$$D_i = \frac{1}{6} \lim_{t \to \infty} \frac{d}{dt} \left\langle \left| r_i^c(t) - r_i^c(0) \right|^2 \right\rangle \tag{4-9}$$

where $r_i(t)$ is the center of mass of the ions at time t and $\langle ... \rangle$ denotes a moving time average. The diffusivities can be obtained through the least square fit of the MSD versus time for the particles

(molecules) transport. The activation energy (E_D) is related to self-diffusion (D) through Arrhenius expression as shown below:

$$D = D_0 e^{-E_D/RT} \tag{4-10}$$

where E_D represents the activation energy of diffusion; D_0 symbolizes the pre-exponential factor of the Arrhenius equation ($m^2\ s^{-1}$); R is the universal gas constant.

4.2.4. Radial Distribution Function Calculation

The radial distribution function (RDF) or the pair correlation function is defined by the following expression [244]:

$$g_{AB}(r) = \frac{\langle \rho_B(r) \rangle}{\langle \rho_B \rangle_{local}} = \frac{1}{\langle \rho_B \rangle_{local}} \frac{1}{N_A} \sum_{i \in A}^{N_A} \sum_{i \in B}^{N_B} \frac{\delta(r_{ij} - r)}{4\pi r^2} \tag{4-11}$$

In Equation (4-11), $\langle \rho_B(r) \rangle$ denotes the particle density of type B at a distance of r around particles A, and $\langle \rho_B \rangle_{local}$ is the particle density of type B averaged with time over all spheres around particles A with the radius of r_{max}. Usually, r_{max} is half of the simulation cell length. N_A and N_B refer to the total number of molecules of A and B, respectively.

4.3. Simulation/modeling methodology

The structures of isolated cations and anions are optimized at the density functional theory (DFT) level, using the 6-311G + (d, p) basis set in the Gaussian 16 package [245]. A set of underlying approximations is made to describe the chemistry of the system. Basis sets are a set of functions to describe the electronic wave functions. The parameters for [Bmim], [BF$_4$], and [Ac] are taken from the OPLS-AA force field, developed by Sambasivarao and Acevedo [231]. The partial

charges of the ILs are scaled uniformly by 0.8 to consider the impact of charge transfer and polarizability in the bulk [246].

In the case of CO_2, the force-field parameters are taken from the literature [231]. A simple schematic of the cations and anions used in this work is depicted in Figure 4-1.

(a)   (b)   (c)
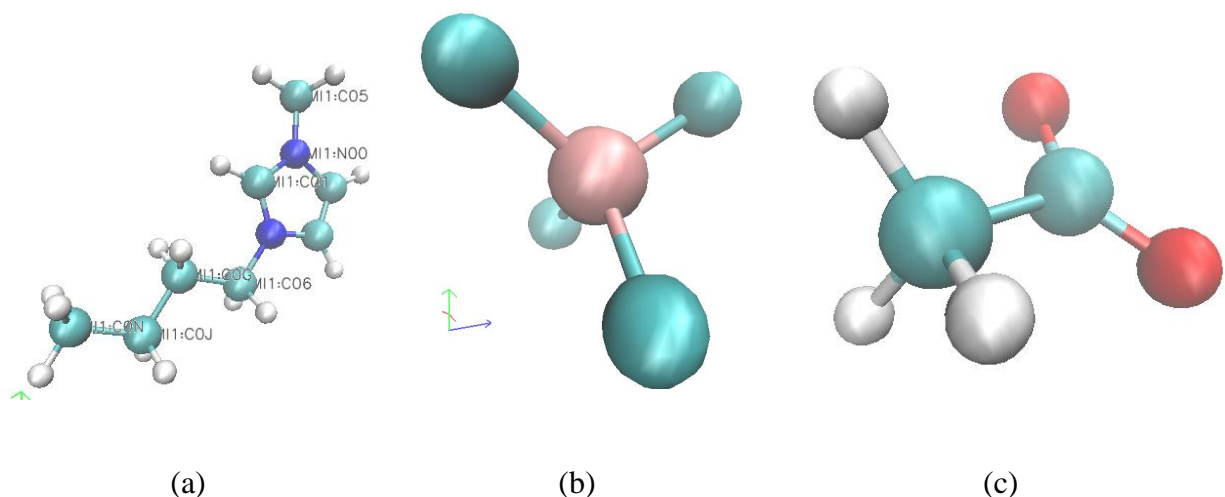
Figure 4-1: Components of the ILs considered in this work, (a) [Bmim]$^+$, (b) [BF$_4$]$^-$ (green for fluoride atom and red for boron atom), and (c) acetate or [Ac]$^-$ (green for carbon, white for the hydrogen atom, and red for oxygen atom).

MD simulations are accomplished by the Gromacs 5.1.4 package [247, 248]. The MD runs are conducted by considering periodic boundary conditions and a time step of 1 fs. The electrostatic interactions are calculated, using the particle-mesh-Ewald (PME) method with a real space cut-off of 1.4 nm. The vdW interactions are calculated, using the Lennard-Jones equation. The Nose-Hoover thermostat [249] and extended Lagrangian method [250] are applied to control the temperature and pressure, respectively. The flowchart presented in Figure 4-2 shows the main steps of the simulation.

155
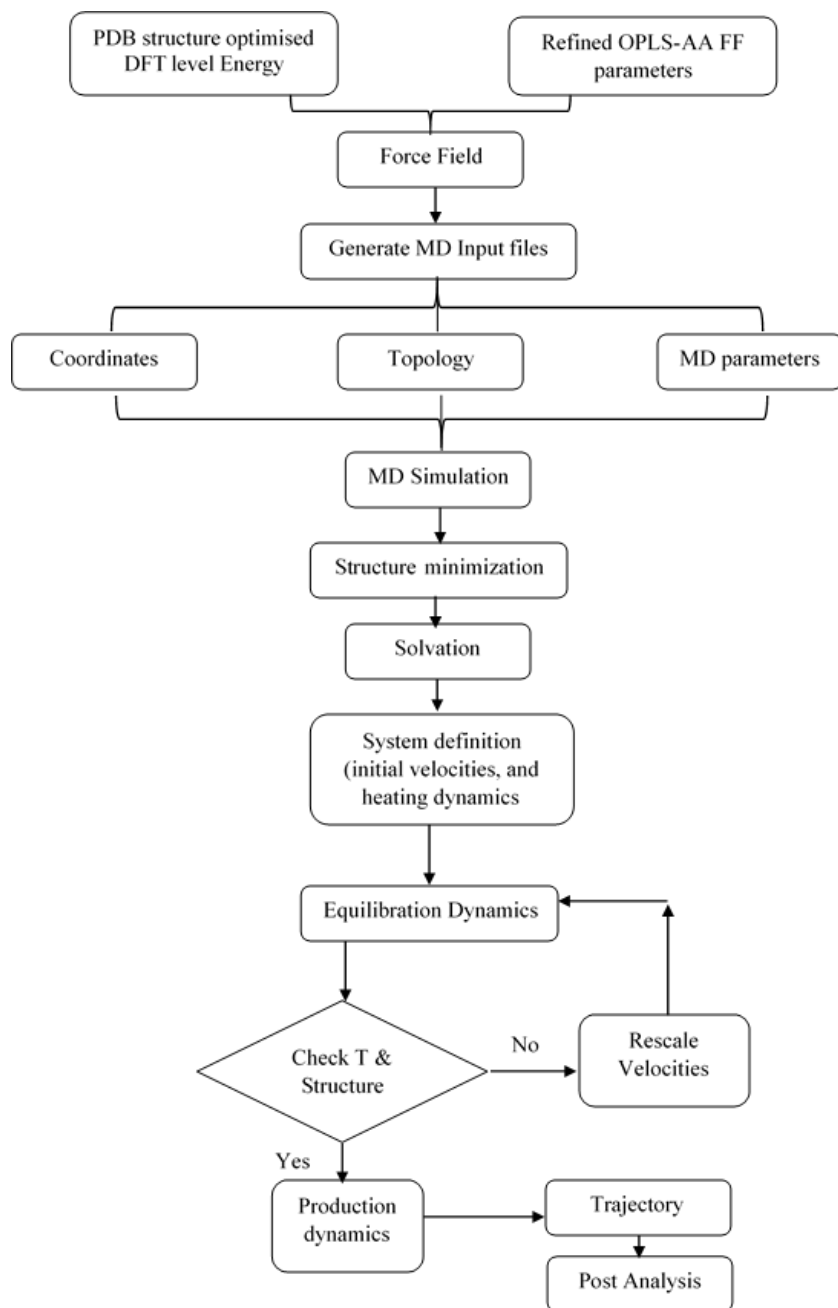
Figure 4-2: An algorithm, showing the key stages of the MD simulation.

First, a cubic box of pure ionic liquids, including 300 pairs of [Bmim][BF$_4$] IL and [Bmim][Ac]

IL is created using Packmol [251]. Then, the energy minimization and annealing processes are

performed on the system to obtain a reliable initial configuration. After that, the system is

equilibrated using two steps of isothermal-isobaric (NPT) ensemble in 1 ns and 4 ns, respectively,

at 300 K, 313 K, and 333 K. The Nose-Hoover pressure coupling is also kept at a pressure of 1 bar. After equilibrium is reached, a trajectory over 4 ns is generated. The production run is then performed for 5–8 ns.

For the bulk system, the simulation box is constructed for the ILs and CO_2 including 300 ion pairs and 5 and 110 CO_2 molecules, based on experimental data, in a cubic box of [Bmim][BF$_4$] and [Bmim][Ac] using Packmol [251], respectively. Three-dimensional periodic boundary conditions consistent with a cubic box were employed to obtain bulk behavior. The system is equilibrated for 4 ns isothermal-isobaric ensemble (NPT) and followed by for 4 ns in the canonical ensemble (NVT). Then, the production run is continued for 5–8 ns. The densities are calculated after the NPT ensemble reached equilibrium. The bulk system MD simulations only represent the system at equilibrium. To investigate the interfacial aspect of the CO_2/IL system, a two-phase box is considered that consists of the IL in the middle and CO_2 on either side. The IL box is extended in the positive and negative z-direction by 5 nm and the cell dimensions are 5 nm×5 nm×15 nm in the x, y, and z directions, respectively. The CO_2 molecules are located on either side of the IL slab, containing 50 and 200 molecules to reach the pressures of 10 bar and 42 bar. The CO_2 molecules diffuse in the gas phase, transfer across the interface, and diffuse through the liquid bulk (see Figure 4-3). The MD simulation for this system represents a non-equilibrium case.
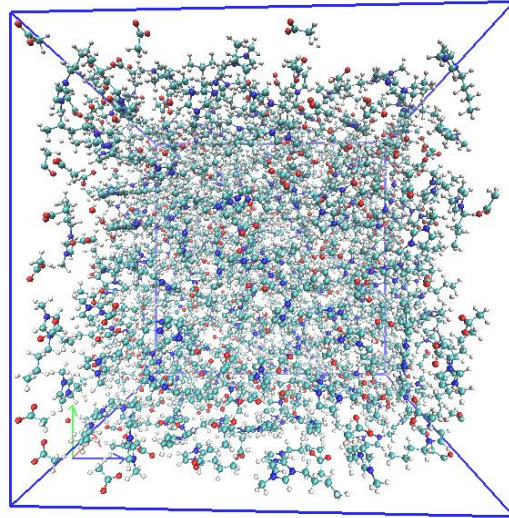
(a)
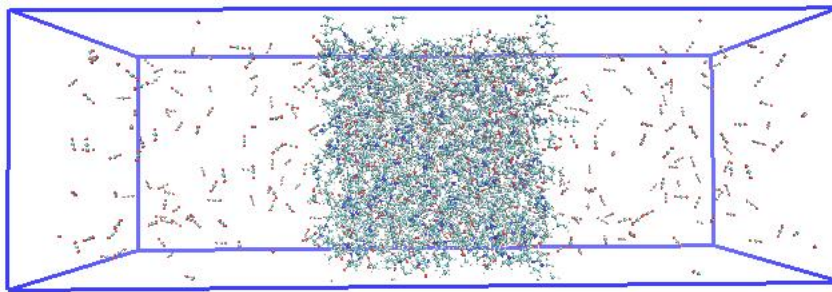
(b)

Figure 4-3: Schematics of (a) bulk system and (b) interface simulation box.

4.4. Limitations of MD Simulations

There are some assumptions and limitations in our MD simulations as listed below:

- The simulations use the classical mechanics of Newton's equation to describe the motion of atoms.

- A conservative force-field in MD simulations is used, which is only a function of positions of the atoms without considering the electron motion. Hence, the electrons remain in the ground state when the atomic positions change. However, we scale the partial charges of

the ILs uniformly by 0.8 to consider the effect of charge transfer and polarizability in the system.

- The force-fields are pair-additive, implying that all non-bonded forces are originated from the sum of the non-bonded pair interactions. Non-pair-additive interactions are considered by the effective pair potentials.

- The long-range interactions, including Lennard-Jones and Coulomb interactions, are cut-off around 1.4 nm.

4.5. Results and discussions

This study investigates important physicochemical and structural properties of various CO_2/IL systems through performing MD simulations. The results and discussions section is divided into three parts, covering the simulation results for pure ILs, CO_2/IL bulk systems, and CO_2/IL interfacial systems.

4.5.1. Pure ILs

Density: The densities of pure [Bmim][BF$_4$] and [Bmim][Ac] ILs are calculated from MD simulations, and the predictions are compared with the experimental values to evaluate the viability of the OPLS-AA force-fields. The densities are determined based on the NPT at three different temperatures of 300, 313, and 333 K; the experimental density data for [Bmim][BF$_4$] and [Bmim][Ac] ILs are taken from literature. [252], [253] A comparison between the experimental and calculated density values is illustrated in Figure 4-4. The magnitude of error (%E) is obtained using the following equation:

$$\% E = \frac{\rho_{\text{exp}} - \rho_{calc}}{\rho_{\text{exp}}} \times 100 \qquad (4\text{-}12)$$

According to Figure 4-4, the experimental values are in great agreement with the calculated densities from MD simulation; the maximum deviations are 0.48% for [Bmim][BF₄] and 0.67% for [Bmim][Ac]. The density results imply that the OPLS-AA force-fields used for the simulations are reliable/appropriate.
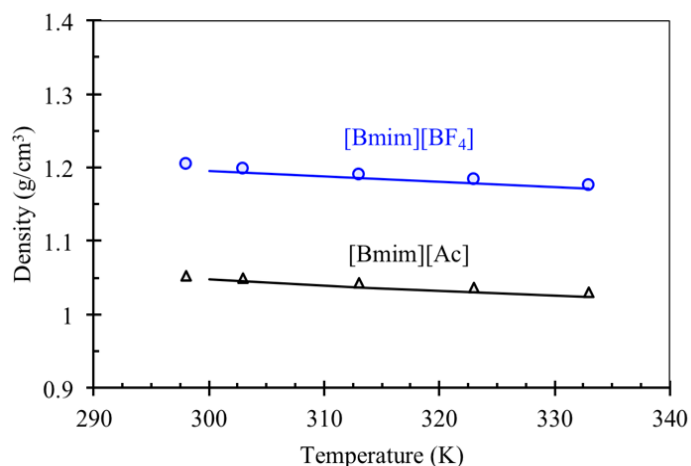
Figure 4-4: Liquid density of pure ILs as a function of temperature at P=1 bar; Markers indicate experimental data.

Viscosity: We also verify the viability of the force-field used in the MD simulation by comparing viscosity values from the experiments and simulations. The viscosity of each IL is calculated from MD simulations at various temperatures and the results are compared with the experimental viscosities, as reported in Figure 4-5. Viscosity is determined using the Green-Kubo equation in the MD simulations at three different temperature levels of 300, 313, and 333 K. The experimental values for the viscosities are obtained from the literature [252, 253]. As it is clear, a good match is noticed between the predictions and real data for viscosities at all temperatures. The error

percentages ($\%E = \dfrac{\left|\eta_{exp} - \eta_{calc}\right|}{\eta_{exp}} \times 100$) in estimating the viscosity of pure ILs are less than 3.4%

for [Bmim][BF$_4$] and less than 2.1% for [Bmim][Ac]. The small differences between the calculated

and experimental viscosities reveal the high accuracy of the OPLS-AA force-field to simulate the

ILs behaviors. According to Figure 4-5, the viscosity of ILs decreases with increasing temperature,

implying that the interaction potentials between the cations and anions are susceptible to

temperature. The relationship between the temperature and viscosity (η) can be generally

expressed with an exponential Arrhenius type ($\eta = \eta_0 \exp(-\dfrac{E_a}{RT})$) correlation. Plotting $\ln \eta$ versus

1/T yields the activation energies -44.3 kJ mol^{-1} and -35.76 kJ mol^{-1} for [Bmim][BF$_4$] and

[Bmim][Ac], respectively, which are close to the experimental values.
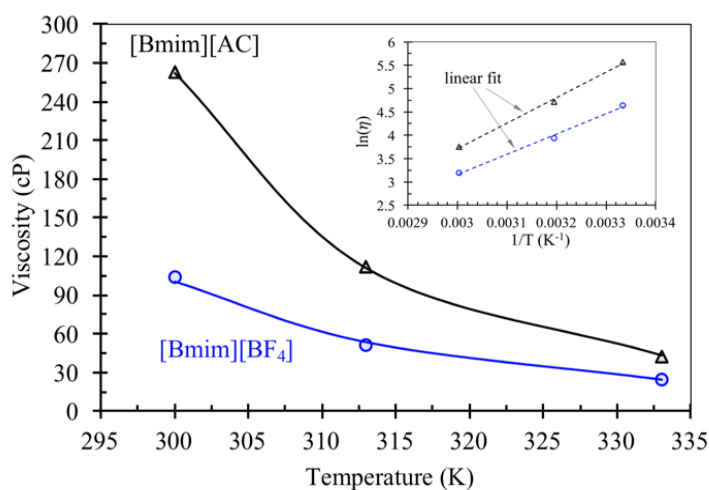
Figure 4-5: Shear viscosity of [Bmim][BF$_4$] and [Bmim][Ac] at various temperatures; Experimental values are shown with filled symbols, and the lines show the simulated results.

RDF: Radial distribution function (RDF) describes the probability of finding an ion at a distance

r from the reference ion. RDF refers to the ratio of the area density of neighbors around a reference

atom/particle and the average density of the entire system, which discovers the distance of a given molecule from other particles in the system. Thus, the interactions between molecules will be explored by analyzing the distribution of particles in the system. To clarify how strong the associations of cation-anion are, we carry out the RDF analysis on the particles; the results are illustrated in Figure 4-6 (a) and (b) for all anions and cations of [Bmim][BF$_4$] and [Bmim][Ac] ILs, respectively. As shown in Figure 4-6 (a), the RDF peak for anion-cation of [Bmim][BF$_4$] IL at 300 K is at a distance of 0.47 nm with a peak value of 2.71. The first minimum is observed at 0.8 nm with a RDF of 0.623, indicating that the chance of finding ions in this separation distance is very low. In Figure 4-6 (a), the RDF diagrams are compared for the center of mass of cation, cation ring, and cation chain with respect to the anion. It is found that the RDF peak happens at 0.47 nm, 0.51 nm, and 0.49 nm for the center of mass of cation, cation ring, and cation chain, respectively. The higher RDF peak for the anion-cation ring reveals that the anions have a stronger association with the ring of imidazolium cation than its chain. The local environments around the key residues of the [Bmim][Ac] IL at 300 K are obtained. As depicted in Figure 4-6 (b), the RDF peak from anion-cation is 2.727, which is obtained at the separation distance of 0.46 nm. Similar to [Bmim][BF$_4$] IL, at the separation distance of 0.76 nm, it is unlikely to find anions at the neighborhood of cation. According to Figure 4-6 (b), the acetate anion has a stronger association with the ring of the [Bmim]$^+$ cation in the [Bmim][Ac] IL. Figure 4-7 (panels (a) and (b)) demonstrates the RDF for the center of mass in cation-cation, anion-anion, and anion-cation pairs for pure ILs at 300 K. As clear from Figure 4-7 (a) and (b), the RDF peak for cation-anion of [Bmim][BF$_4$] and [Bmim][Ac] is higher than RDF for cation-cation and anion-anion pairs; implying the strong associations of the cation-anion pairs.
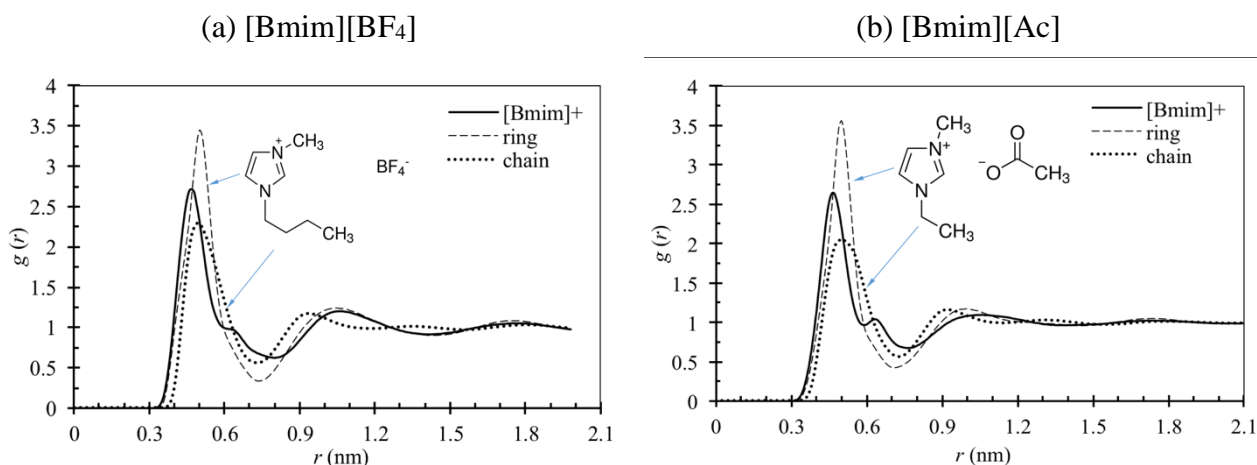
Figure 4-6: Radial distribution function $g(r)$ between the anions with cation and different segments of the cation (ring and chain) for pure ILs: (a) [Bmim][BF$_4$] and (b) [Bmim][Ac] at T=300 K and P=1 bar.
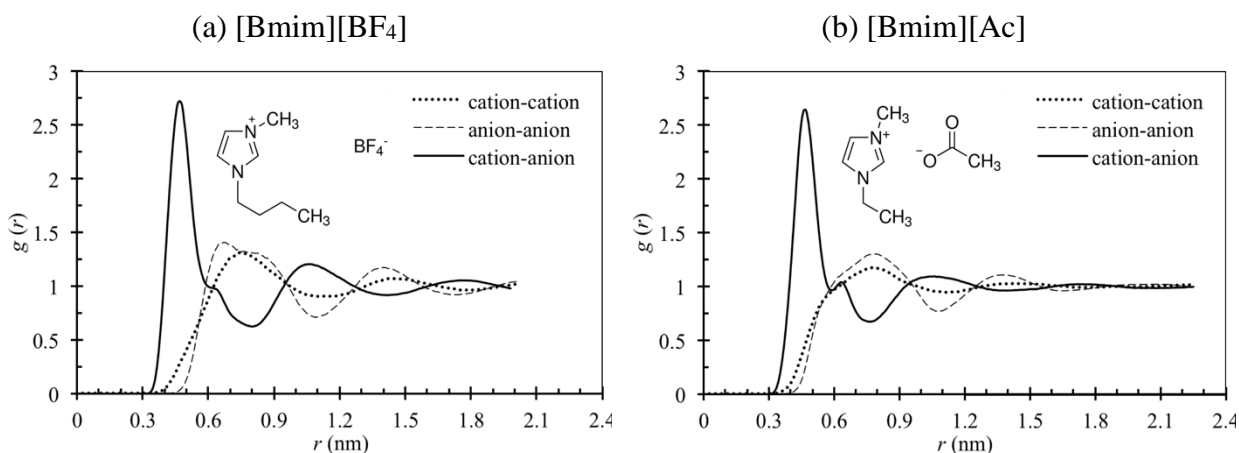
Figure 4-7: Radial distribution function $g(r)$ for the center of mass in cation-cation, anion-anion, and anion-cation pairs for pure ILs at 300 K and 1 bar: (a) [Bmim][BF$_4$] and (b) [Bmim][Ac].

Dynamic characteristics of liquid phase: Mean square displacement (MSD) is a measure of the deviation of the position of an atom with respect to its reference position over time in MD simulations, as presented by Equation (4-8). We compare the MSD variable for the two ILs at temperatures 300, 313, and 333 K (see Figure 4-8). The initial rapid increase in MSD with time until 1 ns reveals that a long simulation is required to evaluate the self-diffusion coefficients of different ions in both ILs. The slopes of the MSDs for the cations are steeper than those for the

anions in both ILs. This suggests that the cations move faster than the anions in the mixture within the timescale of few nanoseconds. The MSDs of the cations and anions for [Bmim][BF$_4$] and [Bmim][Ac] ILs at 300 K are shown in Figure 4-8 (a), for MD results up to 8 ns and 5 ns simulation runs, respectively. The slopes of MSDs with time for the cation and anion of [Bmim][BF$_4$] are steeper than those for [Bmim][Ac]. Thus, it can be concluded that the motion of the cation and anion is faster in [Bmim][BF$_4$], compared to [Bmim][Ac]. It confirms that [Bmim][Ac] is more viscous than [Bmim][BF$_4$]. Also, [Ac]$^-$ anion has a larger gyration radius than [BF$_4$]$^-$ that can be another reason for the slower movement of the ions in [Bmim][Ac]. The larger size of the [Ac]$^-$ anion and its bulky shape (compared to [BF$_4$]$^-$) can also lead to slower diffusion of [Ac]$^-$ than [BF$_4$]$^-$ anion. The self-diffusion coefficients of the cations and anions are calculated by fitting a straight line to the slope of the linear region of the MSD curve from 1 ns to 8 ns, using Equation (4-8). Table 4-1 reports the self-diffusion coefficients for the cations and anions of [Bmim][BF$_4$] and [Bmim][Ac] at 300, 313, and 333 K where the pressure is 1 bar. According to Table 4-1, at 300 K, the self-diffusion coefficients of [Bmim]$^+$ cation in [Bmim][BF$_4$] and [Bmim][Ac] are 10.1×10^{-12} and 5.03×10^{-12} m^2/s, respectively. It is concluded that the [Bmim]$^+$ cations diffuse twice faster in pure [Bmim][BF$_4$] than [Bmim][Ac]. In addition, the self-diffusion coefficients of the [BF$_4$]$^-$ and [Ac]$^-$ anions are 6.67×10^{-12} and 3.34×10^{-12} m^2/s, respectively. The anions, in general, have a lower self-diffusion coefficient, compared to the cations for both ILs at all temperature levels. The results also confirm that [Bmim][Ac] has a lower diffusion coefficient than [bmim][BF$_4$] due to a higher viscosity and larger anion size.
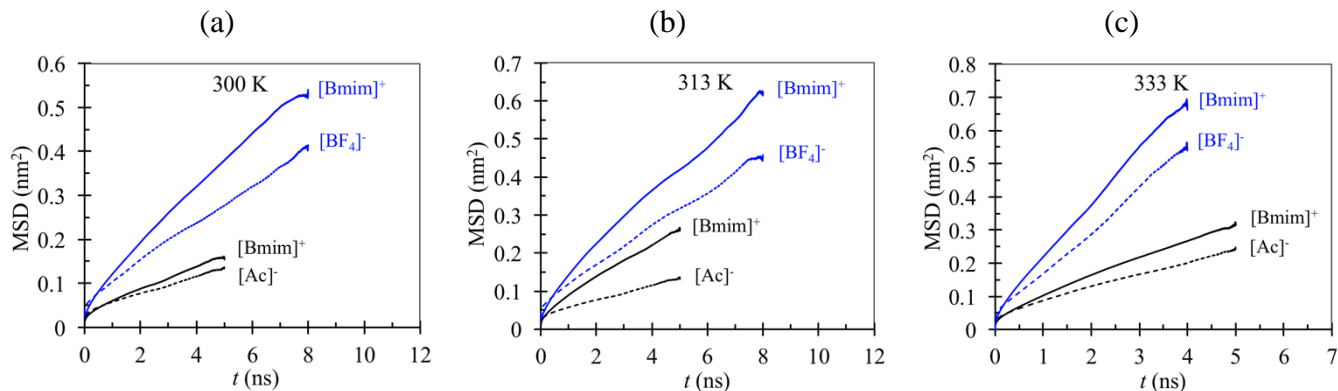
Figure 4-8: A comparison between the mean square displacement (MSD) of anions and cations for [Bmim][BF4] and [Bmim][Ac] at different temperatures: (a) 300 K, (b) 313 K, and (c) 333 K.

Table 4-1: Self-diffusion coefficient of cations and anions for different ILs at 1 bar.

T (K)	IL	$D \times 10^{-12}$ (m^2/s)	
		Cation	**Anion**
300	[Bmim][BF$_4$]	10.01	6.67
	[Bmim][Ac]	5.08	3.34
313	[Bmim][BF$_4$]	11.70	8.33
	[Bmim][Ac]	8.36	5.13
333	[Bmim][BF$_4$]	33.30	16.70
	[Bmim][Ac]	10.04	6.76

4.5.2. CO$_2$-IL Bulk Systems

The analysis of MD simulations for CO$_2$-IL bulk systems is performed by considering: 1) microscopic structural properties, using radial distribution functions (RDFs) and volume expansion upon CO$_2$ absorption, and 2) dynamic properties using mean square displacement (MSD) and diffusion coefficient.

Volume expansion (swelling): The system's total volume increases with the CO$_2$ mole fraction in the liquid phase. The volume expansion percentage is defined as the relative change in the total volume of the IL-CO$_2$ mixture, compared to pure IL [101], as given below [254]:

$$\%V_{expansion,L} = \frac{V_{mix}(T,P,x) - V_{IL}(T,P_0)}{V_{IL}(T,P_0)} \times 100 \tag{4-13}$$

where the subscripts of *mix* and *IL* represent the volume of the IL/CO_2 and IL systems, respectively. P_0 is the standard pressure of 1 bar. The molar volumes of the IL/CO_2 mixtures after CO_2 absorption, volume expansion upon mixing, and the molar volume ratio of mixture to pure IL are calculated for both IL systems (see Figure 4-2). Volumes are computed in the experimental solubility limit of each IL (mole fractions of 0.016 and 0.27 for [Bmim][BF4] and [Bmim][Ac], respectively) at 1 bar and 300 K. Based on the results, the volume expansion increases with increasing temperature. The maximum volume expansion is reported to be 1.31% for [Bmim][BF4] and 6.15% for [Bmim][Ac]. Volume expansion due to CO_2 absorption in [Bmim][Ac] is higher than that in [Bmim][BF4], confirming that higher CO_2 solubility leads to an increase in the total volume of the mixture. Adding CO_2 to normal organic solvents usually increases the liquid volume, and consequently lowers the mixture solvent strength.[255] IL volume expands relatively small upon the addition of CO_2 to IL. It seems that CO_2 has a lower influence on the polarity of the mixture and cannot disrupt the hydrogen bonding and cation-anion interactions between the IL molecules, compared to organic solvents.

Table 4-2: Physical properties of CO_2-IL mixtures at the CO_2 solubility limit.

T (K)	IL	V_m (cm^3/mol)	ΔV (vol%)	$V_{m,mix}/V_{m,IL}$	η (cP) CO_2-IL	η (cP) pure IL[256]·[257]
300	[Bmim][BF4]	195.33	0.84	0.991	96	103.5
	[Bmim][Ac]	158.17	5.01	0.826	186	263
313	[Bmim][BF4]	197.87	1.24	0.995	45	51.3
	[Bmim][Ac]	160.36	5.44	0.830	94	112
333	[Bmim][BF4]	200.32	1.31	0.996	21	24.5
	[Bmim][Ac]	163.37	6.15	0.836	37	42.7

Mixture viscosity: Figure 4-2 also summarizes the viscosity of the CO_2 and IL mixtures. According to Figure 4-2, the viscosity decreases with increasing CO_2 concentration (in the mixture). Also, the viscosity decreases upon an increase in temperature, which is in agreement with the variation of the liquid viscosity with temperature, as reported in the open sources.

RDF: Detailed RDFs for the center of mass of anion-cation, anion-CO_2, and cation-CO_2 for studied ILs are presented in Figure 4-9 and Figure 4-10. The RDFs show very small oscillations beyond r =2.25 nm. The shapes of RDFs for both anions and CO_2 pairs are similar. It is observed that solvated CO_2 mainly resides close to the butyl chain of the cations. In both ILs, CO_2 molecules show stronger association with anions, compared to cations. As demonstrated in Figure 4-9 (a), for [Bmim][BF$_4$], the RDF of the cation-anion at the bulk system is similar to that for the pure [Bmim][BF$_4$] (refer to Figure 4-7 (a)). According to Figure 4-9, the RDF peaks for the anion and cation of [Bmim][BF$_4$] IL at 300 K are located at distances 0.39 nm and 0.52 nm with the peak values of $g(r)$=2.609 and 1.458, respectively. The first minimums for the anions and cations are 0.87 and 0.83 nm, implying that it is unlikely to find a CO_2 molecule at these distances around the anion and cation. The distribution of CO_2-[Bmim]$^+$ shows that the largest peak and the first maximum correspond to the center of mass of [Bmim]$^+$ and [BF$_4$]$^-$ ions at about 0.52 and 0.4 nm at 300 K, respectively. The distribution functions of CO_2 - [BF$_4$]$^-$ have closer peaks (0.4–0.6 nm). The higher peaks with a shorter distance for the case of anions indicate that the anions with smaller size are located in the neighborhood of the CO_2 molecules easier and make powerful interactions. Also, the second peak in the RDFs is located in a shorter distance for the anion than the cation. There is no significant difference in RDFs while investigating the effect of temperature on the peaks of site-site interactions. It means temperature does not have a significant impact on the distribution of molecules and ions in the IL-CO_2 system.

The RDFs for center of mass of the anion-cation, CO_2-anion, and CO_2-cation pairs for the [Bmim][Ac] case at 300 K are demonstrated in Figure 4-10. Like [Bmim][BF$_4$], the RDF of the bulk system is similar to that for the pure [Bmim][Ac] (see Figure 4-7 (b)). According to Figure 4-10, the RDF peaks for the anion-cation pair in [Bmim][Ac]-CO_2 mixture at 300 K are at distances of 0.38 nm and 0.53 nm, with peak values 2.363 and 1.301, respectively. The locations of the first minimums for the anion and cation in the mixture are 0.75 and 1.01 nm, respectively. Thus, the CO_2-anion association is stronger than CO_2 –cation pairs in the [Bmim][Ac]-CO_2 mixture. The distribution of CO_2-cation in [Bmim][Ac] IL shows a peak at a distance of 0.53 nm. The RDF of CO_2-anion has peaked at relatively shorter distances of 0.38 nm and 0.87 nm for the [Bmim][Ac]-CO_2 mixture. When comparing the effect of anions, it seems that the CO_2 molecule is coordinated at a closer distance to [Ac]$^-$ than [BF$_4$]$^-$, which is attributed to the different structures of anions.
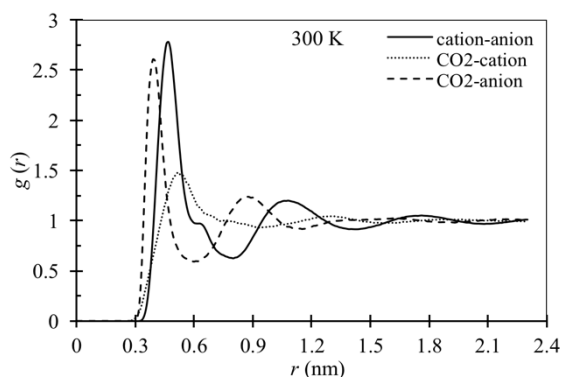
(a)
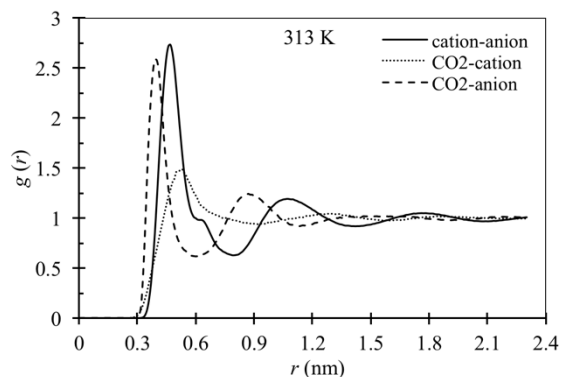
(b)
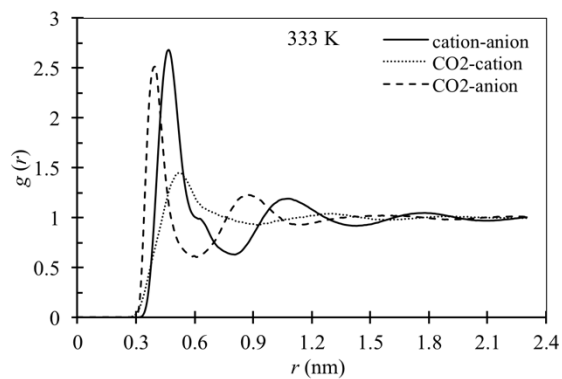
(c)

Figure 4-9: Radial distribution function for the center of mass for pairs of anion-cation, CO_2-anion, and CO_2-cation in the bulk of [Bmim][BF$_4$] IL at 1 bar: (a) 300 K, (b) 313 K, and (c) 333 K.
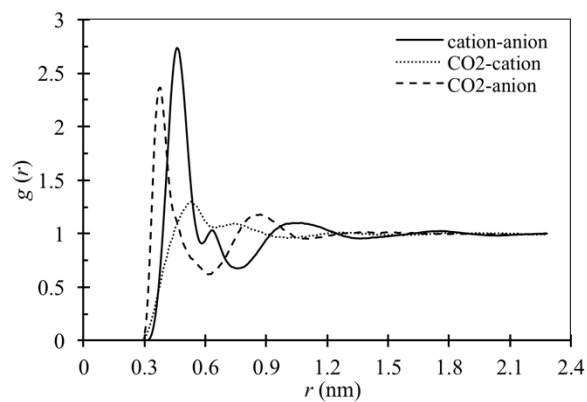
Figure 4-10: Radial distribution function for the center of mass for pairs of anion-cation, CO_2-anion, and CO_2-cation in the bulk of [Bmim][Ac] at 1 bar and 300 K.

MSD: We illustrate the MSD of the center of mass for the ions of CO_2-[Bmim][BF$_4$] and CO_2-[Bmim][Ac] in Figure 4-11 and Figure 4-12, respectively.
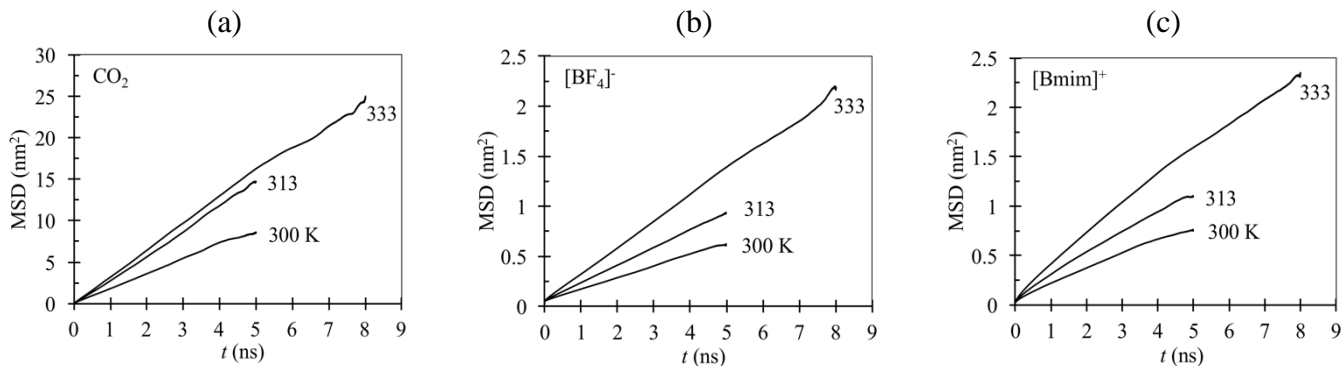
Figure 4-11: Mean square displacement at different temperatures for CO_2-[Bmim][BF_4] bulk system for: (a) CO_2, (b) anion, and (c) cation.
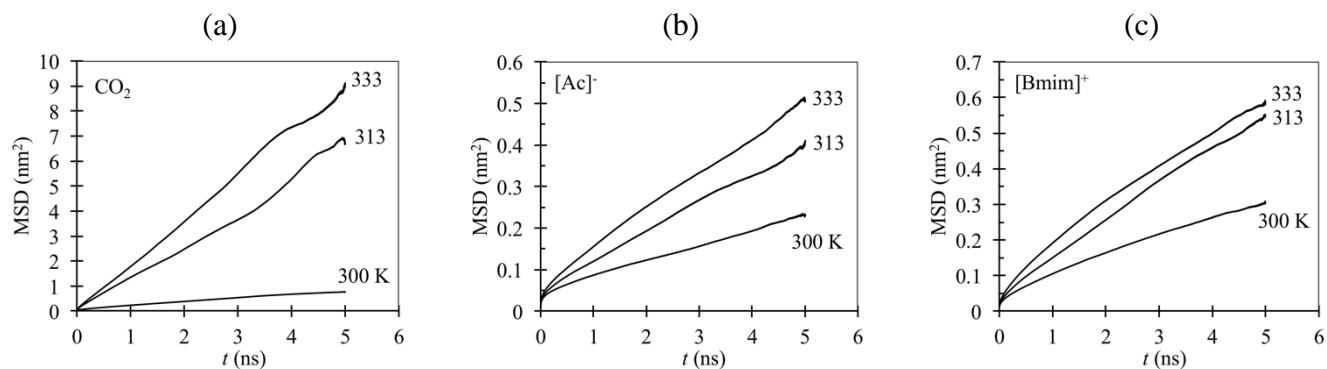
Figure 4-12: Mean square displacement at various temperatures for CO_2-[Bmim][Ac] bulk system for (a) CO_2, (b) anion, and (c) cation.

Based on Figure 4-11 and Figure 4-12, the MSD values for CO_2, cations, and anions are simulated for a run time of 5 ns, except for those of [Bmim][BF_4] at 333 K that are calculated up to 8 ns. The MSD values vary relatively linearly with time, suggesting the significance of normal molecular diffusion during the absorption of CO_2 in the IL. The reason for non-linearity in some points can be related to the presence of natural convection in the IL due to a change in density of the mixture. The MSD values for the cations are higher than those for the anions; this is consistent with our conclusion on higher diffusivity of the cations (compared to anions) in the CO_2-IL mixtures. The MSD profiles for CO_2 in ILs are steeper than those of anions and cations. It implies that CO_2 has

a greater diffusivity and can move faster than the anion and cation in the system. It is noticed that the MSD in [Bmim][BF$_4$] is around 1.5 times higher than that in [Bmim][Ac] (see Figure 4-12). It means that CO_2 diffuses in [Bmim][BF$_4$] easier than in [Bmim][Ac]. The higher solubility of CO_2 in [Bmim][Ac] confirms that it makes a stronger association with this IL. Thus, the diffusivity of CO_2 in [Bmim][Ac] is smaller, compared to [Bmim][BF$_4$] IL. The linear behavior from 1–8 ns can be attributed to the prevalence of molecular diffusion as the governing mechanism for the mass transfer in the liquid phase. Diffusivities of CO_2 in [Bmim][BF$_4$] and [Bmim][Ac] at a pressure of 1 bar, a temperature of 300 K, and a CO_2 mole fraction at solubility limit are calculated to be 3 $\times 10^{-10}\,m^2/s$ and $1.5 \times 10^{-10}\,m^2/s$, respectively, which are in good agreement with the experimental data.[112] The magnitude of CO_2 diffusivity is $10^{-10}\,m^2/s$ that is close to the diffusivity of ILs. It can be concluded again that CO_2 has a higher diffusivity in [Bmim][BF$_4$] than in [Bmim][Ac], while the CO_2 solubility exhibits the opposite trend. The diffusion coefficient generally depends on temperature and pressure, viscosity, molecule size, and concentration. As it is clear, the diffusivity increases with increasing temperature at a constant pressure, which is consistent with free-volume theories. In particular, molecules at higher temperatures retain enough energy to escape from the imposed force-field from their neighbor particles and jump between the neighbor holes [258]. The temperature dependence of the diffusion coefficient is also attributed to the solvent density reduction due to the free volume increment. Self-diffusivity of the cations and anions in [Bmim][BF$_4$] and [Bmim][Ac] after the CO_2 solvation is increased. It follows that a decrease in the mixture viscosity and volume expansion occurs upon the CO_2 addition. In fact, the molecules of CO_2 occupy the spaces between the cations and anions in the solution, which leads to weakening the interactions between these ions. This results in a high diffusion coefficient for the ions in the solution.

4.5.3. CO$_2$-IL Interface

Number density: The number density distributions of the cation [Bmim]$^-$, anion [BF$_4$]$^-$, and CO$_2$ in the *z*-direction are shown at 10 bar and 42 bar in panels a and b of Figure 4-13, respectively. For this phase of the study, the temperature is fixed at 300 K, and the MD simulation is run for up to 8 ns. According to Figure 4-13, a dramatic increase in the number density, as well as considerable fluctuations, are noticed at the interface of the anion and cation. Unlike the ions, the number density of CO$_2$ shows more fluctuations, especially at a higher pressure of 42 bar. Panels a and b of Figure 4-13 elucidate the number density of the cation, anion, and CO$_2$ in the *z*-direction for the case of [Bmim][Ac] and CO$_2$ at 10 bar and 42 bar, respectively. The mixture with a greater concentration of CO$_2$ has a higher density peak at the interface. It is also concluded that the presence of adsorbed CO$_2$ layer at the interface has a minor impact on the order of the number density of the cation and anion oscillations. The number densities for the atoms in the anions are shown in Figure 4-15 (a); Figure 4-15 (b) illustrates the number density distributions for N02, C06, C0G, C0J, and C0N atoms in the cation. The distributions shown in Figure 4-15 (b) are in the order of C0N > C0J > C06 > C0G > N02. At the interface, the anions number density is higher than that for the cations, which is due to the assembly of the anions and tendency of CO$_2$ toward anions of ILs. Also, the cation butyl chain directs into the gas phase in the z-direction. This is a result of self-assembly of the amphiphilic cations at the interface. The maximum gas density is observed at the interface, which is more than the gas layer density in the gas phase and IL slab. This might be attributed to the CO$_2$ van der Waals and quadrupole-charge interactions with the IL. The number density of the [Bmim]$^+$ cation, [Ac]$^-$ anion, and CO$_2$ at various CO$_2$ concentrations and pressures is depicted in Figure 4-14. Similar to [Bmim][BF$_4$], all particle densities increase at the interface. For this IL, higher concentrations of CO$_2$ have more influence on the oscillations of the cation and

anion densities. The final configurations of the different systems, after simulation, are shown in Figure 4-16. For each part/case, the left figure shows only the positions of CO_2 molecules, while the right side of each part (a and b) includes all molecules of IL and CO_2 and their positions after the simulation run is over.

(a)   (b)
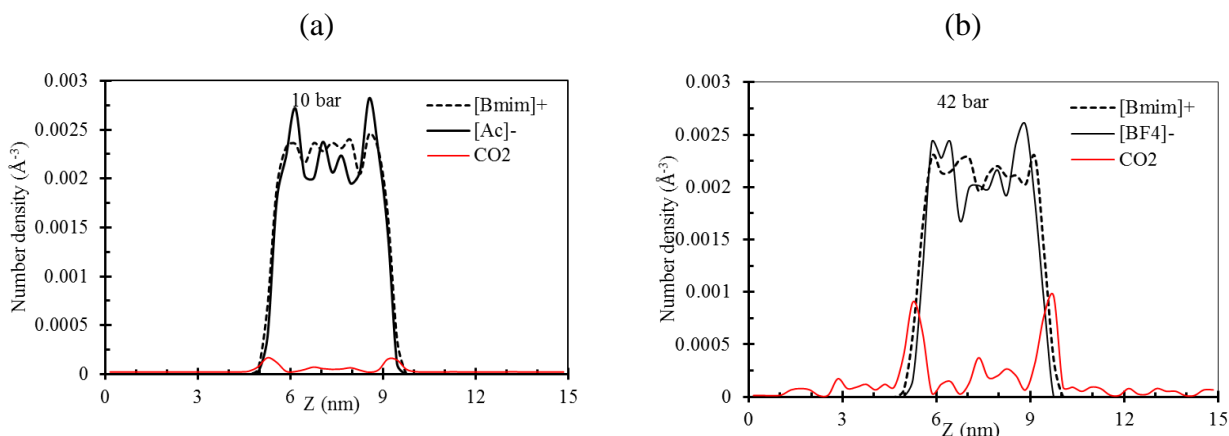
Figure 4-13: The number density for CO_2, $[Bmim]^+$ cation, and $[BF_4]^-$ anion along z-direction for IL-CO_2 system at: (a) 10 bar and (b) 42 bar.

(a)   (b)
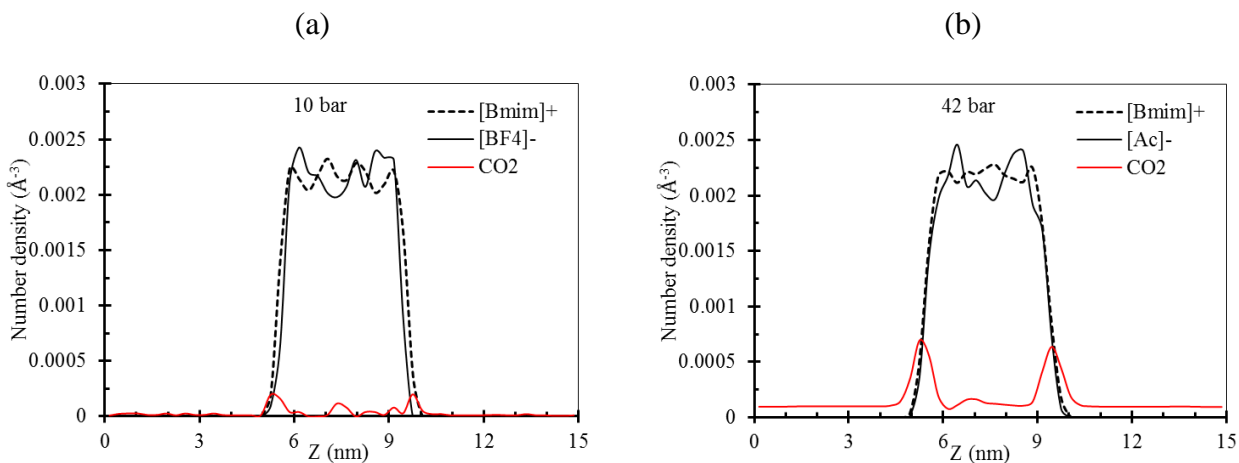
Figure 4-14: The number density for CO_2, $[Bmim]^+$ cation, and $[Ac]^-$ anion along z-direction for IL-CO_2 system at: (a) 10 bar and (b) 42 bar.
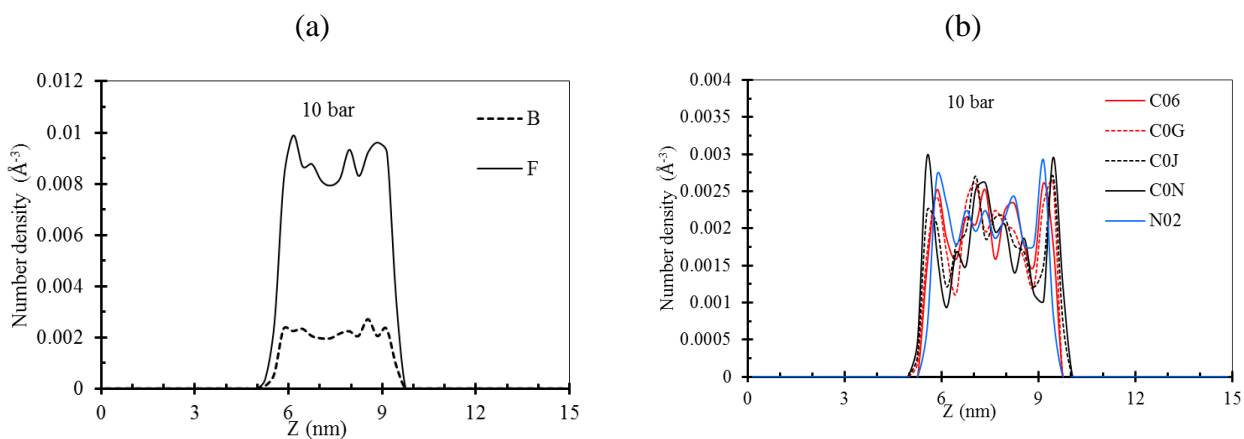
Figure 4-15: The number density for (a) B and F in anion $[BF_4]^-$, and (b) C06, C0G, C0J, C0N, and N02 of cation $[Bmim]^+$ along z-direction for the IL-CO_2 system.
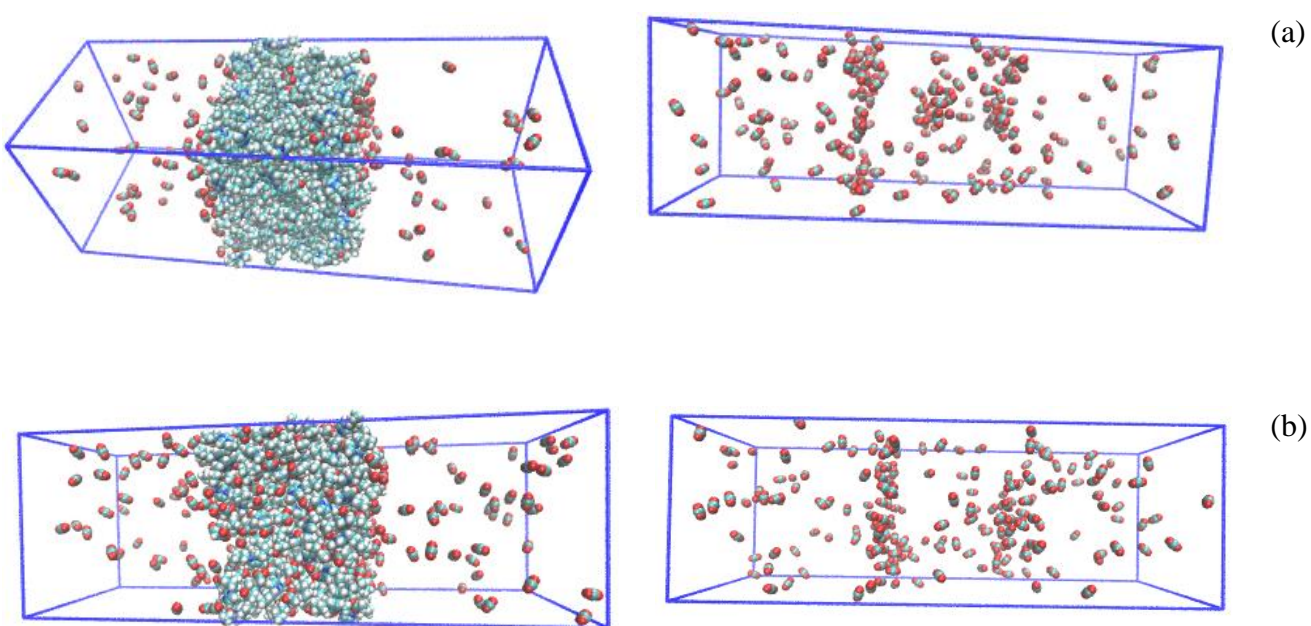
Figure 4-16: Schematic of the simulation box after MD simulation run: (a) $[Bmim][BF_4]$ IL and (b) $[Bmim][Ac]$ IL.

Surface tension: Table 4-3 lists the surface (interfacial) tension calculated for different systems of IL-vacuum and IL-CO$_2$. The predicted surface tension for the IL-vacuum system is close to the value reported in the literature. The experimental surface tension values for pure ILs are in the range of 30–50 mN/m. The surface energy of the IL/CO$_2$ systems is less than that of the IL/vacuum system. In fact, the presence of CO$_2$ has a stabilizing influence on the surface as the IL molecules interact with CO$_2$ molecules and interact less with themselves. The obtained data show a qualitative trend while investigating the effect of gas on the surface tension of ILs. The CO$_2$ layer adsorbed at the interface with [Bmim][Ac] builds a more stable surface, compared to the case of [Bmim][BF$_4$]. This phenomenon can be interpreted by the absorption of CO$_2$ at the interface as depicted in the number density profile. The high density of CO$_2$ at the interface shows the affinity of CO$_2$ and ILs to each other. It also seems that CO$_2$ disrupts the intramolecular interactions of the IL molecules. The surface tension usually decreases with increasing pressure until the IL is saturated with CO$_2$.

Table 4-3: A comparison between the interfacial tensions (γ) of CO$_2$-IL at 300 K.

System	γ (mN/m)	
	[Bmim][BF$_4$]	**[Bmim][Ac]**
IL/Vacuum	58.9[*]	43.9[*]
IL/50 CO$_2$	52.5	42.1
IL/200CO$_2$	50.1	40.2

[*] Literature [235] values are 44.4 (mN/m) for [Bmim][BF$_4$] and 37.6 (mN/m) for [Bmim][Ac]

MD simulations provide a microscopic approach to better explain experimental results and dynamic and structural behaviors of various chemical solutions. Our research work regarding the properties of ILs and behavior of CO$_2$ in the bulk and interface of CO$_2$-ILs systems can help researchers in developing IL absorbents with high efficiency and designing better absorption-

desorption processes. This study may offer useful technical insights into governing mechanisms to separate CO_2 from other flue gases with ILs, which is one of the vital goals toward a green and clean environment.

4.6. Conclusions

Ionic liquids (ILs) have special physicochemical properties (e.g., high thermal stability and negligible vapor pressure) with applications to a wide range of processing and separation operations in energy and environment. However, a limited number of research works have been conducted to explore the bulk and interface properties of ILs in the presence of gases. In this research work, the molecular dynamics (MD) simulation is employed to forecast the properties of pure ILs and diffusivity of CO_2 in the bulk and interface of [Bmim][BF$_4$] and [Bmim][Ac] ILs. The density and viscosity calculated using MD for pure ILs are in good agreement with the experimental data.

The dynamics of the atoms in the alkyl chain domains are different from the imidazolium rings and anions domains. The difference in the motion of atoms in various domains is important to further understand the transport behaviors/characteristics (viscosity and diffusivity) of cations, anions, and solute molecules in the system. Three factors including the molecule size, shape of ions, and the magnitude of interaction energy play an important role while determining the diffusion coefficients of ILs. Diffusion coefficients obtained for the cations and anions of [Bmim][BF$_4$] and [Bmim][Ac] ILs are in the range of $(3\text{--}34)\times10^{-12}$ m^2/s. It should be mentioned that cations have a higher diffusivity than anions. The activation energy is higher for [Bmim][BF$_4$] IL, compared to [Bmim][Ac] IL, leading to a higher diffusion coefficient for CO_2 in [Bmim][BF$_4$]. The greater absolute value of activation energy for [Bmim][BF$_4$] might be due to strong ionic bond

energy within the liquid, which consequently lowers the CO_2 absorption capacity of the IL with [BF$_4$]$^-$ anion.

In the bulk system, the anion has an important role in structuring CO_2 around the cations and anions. CO_2 is located more likely around anion than around cation and has a stronger interaction with anion. The expansion of IL volume is relatively small upon the addition of CO_2 to IL. Solution viscosity decreases dramatically with increasing temperature and CO_2 concentration in the mixture. Diffusivity of CO_2 in [Bmim][BF$_4$] is relatively higher than that in [Bmim][Ac], due to its lower viscosity and smaller anion size. Based on the dynamic properties analysis, the diffusivity has no direct relationship with CO_2 solubility in some ILs.

The presence of CO_2 at the interface of the CO_2/IL systems makes a dense layer and decreases the strong association of cation-anion, causing a reduction in the surface tension. Also, the composition analysis of the interface of CO_2-IL cases shows an increase in the concentration of alkyl side chains of the cations, anions, and CO_2 molecules at the interface.

This study provides a detailed knowledge of IL-CO_2 bulk and interfacial properties using a molecular- scale investigation. The attained information/data can assist to develop and design suitable IL-based absorbents.

NOMENCLATURES

Variables/Parameters	Description
r_{ij}	bond length
Θ_{ijk}	angle
φ_{ijkl}	dihedral angle
V_{ijkl}	Fourier coefficients
$P_{\alpha\beta}$	pressure tensor of the $\alpha\beta$ element
D	diffusion coefficient

E_D	activation energy of diffusion
k_B	Boltzmann constant
q	partial atomic charges
R	universal gas constant
T	temperature
V	volume
x	mole fraction
ε	well depths
σ	Lennard-Jones potential radii

Chemical Formulas

[Bmim][Ac]	1-butyl-3-methylimidazolium acetate
[Bmim][BF$_4$]	1-butyl-3-methylimidazolium tetrafluoroborate
[Bmim][PF$_6$]	1-butyl-3-methylimidazolium hexafluorophosphate
[Bmim][Tf$_2$N]	1-butyl-3-methylimidazolium bis(trifluoromethylsulfonyl)imide
[FAP]	tris(pentafluoroalkyl)-trifluorophosphate
CO_2	carbon dioxide

Acronyms

AAD	Average Absolute Deviation
CCS	Carbon Capture and Storage
CG	Coarse-Grained
DFT	Density Functional Theory
ESP	Electrostatic Potential Surface
GHG	Greenhouse Gases
IL	Ionic Liquid
MSD	Mean Square Displacement
OPLS-AA	All-Atom Optimized Potentials for Liquid Simulations
PME	Particle-Mesh-Ewald
RDF	Radial Distribution Function
UA	United Atom

Greek Letters

γ	surface tension
ρ	density
η	viscosity

5.CHAPTER FIVE

Effect of Water on Molecular Behavior of [Bmim][Ac]/Water/CO$_2$, Using Molecular Dynamics Simulation

Preface

A version of this chapter has been published in the Journal of Physical Chemistry B (2020). I am the primary author of this paper. All authors were involved in the definition of the objectives, outlines of paper structure. I carried out a majority of the literature review, and the MD simulations with the aid of technical comments from co-authors, Sohrab Zendehboudi and Nima Rezaei. The first draft of the manuscript are prepared and revised based on the co-authors' feedback. The co-author, Sohrab Zendehboudi, had a considerable contribution in revising the manuscript in terms of editorial and technical aspects. Nima Rezaei also had a final look to edit the manuscript if some corrections were still needed.

Abstract

Mixing ionic liquids (ILs) with some components such as water appears to be an effective way of designing the ILs applicable in various industries/processes. It might also help to better control the IL solution characteristics. Molecular interactions of IL, water, and carbon dioxide (CO_2) substances are of great importance in the selection of ILs with proper features (e.g., selectivity and solubility) for CO_2 capture. We perform molecular dynamics (MD) simulations to investigate the effect of water concentration on excess energy, molecular distribution, and dynamic behaviors of mixtures of 1-Butyl-3-methylimidazolium acetate ([Bmim][Ac]) IL, water, and CO_2 at different water concentrations. The radial distribution functions, coordination numbers, water clusters, hydrogen bonding, and diffusivity coefficients of [Bmim][Ac]-Water (or IL-W) and [Bmim][Ac]-Water-CO_2 (or IL-W- CO_2) systems are also discussed at various water mole fractions. Water molecules at high concentrations most likely form clusters. Analysis of water clusters in [Bmim][Ac] /W mixture reveals that water clusters are connected mainly with hydrogen bonds. The presence of water in the IL solutions, even at high concentrations of water (>0.7), increases the diffusivity of cation, anion, water, and CO_2 molecules in the mixture due to hydrophilicity of [Bmim][Ac]. Although cations diffuse faster than anions in the mixture anomalously, anion diffusion exceeds cation self-diffusion at high water concentrations, causing that the polar and non-polar regions in the liquid disappear. This study further highlights the important aspects (e.g., diffusion coefficient and cluster formation) of the water presence in IL solution that can assist researchers and engineers for better design and operation of a carbon capture process dealing with IL/W mixtures.

5.1. Introduction

Carbon dioxide (CO_2) is a dominant greenhouse gas (GHG) in the atmosphere, produced in large quantities from industrial processes/plants, such as fossil fuel power plants, refineries, cement and steel production, and natural gas purification [259, 260]. Oceans warming has increased the sea levels that are the consequence of the CO_2 accumulations in the atmosphere, causing an irreversible climate change [261]. The CO_2 existing in natural gas can also accelerate corrosion in pipelines and other process equipment, reduce the gas heating value, and cause catalyst poisoning in several petrochemical processes including ammonia synthesis [262]. CO_2 alone contributes to over 76% of global GHG emissions, followed by contributions from methane and nitrous oxides at 16% and 6%, respectively [263]. Due to the focus of the global community on environmental concerns (e.g., global climate change), conducting systematic research and engineering activities on CO_2 capture, storage, and utilization (CCSU) is imperative. Separation and utilization of CO_2 can have economical and commercial applications, such as conversion process (e.g., synthesis of new chemicals) and utilization as a solvent/working fluid for different operations including enhanced oil recovery and supercritical CO_2 power cycles.

Various methods, such as amine-based absorption, adsorption, and algae-based separation, are currently employed for the separation and capture of CO_2 from flue gases and gas streams. The most commercialized and economical separation approach is absorption with amine-based solvents. However, this technique has several technical and non-technical problems, such as solvent loss due to low vapor pressure and degradability of amines, leading to large investment costs and high energy consumption [259].

In recent years, ionic liquids (ILs) have emerged as promising alternate solvents for physisorption and chemisorption of acid gases due to their unique physiochemical properties, such as negligible

vapor pressure, high thermal stability, tunability, and having a low environmental impact. The properties of imidazolium-based ILs have been studied extensively, suggesting that [FEP]- and [Ac]- based ILs have a high CO_2 solubility [158]. However, the main drawback of ILs is their high viscosity. To overcome this problem, they can be mixed with other organic solvents. One of the best solvents to reduce the mixture viscosity without affecting other IL properties is water with no adverse impact on the environment. Water can decrease the viscosity of ILs without a significant change in the CO_2 capture capacity.

The imidazolium cations have an aromatic ring containing two nitrogen atoms and alkyl groups with varying lengths. Their properties change from being completely miscible with water (hydrophilic) to completely immiscible with water (hydrophobic). In general, cations with long alkyl side chains and large anions (e.g., $[PF_6]^-$) are more hydrophobic than small anions and short alkyl chains [207]. The hydrophilic/hydrophobic behavior of ILs is crucial, not only for the solvation properties of the liquids, such as dissolving reactants but also for the recovery of products through solvent extraction. The solubility of water in ILs depends on the type, length and structure of cation and anion (and groups), pressure, and temperature. Adding water to a pure IL slightly decreases the IL capacity of CO_2 absorption; however, it reduces the IL viscosity that is a favorable feature. Low-viscous IL solvents can promote gas diffusion and lower the operational constraints on their use [128].

Effect of water on IL surface tension was investigated in a study by Freire et al. [264]. Based on their results, low water content leads to a reduction in the surface tension of hydrophilic ILs, while the surface tension of hydrophobic ILs is similar to that of dry ILs. In fact, the hydrogen bonding of water with anions and cations of ILs lowers the electrostatic interactions between ions, resulting in a decrease in the IL surface tension.

ILs have the ability to absorb water at ambient conditions. Adding water to imidazolium-based ILs breaks down the original network of cation-anion in ILs and forms new water-cation/water-anion networks [265]. This process causes a change in the structure and dynamics of ILs, including surface tension, diffusion, and viscosity. The viscosity of ILs decreases rapidly with an increase in the water content [266]. In other words, the presence of water in the IL solution significantly reduces the viscosity of pure ILs and CO_2-saturated ILs; it also causes a slight decrease in the CO_2 absorption capacity [267].

Absorption of CO_2 by the pure ILs, 1-ethyl-3-methylimidazolium acetate and 1-butyl-3-methylimidazolium acetate, within the temperature range of 303 -343 K was reported by Stevanovic et al. [13]. They also investigated the effect of water on CO_2 solubility at various temperatures and compositions [268]. Viscosities of the acetate and chloride-based ILs and their mixture with water have been studied [269]. Their findings show that the addition of a small amount of water into acetate-based ILs at 25ºC reduces the viscosity of the mixture to almost one-half of pure ILs.

The influence of water on the interfacial behaviors of CO_2 and IL systems has been analyzed by Perez-Blanco and Maginn [235], with a focus on [Bmim][Tf_2N]/ W/CO_2 system. It was concluded that H_2O is absorbed into the IL and avoids interfacing.

To design (and choose) appropriate ILs for various purposes such as carbon capture, it is important to understand their properties, structures, and molecular interactions with other molecules involved in corresponding phenomena/processes. Molecular dynamics (MD) simulation strategy is a powerful tool to obtain structural, physiochemical, dynamics, thermophysical, and association characteristics of complex liquids such as ILs. The selection of a reliable force field will help to

effectively simulate the real molecular behaviors of the targeted system(s) through accurate and generalized simulation runs. For gas-liquid systems, MD approaches are able to compute the dilution properties, adsorptions isotherms, solubility, excess chemical potential, and gas dynamics characteristics of the mixtures. The solubility, structure, and molecular interactions/motion of CO_2 in ILs have been studied in the literature [16-18]. There are also a few research investigations in the open sources that discuss the solvation of water in ILs in terms of molecular structure and dynamics [16-18]. However, the interactions, structure, and detailed molecular dynamics of the ternary system of CO_2/IL/W are still a matter of controversy. Moreno et al. [270] studied the dynamics and molecular interactions of the bulk system of H_2O and [Bmim] [BF$_4$] using MD simulations. Their results showed that at low concentrations of water, the diffusivities of cation and anion in a mixture of IL/W are lower, compared to pure ILs. Upon an increase in water concentration, ions diffusivity increases. The dynamics of ILs mixture with water were studied by Hanke et al. [271], revealing that water molecules create small clusters that change the mixture properties. They found that excess energy and water diffusion coefficient in mixtures of either hydrophilic or hydrophobic IL and water differ significantly, while radial distribution functions and ion diffusion coefficients seem irrelevant to the hydrophilicity of ILs. Shi et al. [272] studied water interactions with acetate-based IL using an experimental investigation and ab initio simulation method. Their experiments showed that water makes hydrogen bonding with IL and affects self-diffusivities of ions. In addition, water-acetate interactions dominate water-water and water-cation interactions.

The CO_2 absorption capacity in several IL/W mixtures has been reported experimentally [273, 274]. However, molecular simulations have been rarely applied to explore the influence of water on CO_2 solubility and diffusivity in mixtures. Stevanovic et al. [268] claimed that in the presence

of water, the absorption properties of 1-alkyl-3- methylimidazolium acetate IL significantly change; the mixture viscosity and CO_2 absorption decrease. Although there are a few research works on the influence of water on the solubility of CO_2 in ILs, the impact of water on the CO_2 molecular dynamics and interface behaviour in ternary mixtures has not been discussed in the literature, yet. The current research aims to further explore the water clustering, diffusivity of CO_2 and ions, and excess energies in the binary system of [Bmim][Ac]/W and the ternary system of [Bmim][Ac]/CO_2/W.

In this work, the MD simulation of all-atom force field OPLS-AA [231] is used to study the thermodynamic and physical properties (enthalpy, viscosity, and density), water distribution, radial distribution functions (RDFs) of components, and diffusivity of ions and components in the [Bmim][Ac]/W and CO_2/IL/W systems at various water concentrations.

This chapter is organized as follows: after the introductory section, Section 5.2 provides a brief theory and description on molecular dynamics (MD) simulation methodology. Section 5.3 then presents and discusses the results of MD simulation runs including excess enthalpy and excess volume; radial distribution functions of ions, CO_2, and water; water cluster sizes; mean square displacements of the compounds and their corresponding diffusivity coefficient. Section 5.4 includes the conclusions to highlight the main findings of the study.

5.2. Molecular dynamics simulation: theory and methodology

In this study, molecular dynamics (MD) simulations are implemented to investigate the molecular and thermodynamic characteristics of pure IL, binary [Bmim][Ac] IL/W, and ternary CO_2/[Bmim][Ac] /W systems. The effect of water (as an additive) mole fraction to IL is also assessed where water mole fractions of 0, 0.2, 0.4, 0.6, and 0.9 are considered. The solubility of

CO$_2$ in IL and IL/W mixtures is examined and determined, using Gromacs 5.1.4 package [247, 248]. The structures of the cation 1-butyl-3-methylimidazolium ([Bmim]$^+$) and anion acetate ([Ac]$^-$) are optimized from density functional theory (DFT), using the Becke three parameter Lee-Yang-Parr hybrid correlation functional (B3LYP) method [275] with the Gaussian 16 package [245]. The basis set used were 6-311G+(d,p). The partial charges of the IL molecules are scaled uniformly by 0.8 to compensate for the effects of charge transfer and polarizability in the bulk [246]. The force fields for the IL are taken from OPLS-AA [239, 240]. OPLS-AA forcefield parameters developed and validated for number of ionic liquids [231]. Their parameters were fitted to conformational profiles from gas-phase ab initio calculations at the LMP2/cc-pVTZ(-f)//HF/6-31G(d) theory level and compared to experimental thermodynamic and structural data. Their calculations for ILs density and heats of vaporization from Monte Carlo simulations were in good agreement with experimental values. For CO$_2$, the force field parameters are obtained from the literature [231]. The water molecules are simulated, using the TIP4P model [260]. A simple schematic of the cation and anion used in this work is shown in Figure 5-1.
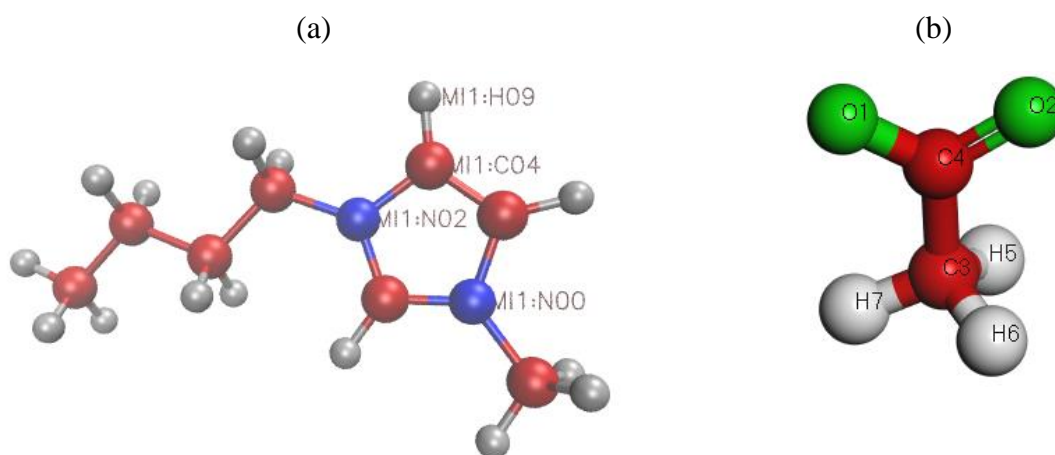
Figure 5-1: Schematic of the IL components considered in this work: (a) [Bmim]$^+$ cations, and (b) [Ac]$^-$ anions; [Atoms: C (red), H (white), and O (Green)].

The OPLS-AA force field is implemented with van der Waals interactions, using Lennard-Jones with a cut-off radius of 1.4 nm. A brief theory on the MD force fields is provided in Appendix A3. The particle mesh Ewald method [276] is applied for the long-range electrostatic interactions. The MD simulations are conducted under periodic boundary conditions with time-steps of 1 fs. Temperature and pressure are controlled by the Nose-Hoover thermostat [249], and Parrinello-Rahman pressure coupling [250], with coupling times τ_T=0.2 ps and τ_P=1.0 ps, respectively.

For all IL/W mixture combinations (with varying water mole fractions), we use 300 pairs of IL ions; the number of water molecules is adjusted to reach the desired water mole fractions. Therefore, a total number of 79, 199, 463 and 2700 molecules of water are included with 300 pairs of the IL ions to reach the target water mole fractions of 0.2, 0.4, 0.6, and 0.9, respectively. After energy minimization, the selected IL/W systems are heated up to 1000 K, and then gradually cooled to the target temperature of 300 K. After that, the system is equilibrated, using a step of isothermal-isobaric (NPT) ensembles in 5 ns; temperature is kept at 300 K using Nose-Hoover thermostat with a coupling constant of 0.5 fs; and the Parrinello-Rahman pressure coupling keeps the pressure at 1 bar. The radial distribution functions (RDFs) calculated at different time regions are compared to infer whether the equilibrium condition is reached. Finally, each equilibrated system is used as an initial configuration for performing 5-ns production runs. The atomic coordinates are saved every 10.0 ps for later analysis.

For the ternary system of CO_2/IL/W, the simulation box consists of 300 ion pairs, various numbers of the water molecules to obtain the desired water concentration in IL/W mixture, and different numbers of CO_2 molecules as dictated by the solubility limit of CO_2 in IL/W mixtures. For sensitivity analysis, we maintain different concentrations of the water molecules in a cubic simulation box, using Packmol [251]. The system is equilibrated for 5 ns NPT and followed by for

4 ns in a canonical ensemble (NVT). Density values are calculated after the NPT ensemble. The production run is then performed in a period of 8 and 5 ns for the IL/W and CO_2/IL/W systems, respectively. The structures of the molecules in the simulation runs are illustrated in Figure 5-2.

(a)   (b)
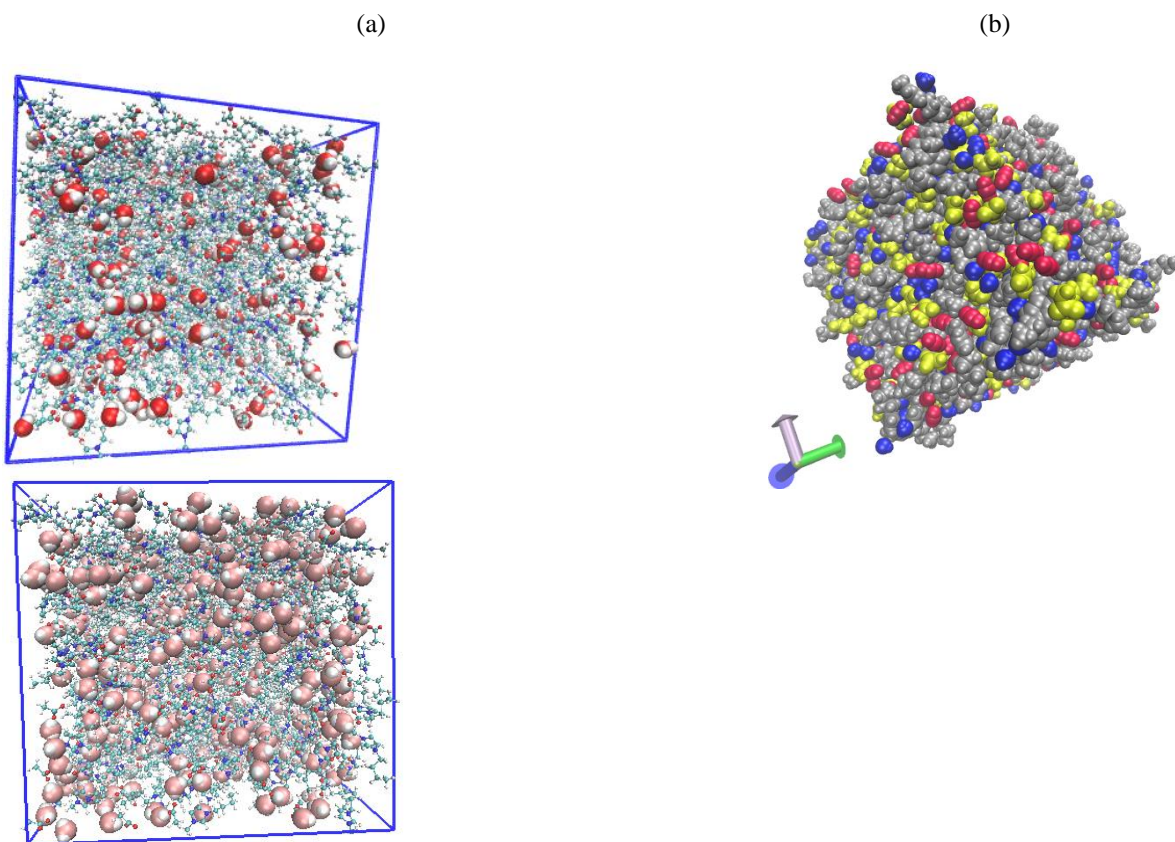
Figure 5-2: Molecular graphical representation of (a) IL/W system and (b) CO_2/IL/W system.

5.3. Results and discussions

In this section, first, we present the physiochemical properties of the IL and water system (e.g., density, viscosity, and excess energy) that are calculated from the MD simulation runs. After that, the structural properties of the system including water clusters and CO_2 distribution in the mixture are discussed. Finally, dynamic analysis of the compounds including radial distribution functions and diffusivity coefficients is presented. More detailed information about the theory of viscosity,

mean square displacement (MSD), and radial distribution function (RDF) is provided in Appendix A3.

5.3.1. Physical and Thermodynamic Properties

Density and molar volume of pure IL ([Bmim] [Ac]) and IL/W mixtures at different compositions are plotted in Figure 5-3 at a temperature of 300 K and a pressure of 1 bar. By increasing the water mole concentration from x_w=0.2 to 0.8, the mixture density decreases from 1.048 g/cm^3 to 1.036 g/cm^3 at x_w=0.8, respectively; the molar volume decreases from 138.2 cm^3/mol to 51.3 cm^3/mol, respectively. The results of MD simulations are in good agreement with the experimental data [253], as can be observed from Figure 5-3.
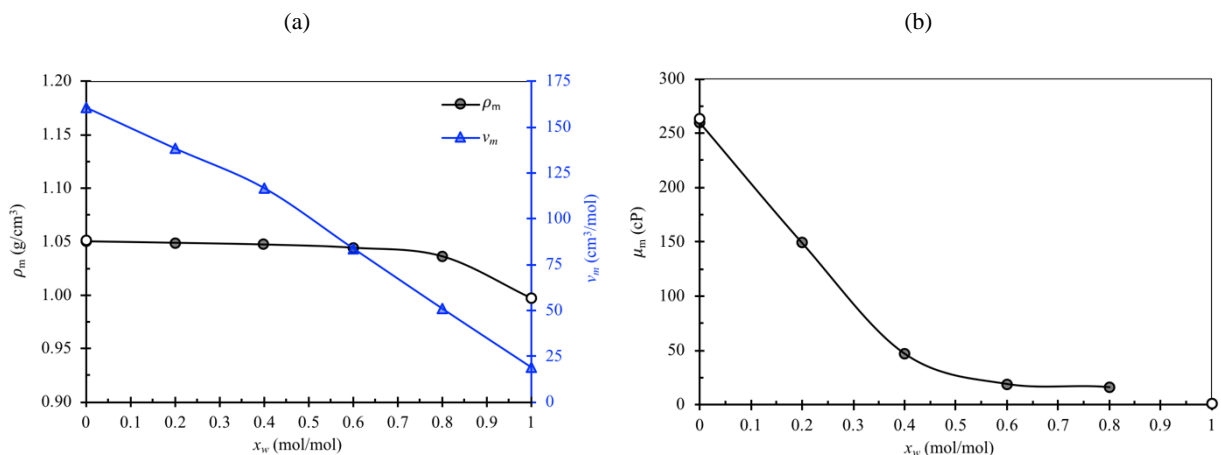
Figure 5-3: Physical properties of IL/W mixtures at different water contents: (a) mixture density and molar volume, and (b) mixture viscosity. The solid circles are experimental data from [253, 277].

Also, the mixture viscosity for the IL/W system at different water concentrations is reported in Figure 5-3 (b). Increasing the water concentration dramatically decreases the viscosity of the IL/W mixture (see Figure 5-3 (b)). At 300 K and atmospheric pressure, the density of water is 0.997 g/cm^3 while it is slightly higher for the IL (e.g., 1.051 g/cm^3). This lower density magnitude of water

contributes to a reduction in IL/W density upon the addition of water. The molar volume is given by the ratio molar mass/mass density where both the numerator and denominator decrease due to adding water. The overall trend for the molar volume shows a decrease by adding water to IL. This behavior may be justified by the stronger association and columbic interactions of water with the ions (in ILs) due to the IL hydrophilicity.

The excess molar volume and excess molar enthalpy for the mixture of IL/W are calculated; the excess molar volume (v^E) is obtained, using the following expression:

$$v^E = v_m - \sum_i x_i v_i \qquad (5\text{-}1)$$

where v_m is the molar volume of the mixture; x_i and v_i represent the mole fraction and the molar volume of pure component i, respectively. The excess molar enthalpy can be written in a similar equation, by replacing enthalpy (h) for the molar volume (v). The effect of water concentration on the excess molar volume and molar enthalpy of the IL/W mixtures at 300 K and 1 bar is illustrated in Figure 5-4. The minimum excess molar volume and minimum excess molar enthalpy are located near water concentrations x_w =0.5 `and 0.7, respectively (see Figure 5-4), which is justified with strong hydrogen bonding (high number of hydrogen bonds as a function of time) between H_2O and [Ac]⁻ in the mole fraction range 0.5–0.7 mol/mol. In an experimental investigation, Alvarez et al. [278] measured the excess molar volume of 2-hyroxyethyl ammonium acetate/water mixture. The minimum excess molar volume occurs for this mixture at x_w=0.7 mol/mol, which is close to the range found in our simulation. However, its minimum excess volume value is smaller than our simulated value. This different value is due to the different type of the cation, and is related to the variation in the force field parameters, underestimating the interaction energy between water and anion. As observed in Figure 5-4, the excess molar volume and excess molar enthalpy have

negative values. Gonzalez et al. [279] studied the effect of ions and temperature on excess properties of binary mixtures of IL/W. Based on their results, the chemical structure of anion plays an important role in the shape of V^E curves, and therefore considerably affects the thermodynamic behavior of the IL/W mixtures [279]. The excess molar volume and excess molar enthalpy simulation data are fitted to the Redlich-Kister polynomial equation, as listed below:

$$\Delta Q_{ij} = x_i x_j \sum_{n=0}^{N} B_n (x_i - x_j)^n \tag{5-2}$$

where ΔQ_{ij} introduces the excess property; x_i is the mole fraction of component i; B_n is the fitting parameter; n stands for the degree of polynomial expansion. The corresponding fitted curve using the Redlich-Kister equation for excess properties (enthalpy and molar volume) is plotted in Figure 5-4 as a function of water mole fraction, at 300 K and 1 bar.

The optimal degree of polynomial expansion is determined through minimizing the deviation (σ) between experimental and calculated values, as defined below:

$$\sigma = \left[\frac{\sum (\Delta Q_{\exp} - \Delta Q_{calc})}{N} \right]^{1/2} \tag{5-3}$$

Where N refers to the total number of experimental points. The magnitudes of B_i and σ for the [Bmim][Ac]/W system at 300 K are reported in Table 5-1.

Table 5-1: Fitting parameters and standard relative deviations (σ) for IL/W mixture at T = 300 K.

Excess property	B_0	B_1	B_2	B_3	B_4	σ
v^E (cm^3·mol^{-1})	-21.170	4.819	19.613	-4.775	-40.788	0.031
h^E (kJ·mol^{-1})	-38.27	45.28	-45.28	-45.00	83.55	0.086
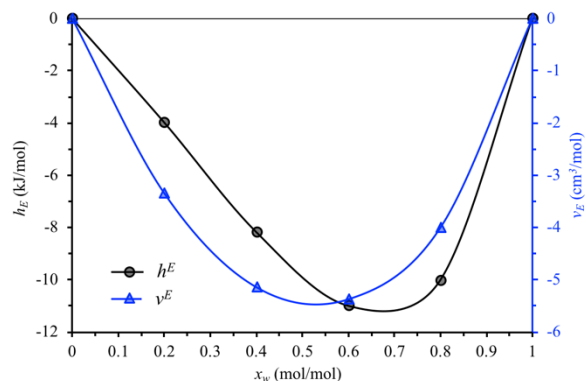
Figure 5-4: Excess molar volume (v^E) and excess molar enthalpy (h^E) for IL/W mixtures as a function of water mole fraction at 300 K and 1 bar. The curves are fitted to the simulated data.

5.3.2. Structural properties

Water and ions distribution. Radial distribution functions (RDFs or g(r)) are used in our system to characterize the spatial coordination of water molecules in the mixture of IL/W. The RDFs are determined based on the distance between the center of mass between water-water (or W-W), W-IL, and cation-anion, as demonstrated in Figure 5-5. In Figure 5-6, the coordination numbers for W-W and IL-W molecule pairs are demonstrated. Figure 5-6, also provides information on the association strength.

(a) W-W	(b) W-IL	(c) Cation-Anion
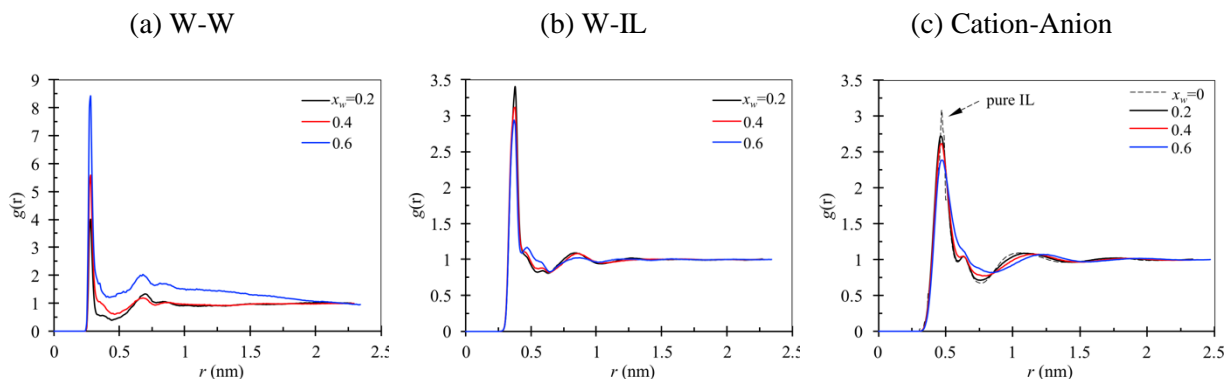
Figure 5-5: RDF in IL/W mixtures at different water concentrations, for the center of mass between molecule pairs: (a) W-W, (b) W-IL, and (c) Cation-Anion at 300 K and 1 bar; [Cation=[Bmim]$^+$, and anion=[Ac]$^-$].

Figure 5-5 (a) shows the RDF ($g(r)$) for the center of mass in W-W pairs. At all water concentration levels, the first peak is obtained at r=0.28 nm, indicating a close contact between the water molecules. Note that the approximate kinetic diameter of the water molecule is 0.275 nm. As the water mole fraction increases, the probability of observing a water molecule around another water molecule increases. It implies that water molecules create a stronger association with themselves. However, the number of close water molecules exhibits a slower increase rate than a number of water molecules in the defined concentration. The RDFs for the W-IL pairs at various mole fractions of water are depicted in Figure 5-5 (b). As it is clear from Figure 5-5 (b), the RDF for the W-IL center of mass decreases with increasing the water mole fraction as the probability of observing a water molecule around ILs in the system lowers. Thus, water molecules create larger clusters at higher concentrations of water and have weak associations with IL molecules. To study the association/interaction strength between the cation-anion, the RDF analysis is described in Figure 5-5(c), where [Bmim]$^+$ and [Ac]$^-$ represent the cation and anion, respectively. The minimum distance of cation-anion is located at the same distance as pure IL; however, their distribution has a slightly smaller peak than pure IL. It implies that the water presence weakened the cation-anion association. The radial distributions for the cation-anion center of mass in IL/W and pure IL (x_w=0 mol/mol) are presented in Figure 5-5 (c), showing that the cation-anion association is stronger in pure IL compared to that in mixtures with a high water concentration (e.g., 0.6 mol/mol). It seems that the water molecules are oriented themselves around the anions; hence, the probability of having a cation-anion close to each other is decreased at elevated water concentrations. According to the RDF plots, the water-water (or W-W) association is more probable than W-IL and cation-anion pairs associations.

The W-IL association becomes weaker as the water concentration increases. The coordination number gives the number of ions in the ionic liquid that a central water molecule can hold as its nearest neighbor in the mixture; its value increases upon an increase in the water mole fraction. In the literature, the common approach for evaluating the coordination number is numerical integration of $4\pi r^2 g(r)$ up to its first minimum [280]. The association of the water molecules becomes stronger at a higher concentration of water (e.g., 0.6 mol/mol, compared to 0.2 mol/mol), as observed in Figure 5-6. It suggests that the water molecules create a smaller cluster at a lower water concentration. The coordination number for the water around IL up to the first minimum at 0.53 nm increases with increasing the water mole fraction in the mixture. The coordination number of water molecules around the central water molecule also increases with increasing water concentration in the mixture.
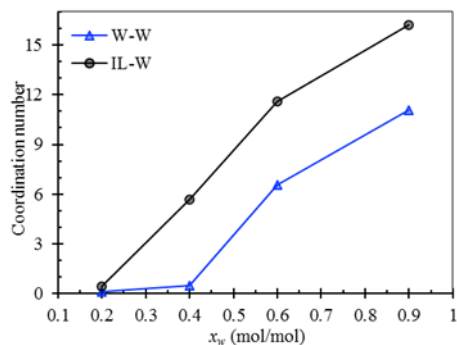
Figure 5-6: The coordination number for W-W and IL-W pairs in IL/W systems at different water concentrations.

The aggregation number, which is the number of molecules in a cluster, is used to monitor the approach to equilibrium and the expected water cluster size. "Hydrogen bond or H-bond" is defined using a geometrical or an energetic criterion in the context of molecular computation [281].

According to the literature, H-bond is considered in a pair of molecules if the distance between the hydrogen atom and the acceptor group is smaller than 0.35 nm and the angle of the donor-hydrogen-acceptor is lower than 30° [281]. The value of r_{HB} = 0.35 nm corresponds to the location of the first minimum of the RDF of SPC water. The water molecules can form a cluster when the minimum distance between the atoms is less than 0.35 nm [282]. The distance between the oxygen atoms and hydrogen atoms on the water molecule is used to determine if each water molecule is located in others' coordination shell. In this study, r_{cut} is set to 0.34 nm which corresponds to the first minimum of the RDF for TIP4P water molecules [283]. The coordination number of the water molecules is considered as an average number of water molecules that are located in each coordination shell. The cluster size is obtained by averaging the number of clusters formed over the entire simulation time. The water clusters are indicated at r_{cut}=0.34 nm, where r_{cut} is the distance between the oxygen atoms and hydrogen atoms in a water molecule at various water concentrations in CO_2/IL/W systems.

The size distribution of water clusters versus water concentration is demonstrated in Figure 5-7. At x_w =0.2 mole fraction, the water clusters contain 2–5 water molecules in the IL/W mixture. As the water mole fraction increases to 0.4 and 0.6, the water cluster size increases to >8 water molecules. The water molecules have less probability to make a cluster at a low water concentration. Thus, at a low mole fraction of water, the probability of forming clusters through hydrogen bonding decreases. Figure 5-7(b) shows the cluster structure in the CO_2/IL/W mixtures in which more clusters are created compared to the IL/W system. It is confirmed that in the CO_2/IL/W mixture, larger water clusters exist at greater water concentrations. This observation can justify the hypothesis that the CO_2 molecules may locate themselves around the IL ions, repelling the water molecules from the proximity of the IL molecules. Therefore, the water

molecules will have the chance to form more clusters with themselves. Moreover, at x_w=0.2, water clusters have approximately the same sizes in both binary and ternary systems. It can be concluded that at low water concentrations, CO_2 is not able to interrupt the association of IL-W molecules. Distribution of the water cluster sizes reveals that monomers and dimers constitute the most common cluster sizes.
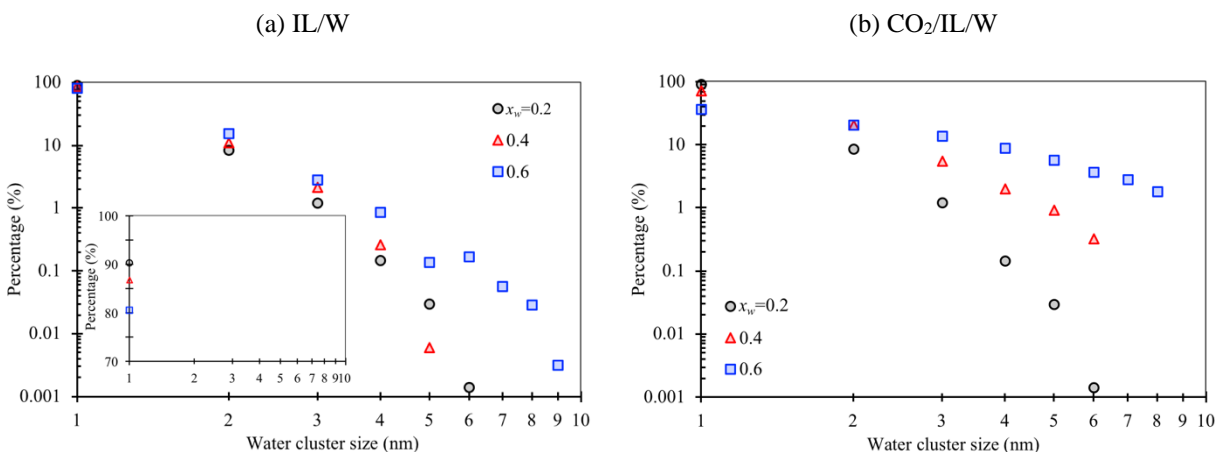
(a) IL/W   (b) CO_2/IL/W

Figure 5-7: Water cluster size distributions in (a) IL/W and (b) CO_2/IL/W mixtures at different water mole fractions.

The average cluster sizes in the solution over 5 ns simulation are calculated to be 4.5, 5.6, and 12.8 nm at the water mole fractions (in IL/W mixtures) of 0.2, 0.4, and 0.6, respectively. The average cluster size as a function of time is depicted in Figure 5-8. The finding implies that water is less soluble in the [Bmim][Ac] at a higher water concentration; consequently, larger clusters can be formed which may lead to phase separation. Since [Bmim][Ac] is hydrophilic, phase separation will occur at high concentrations of water; while for hydrophobic ILs, the phase separation can be noticed even at low concentrations.
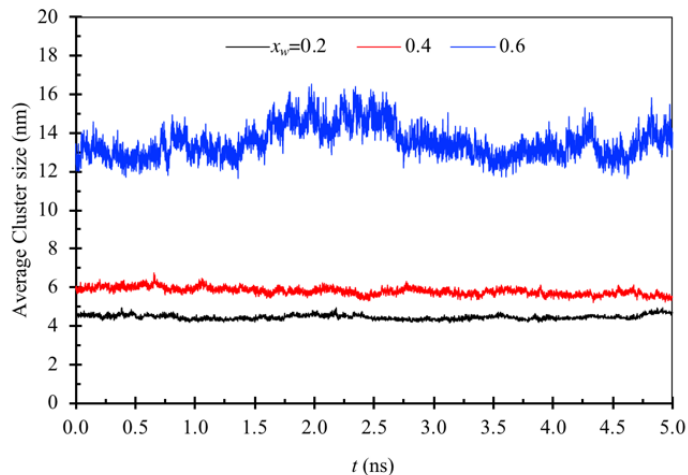
Figure 5-8: Average water cluster size (nm) versus time (ps) based on the simulations of water molecules in IL/W/ CO_2 System.

The connectivity of molecules in the water clusters is mainly through hydrogen bonds, as depicted in Figure 5-9. The cluster structure and connectivity through hydrogen bonding between the water molecules are shown in Figure 5-9 for the IL/W system at x_w =0.4 mol/mol. The presence of water affects the physical properties of ILs, particularly dynamical properties. Thus, it is important to know how these dynamical properties varies upon CO_2 addition and water concentrations. To study the effect of water on CO_2 diffusivity and mixture interactions, the water clusters are investigated in binary and ternary systems. It is necessary to study the water and IL structures at mixture at various water concentrations to find out the optimum water concentration for CO_2 absorption. Because water molecules create clusters that changes the mixture properties.
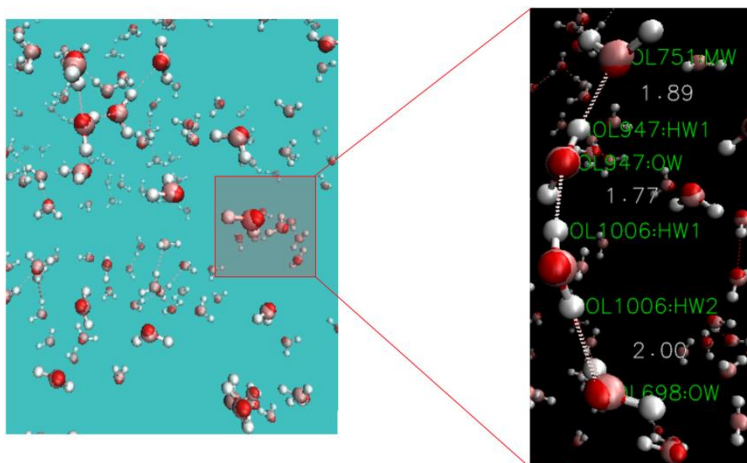
Figure 5-9: Water distribution in IL/W mixtures at x_w =0.4 mol/mol along with information on the H-bond in clusters (Red spheres represent O, white spheres show hydrogen, and dashed lines illustrate H-bonding in Angstrom).

CO₂ Distribution. The radial distribution functions $g(r)$ are calculated from MD simulation runs conducted on CO_2/[Bmim][Ac] IL/W systems. As shown in Figure 5-10, the cation-anion radial distribution functions of the CO_2/IL/W system at water mole fractions of 0.2, 0.4, and 0.6 present a major peak at 2.72 nm, 2.69 nm, and 2.31 nm, and minor peaks in the range of 1.1–1.25 nm. For the pure cation-anion, the peak is at 2.75nm and a small hump is observed at 1 nm (see Figure 5-10).

The center of mass radial distribution of CO_2-[Bmim]$^+$ increases with an increase in the water concentration from 0.2 to 0.6. The peaks in the RDF at water mole fractions of 0.2, 0.4 , and 0.6 are located at 0.52 , 0.53 , and 0.54 nm, respectively for CO_2-[Bmim]$^+$; 0.37, 0.38, and 0.39 nm for CO_2-[Ac]$^-$, respectively; and 0.31, 0.31, and 0.31 nm for CO_2-W, respectively (see Figure 5-11). As shown in Figure 5-11, the radial distribution of CO_2 around the cation and water is approximately the same at all water concentration levels. However, the distribution of CO_2 around anion decreases with an increase in the water mole fraction. It confirms that CO_2 molecules mostly

associate with the anions and have less interaction with the cation imidazolium ring. Electrostatic energy plays an important role in the IL structure and the solvation interactions for quadrupole and dipolar molecules in ILs [282]. CO_2 preferential position around anion was confirmed in a study conducted by Kazarian et al. [284] where an IR spectroscopy was employed. It was found that carbon dioxide interacts with the oxygen atoms of the anion. Thus, with an increase in water concentration of the mixture, carbon dioxide interactions with anion will be most likely interrupted by the water molecules.
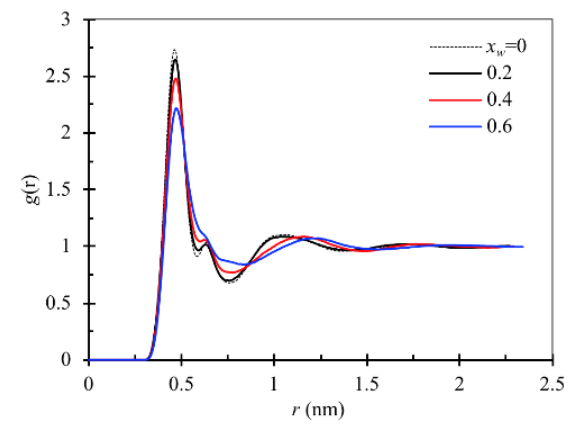
Figure 5-10: RDF of [Bmim]$^+$-[Ac]$^-$ at various water concentrations.
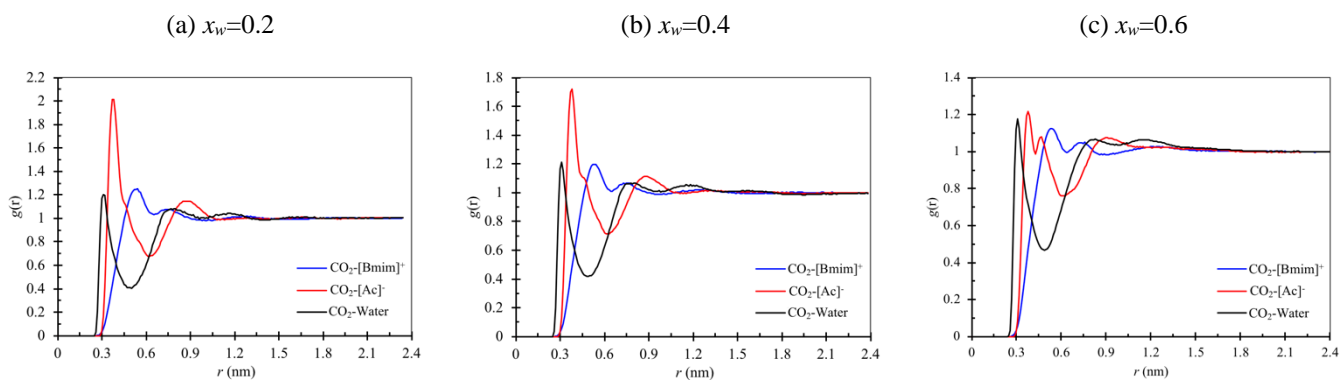
Figure 5-11: RDFs for center of mass of CO_2-[Bmim]+, CO_2-[Ac]$^-$, and CO_2-W in CO_2/IL/W system at (a) x_w=0.2 mol/mol, (b) 0.4, and (c) 0.6.

5.3.3. Dynamic Characteristics

The diffusion coefficients (D_i) for ions, water, and CO_2 are calculated using the mean square displacement (MSD) of the MD trajectories by the Einstein equation, as expressed below:

$$D_i = \lim_{t \to \infty} \frac{\left\langle \Delta r_i^2(t) \right\rangle}{6t} \qquad (5\text{-}4)$$

where $\langle \Delta r_i^2(t) \rangle$ symbolizes the MSD of species i at time t. To attain more reliable MSD results, it is recommended to run MD simulations for longer periods (3-10 ns or more) due to the slow dynamics of the diffusion in ILs because of its high viscosity. The MSD plots of the cation, anion, and water with varying water concentrations are illustrated in Figure 5-12 for the IL/W system. The simulated self-diffusion coefficients of water in [Bmim][Ac] at different water concentrations are reported in Table 5-2. It is noticed that the water self-diffusivity remarkably increases at high water concentrations. This behavior can be due to a decrease in W-IL interactions and the presence of large water clusters in the mixture. Self-diffusivities of cation and anion in the IL/W mixture are also summarized in Table 5-2. In general, the self-diffusivity of $[Bmim]^+$ is larger than that of $[Ac]^-$ at water mole fractions up to 0.6. However, self-diffusivity of $[Ac]^-$ is considerably increased to 25.4 $\times 10^{-11}$ m^2/s at $x_w=0.9$, compared to $[Bmim]^+$ whose diffusivity is 18.21 $\times 10^{-11}$ m^2/s. This behavior is probably due to the decreased interaction of water-anion, resulting in faster diffusion of anions. In general, anions should move faster than imidazolium cations due to their smaller size. However, the existence of polar- and non-polar regions in imidazolium-based ILs leads to opposite behavior/phenomenon. It can be concluded that at higher water concentrations, this unusual behavior of polar and non-polar regions does not happen anymore. Thus, the diffusivity of the anion becomes larger than that of the cation.
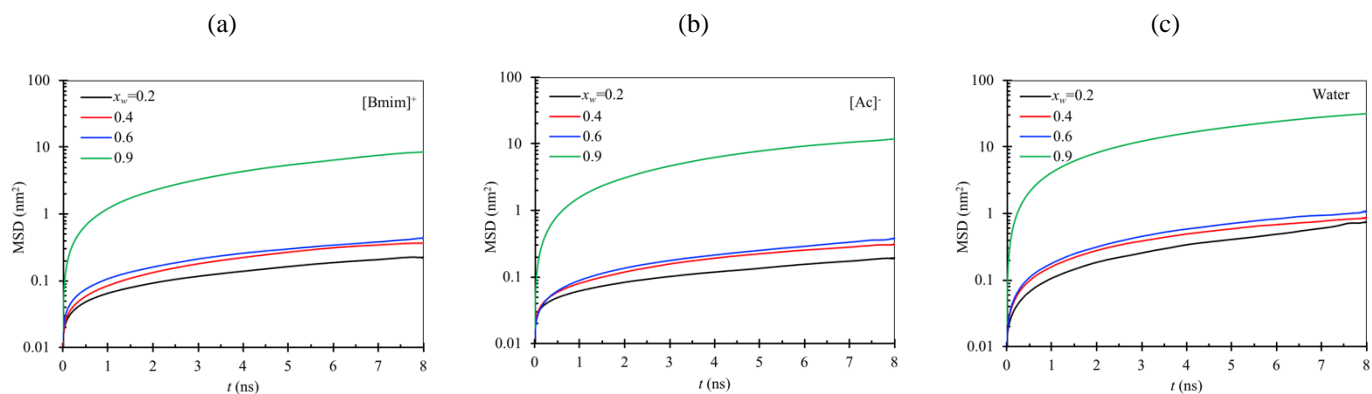
Figure 5-12: MSD dynamics in IL/W system at different water mole fractions for: (a) $[Bmim]^+$ (cation), (b) $[Ac]^-$ (anion), and (c) water.

In Figure 5-13, the MSD dynamic behaviors of the cation, anion, water, and CO_2 in the ternary system of $CO_2/IL/W$ is illustrated. An increase in the diffusion of all species is observed in the IL/W and $CO_2/IL/W$ systems by increasing the water concentration; diffusivity of water molecules increases upon an increase in the water mole fraction. It is obvious that the presence of water in hydrophilic [Bmim][Ac] IL decreases the mixture viscosity. Hence, the dynamics of the molecules becomes faster than usual. It is concluded that the diffusivity of all species increases upon the addition of water to the system, which is justified with a decrease in the mixture viscosity. According to Menjoge et al. [285], an increase in the diffusivity of ions with adding water is observed for Ethylmethylimidazolium ethylsulfate $([C_2C_1Im]+[EtSO_4]^-)$ and Ethylmethylimidazolium triflate $([C_2C_1Im]+[TfO]^-)$ ILs, which is attributed to a decrease in the activation energy (based on relationship of the self-diffusion with activation energy in the Arrhenius equation). In general, the relationship between the activation energy, temperature, and viscosity can be expressed with the Arrhenius exponential equation ($\eta = \eta_0 \exp(-\frac{E_a}{RT})$). Where E_a represents the activation energy of diffusion, η_0 is the pre-exponential factor of the Arrhenius equation (Pa.s), and R refers to the universal gas constant. Adding water to IL, a decrease in the

activation energy (of self-diffusion) occurs; this reduction becomes less significant at high water concentrations. In fact, water plays an important role in increasing the self-diffusion coefficient of compounds at low water mole fractions. This impact would be more significant at high water concentrations.
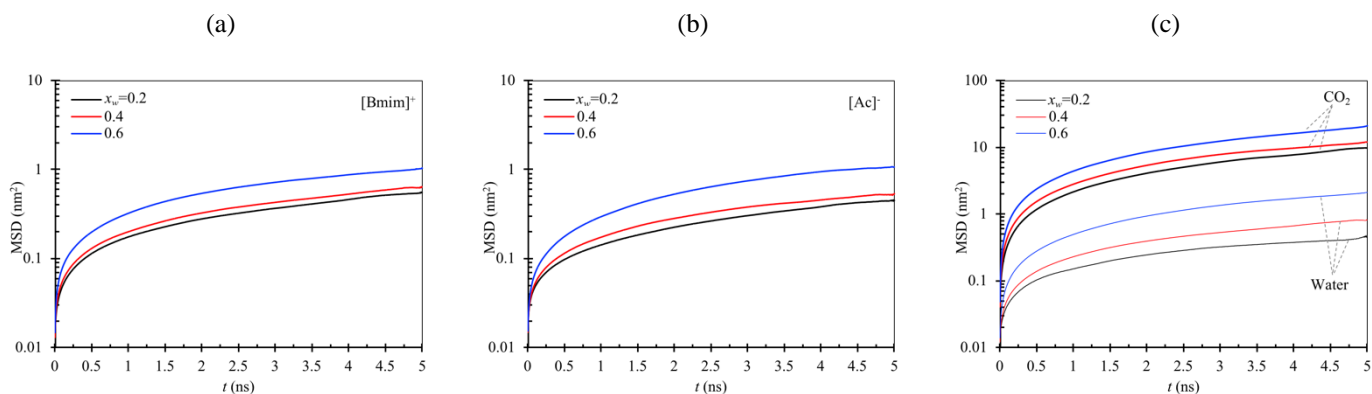
Figure 5-13: MSD dynamics in CO_2/IL/W system at different water mole fractions: (a) $[Bmim]^+$ (cation), (b) $[Ac]^-$ (anion), and (c) water and CO_2.

The effect of temperature on the MSD dynamics of CO_2 in pure IL is shown in Figure 5-14 in which both the rate of change in MSD and diffusivity increase with increasing temperature in the range 300–333 K.
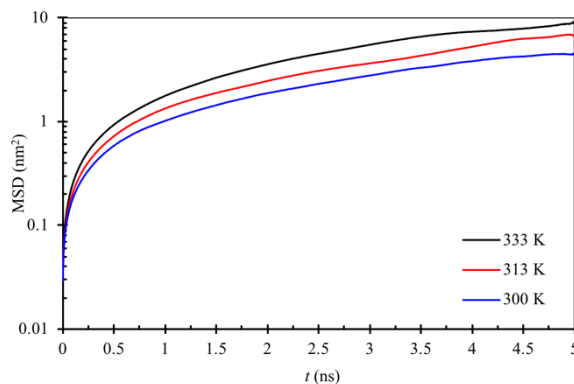
Figure 5-14: MSD of CO_2 in the bulk system of CO_2/[Bmim][Ac] as a function of time and temperature at the atmospheric pressure (1 bar).

A summary of the diffusion coefficients for water, cation, anion, and CO_2 at various concentrations of water is provided in Table 5-2. The diffusivities of $[Bmim]^+$ and $[Ac]^-$ in the pure IL at 300 K are obtained to be 0.51×10^{-11} and 0.32×10^{-11} m^2/s, respectively. The diffusion coefficient of pure water from the TIP4P model at 300 K is determined to be 2.35×10^{-9} m^2/s, which is in agreement with the experimental data [286].

Table 5-2: Diffusivity of cation, anion, water, and CO_2 in IL/W and CO_2/IL/W systems at different water contents at 300 K and P=1 bar.

x_w (mol/mol)	D (1×10^{-11} m^2/s)						
	CO_2/IL/W				IL/W		
	Water	$[Bmim]^+$	$[Ac]^-$	CO_2	Water	$[Bmim]^+$	$[Ac]^-$
0	-	1.01	0.61	13.30	-	0.51	0.33
0.2	1.25	1.60	1.34	31.31	1.32	0.58	0.39
0.4	2.40	1.84	1.57	38.67	1.69	0.77	0.61
0.6	6.80	3.06	3.58	65.19	2.15	0.90	0.71
0.9	-	-	-	-	66.3	18.21	25.4

The MSDs behaviors for cation, anion, water, and CO_2 in pure IL, binary IL/W, and ternary CO_2/IL/W systems are illustrated in Figure 5-12 and Figure 5-13. With an increase in water concentration, the diffusion of cation and anion in pure IL, IL/W, and CO_2/IL/W systems increase. The self-diffusivity rises with increasing the concentrations of water in the IL/W system, as shown in Table 5-2. At high water concentrations (>0.7), phase separation may occur due to the immiscibility of the IL and water; for hydrophobic ILs, the phase separation may even occur at low water concentrations. According to Table 5-2, the diffusion coefficient of water in the IL is larger than that of the cation and anion; however, the water diffusivity in the IL solution is much smaller than that for pure water (2.3×10^{-9} m^2/s at 298 K) [287]. In pure [Bmim][Ac], the self-diffusivity of the cation (which is larger) is higher than that of the anion (which is smaller). Indeed, larger molecules are expected to diffuse slower than smaller molecules, according to the classical Stokes-Einstein relation. This unusual behavior is well explained in previous experimental and

computational investigations where the existence of polar- and non-polar regions are confirmed in imidazolium-based ILs [265]. The addition of water to the ILs leads to the formation of complexes of water with ions [265, 288]. At a low water concentration, these complexes can be described as hydrogen-bonded complexes, anion $\cdots$ HOH $\cdots$ anion. Hence, the water molecules tend to be isolated from each other and preferably interact with anions; this observation is also confirmed in Figure 5-7. However, at higher water mole fractions (>0.75), water clusters with a high number of molecules are created, resulting in phase separation.

MD simulations provide a microscopic approach to explain experimental results, and dynamics and structural behaviors of various chemical systems. Our research to further explore the effect of water presence on the static and dynamic properties of hydrophilic IL [Bmim][Ac] with and without CO_2, can help researchers to utilize water as an inexpensive and safe additive for reducing the viscosity of ILs, and to improve their applicability in the chemical industry. This work may offer useful technical insights into the influences of water on viscosity, excess properties, transport dynamics, and radial distribution of the molecules in various mixtures.

5.4. Conclusions

The molecular behaviors of binary W/[Bmim][Ac] and ternary CO_2/[Bmim][Ac]/W systems are investigated, using molecular dynamics (MD) simulations. The excess energy, radial pair distribution function, coordination number, water clusters, and dynamic properties of compounds are obtained from the analysis of the MD trajectories.

The mixture viscosity decreases by 40% in the presence of water where the mole fraction of water in [Bmim][Ac] IL is 0.2. Excess volume and excess enthalpy of the mixture are obtained upon the

water solvation in IL. Both properties/parameters hold negative values and are fitted to the Redlich-Kister equation.

The water molecules can form clusters at high water concentrations and the water structure depends on the strength of water-anion interactions. Analysis of water clusters in [Bmim][Ac] /W mixture reveals that the water clusters are connected mainly through hydrogen bonds. Due to hydrophilicity of [Bmim][Ac] IL, phase separation does not happen at the water mole fraction below 0.6. This implies that the association of polar solvents (e.g., water) is affected by the hydrophilicity of anions and their sizes.

The presence of water in [Bmim][Ac] IL within the mole fraction range of 0.2–0.6, leads to a significant increase in the diffusivities and activation energies for ions in comparison to self-diffusivities in pure IL. A further increase in the water mole fraction (>0.8) results in a sharp change in the ions diffusion coefficients. This can be explained that the presence of one water molecule per two ion pairs can ensure the formation of hydrogen bonding in anion-water pairs. Hence, increasing the water mole fraction beyond 0.8 does not increase the number of anions interacting directly with the water molecules; however, the diffusivity of molecules is significantly increased due to the low viscosity of the mixture. Diverse nanometer-sized water clusters form and grow with addition of water to the mixture; at high water concentrations, water continues to separate the dissolved state and water only phase.

In pure [Bmim][Ac], the self-diffusivities of cations are larger than those for the anions. This anomalous relationship between the size of the molecules and diffusivity of species can be attributed to the presence of local polar and non-polar regions in the IL. Adding water to the

mixture reduces the magnitude of the anomalous difference between the diffusivities of the cation and anion.

Appendix A3

Force Field Parameters: The standard form of force filed includes intramolecular interactions (U) contributions from bond stretching ($U_{stretch}$), angle bending (U_{bend}), dihedral torsion ($U_{torsion}$), non-bonded interactions Lennard-Jones (U_{LJ}), and Columbic interactions ($U_{Coulomb}$), as presented below:

$$U = U_{stretch} + U_{bend} + U_{torsion} + U_{LJ} + U_{Coulomb} \qquad (A3\text{-}1)$$

The functional forms of these individual potential terms are obtained from OPLS-AA force fields [239]; they are used in this research as given below [240]:

$$U_{stretch} = \sum_{ij}^{bonds} \frac{k_{r,ij}}{2}(r_{ij} - r_{0,ij})^2 \qquad (A3\text{-}2)$$

$$U_{bend} = \sum_{ij}^{angles} \frac{k_{\theta,ij}}{2}(\theta_{ij} - \theta_{0,ijk})^2 \qquad (A3\text{-}3)$$

$$U_{torsion} = \sum_{ij}^{dihedrals} \sum_{m=1}^{4} \frac{V_{m,ijkl}}{2}[1 + (-1)^m \cos(m\varphi_{ijkl})] \qquad (A3\text{-}4)$$

$$U_{LJ} = \sum_{i} \sum_{j \neq i} 4\varepsilon_{ij}[(\frac{\sigma_{ij}}{r_{ij}})^{12} - (\frac{\sigma_{ij}}{r_{ij}})^6] \qquad (A3\text{-}5)$$

$$U_{Coulomb} = \sum_{i} \sum_{j \neq i} \frac{1}{4\pi\varepsilon_{ij}} \frac{q_i q_j}{r_{ij}} \qquad (A3\text{-}6)$$

in which, r_{0ij} , $\theta_{0,ijk}$, and $\varphi_{0,ijkl}$ stand for the initial bond length, angle, and dihedral angle, respectively. Other parameters are the force constant k, the Fourier coefficients V, the partial atomic charges q, and the Lennard-Jones potential radii and well depths (σ and ε). The repulsive and dispersive terms are described by Lennard-Jones 12-6 potential. The electrostatic interactions are obtained by the Coulombic potential. These two potentials are between sites in different molecules and sites within the same molecule.

Viscosity: The shear viscosity (η) of each IL is calculated using the Green-Kubo relation [241, 242]. The shear viscosity is obtained from the integral over time of the pressure tensor autocorrelation function, based on the Green-Kubo equation, as follows:

$$\eta = \frac{V}{k_B T} \lim_{t \to \infty} \int_0^t \langle P_{\alpha\beta}(0) P_{\alpha\beta}(t) \rangle dt \tag{A3-7}$$

In Equation (A3-7), V refers to the system volume; T represents the temperature; k_B is the Boltzmann constant. The brackets mean that pressure tensors are averaged over time. $P_{\alpha\beta}$ denotes the pressure tensor of the $\alpha\beta$ element. To attain more accurate and reliable results, the shear viscosity is calculated by taking the averaging over three independent terms of pressure tensor, namely, P_{xy} , P_{yz} , and P_{xz} .

Diffusivity: The dynamic properties of the ionic liquid (ILs) in the liquid phase are calculated in terms of mean-square displacements (MSDs) for the center of mass of the ion, as expressed below:

$$MSD = \frac{1}{N} \left\langle \sum_{i=1}^N \left| r_i(t) - r_i(t) \right|^2 \right\rangle = \Delta |r(t)|^2 \tag{A3-8}$$

The diffusivities are also determined using the MSDs averaged over time, through Einstein relation shown in Equation (A5-9) [243]:

$$D_i = \frac{1}{6}\lim_{t\to\infty}\frac{d}{dt}\left\langle \left| r_i\,(t) - r_i\,(0) \right|^2 \right\rangle \tag{A3-9}$$

where $r_i(t)$ represents the center of mass of ion i at time t and $\langle ... \rangle$ denotes a moving time average. Diffusivities can be obtained through the least square fit of the MSD versus time for the molecule transport.

Radial distribution function (RDF): The radial distribution function (RDF) is the pair correlation function as defined below [244]:

$$g_{AB}(r) = \frac{\langle \rho_B(r) \rangle}{\langle \rho_B \rangle_{local}} = \frac{1}{\langle \rho_B \rangle_{local}}\frac{1}{N_A}\sum_{i\in A}^{N_A}\sum_{i\in B}^{N_B}\frac{\delta(r_{ij}-r)}{4\pi r^2} \tag{A3-10}$$

In Equation (A3-10), $\langle \rho_B(r) \rangle$ resembles the density of molecule B at a distance of r around molecules A; and $\langle \rho_B \rangle_{local}$ is the density of molecule B averaged in time over all spheres around molecules A with the maximum radius r_{max}. Usually, r_{max} is calculated as the half length of the simulation box; and N_A and N_B refer to the total numbers of the molecules of A and B, respectively.

NOMENCLATURES

Acronyms	
AAD	Average Absolute Deviation
CCSU	Carbon Capture, Storage, And Utilization
CG	Coarse-Grained
DFT	Density Functional Theory
ESP	Electrostatic Potential Surface
GHG	Greenhouse Gases
IL	Ionic Liquid
IR	Infrared Spectroscopy

MD	Molecular Dynamics
MSD	Mean Square Displacement
NPT	Isothermal-Isobaric Ensemble
NVT	Canonical Ensemble
OPLS-AA	All-Atom Optimized Potentials for Liquid Simulations
PME	Particle-Mesh-Ewald
RDF	Radial Distribution Function
UA	United Atom

Chemical Formula

[Bmim][Ac]	1-Butyl-3-methylimidazolium acetate
[Bmim][Tf$_2$N]	1-Butyl-3-methylimidazolium bis(trifluoromethylsulfonyl)imide
CO_2	Carbon dioxide

Greek Letters

θ_{ijk}	angle
φ_{ijkl}	dihedral angle
ε	well depths
ρ	density
σ	Lennard-Jones potential radii
η	viscosity

Variables/Parameters	**Description**
r_{ij}	bond length
V_{ijkl}	Fourier coefficients
$P_{\alpha\beta}$	pressure tensor of the $\alpha\beta$ element
k_B	Boltzmann constant
$U_{stretch}$	bond stretching
U_{bend}	angle bending
$U_{torsion}$	dihedral torsion
U_{LJ}	Lennard-Jones interactions
$U_{Coulomb}$	Columbic interactions
r_{cut}	cut-off radius
D	diffusion coefficient
E_a	the activation energy of diffusion
h^E	excess molar enthalpy
k_B	Boltzmann constant
N	the total numbers of the molecules
q	the partial atomic charges
R	universal gas constant
T	temperature
t	time
V	volume
v	molar volume
v^E	excess molar volume
x	mole fraction

6. CHAPTER SIX

Estimation of CO₂ Solubility in Ionic Liquids Using Connectionist Tools

Based on Thermodynamic and Structural Characteristics

Preface

A version of this chapter has been published in the Journal of Fuel, 117984 (2020). I am the primary author of this paper. Sohrab Zendehboudi and I were involved in the literature review, definition of objectives, modeling approach, and design of the manuscript. I prepared the first draft of the manuscript and subsequently revised the manuscript based on the feedback/comments from the co-author. The coauthor, Sohrab Zendehboudi, significantly helped in reviewing and revising the manuscript.

Abstract

Ionic Liquids (ILs) are a promising alternative to conventional amine-based solvents in CO_2 absorption processes. Relatively high cost and viscous nature of ILs tempt researchers to find an appropriate combination of cations and anions for targeting a competitive absorbent close to amines in terms of CO_2 absorption capacity. Conducting extensive experimental studies appears to be time-consuming and expensive for a large number of common CO_2/ILs systems. One of the fast and reliable approaches to predict the solubility of CO_2 in ILs is Machine Learning (ML)-based models or smart tools where the thermodynamic-based and structure-based property relationships can be explored. Four ML methods including Least Square Support Vector Machine (LSSVM), Decision Tree (DT), Random Forest (RF), and Multilinear Regression (MLR) are employed to obtain CO_2 solubility in a structurally diverse set of ILs based on thermodynamic properties and Quantitative Structure-Activity Relationship (QSPR) model. In this chapter, two datasets of CO_2 solubility (taken from the literature) at various operating conditions are used; one model (or dataset) considers critical properties, molecular weight, and acentric factor of pure ILs as the input information, and the second one includes structural descriptors of cations and anions as the input parameters. Among different types of descriptors, the most important input variables (e.g., Chi_G/D 3D and Homo/Lumo fraction (anion); SpMax_RG and Disps (cation)) are selected using Genetic Algorithm (GA)-MLR method. The predictive ability of the introduced models is also analyzed using a 4-fold external cross-validation procedure. A great match between the predicted values and experimental measurements is attained while using RF and DT techniques developed based on descriptors and thermodynamics properties. The structural descriptors-based models are more accurate and robust than those built on critical properties. The feature selection approach is also applied to identify the most effective cations and anions descriptors. For both

thermodynamic and QSPR modeling approaches, pressure has the maximum relative importance in the estimation of CO_2 solubility in ILs. In the absence of temperature and pressure impacts, the critical pressure and Homo/Lumo fraction have the highest contribution to the thermodynamic-based and structural-based tools, respectively.

6.1.Introduction

The increased concentration of greenhouse gases (GHG), particularly CO_2, in the atmosphere is a result of human activities in the last 150 years [1]. The shares of industry and electricity sectors in GHG emissions/production are, respectively, 22.2 and 28 percent in 2017 [1]. The GHG emissions mainly come from power plants, cement/brick factories, and generally industries/sectors operating with burning fossil fuels, mostly coal and natural gas. Significant efforts have been made (and are being made) by both academia and industry to find effective solutions for the reduction of GHG emissions and/or to mitigate their adverse environmental impacts. One of the effective remedies implemented in the coal-fired power plants is post-combustion CO_2 capture from emitted flue gases [289].

The most widely used technology for carbon capture is post-combustion CO_2 absorption approach that mainly utilizes amines as solvents. However, there are some drawbacks to this method including high energy consumption, volatility, corrosive nature, and thermal and chemical stability of amines [290]. One of the promising alternatives to aqueous amines are Ionic Liquids (ILs) including conventional and task-specific IL solvents. In general, task-specific ILs can absorb CO_2 through a chemical reaction, while the main absorption mechanism is physical while utilizing Conventional ILs. There are some research works on CO_2 capture with various ILs in the literature [29, 291, 292], though still more research investigations are required to further explore the CO_2

absorption mechanisms, roles of cations and anions, and molecular interactions between ILs and CO_2 at the different process and thermodynamic conditions.

There are a large number of ILs with a variety of physical and chemical properties. The high degree of tunability of ILs makes them an appropriate solvent for the dissolution of acid gases. Hence, cations and anions can be modified (e.g., changing cation chain size and functionalizing ions) for the synthesis of various ILs [293, 294]. Physiochemical and thermophysical characteristics of ILs can be determined through a series of static and dynamic experiments. Although experimental runs can provide reliable and accurate phase behavior and physicochemical data of ILs and IL/gas systems, some limitations such as costs and timely procedure might exist. Providing further information, a large number of ILs and their high expenses make experiments expensive, time-consuming, leading to rigorous quality assurance for sample synthesis and experimental procedure [158]. Supporting this claim, a majority of the experiments have been carried out on most common imidazolium cations and adequate data are not available for other groups of cations and anions combinations. Thus, besides conducting more experimental tests, it seems essential to employ appropriate/ reliable modeling and screening methods.

Modeling phase behavior and physical properties of solvents using thermodynamic Equations of State (EOS) is a well-known strategy in chemical engineering, particularly while dealing with various applications/processes in energy and environment fields. Some of the EOSs such as Peng-Robinson [81], Redlich-Kwong-Soave [295], and Statistical Associating Fluid Theory (SAFT) EOSs [296] are widely used to obtain properties of ILs. Despite numerous advantages of the EOS modeling, this approach requires experimental data for determining EOSs parameters/coefficients; EOSs need to be tuned using experimental data for accurate prediction. In other words, the precision and reliability of EOS modeling strongly depend on the type of EOS, laboratory tests,

mixing rules, and tuning procedures [297]. In addition, molecular simulations such as Monte Carlo, Molecular Dynamics (MD), and Quantitative Structure-Property Relationships (QSPR) [2, 3] are implemented to simulate/model the thermodynamic and physical/chemical characteristics of pure ILs and their mixtures with other chemicals.

It would be desirable to develop fast screening and deterministic tools that can help forecast the component (or chemical) properties such as solubility, density, viscosity, melting points, and thermal decomposition at different conditions. Recently, advanced computational approaches based on artificial intelligence have been employed in various science and engineering disciplines [200, 298]. Artificial Neural Networks (ANNs) are a well-known category of connectionist models [299, 300]. As a powerful non-linear regression approach, ANNs - evolved from the human brain's data analysis pattern- represent networks of parallel distributed processing elements called neurons. They have some limitations including the black box nature and over-fitting; considerable user interference of relations is also required to adjust parameters of networks [301]. Other ML methods, which have been recently used for prediction and classification, include Least Square Support Vector Machine (LSSVM) [302], Decision Tree (DT) [303], Random Forest (RF) [304], and Gene expression Programming (GEP) [305]. Like other deterministic methods, there are some advantages and disadvantages with smart models. For instance, Support Vector Machines (SVM) techniques [306] are useful due to their simplicity in solving complex equations/systems. However, the SVM algorithm is not proper for the cases with a large number of data points [307].

Smart models can be used along with the QSPR-based method to find the mathematical relationships between molecular properties of chemicals and the response of interest [308]. The theory or model of QSPR/QSAR is employed to obtain a correlation between property/activity and structural descriptors of compounds. Thus, it is possible to design and develop new chemicals or

214

solvents using this method for various applications. The molecular descriptors can provide important insights into the physiochemical nature of a specific characteristic under study [309]. Most of the studies have used thermodynamic critical properties of ILs in order to estimate the solubility parameter and/or physiochemical property of ILs. Since the critical characteristics of some ILs are not available in the open sources, it is more logical to develop a model based on the structural properties of ILs. In addition, structural features for most compounds are available and a model based on structural properties will offer robust, and more accurate predictions [309].

Several research investigations have been conducted on the prediction of solubility using a variety of correlations and deterministic methods, however, a limited number of data have been utilized and only critical properties of solvents have been considered as input parameters [298, 310, 311] . For example, Baghban et al. predicted the solubility of CO_2 in 14 ILs using a multi-layer perceptron artificial neural network (MLP-ANN) model and an adaptive neuro-fuzzy interference system (ANFIS) model based on critical properties [298]. It was reported that MLP-ANN exhibits a better performance in determining the solubility of CO_2. The QSPR model was employed for predicting Henry's Law Constant (HLC) for CO_2 solvation in 32 ILs [312]. It was found that the proposed QSPR models linked with MLR and LSSVM methods are reliable so that the coefficient of determination (R^2) values are 0.935 and 0.965, respectively.

In this research work, an extensive amount of CO_2 solubility data in ILs at various operating conditions is first collected from the literature; the critical properties, acentric factor, and thousands of molecular descriptors of ILs are also obtained. We employ four advanced ML approaches including Random Forest (RF), Least Squares Support Vector Machine (LSSVM), Decision Tree (DT), and Multilinear Regression (MLR) for prediction of CO_2 solubility in 46 ILs over wide ranges of temperature and pressure based on thermodynamic features including critical properties,

molecular weight, and acentric factor. In addition, the solubility of CO_2 in 40 ILs in terms of their structural properties using the QSPR method is determined. Besides the prediction of the objective function, the feature selection method is applied to reduce the number of input parameters from +1000 for cations and anions to develop a model with a limited number of input parameters. The performance of developed models (on the basis of both approaches) in terms of accuracy and robustness is compared. It is worth noting that various combinations of cations and anions are taken into account in this work to model the CO_2 solubility in different ILs using ML techniques. The performance of all methods is evaluated through conducting a statistical analysis where important statistical parameters such as relative error percentages and coefficient of determination are calculated.

To the best of our knowledge, this research is the first work that uses large datasets of CO_2 solubility in ILs, considering important structural descriptors and thermodynamic properties. Also, no research work in the literature uses RF and DT methods based on the QSPR model and critical properties for estimation of CO_2 solubility in ILs.

This chapter is organized as follows: after the introduction, the background/theory and methodology of used predictive techniques such as MLR, RF, DT, and LSSVM are provided in Section 6.2. Data collection is given in Section 6.3. Section 6.4 presents the results obtained from the developed models as well as discussions on the trends/behaviors and corresponding figures and tables. Finally, the main findings of the study are highlighted in Section 6.5 (Conclusions).

6.2. Theory and methodology

Quantitative Structure-Property Relationships (QSPR). This technique is used to predict the solubility of CO_2 in ILs by representing the chemical characteristics of ILs. The structural properties of compounds are encrypted in a form of molecular descriptors. We obtain 1500 molecular descriptors from Dragon 5.9, including constitutional, geometrical, charge, Weighted Holistic Invariant Molecular (WHIM) descriptors, information indices, P_VSA_like descriptors, 3d matrix-based descriptors, and molecular properties [313]. 25 quantum-chemical descriptors are provided from Mopac software [314], Molecular Orbital Package– Austin model (MOPAC) 7.1 descriptors. A simple flowchart of the main steps of the QSPR method is demonstrated in Figure 6-1.
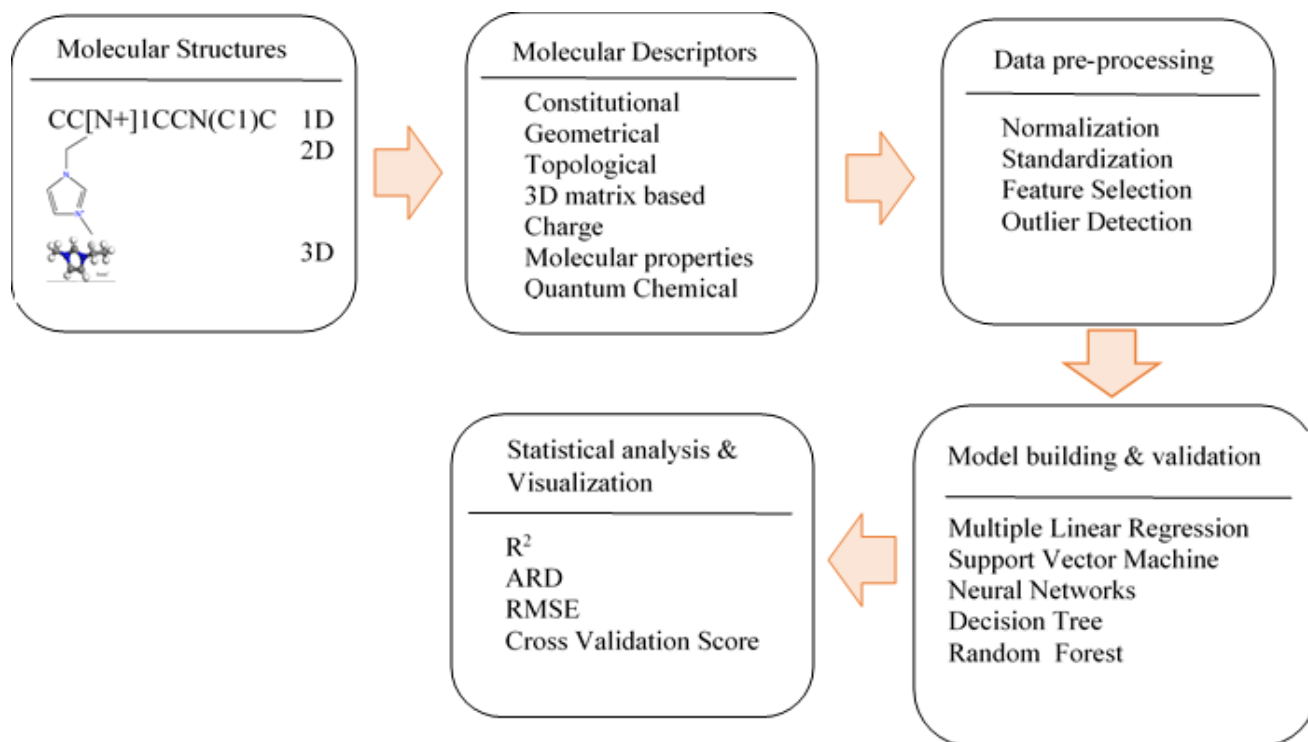
Figure 6-1: Main steps to develop a QSPR model.

Genetic Algorithm-Multilinear Regression (GA-MLR). Due to the presence of a large number of descriptors, the best possible combinations of features should be identified for the QSPR model. In order to ensure the diversity in both training and testing data, a diversity test using Principal Component Analysis (PCA) is conducted; this technique is applied with the structural descriptors of the entire dataset to measure the diversity that assists in the separation of training and testing data points. After splitting the data into training and testing series, the important features for the solubility of CO_2 in ILs need to be selected. GA is used to find the most relevant descriptors for obtaining linear models with the highest predictive performance using the training stage. It should be noted that GA is an evolutionary widely used approach in QSPR/QSAR feature selection [294]. In this study, feature selection with GA simulates the evolution of the population which each individual defined by a chromosome of binary values representing descriptors subset (1, if the descriptor is included in the subset; otherwise, it takes zero value) [315]. A fitness function (η) is calculated from the Root Mean Square Errors (RMSE) of training and validation phases to ensure the performance of each neuron. The following fitness function proposed by Depczynsky et al. is used in this study [316]:

$$\eta = \left\{ [(m_t - n - 1)RSME_T^2 + m_v RMSE_V^2] / (m_v + m_t - n - 1) \right\}^{1/2} \qquad (6\text{-}1)$$

where m_t and m_v stand for the number of data points in the training and validation sets, respectively; and n denotes the number of selected descriptors. The most significant descriptors based on the GA-MLR algorithm are Chi_G/D 3D and HomoLumoFraction for anion, and Disps and SpMax_RG for cation.

The Variance Inflation Factor (VIF) is employed to investigate the existence of multicollinearity among the nominated descriptors [317]:

$$VIF = \frac{1}{(1 - R_i^2)} \qquad \qquad (6\text{-}2)$$

In Equation (6-2), R_i represents the correlation coefficient between the ith descriptor regressed against all other descriptors in the model. When VIF=1.0 ($R_i^2 = 0$), it implies that no inter-correlation exists among the descriptors; if 1.0<VIF<5.0, the developed model is acceptable; and if VIF > 10.0, the model is unstable.

The quality of the QSPR model is assessed based on its fitting capability and prediction accuracy; the prediction ability is more important. In order to build the QSPR model, a dataset of CO_2 solubility in 40 ILs which is divided into tow set of training and testing sets, are used. The four selected molecular descriptors from 2000+ descriptors with the corresponding detailed description are illustrated in Table 6-1.

Table 6-1: Selected molecular descriptors and their corresponding description and types.

Ion	Molecular Descriptor	Description	Type	VIF
Anion	Chi_G/D 3D	Randic-like index from distance/distance matrix	Matrix-based descriptors	2.56
Cation	Disps	Displacement value / weighted by I-state	Geometrical descriptors	3.12
Cation	SpMax_RG	Leading eigenvalue from reciprocal squared geometrical matrix	3D matrix-based descriptors	3.67
Anion	HomoLumoFraction	The energy (eV) of the lowest unoccupied molecular orbital calculated using the PM3 Hamiltonian [MOPAC]/ the energy (eV) of the highest occupied molecular orbital calculated using the PM3 Hamiltonian [MOPAC].	Quantum-chemical	2.89

Decision Tree (DT). The DT technique is a non-parametric and nonlinear supervised learning algorithm that can be used in regression and classification problems. The DT divides the original dataset into several sub-groups using particular graphical rules. The tree includes a root node (all data), several internal nodes (subgroups), and some terminal nodes (leaves), as depicted in Figure 6-2 [303]. The root node is where the training set is split into nodes as the first layer of subsets. The internal nodes represent input features and perform a test, leading another layer of internal nodes or terminal leaves. The input variables are divided into branches in a way to minimize the objective function (sum of the squared deviations from the mean in the separate parts). The branch represents a decision rule of a tree. The leaf nodes signify the outcomes that are either a class label in classification trees or the average predicted value of the training data in regression problems. The leaves of the regression trees are called prediction values (y_i) as the local average of output variables that are obtained as follows [318]:

$$\hat{y}_i = \frac{1}{|L_j|} \sum_{(x^i,x^j):x^i \in L_j} y_i \tag{6-3}$$

where $|L_j|$ resembles the number of learning cases that reach the leaf node L_j .

DT regression can be used to estimate objective functions such as solubility of CO_2 in ILs. The regression tree is also being constructed based on the iterative splitting procedure, which is also known as binary recursive subdividing. The dataset is initially divided into two groups of training and testing samples. Then, the training data are used to construct the tree's structure. The splitting procedure continues until each node reaches the defined minimum node size [319]. In other words, DT maps a suitable regression to solubility data by splitting a complex decision (dataset) into several simpler decisions. QSPR model is represented as DTs to solve classification and regression

solubility problems [320]. DTs are applied to create a model, which is able to predict solubility through learning simple decision rules. The rules are obtained from the thermodynamic and structural features of ILs dataset for modeling purposes.
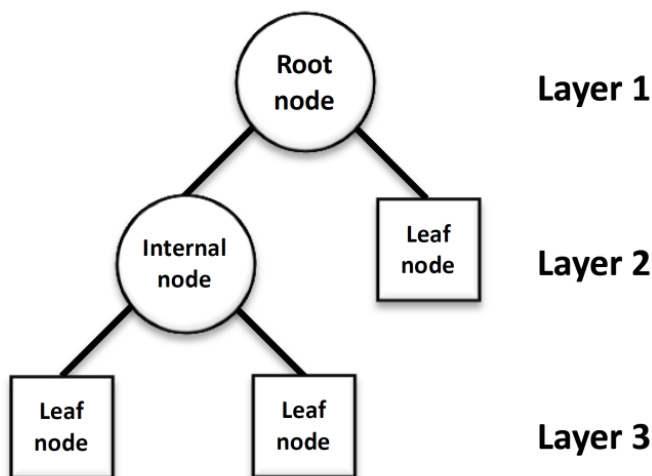
Figure 6-2: A simple structure of the Decision Tree (DT) model.

Random Forest (RF). This is a statistical approach for classification and regression cases [321]. Recent studies have suggested that RF is appealing for developing QSPR models since it is an effective non-parametric statistical technique for the analysis of large databases [297]. RF approach is an ensemble of single DTs built by Classification and Regression Trees (CART) [321]. DTs are an ensemble of hierarchically structured rules (see Figure 6-3). In the RF method, bootstrap samples are generated from the training samples of the original dataset. For each bootstrap, an unpruned regression tree is constructed. In each stage, unlike the decision tree method which selects the best split among all predictors, a random sample of the predictors is created and the best split among these variables is selected. The data, which are not used for the growth of a tree, are known as Out-of-Bag (OOB) sample. The average of predictions of all trees

for their OOB samples provides an estimation on the model's error, variable importance, and OOB validation.

RF utilizes the ensemble of DTs that are trained using random small samples of the dataset. The final output in the RF technique is decided based on averaging the predictions of all trees. Some of the key RF features are their tolerance to noise in experimental data, the reliable procedure for the development of an accurate model, internal predictive ability, and the possibility of analysis of molecules with various mechanisms within one dataset [322]. RF algorithm tries to find common criteria for objects from the same class using the selected descriptors. In this research work, 100 DTs are built with a reduced number of descriptors.

As mentioned earlier, RF is a reliable statistical method, which can be used for both validation and model selection. Although the RF algorithm has not been widely used for QSPR approaches yet, it seems effective to be used in this "structure – aqueous solubility" investigation.
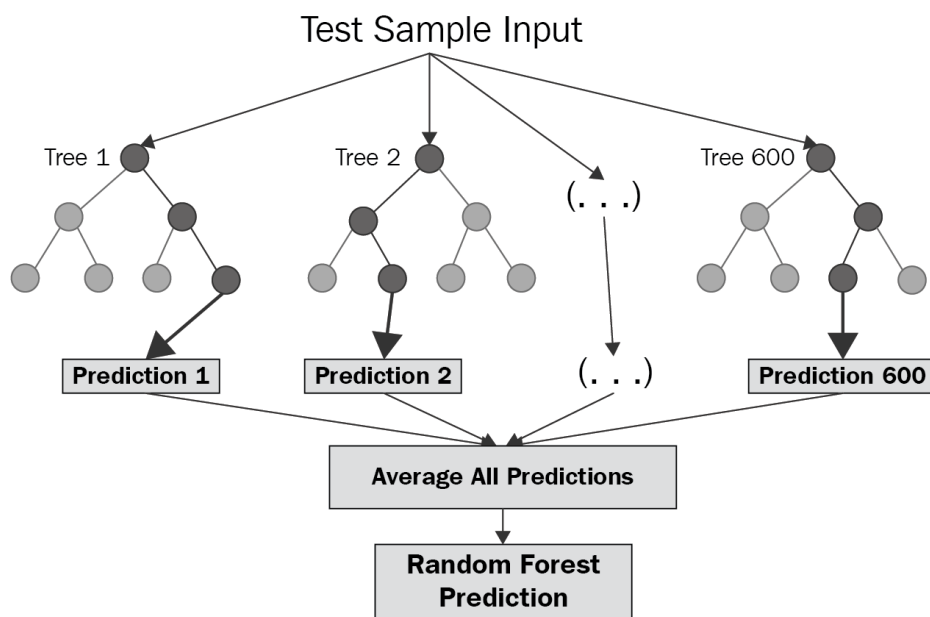
Figure 6-3: A simple schematic of the Random Forest (RF) technique.

Least Squares Support Vector Machine (LSSVM). Support vector machine (SVM) is introduced as an effective non-linear supervised machine learning model for accurate prediction, classification, clustering, and regression analysis [323]. Further theory and background on the SVM can be found in the literature [324, 325]. SVM models have several assets that make them popular, including, stability, robustness, and generality in contact with ANNs [326]. Furthermore, they have generalization ability and superior performance, compared to ANNs, in classification tasks [325]. The modified version of SVM method called least squares SVM (LSSVM) has been introduced by Suykens and Vandewalle, which solves a set of linear equations instead of a set of non-linear equations (quadratic programming) while implementing the LSSVM approach [327, 328]. This method has low computation time and easier to apply for complicated systems.

A regression model for a given set of (x_i, y_i), which x_i is the input vector and y_i introduces the expected outputs, can be used as follows [329]:

$$y = \langle w, \phi(x) \rangle + b \qquad \text{(6-4)}$$

Equation (6-4), w is the weight vector; $\phi(x)$ refers to a nonlinear mapping function, and b represents a bias term. The term $\langle w, \phi(x) \rangle$ introduces the scalar product of w and $\phi(x)$. A least square cost function, Q_{LSSVM}, has been proposed to solve a set of linear equations. The following LSSVM cost function needs to be minimized by considering the equality constraint (Equation (6-6)), as given below [329]:

$$Q_{LSSVM} = \frac{1}{2} w^T w + \gamma \sum_{k=1}^{n} e_k^2 \qquad \text{(6-5)}$$

$$y_i = \langle w, \phi(x) \rangle + b + e_k \qquad \text{(6-6)}$$

where w, γ , and e_k stand for the regression weight, the relative weight of regression errors summation, and error of the regression, respectively; superscript T indicates the transpose matrix; K represents each training data point, and n denotes the number of training data points. The Lagrange function of the LSSVM cost function is expressed below [327]:

$$Q_{LSSVM} = \frac{1}{2}\|w\|^2 + \frac{1}{2}\gamma \sum_{k=1}^{n} e_k^2 - \sum_{k=1}^{n} \alpha_i \left\{ \langle w, \phi(x) \rangle + b + e_k - y_i \right\} \tag{6-7}$$

where α_i s introduce the Lagrange multipliers. The optimal parameters/results are given below [327]:

$$\begin{cases} \dfrac{\partial L_{LSSVM}}{\partial w} = 0 \rightarrow w = \sum_{k=1}^{n} \alpha_k \phi(x_k) \\[2mm] \dfrac{\partial L_{LSSVM}}{\partial b} = 0 \rightarrow w = \sum_{k=1}^{n} \alpha_k = 0 \\[2mm] \dfrac{\partial L_{LSSVM}}{\partial e_k} = 0 \rightarrow \alpha_k = \gamma e_k \\[2mm] \dfrac{\partial L_{LSSVM}}{\partial \alpha_k} = 0 \rightarrow \langle w, \phi(x) \rangle + b + e_k - y = 0 \end{cases} \tag{6-8}$$

By eliminating the variables of w and e_k , the following linear equation is attained:

$$\begin{bmatrix} 0 & 1_N^T \\ 1_N & \Omega + \gamma^{-\frac{1}{N}} \end{bmatrix} \begin{bmatrix} b \\ \alpha \end{bmatrix} = \begin{bmatrix} 0 \\ y \end{bmatrix} \tag{6-9}$$

where $1_N = [1,...,1]$, $\alpha = [\alpha_1,...,\alpha_N]$, $y = [y_1,...,y_N]$, and Ω_{ij} is the Kernel function as defined below [327]:

$$\Omega_{ij} = \Omega(x_i)^T \phi(x_j) = K(x_i, x_j) \qquad \text{For } i \text{ and } j \ 1,2,\ldots,N. \qquad (6\text{-}10)$$

Here, $K(x_i, x_j)$ refers to the Kernel function. Kernel functions using inner products of images of all data pairs in the feature space enable ML operations in multidimensional implicit feature spaces. This eliminates the need to compute the coordinates of the data points in those spaces. In this work, Radial Basis Kernel Function (RBF) is used as a Kernel function in the LSSVM model. The RBF has strong nonlinear mapping ability and wide convergence domain, as shown below [327]:

$$(6\text{-}11)$$
$$K(x_i, x_j) = \exp\left(-\frac{\|x_i - x_j\|^2}{\sigma^2} \right)$$

where σ symbolizes the width of the RBF. The convergence speed is linked to the RBF width σ and regularization parameter (γ). Thus, these two parameters need to be optimized to guarantee good generalization and fast convergence of the model.

Assessment Criteria. To evaluate the performance of each model in predicting the solubility of CO_2 in ILs at various operating conditions, the following statistical parameters are utilized:

$$(6\text{-}12)$$
$$R^2 = 1 - \frac{\sum_{i}^{N}(Calc.(i) - Exp.(i))^2}{\sum_{i}^{N}(Calc.(i) - average(Exp.(i)))^2}$$

$$(6\text{-}13)$$
$$\% AARD = \frac{100}{N} \sum_{i}^{N} \frac{|Calc.(i) - Exp.(i)|}{Exp.(i)}$$

$$Std = \frac{1}{N} \sum_{i}^{N} \sqrt{(Calc.(i) - average(Calc.(i) / Exp.(i)))^2} \qquad (6\text{-}14)$$

$$RMSE = (\frac{\sum_{i}^{N} (Calc.(i) - Exp.(i))^2}{N})^{1/2} \qquad (6\text{-}15)$$

$$ME = \max_{i} |Calc.(i) - Exp.(i)| \qquad (6\text{-}16)$$

where R^2, AARD%, *Std*, *RMSE* and *ME* introduce the coefficient of determination, average absolute relative deviation percent, standard deviation, root mean square error, and maximum error, respectively; *Calc.* and *Exp.* refer to the predicted (calculated) value and the experimental value of the objective function, respectively; and N denotes the number of samples in each category (training and testing).

In both methods, the collected data points are divided into two series: 80% percent for the training phase and the rest for the testing phase. The final output is averaged between four random splitting series of data points using a cross-validation technique.

6.3. Data collection

The accuracy, reliability, and robustness of an ML model strongly depend on the quality of the input dataset [330]. A review of the previous studies on the modeling of solubility of CO_2 in solvents reveals that this parameter is a function of thermodynamics properties and molecular and structural properties of solvents [329-331]. In this study, two datasets of relevant thermodynamics and structural properties are utilized to determine the solubility. The first dataset includes experimental solubility data for a group of 36 ILs with their corresponding critical properties, acentric factors, and molecular weights, as presented in Table 6-2. The second category contains IL/CO_2 solubility data based on cation and anions structural descriptors obtained from the QSPR

model (see Table 6-3). It is confirmed that the collected data are well distributed over various combinations of cations, anions, temperatures, and pressure; thus, they can lead to attaining a reliable generalized model for prediction of CO_2 solubility in ILs.

The structures of cations and anions used in this work are tabulated in Tables A4-1 and A4-2 (in Appendix). The thermodynamic characteristics (e.g., critical properties) and structural properties of the ILs are also provided in Appendix A4.

In the QSPR model, the thermodynamic and transport phenomena behaviors of pure ILs and their mixtures with chemicals are proportional to their molecular descriptors such as constitutional, topological, geometrical, charge, and information indices. To obtain a model based on the QSPR, different types of descriptors are calculated using the optimized structures of ILs. 3D structure of all cations and anions are optimized at the Density Functional Theory (DFT) level using the 6-311G+(d,p) basis set with Gaussian 16 package. After that, the descriptors of the optimized structures are calculated using open-source Dragon software [332] and Mopac software [314]. To quantify the solubility based on these descriptors, the most important and effective descriptors should be selected among a large number of descriptors (nearly 2000 descriptors). First, the descriptors with zero and constant values are eliminated. Using the GA method, the most vital features are chosen.

Table 6-2: Summary of the solubility data (Dataset 1).

No.	Ionic liquid	Temperature range (K)	Pressure range (kPa)	CO_2 solubility range (mole fraction)	No. of data points	Ref.
1	[Bmim][PF$_6$]	283-323	0.01-1300	6.6e-06-0.262	160	[161]
2	[Bmim][PF$_6$]	298-352	590-73500	0.1-0.65	99	[333]
3	[Hmim][PF$_6$]	309-342.8	640-94600	0.098-0.727	90	[169]

4	[Omim][PF$_6$]	293-353.15	10000-20000	0.101-0.402	48	[334]
5	[Bmim][BF$_4$]	283-323	1-1300	4.7e-06-0.243	90	[161]
6	[Hmim][BF$_4$]	293-362	540-86600	0.103-0.703	90	[335]
7	[Omim][BF$_4$]	308.22-357.4	571-85800	0.1-0.75	100	[100]
8	[Bmim][MeSO$_4$]	293-413.1	908-9805		54	[336]
9	[Bmim][MeSO$_4$]	303.18-333.05	49.9-1500	0.005-0.092	28	[337]
10	[Bmim][Ac]	303.15-343.15	112-3708.2	0.194-0.4098	27	[338]
11	[Bmim][TFA]	293-363	979-56900	0.3-0.679	46	[339]
12	[Bmim][TfO]	303-344	850-14700	0.218-0.576	49	[175]
13	[Bmim][DCA]	303-373	820-28100	0.174-0.514	56	[340]
14	[Bmim][SCN]	303-373	8600-95500	0.422-0.514	48	[340]
15	[Emim][NTf$_2$]	312-450.5	2743-11520	0.212-0.519	98	[341]
16	[Emim][TfO]	302-344	800-16500	0.179-0.543	37	[175]
17	[Emim][TfO]	303-343.2	180-5884	0.102-0.965	30	[342]
18	[Hmim][FAP]	298-333.13	0.826-1300	0.00023-0.243		[202]
19	[N$_{4,1,1,1}$][NTf$_2$]	303-342	100-14550	0.0776-0.6711	50	[343]
20	[P$_{6,6,6,14}$][NTf$_2$]					[114]
21	[THTDP][NTf$_2$]	293-361	106-72180	0.169-0.879	120	[114]
22	[THTDP][Cl]	303-363	168-24570	0.119-0.8	69	[114]
23	[P$_{6,6,6,14}$][Cl]					[114]
24	[P$_{6,6,6,14}$][dc]	298-363	304-13400	0.111-0.758	56	[344]
25	[P$_{6,6,6,14}$] [TMPP]	298-363	163-14000	0.15-0.815	46	[344]
26	[P$_{6,6,6,14}$][MeSO$_4$]	307-322	4480-8730		28	[345]
27	[P$_{6,6,6,14}$][FAP]	303-343	67.8-78.8	0.0266-0.0355-	15	[346]
28	[N-BuPy][BF$_4$]	313-333	1550-9580	0.144-0.549		[76]
29	[MeBuPyrr][DCA]	303-343	420-14800	0.109-0.564	47	[347]
30	[bmpyr] [Tf$_2$N]	303-343	390-20400	0.1423-0.744	50	[347]
31	[TBP][FOR]	298	10-999	0.008-0.203	9	[5]

32	[BmPyrr][FEP]	303-343	63-74	0.0163-0.0246	15	[346]
33	[Hmpy] [Nf$_2$T]	298				[116]
34	HEF	313-333	1850-4550	0.086-0.308		[348]
35	HEA	313-333	8030-10980	0.0918-0.409		
36	HEL	313-333	2520-5710	0.0584-0.242		
37	THEAA	313-333	2400-2050	0.0614-0.256		
38	THEAL	313-333	1840-8470	0.0835-0.4032		
39	HEAF	313-333	2100-8520	0.0863-0.1348		
40	HEAA	313-333	1500-3470	0.166-0.239		
41	HEAL	313-333	2510-5370	0.131-0.486		
42	[bheaa]	298-328				[349]
43	[hhemea]	298-328				
44	[bheal]	298-328				[349]
45	[hhemel]	298-328				[349]
46	[TMG][La]	289-333				[51]

Table 6-3: Summary of the solubility data (Dataset 2).

IL	Abbreviation	Ref.
Tributylmethylammonium bis((trifluoromethyl)sulfonyl)imide	[N$_{4,4,4,1}$][Nf$_2$T]	[161]
Butyltrimethylammonium bis(trifluoromethylsulfonyl)imide	[N$_{1,1,1,4}$][Nf$_2$T]	[343]
ethylammonium nitrate	[EA][NO$_3$]	[350]
Choline bis(trifluoromethylsulfonyl)imide	[C$_5$H$_{14}$NO][Nf$_2$T]	[202]
N-ethyl-N,N-dimethyl-1-propanaminium 1,1,1-trifluoro-N [(trifluoromethyl)sulfonyl]methanesulfonamide	[N$_{2,1,1,3}$][Nf$_2$T]	[351]
2-hydroxyethylammonium lactate	[hea][La]	[349]
methyltrioctylammonium 1,1,1-trifluoro-N-[(trifluoromethyl)sulfonyl]methanesulfonamide	[N$_{8,8,8,1}$][Tf$_2$N]	[343]

N,N-dimethyl-N-ethyl-N-pentylammonium bis(trifluoromethylsulfonyl)	$[N_{1,1,2,5}][Tf_2N]$	[352]
trihexyl(tetradecyl)phosphonium bis[(trifluoromethyl)sulfonyl]imide	$[P_{6,6,6,14}][Nf_2T]$	[114]
Trihexyl(tetradecyl)phosphonium chloride	$[P_{6,6,6,14}][Cl]$	[114]
Tetradecyl(trihexyl)phosphonium dicyanamide	$[P_{6,6,6,14}][SCN]$	[344]
Tributylmethylphosphonium bis[(trifluoromethyl)sulfonyl]imide	$[P_{4,4,4,1}][Nf_2T]$	[353]
1,1,3,3-tetramethylguanidinium lactate	[Gau][La]	[354]
1-butyl-1-methylpyrrolidinium tricyanomethanide	[BMpyrrol][TCM]	[355]
1-(methoxymethyl)-1-methylpyrrolidinium bis(fluorosulfonyl)amide	[Metomepyrrol][FSA]	[356]
1-methyl-1-propylpiperidinium bis(fluorosulfonyl)imide	[Meprpip][FSA]	[357]
1-butyl-4-methylpyridinium tricyanomethanide	[Bumepyr]][TCM]	[355]
N-benzylpyridinium bis(trifluoromethylsulfonyl)amide	$[Benzpyr][Nf_2T]$	[358]
3-methyl-1-propylpyridinium bis(trifluoromethylsulfonyl)imide	$[Meproppyr][Nf_2T]$	[359]
1-(2-hydroxyethyl)-pyridinium bis(trifluoromethylsulfonyl)imide	$[Hydethpyr][Nf_2T]$	[360]
1-(2-(2-(2-methoxyethoxy)ethoxy)ethyl)pyridinium bis(trifluoromethylsulfonyl)amide	$[Methethpyr][Nf_2T]$	[361]
1-ethyl-3-methylimidazolium acetate	[Emim][Ace]	[362]
1-ethyl-3-methylimidazolium bis[(trifluoromethyl)sulfonyl]imide	$[Emim][Nf_2T]$	[341]
1-ethyl-3-methyl-1H-imidazolium tricyanomethanide	[Emim][TCM]	[171]
1-ethyl-3-methylimidazolium ethyl sulfate	$[Emim][EtSO_3]$	[362]
1-ethyl-3-methylimidazolium tris(pentafluoroethyl)trifluorophosphate	[Emim][FAP]	[363]
1-ethyl-3-methylimidazolium dicyanamide	[Emim][diSCN]	[364]
1-ethyl-3-methylimidazolium thiocyanate	[Emim][tiSCN]	

1-ethyl-3-methylimidazolium trifluoromethanesulfonate	[Emim][TFO]	[175]
1-ethyl-3-methylimidazolium lactate	[emim][La]	[359]
1-ethyl-3-methylimidazolium tetrafluoroborate	[Emim][BF$_4$]	[365]
1-ethyl-3-methylimidazolium tetracyanoborate	[Emim][tcb]	[352]
3-hexyl-1-methylimidazolium tricyanomethanide	[Hmim][trSCN]	
1-hexyl-3-methylimidazolium bis[(trifluoromethyl)sulfonyl]imide	[Hmim][Nf$_2$T]	[366]
1-hexyl-3-methylimidazolium nitrate	[Hmim][NO$_3$]	[367]
1-hexyl-3-methylimidazolium tris(heptafluoropropyl)trifluorophosphate	[Hmim][FAP]	[202]
1-hexyl-3-methylimidazolium hexafluorophosphate	[Hmim][PF$_6$]	[200]
1-methyl-3-octylimidazolium tricyanomethanide	[Omim][tricynme]	[171]
1-octyl-3-methylimidazolium bis[(trifluoromethyl)sulfonyl]imide	[Omim][Nf$_2$T]	[368]
1-octyl-3-methylimidazolium hexafluorophosphate	[Omim][PF$_6$]	[368]

6.4. Results and discussions

Four models are developed in this study to estimate the solubility of CO_2 in various ILs using critical properties and the QSPR model. In this section, the modeling results and discussions are divided into two main parts: development of predictive models for solubility based on dataset 1 with thermodynamic variables (molecular weight, critical properties, and acentric factor) and introduction of models using dataset 2 with molecular structural variables or descriptors such as geometrical, topological, information indices, 3D matrix-based descriptors, and quantum chemical characteristics.

Performance Evaluation of Thermodynamic-Based Models. According to dataset 1, the solubility of CO_2 in ILs is determined where the temperature (*T*), pressure (*P*), critical temperature

(*Tc*), critical pressure (*Pc*), acentric factor (ω), and molecular weight (Mw) are the input parameters. The accuracy of predictions obtained from various models including DT, RF, LSSVM, and MLR is compared in Table 6-4 and Figure 6-4. In this work, the statistical parameters including coefficient of determination (R^2), average absolute relative deviation (AARD), maximum error (ME) and average relative deviation (ARD) are utilized for reliability and accuracy assessment of the models. The optimal model is determined based on statistical analysis. It should be noted that the fitted model can perform differently in various ranges of the data points. Cross-validation strategies can help to visually explore the model performance variations. For dataset 1, the RF and DT algorithms yield better predictive performance with having an R^2 of 0.96 and 0.94, respectively. The lowest predictive performance based on the comparison of experimental data and predictions is attained for the MLR method with an R^2 of 0.55, indicating that CO_2 solubility does not have a linear relationship with thermodynamic properties. A similar conclusion can be made by comparing the AARD% and ARD% of the deterministic tools. The error values of all models confirm a higher accuracy and robustness of the RF model in comparison with LSSVM, MLR, and DT techniques. To further evaluate the accuracy of the studied models in both training and testing phases, the relative error, which is the difference between the predictions and the corresponding experimental solubility values, is also obtained by the following equation:

$$Relative\_Error = \frac{X_i - (X_p)_i}{X_i} \qquad (6\text{-}16)$$

The relative error value can be positive or negative, indicating underestimation or overestimation of the model with respect to the real data. Figure 6-5 shows the relative error versus the data index.

Four-fold cross-validation is applied for each algorithm to model the internal validation. The values reported in the cross-section column of Table 6-4 reflect the average accuracy of each fold.

As expected, RF and DT algorithms have a better performance in predicting the experimental data in different folds of a dataset with cross-validation scores of 0.76 and 0.70, respectively. According to Figure 6-4 and 6-5, it can be concluded that the predicted values obtained from DT and RF models are in good agreement with experimental data. However, other ML algorithms generally fail to estimate the CO_2 solubility with acceptable precision.

Table 6-4: Statistical parameters of models developed based on thermodynamic variables using dataset 1.

Model		Statistical Parameters				
		R^2	AARD%	ARD%	ME	Cross-Validation Score with CV=4
DT	Training	0.965	2.85	1.97e-16	0.17	
	Testing	0.94	21.24	11.42	0.22	0.70
RF	Training	0.988	4.72	0.72	0.18	
	Testing	0.96	12.05	2.12	0.21	0.76
LSSVM	Training	0.72	29.73	10.08	0.36	
	Testing	0.75	31.01	11.54	0.36	0.56
MLR	Training	0.42	42.42	2.91	0.31	
	Testing	0.55	40.48	8.54	0.31	0.21

(a)

DT (Training)
$R^2 = 0.9428$
Predicted X_{CO2}
Experimental X_{CO2}

(b)

DT (Testing)
$R^2 = 0.9883$
Predicted X_{CO2}
Experimental X_{CO2}
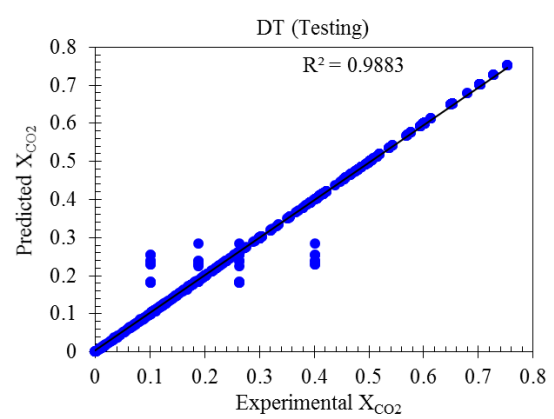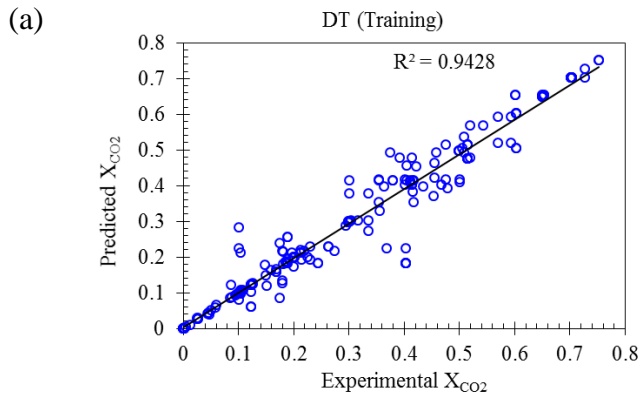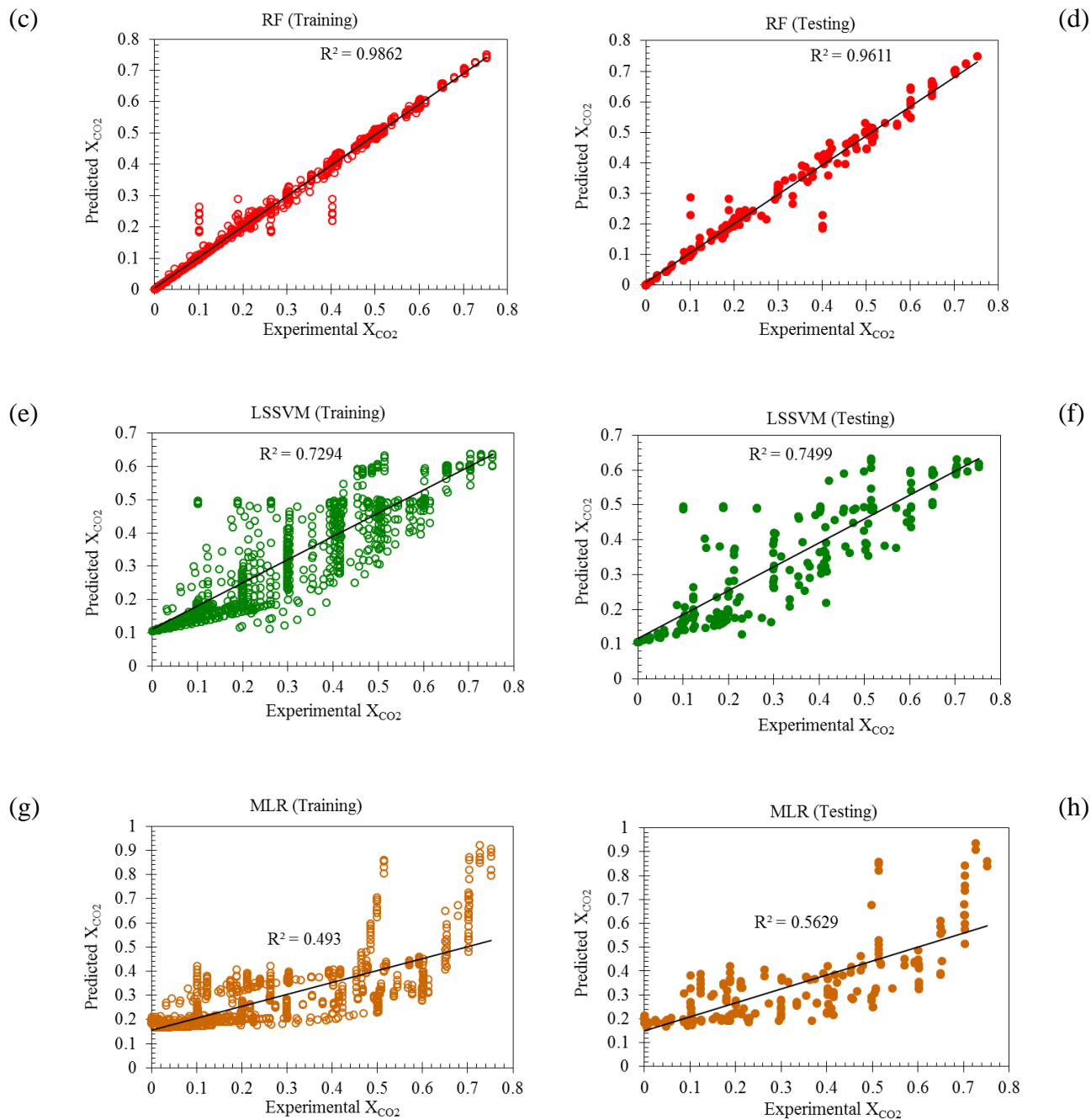
Figure 6-4: Cross plot of the model outputs versus corresponding experimental values of CO_2 solubility in ILs with thermodynamic features using DT (panels a and b), RF (Panels c and d), LSSVM (panels e and f), and MLR (panels g and f).
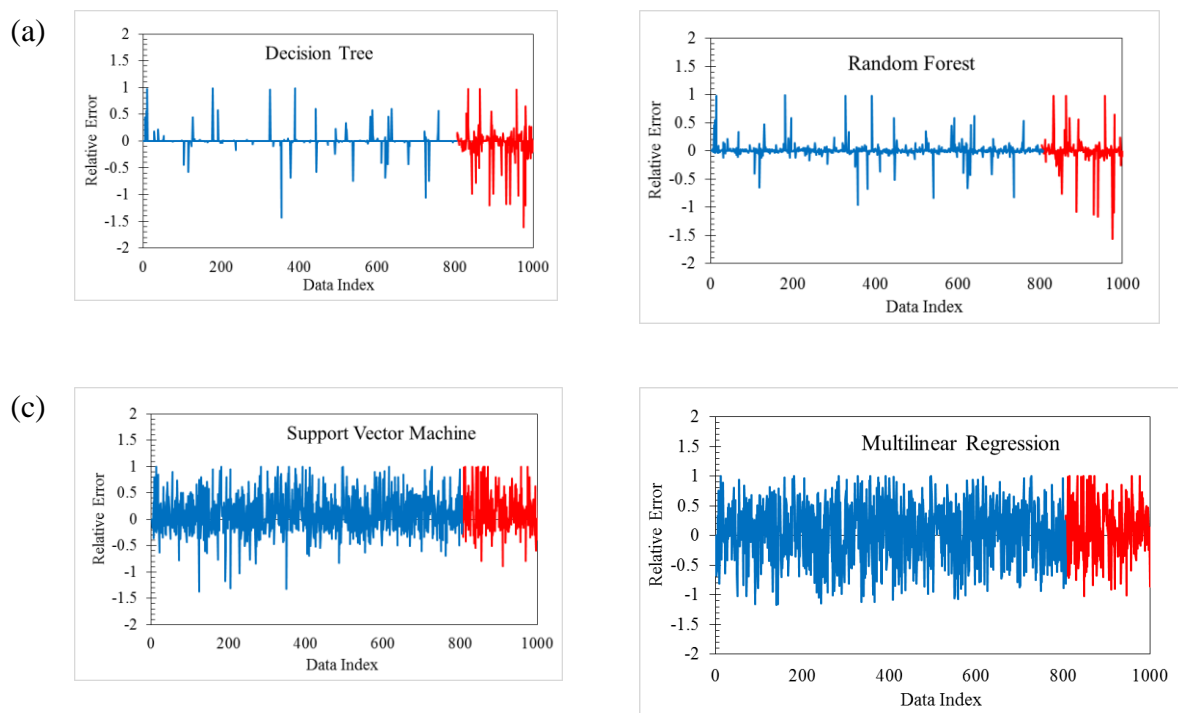
Figure 6-5: Relative error versus data index for introduced models: (a) DT, (b) RF, (c) LSSVM (d) MLR [The blue points represent the training data and the red points show the testing data].

Performance Evaluation of Deterministic Tools Based on the QSPR Model. For the second data series, four models (e.g., DT, RF, LSSVM, and MLR) are also developed for prediction of CO_2 solubility using the structural properties attained from descriptors of ILs, including Chi_G/D 3D, Disps, SpMax_RG, and HomoLumoFraction, as well as temperature and pressure, as input variables. In dataset 2, more than 2000 experimental solubility data are included. Table 6-5 lists the magnitudes of statistical quality measures for all models used for prediction purposes. The regression plots for training and testing phases of introduced predictive tools are depicted in Figure 6-6. According to the attained results, AARD% values of the testing phase are 20.26, 12.36, 44, 64, and 55.36 for the DT, RF, LSSVM, and MLR methods, respectively. Similar to the first dataset, developed DT and RF models exhibit a better (or stronger) correlation between the predicted and target values, compared to the LSSVM and MLR approaches. Relative errors of both training and

235

testing steps of all introduced models are shown in Figure 6-7. Although the DT model leads to having a higher error for a few data points, the overall predictive performance of the DT model is acceptable, showing low relative errors as well as a good match between the real data and modeling results. However, the LSSVM and LMR models result in higher relative errors for a high number of data points, compared to the DT and RF techniques.

Comparing the performance of deterministic tools based on dataset 1 and dataset 2, a small improvement in the accuracy of all models except MLR is noticed for the second dataset. This implies that molecular descriptors such as Chi_G/D 3D, Disps, SpMax_RG, and HomoLumoFraction appear to be better features for prediction of the CO_2 solubility in ILs, compared to thermodynamic properties of ILs.

Table 6-5: Statistical analysis to evaluate the performance of predictive models based on dataset 2.

Model		Statistical Parameters				
		R^2	AARD%	ARD%	ME	Cross-Validation Score with CV=4
DT	Training	0.999	0.53	0.143	0.003	0.77
	Testing	0.96	20.26	6.52	0.2	
RF	Training	0.99	5.89	1.91	0.15	0.83
	Testing	0.98	12.36	0.65	0.21	
LSSVM	Training	0.71	42.61	14.32	0.41	0.60
	Testing	0.76	44.64	13.48	0.46	
MLR	Training	0.24	55.65	3.39	0.52	0.15
	Testing	0.28	55.36	4.68	0.59	

(a) DT (Training) — $R^2 = 1$

(b) DT (Testing) — $R^2 = 0.9584$

(c) RF (Training) — $R^2 = 0.9967$

(d) RF (Testing) — $R^2 = 0.9828$

(e) LSSVM (Training) — $R^2 = 0.6983$

(f) LSSVM (Testing) — $R^2 = 0.6976$

(g)

MLR (Training)

$R^2 = 0.2344$

(h)

MLR (Testing)

$R^2 = 0.2693$
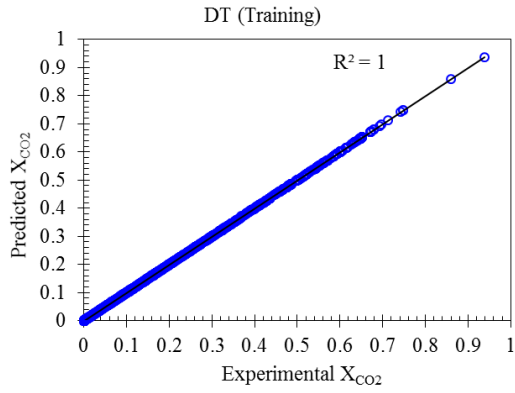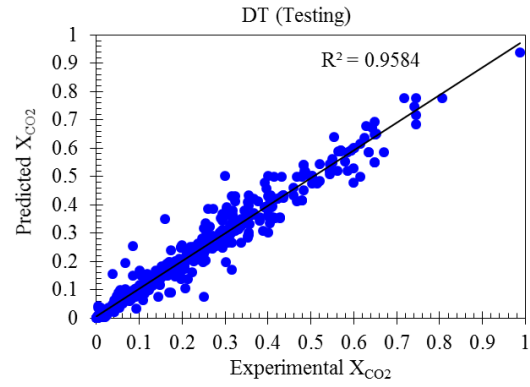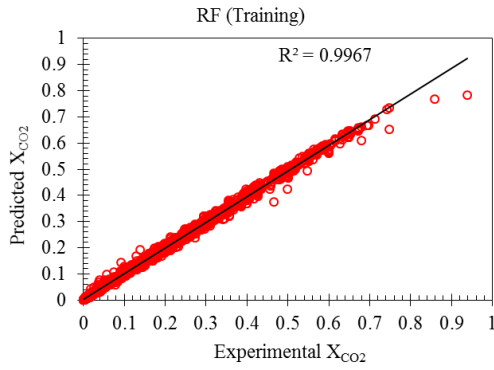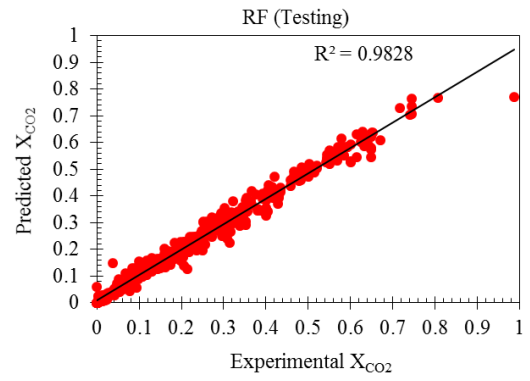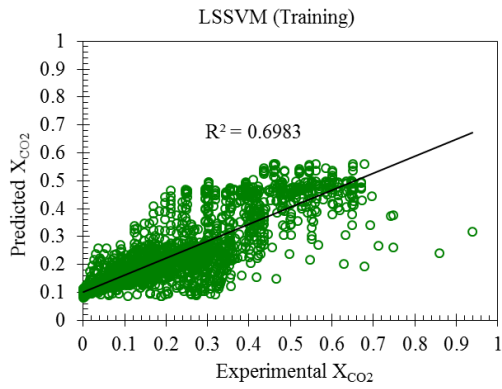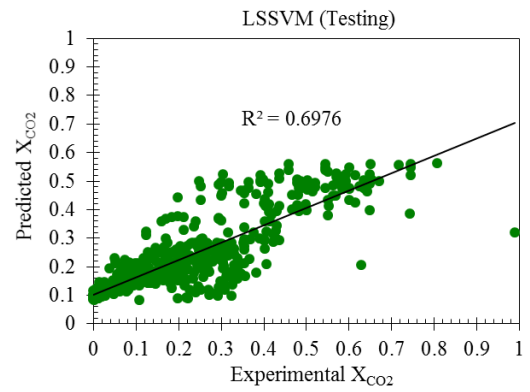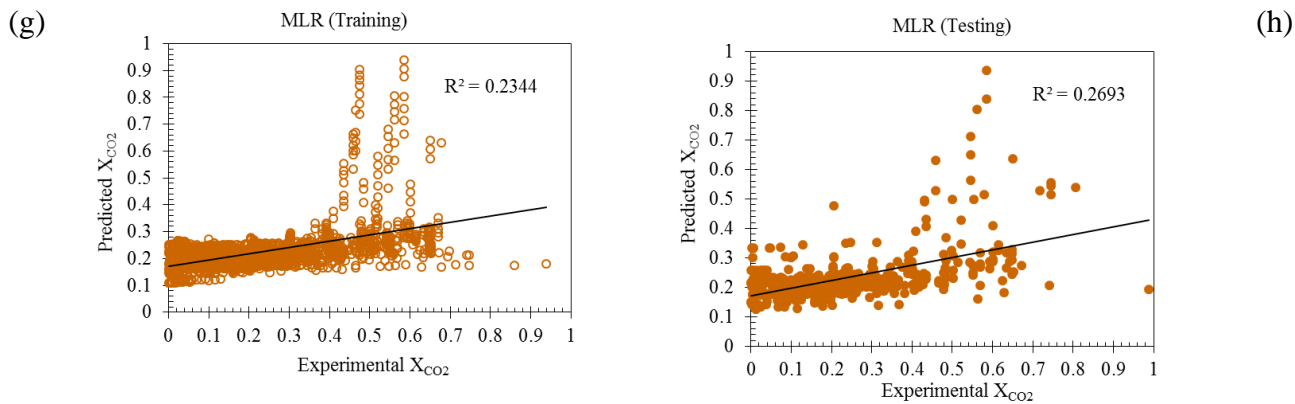
Figure 6-6: Estimated versus experimental CO_2 solubility in ILs based on the QSPR approach using DT (panels a and b), RF (panels c and d), LSSVM (panels e and f), and MLR (panels g and h).

(a)

DT

(b)

RF

(c)

SVM

(d)

MLR
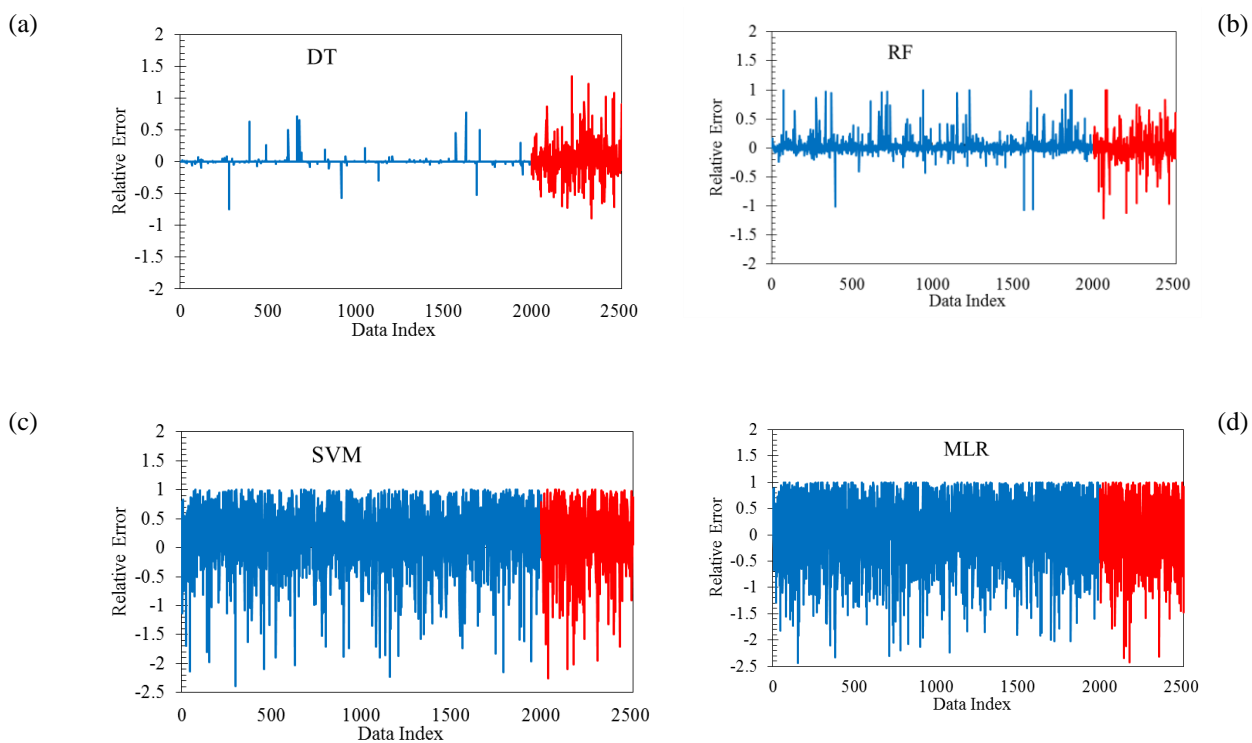
Figure 6-7: Relative error values for both training and testing phases while using (a) DT, (b) RF, (c) LSSVM, and (d) MLR.

Sensitivity Analysis. The solubility of CO_2 in the IL of 1-ethyl-3-methyl-1H-imidazolium tricyanomethanide is determined at four constant pressures (see Figure 6-8). We also obtain this parameter for three ILs including 1-ethyl-3-methylimidazolium dicyanamidetemperature, 1-ethyl-3-methylimidazolium tetracyanoborate, and 1-butyl-3-methylimidazolium bis(trifluoromethylsulfonyl)imide at a constant temperature of 298 K, as reported in Figure 6-9. It should be noted that the most accurate model (e.g., DT) is selected to show the variations of solubility with temperature and pressure based on the model predictions and also to compare the modeling and experimental values. As depicted in Figure 6-8 and Figure 6-9, the mole fraction of CO_2 in the solvent increases with an increase in pressure. However, the solubility lowers if the temperature is decreased (see Figure 6-8). These results are in agreement with the theory on the variations of solubility with temperature and pressure. It is also concluded from Figure 6-8 and Figure 6-9 that the DT model can simulate the experimental data precisely so that there is no considerable error based on the comparison of estimated and real solubility values.
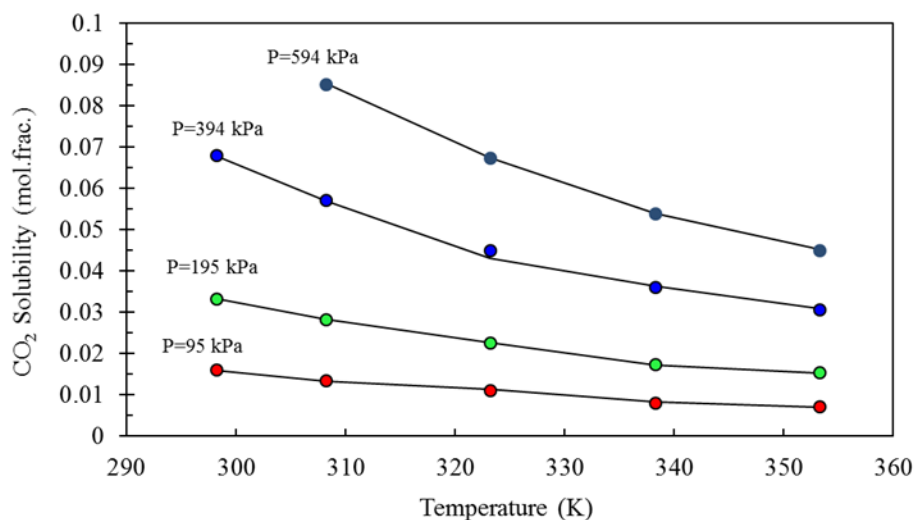
Figure 6-8: Influence of temperature and pressure on CO_2 solubility in 1-ethyl-3-methyl-1H-imidazolium tricyanomethanide [emim][C_4N_3] [The symbols show the experimental data and the solid lines represent the DT modeling results].
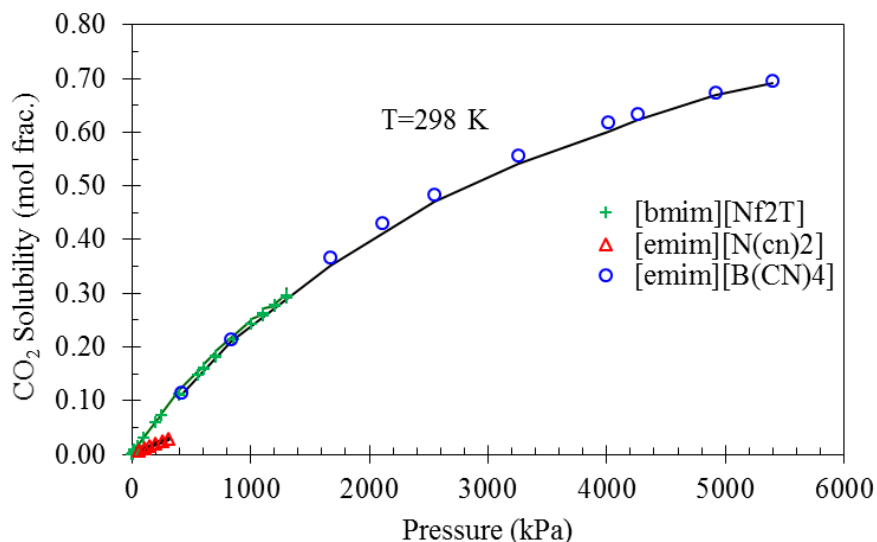
Figure 6-9: CO_2 solubility versus pressure at a temperature of 298 K for three ILs such as 1-ethyl-3-methylimidazolium dicyanamide [emim][N(cn)$_2$], 1-ethyl-3-methylimidazolium tetracyanoborate [emim][B(CN)$_4$], and 1-butyl-3-methylimidazolium bis(trifluoromethylsulfonyl)imide [bmim][Nf$_2$T] [The symbols represent the experimental data points and the solid lines indicate the DT predictions].

Feature Selection in QSPR Model. In the ML models, feature selection is an important aspect, which helps to identify the features/parameters mostly contributing to the objective function(s). After specifying the most vital input parameters, the partially relevant or entirely irrelevant features can be removed to avoid overfitting, lower the computational costs, and improve the accuracy of the model and its applicability.

In QSPR modeling, four important descriptors are selected from 2000+ descriptors of ILs using the GA-MLR method. The Extra Trees feature selection method is employed to rank the input parameters based on their influence on the CO_2 solubility in ILs. In Extra Trees classifier each decision stump built with all the data available in the training set. Splits of each node is determined randomly by searching in a subset of randomly selected features with a size of sqrt(number of features). Thus, by pruning trees below a particular node, a subset of the most important features

will be created. The results of feature ranking are presented in Figure 6-10 and 6-11 for data series 1 and 2, respectively. According to Figure 6-10, pressure has the highest contribution to the solubility of CO_2 in ILs with %81 relative importance, followed by temperature with a relative importance of about 10%; the remaining four features (critical temperature, critical pressure, molecular weight, and acentric factor) have a considerably smaller relative importance. It can be also concluded from Figure 6-11 that the ranking order of the input parameters/properties are pressure, temperature, HomoLumoFraction (anion), SpMax_RG (cation), and Disps (cation), from the highest to the minimum relative importance. Thus, Homo/Lumo fraction has the most impact on the solubility based on the DT and RF models, if the temperature and pressure remain unchanged.

The feature reduction is useful while predicting compounds' characteristics, particularly if an adequate number of thermodynamics properties are not available. In addition, a model with a large number of descriptors might not be appropriate to be used for theoretical and practical implications. Thus, identification of important features from thousands of descriptors for a particular process or phenomenon can be useful in various stages such as design, operation, and optimization of the process. For instance, it is important to recognize the important features of ILs and consider them in designing suitable cations and anions for the synthesis of ILs with effective properties for CO_2 absorption.

ML models provide a fast screening technique to study the significant properties of solvents. The developed models in this work, can help researchers to estimate the CO_2 solubility in ILs based on structural and thermodynamic properties of pure ILs. This work may offer useful information/data on designing technically effective and environmentally safe ILs for CO_2 capture systems.
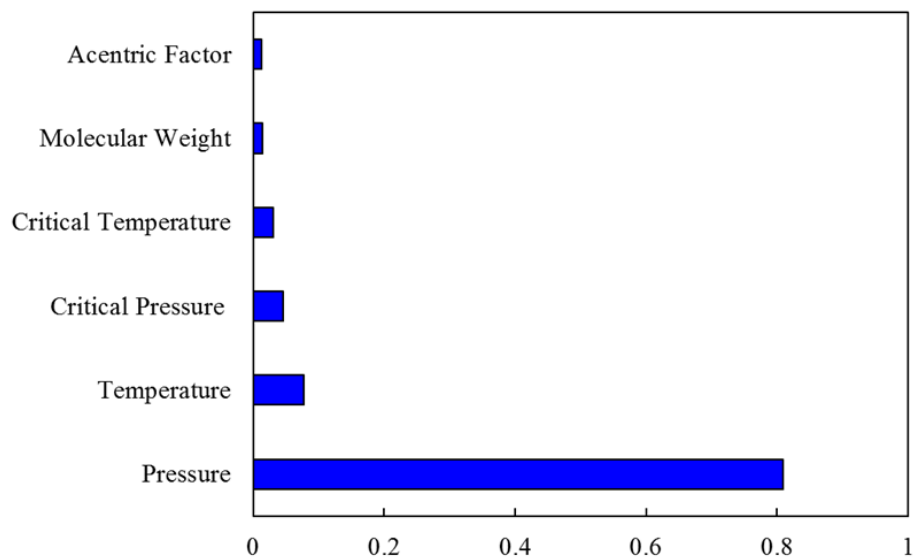
Figure 6-10: Feature importance of input parameters involved in the predictive model based on dataset 1.
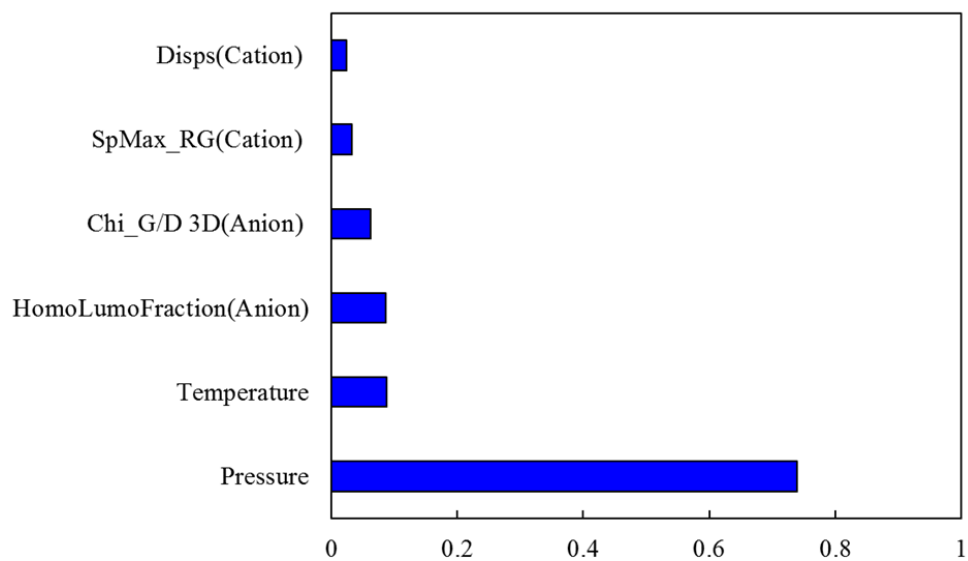
Figure 6-11: The relative importance of structural properties and operating conditions based on dataset 2 for estimation of CO_2 solubility in ILs.

6.5. Summary and conclusions

In this study, four models, namely Decision Tree (DT), Least Square Support Vector Machine (LSSVM), Random Forest (RF), and Multilinear Regression (MLR), are developed for the estimation of the solubility of CO_2 in various Ionic Liquids (ILs) at a wide range of operating conditions where the thermodynamic and structural properties of ILs are considered as the input parameters. Two large datasets are used for development of the predictive tools. In the first data bank, in addition to temperature and pressure, the critical properties such as critical temperature, critical pressure, molecular weight, and acentric factor of ILs are the input variables. The models developed on the basis of the Quantitative Structure–Activity Relationship (QSPR) model include the structural characteristics (e.g., Chi_G/D 3D, Disps, SpMax_RG, and HomoLumoFraction), which are selected among a large number of descriptors, and process conditions (temperature and pressure) while using dataset 2. The predictive performance of all introduced models is assessed through conducting an error analysis where the statistical parameters such as coefficient of determination (R^2), average absolute relative deviation (AARD), and average relative deviation (ARD) are obtained. Based on the study results, the following conclusions can be drawn:

- For both datasets, the DT and RF models show greater performance (in terms of accuracy and reliability) in predicting CO_2 solubility in ILs, compared to the LSSVM and MLR approaches.

- The errors resulted from QSPR-based models are slightly lower than the thermodynamic-based models. This might be due to the strong relationship between ILs structural properties and CO_2 solubility in ILs. Hence, the models developed based on dataset 2 is more reliable and accurate (compared to the models obtained from dataset 1), since the ILs
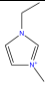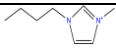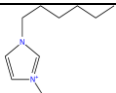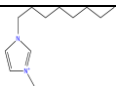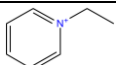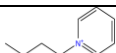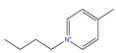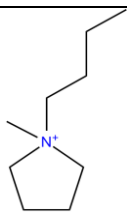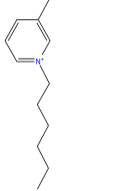
descriptors in the QSPR model generally take into account the key geometrical, structural, charge, and quantum chemical characteristics of ILs.
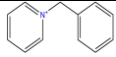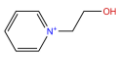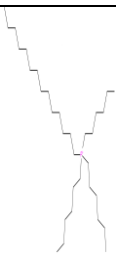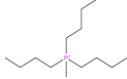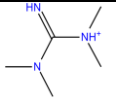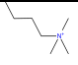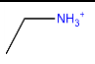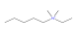
- The RF model is capable of forecasting the solubility of CO_2 in ILs with an average absolute relative deviation of 12.05 and 12.36 with respect to the experimental data for datasets 1 and 2, respectively. It is found that there is a non-linear relationship between molecular descriptors and CO_2 solubility in ILs.

- The DT and RF models developed based on the QSPR model provide the key insights into the structural properties. The sensitivity analysis reveals that pressure has the highest impact on CO_2 solubility in ILs. The important structural characteristics affecting the solubility of CO_2 in ILs are relevant to the structure of ions, 3D matrix of ions, orbital energy, and the complexity and polarity of the molecules.

- It is recommended to collect more experimental data for a variety of IL cases under broad thermodynamic conditions and physical (and chemical) properties. This can lead to more generalized predictive tools for the determination of CO_2 solubility in ILs. It might be also useful to develop more connectionist models with optimal parameters and screen the most deterministic tools for prediction and classification purposes. Such a strategy can result in designing and finding suitable ILs for carbon capture.

Appendix A4

The cation structures of ILs investigated in this study are given in Table A4-1.

Table A4-1: Structures of cations for ILs studied in this work.

Cation	Name	Smiles	Structure
Emim	1-ethyl-3-methylimidazolium		
Bmim	1-Butyl-3 methylimidazolium	CCCCN1C=C[N+](C)=C1	
Hmim	3-hexyl-1-methylimidazolium		
Omim	1-octyl-3-methylimidazolium		
Epyr	1-ethylpyridinium		
N-Bpyr	1-Butylpyridinium	CCCC[N+]1=CC=CC=C1	
Bu-Mepyr	1-butyl-4-methylpyridinium		
MeBuPyr r	1-Butyl-1-methylpyrrolidinium	CCCC[N+]1(C)CCCC1	
HMePyr	1-hexyl-3-methylpyridinium		

benzylpyr	N-benzylpyridinium		
	1-(2-hydroxyethyl)-pyridinium		
	1-(2-(2-(2-methoxyethoxy)ethoxy)ethyl)pyridinium		
P6,6,6,14	trihexyl(tetradecyl)phosphonium	CCCCCCCCCCCCCC[P+](CCCCCC)(CCCCCC)CCCCCC	
	Tributylmethylphosphonium		
TMG	1,1,3,3-Tetramethylguanidinium	CN\C(=N\C)N(C)C	
	Octyl trimethyl ammonium		
	methyltrioctylammonium		
	butyltrimethylammonium		
	ethyl ammonium		
	N,N-dimethyl-N-ethyl-N-pentylammonium		
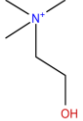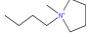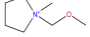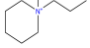
2-(2-Hydroxyethoxy)ethylammonium	[NH3+]CCOCCO	
trimethyl-butylammonium	CCCC[N+](C)(C)C	
Choline	(2-hydroxyethyl)trimethylammonium	
1-butyl-1-methylpyrrolidinium		
1-(methoxymethyl)-1-methylpyrrolidinium		
1-methyl-1-propylpiperidinium		

Table A4-2 also provides the anion structures of ILs studied in this research.

Table A4-2: Structures of the anions studied in this work.

Anion		Structure
PF$_6$		
Nf$_2$T	bis[(trifluoromethyl)sulfonyl]imide	
Tricyanomethanide	TCM	
BF$_4$	tetrafluoroborate	
DCA	dicyanamide	
MeSO$_3$	methyl sulfate	
Trifluoromethanesulfonate	OTf	

Chloride	Cl	Cl^-
Thiocyanate	SCN	$^-S-C\equiv N$
methanesulfonate	OMS	
TFA	trifluroacetate	
Acetate	Ace	
Tetrachloroferrate	FeCl4	
Nitrate	NO3	

Tris(pentafluoroethyl)trifluorophosphate	FAP	

Propanoate	Prop	

2,2-dimethylpropanoate	Pivalate	

Table A6-3 lists the critical properties, molecular weight, and acentric factor of the ILs used in this research. The structural characteristics of employed ILs are also given in Table A6-4.

Table A4-3: Critical properties, acentric factors, and molecular weights of ILs investigated in this work [2].

Ionic liquid	global	M	Tb (K)	Tc (K)	Pc (bar)	ω
[bmim][PF$_6$]	C8H15N2PF6	284.2	554.6	719.4	17.3	0.7917
[hmim][PF$_6$]	C10H19N2PF6	312.2	600.3	764.9	15.5	0.8697
[omim][PF$_6$]	C12H23N2PF6	340.3	646.1	810.8	14	0.9385

[bmim][BF₄]	C8H15N2BF4	226	495.2	643.2	20.4	0.8877
[hmim][BF₄]	C10H19N2BF4	254.1	541	690	17.9	0.9625
[omim][BF₄]	C12H23N2BF4	282.1	586.7	737	16	1.0287
[bmim][MeSO₄]	C9H18N2SO4	250.3	735.6	1081.6	36.1	0.4111
[bmim][Ac]	C10H18N2O2	198.3	624.6	847.3	24.5	0.6681
[bmim][ta]	C10H15N2F3O2	252.2	619.2	826.8	20.9	0.6891
[bmim][TfO]	C9H15N2F3SO3	288.3	707.7	1023.5	29.5	0.4046
[bmim][dca]	C10H15N5	205.3	783	1035.8	24.4	0.8419
[bmim][tca]	C9H15N3S	197.3	763.1	1047.4	19.4	0.4781
[bmim][Nf₂T]	C10H15N3F6S2O4	419.4	862.4	1269.9	27.6	0.3004
[emim][TfO]	C7H11N2F3SO3	260.2	662	992.3	35.8	0.3255
[Emim][eFAP]		556..2	760.5	830.67	100.3	0.8743
[Hmim][FAP]		612.28		847.9	13.93	
[NHHH,(CH2)₂OH][Ac]	C4H11NO3	121.1	514.8	699.2	41.39	0.9359
[NHHH,(CH2)₂OH][La]	C5H13NO4	151.2	629.4	812.6	39.38	1.3579
[N₁₄₄₄][Nf₂T]	C15H30N2F6S2O4	480.5	852.7	1136.3	17.7	0.6068
[P₆,₆,₆,₁₄][Nf2T]	C34H68NF6PS2O4	764	1310.6	1586.7	8.5	0.8915
[P₆,₆,₆,₁₄][Cl]	C32H68PCl	519.3	1006.2	1222.8	7.9	0.7947

[bpy][BF$_4$]	C9H14NBF4	223	456.9	597.6	20.3	0.8307
[mbpyr][dca]	C11H20N4	208.3	680.3	887.2	20.6	0.8555
[bmpyr][Nf$_2$T]	C11H20N2F6S2O4	422.4	759.8	1093.1	24.3	0.3467
[TBP][FOR]	303.44		933.6	18.3		
[hmim][BF$_4$]	C10H19N2BF4	254.1	541	690	17.9	0.9625
[omim][BF$_4$]	C12H23N2BF4	282.1	586.7	737	16	1.0287
[bmim][MSO$_4$]	C9H18N2SO4	250.3	735.6	1081.6	36.1	0.4111
[bmim][Ac]	C10H18N2O2	198.3	624.6	847.3	24.5	0.6681
[bmim][ta]	C10H15N2F3O2	252.2	619.2	826.8	20.9	0.6891
[bmim][TfO]	C9H15N2F3SO3	288.3	707.7	1023.5	29.5	0.4046

Table A4-4: Structural properties of compounds used in the QSPR model.

Name	DISPs+	SpMax_RG+	Chi_G/D-	HomoLumoFraction-
tributylmethylammonium bis(trifluoromethylsulfonyl)imide	0.016	4.61	0.834	1.79
butyltrimethylammonium bis(trifluoromethylsulfonyl)imide	0.041	3.94	0.834	1.79
ethylammonium nitrate	0.221	2.8	0.918	1.08
Choline bis(trifluoromethylsulfonyl)imide	0.347	3.71	0.834	1.79
N-ethyl-N,N-dimethyl-1-propanaminium1,1,1-trifluoro-N-	0.017	4.0	0.834	1.79

[(trifluoromethyl)sulfonyl]methanesulfonamide				
2-hydroxyethylammonium2-hydroxyethylammonium lactate	0.424	2.5	0.961	0.826
trihexyl(tetradecyl)phosphonium bis[(trifluoromethyl)sulfonyl]imide	0.022	5.25	0.834	1.79
trihexyl(tetradecyl)phosphonium chloride	0.022	5.25	0	0.737
tetradecyl(trihexyl)phosphonium dicyanamide	0.022	5.25	0.869	0.973
Tributylmethylphosphonium bis[(trifluoromethyl)sulfonyl]imide	0.021	4.3	0.834	1.79
N,N-dimethyl-N-ethyl-N-pentylammonium bis(trifluoromethylsulfonyl)	0.034	4.18	0.834	1.79
1-butyl-1-methylpyrrolidinium tricyanomethanide	0.03	4.11	0.824	1.21
1-(methoxymethyl)-1-methylpyrrolidinium bis(fluorosulfonyl)amide	0.184	3.88	4.6	1.34
1-methyl-1-propylpiperidinium bis(fluorosulfonyl)imide	0.035	4.41	4.6	1.34
1-butyl-4-methylpyridinium tricyanomethanide	0.159	3.59	0.824	1.21
N-benzylpyridinium bis(trifluoromethylsulfonyl)amide	0.032	3.3	0.834	1.79
3-methyl-1-propylpyridinium bis(trifluoromethylsulfonyl)imide	0.154	3.47	0.834	1.79
1-(2-hydroxyethyl)-pyridinium bis(trifluoromethylsulfonyl)imide	0.424	2.5	0.834	1.79
1-(2-(2-(2-methoxyethoxy)ethoxy)ethyl)pyridinium bis(trifluoromethylsulfonyl)amide	0.102	3.67	0.834	1.79
1-ethyl-3-methylimidazolium acetate	0.1	3.2	0.941	0.835

1-ethyl-3-methylimidazolium bis[(trifluoromethyl)sulfonyl]imide	0.1	3.2	0.834	1.79
1-ethyl-3-methyl-1H-imidazolium tricyanomethanide	0.1	3.2	0.824	1.21
1-ethyl-3-methylimidazolium ethyl sulfate	0.1	3.2	0.899	1.11
1-ethyl-3-methylimidazolium tris(pentafluoroethyl)trifluorophosphate	0.1	3.2	0.822	2.83
1-ethyl-3-methylimidazolium dicyanamide	0.1	3.2	0.869	0.973
1-ethyl-3-methylimidazolium thiocyanate	0.1	3.2	0.75	1.04
1-ethyl-3-methylimidazolium trifluoromethanesulfonate	0.1	3.2	0.776	1.48
1-ethyl-3-methylimidazolium lactate	0.1	3.2	0.961	0.826
1-ethyl-3-methylimidazolium tetracyanoborate	0.1	3.2	0.784	6.8
1-Butyl-3 methylimidazolium Hexafluorophosphate	0.18	3.55	0.716	4.18
1-Butyl-3 methylimidazolium bis[(trifluoromethyl)sulfonyl]imide	0.18	3.55	0.834	1.79
1-Butyl-3 methylimidazolium tricyanomethanide	0.18	3.55	0.824	1.21
1-Butyl-3 methylimidazolium Tetrafluoroborate	0.18	3.55	0.741	4.74
1-Butyl-3 methylimidazolium dicyanamide	0.18	3.55	0.869	0.973
1-Butyl-3 methylimidazolium methyl sulfate	0.18	3.55	0.882	1.11
1-Butyl-3 methylimidazolium Thiocyanate	0.18	3.55	0.75	1.04
1-Butyl-3 methylimidazolium methanesulfonate	0.18	3.55	0.846	1.12
1-Butyl-3 methylimidazolium trifluroacetate	0.18	3.55	0.85	1.03
1-Butyl-3 methylimidazolium Acetate	0.18	3.55	0.941	0.835

1-Butyl-3 methylimidazolium tetrachloroferrate	0.18	3.55	0.472	
1-Butyl-3 methylimidazolium Nitrate	0.18	3.55	0.918	1.08
1-Butyl-3 methylimidazolium Trifluoro[tris(pentafluoroethyl)]phosphate	0.18	3.55	0.822	2.83
1-Butyl-3 methylimidazolium propanoate	0.18	3.55	0.943	0.837
3-hexyl-1-methylimidazolium tricyanomethanide	0.285	3.69	0.824	1.21
1-hexyl-3-methylimidazolium bis[(trifluoromethyl)sulfonyl]imide	0.285	3.69	0.834	1.79
1-hexyl-3-methylimidazolium nitrate	0.285	3.69	0.918	1.08
1-hexyl-3-methylimidazolium tris(heptafluoropropyl)trifluorophosphate	0.285	3.69	0.822	2.83
1-hexyl-3-methylimidazolium hexafluorophosphate	0.285	3.69	0.716	4.18
1-methyl-3-octylimidazolium tricyanomethanide	0.32	3.89	0.824	1.21
1-octyl-3-methylimidazolium bis[(trifluoromethyl)sulfonyl]imide	0.32	3.89	0.834	1.79
1-octyl-3-methylimidazolium hexafluorophosphate	0.32	3.89	0.716	4.18

NOMENCLATURES

Acronyms	Description
AARD%,	Average Absolute Relative Deviation Percent
ANFIS	Adaptive Neuro-Fuzzy Interference System
ANN	Artificial Neural Networks
CART	Classification and Regression Trees
DT	Decision Tree
EOS	Equation of State
GA	Genetic Algorithm

GHG	Greenhouse gases
IL	Ionic Liquid
LSSVM	Least Square Support Vector Machine
MD	Molecular Dynamics
ME	Maximum Error
MLR	Multilinear Regression
QSPR	Quantitative Structure-Activity Relationship
RF	Random Forest
RMSE	Root Mean Square Error
Std	Standard deviation
VIF	Variance Inflation Factor

Chemical Formulas

[bmim][Ac]	1-butyl-3-methylimidazolium acetate
[bmim][BF$_4$]	1-butyl-3-methylimidazolium tetrafluoroborate
[bmim][PF$_6$]	1-butyl-3-methylimidazolium hexafluorophosphate
[bmim][Tf$_2$N]	1-butyl-3-methylimidazolium bis(trifluoromethylsulfonyl)imide
[FAP]	tris(pentafluoroalkyl)-trifluorophosphate
CO$_2$	carbon dioxide
[bmim] [PF$_6$]	1-butyl-3-methylimidazolium hexafluorophosphate
[hmim] [PF$_6$]	1-hexyl-3-methylimidazolium hexafluorophosphate
[omim] [PF$_6$]	1-octyl-3-methylimidazolium hexafluorophosphate
[bmim] [BF$_4$]	1-butyl-3-methilimidazolium tetrafluoroborate
[hmim] [BF$_4$]	1-hexyl-3-methylimidazolium tetrafluoroborate
[omim] [BF$_4$]	1-octyl-3-methylimidazolium tetrafluoroborate
[bmim] [MSO$_4$]	1-butyl-3-methylimidazolium methylsulfate
[bmim] [Ac]	1-butyl-3-methylimidazolium acetate
[bmim] [ta]	1-butyl-3-methylimidazolium trifluoroacetate
[bmim] [TfO]	1-butyl-3-methylimidazolium trifluoromethanesulfonate
[bmim] [dca]	1-butyl-3-methylimidazolium dicyanamide
[bmim] [tca]	1-butyl-3-methylimidazolium thiocyanate
[bmim] [bti]	1-butyl-3-methylimidazolium bis[(trifluoromethyl)sulfonyl]imide
[emim] [TfO]	1-ethyl-3-methylimidazolium trifluoromethanesulfonate
[C$_2$mim][eFAP]	1-ethyl-3-methylimidazolium tris(pentafluoroethyl)trifluorophosphate
[hmim][FAP]	1-hexyl-3-methylimidazolium tris(pentafluoroethyl)trifluorophosphate
[NHHH,(CH2)$_2$OH] [Ac]	2-hydroxyethylammonium acetate
[NHHH,(CH2)$_2$OH] [lactate]	2-hydroxyethylammonium lactate
[N1444] [bti]	Tributylmethylammonium bis[(trifluoromethyl)sulfonyl]imide
[P$_{6,6,6,14}$] [bti]	Trihexyltetradecylphosphonium bis[(trifluoromethyl)sulfonyl]imide
[P$_{6,6,6,14}$] [Cl]	trihexyltetradecylphosphonium chloride
[bpy] [BF$_4$]	1-butylpyridinium tetrafluoroborate
[mbpyr] [dca]	n-methyl-n-butylpyrrolidinium dicyanamide

[bmpyr] [bti]	1-butyl-1-methylpyrrolidinium bis[(trifluoromethyl)sulfonyl]imide
[TBP][FOR]	
[bmim] [PF$_6$]	1-butyl-3-methylimidazolium hexafluorophosphate
[hmim] [PF$_6$]	1-hexyl-3-methylimidazolium hexafluorophosphate
[omim] [PF$_6$]	1-octyl-3-methylimidazolium hexafluorophosphate
[bmim] [BF$_4$]	1-butyl-3-methilimidazolium tetrafluoroborate
[hmim] [BF$_4$]	1-hexyl-3-methylimidazolium tetrafluoroborate
[omim] [BF$_4$]	1-octyl-3-methylimidazolium tetrafluoroborate
HEF	2-Hydroxy ethylammonium formate (HEF)
HEA	2-Hydroxy ethylammonium acetate (HEA)
HEL	2-Hydroxy ethylammonium lactate
THEAA	Tri-(2-hydroxy ethyl)-ammonium acetate
THEAL	Tri-(2-hydroxy ethyl)-ammonium lactate
HEAF	2-(2-Hydroxy ethoxy)-ammonium formate
HEAA	2-(2-Hydroxy ethoxy)-ammonium acetate
HEAL	2-(2-Hydroxy ethoxy)-ammonium lactate

Greek Letters

σ	RBF width
γ	regularization parameter
$\phi(x)$	nonlinear mapping function

Variables/Parameters

R^2	coefficient of determination
AARD%,	the average absolute relative deviation percent
Std	standard deviation
L_j	leaf node
w	weight vector
$\phi(x)$	nonlinear mapping function
b	a bias term
Calc.	predicted (calculated) value
Exp.	experimental value
N	the number of samples in each category (training and testing)

7.CHAPTER SEVEN

Summary and Recommendations for Future Work

The current CO_2 capture techniques mainly suffer from high capital and operating costs, solvent degradation, solvent loss, corrosivity, toxicity, large equipment size, and high energy consumption for solvent recovery. Development, characterization, and evaluation of promising solvents such as ILs for post-combustion CO_2 capture are the main objectives of this thesis. Imidazolium based ILs with various alkyl chain and anion types are mostly studied in this work. The favorable properties of ILs (negligible vapor pressure, environmentally safe, and acceptable absorption capacity) reveal that they are suitable for a wide range of applications in the energy and chemical industries. However, many challenges should be addressed before broadly using them in large practical scales.

Determining the solubility of CO_2 in ILs using thermodynamic models and attaining a reasonable match with experimental data appear to be important challenges. A reliable EOS is required to simulate the VLE data at different operating conditions. In this case, it would be possible to predict the solubility of CO_2 in a variety of imidazolium-based ILs with acceptable precision. ILs with different affinities toward water molecules, hydrophilic and hydrophobic ILs, show different behaviors in Water/ IL mixtures. Hence, CO_2 capture should be evaluated in both types of ILs.

Another challenge while using ILs for absorption is their high viscosity, which adversely affects mass transfer (convection and diffusion) in the absorption column. One of the suitable approaches to overcome the high-viscosity issue is using additives such as water for viscosity reduction. It seems interesting to investigate the diffusion mechanisms of CO_2 in the IL/Water mixtures with different properties and wetness affinities.

The properties of ILs and their mixtures can be evaluated using molecular simulations instead of expensive and time-consuming experiments. MD simulations can accurately predict the thermophysical properties of ILs (e.g., density, viscosity, pressure, enthalpy, entropy, heat

capacity, and thermal conductivity), transport properties such as diffusion coefficient, and interaction energies (e.g., van der Waals forces, electrostatic forces, and hydrogen bonding), resulting in good accordance with experimental data. The MD results are generally dependent on the type of force field. Also, powerful molecular simulations are capable of computing properties, which are needed for the efficient design of ILs for particular purposes. Hence, the effects of cation and anion types, operating conditions, presence of solvents such as water, diffusivity, and structuring species in the bulk system and interface should be systematically investigated to evaluate the capability of ILs in CO_2 absorption.

It seems essential to develop fast predictive tools to estimate the properties of ILs and solubility of various gases in ILs due to the existence of a large number of ILs. Although there are several experimental methods for estimating solubility of acid gases in ILs, it is expensive, laborious, and time-consuming to conduct many laboratory tests. Alternative strategies for properties determination are thermodynamic EOS models, correlations, smart techniques, and molecular simulations. Thermodynamic models generally lead to accurate results at low and moderate pressures; however, they might suffer from some downsides. For instance, they need an adequate number of experimental data for the optimization of adjustable parameters and model validation. Hence, developing more general and accurate thermodynamic models is of great importance. Recently, machine or statistical learning approaches have attracted the attention of researchers in different research fields. Artificial Neural Networks (ANN), Fuzzy Logic (FL), Multilinear Regression (MLR), Decision Tree (DT), and Random Forest or RF (as computational intelligence methods) can model complicated non-linear processes (or phenomena) and obtain thermodynamic and physical properties. Most of the machine learning tools are inspired in physical sciences by

quantitative structure-property/activity relationships, QSPR/QSAR. This type of model can be applied for forecasting solubility of CO_2 in ILs and designing new ILs for absorption applications.

In this thesis, a part of the major challenges is addressed. After a comprehensive review of CO_2 capture using ILs, the thermodynamic modeling of the system using PR and PC-SAFT EOSs is discussed in Chapter 3. The molecular dynamics simulations of pure ILs and IL/ CO_2 cases are implemented; the chemiophysical properties, structural characteristics, and dynamics behaviors are investigated in Chapter 4. The effect of water on the structure and dynamics of species in the mixture is assessed in Chapter 5. The soft-computing models are developed in Chapter 6 to estimate the CO_2 solubility in ILs.

7.1. Literature Review (Chapter 2)

This phase of the study provides an overview of the research works conducted on various challenges in terms of technical, economical, and environmental prospects of CO_2 capture. The main findings/conclusions of the first phase are as follows:

- The current CO_2 capture techniques mainly suffer from high capital and operating costs. The main technical problems of post-combustion absorption systems are solvent degradation, high solvent loss, corrosive nature of solvents, the toxicity of solvents, required large absorption equipment, and high energy consumption for solvent regeneration.

- The functionalized ILs though have higher CO_2 absorption capacity, they are 2-4 times more expensive than conventional ILs. The viscous complex ILs after reaction with CO_2 makes them an inappropriate choice for absorption-desorption processes. They will have

an energy-intensive regeneration process, similar to amines; viscous products will make the absorption process ineffective.

- The best ILs in terms of technical and economic perspectives are screened. It is concluded that Guanidinium cations; and acetate-based [Ac] and fluorinated anions including [BF$_4$], [FEP], and [PF$_6$] exhibit high CO_2 solubility.

- To commercialize CO_2 capture technology with ILs, it is vital to find cheap but suitable IL/additive mixtures with relatively high solubility and selectivity where important mass transfer and thermodynamic prospects of CO_2/Water/IL/additive systems (diffusivity, mass transfer rate, vapor pressure, and equilibrium conditions) are well explored through experimental and modeling studies.

- ILs as green solvents offer a promising CO_2 capture technique where an acceptable absorption rate can be attained if a proper ion or chemical is added to IL. In addition to engineering design aspects, their high viscosity, cost, availability, compatibility, and purity are the main challenges to developing appropriate absorption systems for CO_2 capture using ILs at an industrial scale.

- There are not enough experimental data for acid gas solubility in different ILs. Fast screening methods are required to be implemented to study the phase behavior of gas-IL, dynamics of gas in ILs, and absorption mechanisms. Thermodynamic modeling, molecular dynamics simulations, and soft-computing methods are powerful approaches to further study the ILs properties, and their behaviors in different systems (bulk and the interface).

7.2. Thermodynamic Modeling (Chapter 3)

The main objective of this chapter is to conduct thermodynamic modeling for performance evaluation of the PR and PC-SAFT EOSs in predicting solubility of acid gases in ILs within a wide range of temperatures and pressures. In addition, the influence of adding solvents (e.g., water and toluene) on CO_2 solubility and viscosity of corresponding mixtures is studied through using PC-SAFT EOS.

PR and PC-SAFT EOSs are applied in various IL/CO_2 systems. The association contribution and binary interactions between components are considered in the modeling. PC-SAFT EOS model exhibits better performance and more accurate results than PR while predicting the CO_2 solubility in ILs. This precision is originated from the characteristic/nature of SAFT EOSs where they take into account the effect of molecular structure and interactions on the bulk properties and phase behavior, unlike the cubic EOSs that assume molecules as a hard-sphere. The effect of different water mole fractions on the solubility of CO_2 in ILs/water mixtures is properly evaluated using PC-SAFT EOS. It is concluded that the presence of water in the solvent will decrease the viscosity of ILs; it also leads to solubility reduction. The viscosity reduction is highlighted in hydrophilic ILs, compared to hydrophobic ones. In ILs with more hydrophilic behavior such as [Bmim][Ac], the addition of various concentrations of water will decrease the viscosity, but the solubility reduction is minor. The ratio of solubility reduction to viscosity reduction in hydrophobic ILs (e.g., [Bmim][BF$_4$]) is considerable; it makes them inappropriate choices to be used with water for carbon capture.

7.3. Molecular Dynamics Simulation (Chapters 4 and 5)

This study phase assesses the thermophysical properties, local structure, and transport properties of pure ILs and their mixture with water and CO_2. We calculate the densities, viscosities, transport properties of pure cations and anions of ILs. MD simulations are performed to determine the bulk properties of [Bmim][BF$_4$] and [bmim][Ac] ILs using OPLS-AA force field. Densities of ILs are in good agreement with experimental data within a broad range of temperatures. Dynamics of ions shows that cations diffuse faster than anions, which is not consistent with the relationship between the diffusivity and size of the ions. It is explained with polar and non-polar locations in the mixture. Radial distribution functions (RDFs) are obtained at different temperatures; it is found that anion is willing to locate around the ring of the imidazolium cation.

At the bulk system of CO_2 in IL, structuring CO_2 around cation and anion, and volume expansion upon CO_2 absorption are analyzed; it is concluded that anions have an important role in CO_2 absorption. Diffusion coefficients of CO_2 in ILs are in the range of (1-3) $\times 10^{-10}$ m^2/s, depending on temperature, CO_2 concentration, and mixture viscosity.

MD simulations are also implemented to study the molecular and structural behaviors of the interface of IL/CO_2 systems at various CO_2 concentrations. CO_2 creates a dense layer at the interface, which interrupts the association between cation and anion and eventually decreases the surface tension. It is found that the diffusion of CO_2 in the bulk occurs slowly. The results corresponding to interfacial behavior and transport properties of CO_2 and ILs are useful to design ILs with high solubility and diffusivity.

The molecular behaviors of binary Water/[Bmim][Ac] and ternary CO_2/[Bmim][Ac]/Water systems are also studied, using MD simulations. The excess energy, radial pair distribution

function, coordination number, water clusters, and dynamic properties of compounds are attained from the analysis of the MD results. The mixture viscosity decreases by 40% in the presence of water where the mole fraction of water in [Bmim][Ac] IL is 0.2. The presence of water in [Bmim][Ac] IL within the mole fraction range of 0.2–0.6, leads to a significant increase in the diffusivities and activation energies for ions in comparison to self-diffusivities in pure IL. A further increase in the water mole fraction (>0.8) results in a sharp change in the ions diffusion coefficients. In general, this phase of the research work offers useful tips in further understanding of solubility and diffusivity behavior of ILs, volume expansivity upon CO_2 absorption, interfacial behaviors of CO_2/ILs, and effect of water in viscosity and diffusivity coefficients which are crucial in designing ILs for various applications in energy and environment sectors at different conditions.

7.4. Rigorous Connectionist Models to Predict CO₂ Solubility in ILs (Chapter 6)

This research phase aims to develop robust and reliable machine learning models for the prediction of CO_2 solubility in ILs. Four approaches including Least Square Support Vector Machine (LSSVM), Decision Tree (DT), Random Forest (RF), and Multilinear Regression (MLR) are applied under various thermodynamic and operating conditions where the thermodynamic and structural properties of ILs are considered as the input parameters. Statistical parameters such as determination coefficient (R^2), Average Relative Deviation (ARD), and Root Mean Square Error (RMSE) are used to evaluate the accuracy and reliability of the developed methods. The DT and RF models show greater performance (in terms of accuracy and reliability) in predicting CO_2 solubility in ILs, compared to the LSSVM and MLR approaches. The errors resulted from QSPR-based models are slightly lower than the thermodynamic-based models. This might be due to the strong relationship between ILs structural properties and CO_2 solubility in ILs. Hence, the models developed based on structural properties are more reliable and accurate (compared to the models

obtained from critical properties), since the ILs descriptors in the QSPR model generally take into account the key geometrical, structural, charge, and quantum chemical characteristics of ILs.

7.5. Recommendations for Future Work

The application of ILs for the CO_2 absorption needs further research and engineering investigations to explore important aspects such as combinations of cations and anions, absorption mechanisms, optimal process design and operation, mass transfer coefficient, component diffusivity, and addition of chemicals/solvents. The recommendations for future work based on the results of this thesis are summarized below:

- The CO_2 capture capacity of other ILs such as phosphonium based, ammonium-based, and guanidinium-based ILs (as potential CO_2 absorbents) has been rarely investigated in the literature. Hence, further research is required to comprehensively screen and design new effective ILs with high performance. Deep eutectic solvents (DESs) are also novel solvents that can be studied for possible CO_2 capture.

- In practice, flue gas streams contain other gases including N_2, H_2, H_2S, SO_X, and NO_X. The presence of impurities/gases can considerably affect the CO_2 capture capacity of solvents and their selectivity. They can also alter the micro and macro characteristics of the bulk and interface in CO_2/ ILs systems.

- Analysis of molecular-level behaviors of the ILs mixtures is still at an early stage. Further multiscale modeling/simulation works need to be conducted for accurate determination of physicochemical and thermophysical characteristics of pure ILs and their mixtures with other chemicals (and/or gases).

- It would be useful to study the influence of adding solvents/chemicals such as amines to ILs on physical and chemical properties as well as the absorption capacity of ILs. They might have a positive impact on CO_2 capture capacity and reduce IL viscosity. Also, a mixture of two or more ILs can be recommended for CO_2 capture. This strategy might lead to a greater CO_2 absorption capacity.

- MD and Monte Carlo simulations (or multi-scale simulations) can be employed to determine thermodynamic and phase behaviors of Additive/IL/CO_2 systems. The results can be then compared with those obtained from EOS thermodynamic modeling where various EOSs are examined.

- Utilization of various soft computing methods such as ANN and RF to predict the solubility of acid gases in mixtures of ILs and water or organic solvents can be an interesting future study in this area. It is expected that more robust and generalized deterministic models can be presented to obtain the solubility of CO_2 in pure ILs and solvent/IL systems if a large number of experimental data are available.

- It would also be of interest in the future to carry out accelerated dynamics simulations of IL/CO_2/Solvent mixtures with more effective force fields and longer simulation periods to attain more precise results.

- The economic and environmental prospects of ILs (cost and toxicity) can be systematically studied through employing QSPR models.

- Challenges with the theoretical and practical implementation of CO_2 capture plant with IL can be addressed through dynamic simulation and optimization tools as a future study.

- Energy and exergy analysis of a potential carbon capture plant (with ILs) can be an interesting research work.

References

1. Danesh, A., *PVT and phase behaviour of petroleum reservoir fluids*. Vol. 47. 1998: Elsevier.
2. Valderrama, J.O. and R.E. Rojas, *Critical properties of ionic liquids. Revisited.* Industrial & Engineering Chemistry Research, 2009. **48**(14): p. 6890-6900.
3. Torralba-Calleja, E., J. Skinner, and D. Gutiérrez-Tauste, *CO 2 capture in ionic liquids: a review of solubilities and experimental methods.* Journal of Chemistry, 2013. **2013**.
4. Ghandi, K., *A review of ionic liquids, their limits and applications.* Green and sustainable chemistry, 2014. **2014**.
5. Yokozeki, A., et al., *Physical and chemical absorptions of carbon dioxide in room-temperature ionic liquids.* The Journal of Physical Chemistry B, 2008. **112**(51): p. 16654-16663.
6. Figueroa, J.D., et al., *Advances in CO 2 capture technology—the US Department of Energy's Carbon Sequestration Program.* International journal of greenhouse gas control, 2008. **2**(1): p. 9-20.
7. Bolin, B. and E. Eriksson, *Changes in the carbon dioxide content of the atmosphere and sea due to fossil fuel combustion.* The atmosphere and the sea in motion, 1959. **1**: p. 30-142.
8. Coninck, H.d., et al., *IPCC special report on carbon dioxide capture and storage.* Intergovernmental Panel on Climate Change, 2005.
9. Yu, K.M.K., et al., *Recent advances in CO2 capture and utilization.* ChemSusChem, 2008. **1**(11): p. 893-899.
10. Rahman, F.A., et al., *Pollution to solution: Capture and sequestration of carbon dioxide (CO2) and its utilization as a renewable energy source for a sustainable future.* Renewable and Sustainable Energy Reviews, 2017. **71**: p. 112-126.
11. Chen, Y., F. Mutelet, and J.-N.l. Jaubert, *Modeling the solubility of carbon dioxide in imidazolium-based ionic liquids with the PC-SAFT equation of state.* The Journal of Physical Chemistry B, 2012. **116**(49): p. 14375-14388.
12. Bailera, M., et al., *Power to Gas projects review: Lab, pilot and demo plants for storing renewable energy and CO2.* Renewable and Sustainable Energy Reviews, 2017. **69**: p. 292-312.
13. Sreedhar, I., et al., *Process and engineering trends in membrane based carbon capture.* Renewable and Sustainable Energy Reviews, 2017. **68**: p. 659-684.
14. Force, C.A.T., *Advanced Post-Combustion CO2 Capture.* Freund, H., J. Bauer, T. Zeiser and G. Emig (2005)." Detailed simulation of transport processes in fixed-beds." Industrial & engineering chemistry research, 2009. **44**(16): p. 6423-6434.
15. Sreedhar, I., et al., *Carbon capture by absorption–path covered and ahead.* Renewable and Sustainable Energy Reviews, 2017. **76**: p. 1080-1107.
16. Mirzaei, S., A. Shamiri, and M.K. Aroua, *A review of different solvents, mass transfer, and hydrodynamics for postcombustion CO2 capture.* Reviews in Chemical Engineering, 2015. **31**(6): p. 521-561.
17. Global, C., *Institute (GCCSI)(2012) The Global Status of CCS: 2012*. Canberra, Australia.
18. Rochelle, G.T., *Amine scrubbing for CO2 capture.* Science, 2009. **325**(5948): p. 1652-1654.

19. Riemer, P.W. and W.G. Ormerod, *International perspectives and the results of carbon dioxide capture disposal and utilisation studies.* Energy Conversion and Management, 1995. **36**(6): p. 813-818.

20. Kothandaraman, A., *Carbon dioxide capture by chemical absorption: a solvent comparison study.* 2010, Massachusetts Institute of Technology.

21. Yu, C.-H., C.-H. Huang, and C.-S. Tan, *A review of CO2 capture by absorption and adsorption.* Aerosol Air Qual. Res, 2012. **12**(5): p. 745-769.

22. Anthony, J.L., E.J. Maginn, and J.F. Brennecke, *Solubilities and thermodynamic properties of gases in the ionic liquid 1-n-butyl-3-methylimidazolium hexafluorophosphate.* The Journal of Physical Chemistry B, 2002. **106**(29): p. 7315-7320.

23. Johnson, K.E., *What's an ionic liquid?* Interface-Electrochemical Society, 2007. **16**(1): p. 38-41.

24. Henni, A., et al., *Quantum-Mechanical and Thermodynamic Study of Amines and Ionic Liquids for CO2 Capture.* 2013, Faculty of Graduate Studies and Research, University of Regina.

25. Zhang, S., et al., *Physical properties of ionic liquids: database and evaluation.* Journal of physical and chemical reference data, 2006. **35**(4): p. 1475-1517.

26. Wasserscheid, P. and T. Welton, *Ionic liquids in synthesis.* Vol. 1. 2008: Wiley Online Library.

27. Welton, T., *Room-temperature ionic liquids. Solvents for synthesis and catalysis.* Chemical reviews, 1999. **99**(8): p. 2071-2084.

28. Blanchard, L.A., et al., *Green processing using ionic liquids and CO2.* Nature, 1999. **399**(6731): p. 28-29.

29. Ramdin, M., T.W. de Loos, and T.J. Vlugt, *State-of-the-art of CO2 capture with ionic liquids.* Industrial & Engineering Chemistry Research, 2012. **51**(24): p. 8149-8177.

30. Kirchner, B., *Ionic liquids.* Vol. 290. 2009: Springer.

31. Krupiczka, R., A. Rotkegel, and Z. Ziobrowski, *Comparative study of CO 2 absorption in packed column using imidazolium based ionic liquids and MEA solution.* Separation and Purification Technology, 2015. **149**: p. 228-236.

32. Shannon, M.S. and J.E. Bara, *Properties of alkylimidazoles as solvents for CO2 capture and comparisons to imidazolium-based ionic liquids.* Industrial & Engineering Chemistry Research, 2011. **50**(14): p. 8665-8677.

33. Kroon, M.C., et al., *Modeling of the carbon dioxide solubility in imidazolium-based ionic liquids with the tPC-PSAFT equation of state.* The Journal of Physical Chemistry B, 2006. **110**(18): p. 9262-9269.

34. Yokozeki, A. and M.B. Shiflett, *Gas solubilities in ionic liquids using a generic van der Waals equation of state.* The Journal of Supercritical Fluids, 2010. **55**(2): p. 846-851.

35. Shiflett, M.B. and A. Yokozeki, *Separation of carbon dioxide and sulfur dioxide using room-temperature ionic liquid [bmim][MeSO4].* Energy & Fuels, 2009. **24**(2): p. 1001-1008.

36. Andreu, J.S. and L.F. Vega, *Modeling the solubility behavior of CO2, H2, and Xe in [C n-mim][Tf2N] ionic liquids.* The Journal of Physical Chemistry B, 2008. **112**(48): p. 15398-15406.

37. Shiflett, M.B. and A. Yokozeki, *Separation of CO 2 and H 2 S using room-temperature ionic liquid [bmim][PF 6].* Fluid Phase Equilibria, 2010. **294**(1): p. 105-113.

38.   Zhou, L., J. Fan, and X. Shang, *CO2 Capture and Separation Properties in the Ionic Liquid 1-n-Butyl-3-Methylimidazolium Nonafluorobutylsulfonate.* Materials, 2014. **7**: p. 3867-3880.
39.   Valderrama, J.O., F. Urbina, and C.A. Faúndez, *Gas-liquid equilibrium modeling of mixtures containing supercritical carbon dioxide and an ionic liquid.* The Journal of Supercritical Fluids, 2012. **64**: p. 32-38.
40.   Karakatsani, E.K., et al., *tPC-PSAFT modeling of gas solubility in imidazolium-based ionic liquids.* The Journal of Physical Chemistry C, 2007. **111**(43): p. 15487-15492.
41.   Statistics, I., *CO2 emissions from fuel combustion-highlights.* IEA, Paris http://www. iea. org/co2highlights/co2highlights. pdf. Cited July, 2011.
42.   Statistics, I.E.A.I., *CO2 emissions from fuel combustion-highlights.* 2016: Paris
43.   EIA, U., *International energy statistics.* US Energy and Information Administration, Washington, DC [available at http://www. eia. gov/countries/data. cfm], 2011.
44.   Statistics, O., *Greenhouse gas emissions* 2017.
45.   *2016 on Track for Record Rate of Atmospheric CO2 Increase*. 2016; Available from: https://robertscribbler.com/2016/11/01/.
46.   Kurihara, H. and Y. Shirayama, *Effects of increased atmospheric CO2 on sea urchin early development.* Marine Ecology Progress Series, 2004. **274**: p. 161-169.
47.   Matin, A., et al., *Canada's greenhouse gas inventory 1990-2002*. 2004, Greenhouse Gas Division, Environment Canada Ottawa, Canada.
48.   Yalkowski, S., Y. He, and P. Jain, *Handbook of aqueous solubility data second edition*. 2010, New York: CRC Press.
49.   Haynes, W.M., *CRC handbook of chemistry and physics*. 2014: CRC press.
50.   Sovova, H. and J. Prochazka, *Calculations of compressed carbon dioxide viscosities.* Industrial & engineering chemistry research, 1993. **32**(12): p. 3162-3169.
51.   Fenghour, A., W.A. Wakeham, and V. Vesovic, *The viscosity of carbon dioxide.* Journal of Physical and Chemical Reference Data, 1998. **27**(1): p. 31-44.
52.   Austgen, D.M., et al., *Model of vapor-liquid equilibria for aqueous acid gas-alkanolamine systems using the electrolyte-NRTL equation.* Industrial & Engineering Chemistry Research, 1989. **28**(7): p. 1060-1073.
53.   Wilcox, J., *Carbon capture*. 2012: Springer Science & Business Media.
54.   Palma Chilla, L., J. Lazzús, and A. Pérez Ponce, *Particle swarm modeling of vapor-liquid equilibrium data of binary systems containing CO 2+ imidazolium ionic liquids based on bis [(trifluoromethyl) sulfonyl] imide anion.* Journal of Engineering Thermophysics, 2011. **20**(4): p. 487-500.
55.   Hayes, R., G.G. Warr, and R. Atkin, *Structure and nanostructure in ionic liquids.* Chemical reviews, 2015. **115**(13): p. 6357-6426.
56.   Tomé, L.I., et al., *Measurements and correlation of high-pressure densities of imidazolium-based ionic liquids.* Journal of Chemical & Engineering Data, 2008. **53**(8): p. 1914-1921.
57.   Dymond, J. and R. Malhotra, *The Tait equation: 100 years on.* International journal of thermophysics, 1988. **9**(6): p. 941-951.
58.   Bonhote, P., et al., *Hydrophobic, highly conductive ambient-temperature molten salts.* Inorganic chemistry, 1996. **35**(5): p. 1168-1178.

59.   Huddleston, J.G., et al., *Characterization and comparison of hydrophilic and hydrophobic room temperature ionic liquids incorporating the imidazolium cation.* Green chemistry, 2001. **3**(4): p. 156-164.

60.   Valderrama, J. and P. Robles, *Critical properties, normal boiling temperatures, and acentric factors of fifty ionic liquids.* Industrial & Engineering Chemistry Research, 2007. **46**(4): p. 1338-1344.

61.   Lydersen, A.L. and M.E.E. Station, *Estimation of critical properties of organic compounds by the method of group contributions.* 1955: University of Wisconsin.

62.   Joback, K.G. and R.C. Reid, *Estimation of pure-component properties from group-contributions.* Chemical Engineering Communications, 1987. **57**(1-6): p. 233-243.

63.   Maia, F.M., et al., *Modeling of Ionic Liquid Systems: Phase Equilibria and Physical Properties.* 2013: INTECH Open Access Publisher.

64.   Valderrama, J.O., W.W. Sanga, and J.A. Lazzús, *Critical properties, normal boiling temperature, and acentric factor of another 200 ionic liquids.* Industrial & Engineering Chemistry Research, 2008. **47**(4): p. 1318-1330.

65.   Alvarez, V. and J. Valderrama, *A modified Lydersen-Joback-Reid method to estimate the critical properties of biomolecules.* Alimentaria, 2004. **254**: p. 55-66.

66.   Valderrama, J.O. and L.A. Forero, *An analytical expression for the vapor pressure of ionic liquids based on an equation of state.* Fluid Phase Equilibria, 2012. **317**: p. 77-83.

67.   Valderrama, J.O. and W.W. Sanga, *Critical Properties and Vapor Pressure of Twenty Imidazolium based Ionic Liquids used in Extraction Bioprocesses.* 2008, Dechema Veranstaltungen: Frankfurt.

68.   Paulechka, Y., et al., *Vapor pressure and thermal stability of ionic liquid 1-butyl-3-methylimidazolium Bis (trifluoromethylsulfonyl) amide.* Thermochimica Acta, 2005. **439**(1): p. 158-160.

69.   Emel'yanenko, V.N., S.P. Verevkin, and A. Heintz, *The gaseous enthalpy of formation of the ionic liquid 1-butyl-3-methylimidazolium dicyanamide from combustion calorimetry, vapor pressure measurements, and ab initio calculations.* Journal of the American Chemical Society, 2007. **129**(13): p. 3930-3937.

70.   Langmuir, I., *The vapor pressure of metallic tungsten.* Physical review, 1913. **2**(5): p. 329.

71.   Phang, P., D. Dollimore, and S.J. Evans, *A comparative method for developing vapor pressure curves based on evaporation data obtained from a simultaneous TG–DTA unit.* Thermochimica acta, 2002. **392**: p. 119-125.

72.   Aschenbrenner, O., et al., *Measurement of vapour pressures of ionic liquids and other low vapour pressure solvents.* Green Chemistry, 2009. **11**(8): p. 1217-1221.

73.   Ficke, L.E., R.R. Novak, and J.F. Brennecke, *Thermodynamic and thermophysical properties of ionic liquid+ water systems.* Journal of Chemical & Engineering Data, 2010. **55**(11): p. 4946-4950.

74.   Dohrn, R., J.M. Fonseca, and S. Peper, *Experimental methods for phase equilibria at high pressures.* Annual review of chemical and biomolecular engineering, 2012. **3**: p. 343-367.

75.   Torralba-Calleja, E., J. Skinner, and D. Gutiérrez-Tauste, *CO2 Capture in Ionic Liquids: A Review of Solubilities and Experimental Methods.* Journal of Chemistry, 2013: p. 1-16.

76.   Blanchard, L.A., Z. Gu, and J.F. Brennecke, *High-pressure phase behavior of ionic liquid/CO2 systems.* The Journal of Physical Chemistry B, 2001. **105**(12): p. 2437-2444.

77.   Blanchard, L.A., Z. Gu, and J.F. Brennecke, *High-Pressure Phase Behavior of Ionic Liquid/CO2 Systems.* Journal of Physical Chemistry, 2001. **105**: p. 2437-2444.

78.   *Density Measuring Module: DMA 4500 ME*, in *Anton Paar*. 2016.

79.   Chilla, L.P., J. Lazzús, and A.P. Ponce, *Particle swarm modeling of vapor-liquid equilibrium data of binary systems containing CO 2+ imidazolium ionic liquids based on bis [(trifluoromethyl) sulfonyl] imide anion.* Journal of Engineering Thermophysics, 2011. **20**(4): p. 487-500.

80.   Li, H., *Thermodynamic properties of CO2 mixtures and their applications in advanced power cycles with CO2 capture processes.* 2008.

81.   Peng, D.-Y. and D.B. Robinson, *A new two-constant equation of state.* Industrial & Engineering Chemistry Fundamentals, 1976. **15**(1): p. 59-64.

82.   Patel, N.C. and A.S. Teja, *A new cubic equation of state for fluids and fluid mixtures.* Chemical Engineering Science, 1982. **37**(3): p. 463-473.

83.   Redlich, O. and J.N. Kwong, *On the Thermodynamics of Solutions. V. An Equation of State. Fugacities of Gaseous Solutions.* Chemical reviews, 1949. **44**(1): p. 233-244.

84.   Soave, G., *Equilibrium constants from a modified Redlich-Kwong equation of state.* Chemical Engineering Science, 1972. **27**(6): p. 1197-1203.

85.   Stryjek, R. and J. Vera, *PRSV2: a cubic equation of state for accurate vapor—liquid equilibria calculations.* The Canadian Journal of Chemical Engineering, 1986. **64**(5): p. 820-826.

86.   Ren, W., B. Sensenich, and A.M. Scurto, *High-pressure phase equilibria of {carbon dioxide (CO 2)+ n-alkyl-imidazolium bis (trifluoromethylsulfonyl) amide} ionic liquids.* The Journal of Chemical Thermodynamics, 2010. **42**(3): p. 305-311.

87.   Freitas, A., et al., *Modeling vapor liquid equilibrium of ionic liquids+ gas binary systems at high pressure with cubic equations of state.* Brazilian Journal of Chemical Engineering, 2013. **30**(1): p. 63-73.

88.   Maia, F.M., et al., *Modeling of ionic liquid systems: phase equilibria and physical properties*, in *Ionic Liquids-New Aspects for the Future*. 2013, InTech.

89.   Maia, F.M., et al., *Equation of state modelling of systems with ionic liquids: Literature review and application with the Cubic Plus Association (CPA) model.* Fluid Phase Equilibria, 2012. **332**: p. 128-143.

90.   Uygur, T.J., *Experimental and thermodynamic studies of ionic liquids for carbon dioxide separation*. 2013, Faculty of Graduate Studies and Research, University of Regina.

91.   Soave, G., *Improvement of the van der Waals equation of state.* Chemical engineering science, 1984. **39**(2): p. 357-369.

92.   Chapman, W.G., G. Jackson, and K.E. Gubbins, *Phase equilibria of associating fluids: chain molecules with multiple bonding sites.* Molecular Physics, 1988. **65**(5): p. 1057-1079.

93.   Gil-Villegas, A., et al., *Statistical associating fluid theory for chain molecules with attractive potentials of variable range.* The Journal of chemical physics, 1997. **106**(10): p. 4168-4186.

94.   Pàmies, J.C. and L.F. Vega, *Vapor− liquid equilibria and critical behavior of heavy n-alkanes using transferable parameters from the soft-SAFT equation of state.* Industrial & engineering chemistry research, 2001. **40**(11): p. 2532-2543.

95.   Felipe, J., *Thermodynamic behaviour of homonuclear and heteronuclear Lennard-Jones chains with association sites from simulation and theory.* Molecular Physics, 1997. **92**(1): p. 135-150.

96.   Gross, J. and G. Sadowski, *Perturbed-chain SAFT: An equation of state based on a perturbation theory for chain molecules.* Industrial and Engineering Chemistry Research, 2001. **40**(4): p. 1244-1260.

97.   Yazdizadeh, M., F. Rahmani, and A.A. Forghani, *Thermodynamic modeling of CO2 solubility in ionic liquid ([Cn-mim][Tf2N]; n=2, 4, 6, 8) using Wong-Sandler mixing rule, Peng-Robinson equation of state (EOS) and differential evolution (DE) method.* Korean Journal of Chemical Engineering, 2011. **1**: p. 246-251.

98.   Zhang, H., et al., *Novel bare-bones particle swarm optimization and its performance for modeling vapor–liquid equilibrium data.* Fluid Phase Equilibria, 2011. **301**(1): p. 33-45.

99.   Gutkowski, K.I., A. Shariati, and C.J. Peters, *High-pressure phase behavior of the binary ionic liquid system 1-octyl-3-methylimidazolium tetrafluoroborate + carbon dioxide.* The Journal of Supercritical Fluids, 2006. **39**: p. 187-191.

100.   Gutkowski, K., A. Shariati, and C. Peters, *High-pressure phase behavior of the binary ionic liquid system 1-octyl-3-methylimidazolium tetrafluoroborate+ carbon dioxide.* The Journal of supercritical fluids, 2006. **39**(2): p. 187-191.

101.   Aki, S.N., et al., *High-pressure phase behavior of carbon dioxide with imidazolium-based ionic liquids.* The Journal of Physical Chemistry B, 2004. **108**(52): p. 20355-20365.

102.   Camper, D., et al., *Room-temperature ionic liquid− amine solutions: Tunable solvents for efficient and reversible capture of CO2.* Industrial & Engineering Chemistry Research, 2008. **47**(21): p. 8496-8498.

103.   Lazzús, J.A., *Thermodynamic Modeling Based on Particle Swarm Optimization to Predict Phase Equilibrium of Binary Systems Containing Ionic Liquids.* Journal of Molecular Liquids, 2013. **186**: p. 44-51.

104.   Lazzús, J.A., *Optimization of High-Pressure Vapor-Liquid Equilibrium Modelling of Binary Mixtures (Supercritical Fluid + Ionic Liquid) by Particle Swarm Algorithm.* Communications in Mathematical and in Computer Chemistry, 2015. **73**: p. 663-688.

105.   Lazzús, J.A., *Neural network-particle swarm modeling to predict thermal properties.* Mathematical and Computer Modelling, 2013. **57**(9): p. 2408-2418.

106.   Klamt, A., F. Eckert, and W. Arlt, *COSMO-RS: An Alternative to Simulation for Calculating Thermodynamic Properties of Liquid Mixtures.* The Annual Review of Chemical and Biomolecular Engineering, 2010. **1**: p. 101-122.

107.   Diamantonis, N.I., et al., *Evaluation of cubic, SAFT, and PC-SAFT equations of state for the vapor–liquid equilibrium modeling of CO2 mixtures with other gases.* Industrial & Engineering Chemistry Research, 2013. **52**(10): p. 3933-3942.

108.   Ting, P.D., et al., *Application of the PC-SAFT equation of state to asphaltene phase behavior*, in *Asphaltenes, heavy oils, and petroleomics*. 2007, Springer. p. 301-327.

109.   Yazdizadeh, M., F. Rahmani, and A.A. Forghani, *Thermodynamic modeling of CO2 solubility in ionic liquid ([C n-mim][Tf2N]; n= 2, 4, 6, 8) with using Wong-Sandler mixing rule, Peng-Rabinson equation of state (EOS) and differential evolution (DE) method.* Korean Journal of Chemical Engineering, 2011. **28**(1): p. 246-251.

110.   Zhang, X., Z. Liu, and W. Wang, *Screening of ionic liquids to capture CO2 by COSMO-RS and experiments.* AIChE journal, 2008. **54**(10): p. 2717-2728.

111.   Perez-Salado Kamps, A., et al., *Solubility of CO2 in the ionic liquid [bmim][PF6].* Journal of Chemical & Engineering Data, 2003. **48**(3): p. 746-749.

112. Shiflett, M.B. and A. Yokozeki, *Solubilities and diffusivities of carbon dioxide in ionic liquids:[bmim][PF6] and [bmim][BF4].* Industrial & Engineering Chemistry Research, 2005. **44**(12): p. 4453-4464.

113. Shin, E.-K., B.-C. Lee, and J.S. Lim, *High-pressure solubilities of carbon dioxide in ionic liquids: 1-alkyl-3-methylimidazolium bis (trifluoromethylsulfonyl) imide.* The Journal of Supercritical Fluids, 2008. **45**(3): p. 282-292.

114. Carvalho, P.J., et al., *High carbon dioxide solubilities in trihexyltetradecylphosphonium-based ionic liquids.* The Journal of Supercritical Fluids, 2010. **52**(3): p. 258-265.

115. Kilaru, P.K. and P. Scovazzo, *Correlations of low-pressure carbon dioxide and hydrocarbon solubilities in imidazolium-, phosphonium-, and ammonium-based room-temperature ionic liquids. Part 2. Using activation energy of viscosity.* Industrial & Engineering Chemistry Research, 2008. **47**(3): p. 910-919.

116. Anderson, J.L., J.K. Dixon, and J.F. Brennecke, *Solubility of CO2, CH4, C2H6, C2H4, O2, and N2 in 1-Hexyl-3-methylpyridinium Bis (trifluoromethylsulfonyl) imide: Comparison to Other Ionic Liquids.* Accounts of chemical research, 2007. **40**(11): p. 1208-1216.

117. Goodrich, B.F., et al., *Experimental measurements of amine-functionalized anion-tethered ionic liquids with carbon dioxide.* Industrial & Engineering Chemistry Research, 2010. **50**(1): p. 111-118.

118. Galan-Sanchez, L.M., *Functionalised ionic liquids, absorption*

solvents for CO2 and olefin separation [Ph.D. thesis]. 2008.

119. Brennecke, J.F. and E.J. Maginn, *Ionic liquids: innovative fluids for chemical processing.* AIChE Journal, 2001. **47**(11): p. 2384-2389.

120. Ren, W., B. Sensenich, and A.M. Scurto, *High-pressure phase equilibria of {carbon dioxide (CO2) + n-alkyl-imidazolium bis(trifluoromethylsulfonyl)amide} ionic liquids.* J. Chem. Thermodynamics, 2010. **42**: p. 305-311.

121. Brennecke, J.F. and E.J. Maginn, *Ionic Liquids: Innovative Fluids for Chemical Processing.* American Institute of Chemical Engineers, 2001. **47**(11): p. 2384-2389.

122. Shariati, A., K. Gutkowski, and C.J. Peters, *Comparison of the Phase Behavior of Some Selected Binary Systems with Ionic Liquids.* American Institute of Chemical Engineers, 2005. **51**(5): p. 1532-1540.

123. Palma Chilla, L.O., J.A. Lazzús, and A.A. Pérez Ponce, *Particle Swarm Modeling of Vapor-Liquid Equilibrium Data of Binary Systems Containing CO2 + Imidazolium Ionic Liquids Based on Bis[(trifluoromethyl)sulfonyl]imide Anion.* Journal of Engineering Thermophysics, 2011. **20**(4): p. 487-500.

124. Carroll, J.J. and A.E. Mather, *The system carbon dioxide-water and the Krichevsky-Kasarnovsky equation.* Journal of Solution Chemistry, 1992. **21**(7): p. 607-621.

125. Carvalho, P.J., et al., *High carbon dioxide solubilities in trihexyltetradecylphosphonium-based ionic liquids.* The Journal of Supercritical Fluids, 2010. **52**: p. 258-265.

126. Rosli, A., et al., *Advances in Liquid Absorbents for CO^ sub 2^ Capture: A Review.* Journal of Physical Science, 2017. **28**: p. 121.

127. Burr, B. and L. Lyddon. *A comparison of physical solvents for acid gas removal.* in *87th Annual Gas Processors Association Convention, Grapevine, TX, March.* 2008.

128. Zhang, X., et al., *Carbon capture with ionic liquids: overview and progress.* Energy & Environmental Science, 2012. **5**(5): p. 6668-6681.

129. Xie, Y., et al., *Energy consumption analysis for CO 2 separation using imidazolium-based ionic liquids.* Applied Energy, 2014. **136**: p. 325-335.

130. Zhang, Y., et al., *Dual Amino-Functionalised Phosphonium Ionic Liquids for CO2 Capture.* Chemistry–A European Journal, 2009. **15**(12): p. 3003-3011.

131. Gurkan, B.E., et al., *Equimolar CO2 absorption by anion-functionalized ionic liquids.* Journal of the American Chemical Society, 2010. **132**(7): p. 2116-2117.

132. Bates, E.D., et al., *CO2 capture by a task-specific ionic liquid.* Journal of the American Chemical Society, 2002. **124**(6): p. 926-927.

133. Zhang, X., et al., *Gas–liquid mass-transfer properties in CO2 absorption system with ionic liquids.* AIChE Journal, 2014. **60**(8): p. 2929-2939.

134. Bara, J.E., et al., *Room-temperature ionic liquids and composite materials: platform technologies for CO2 capture.* Accounts of Chemical Research, 2009. **43**(1): p. 152-159.

135. Yang, J., et al., *CO2 capture using amine solution mixed with ionic liquid.* Industrial & Engineering Chemistry Research, 2014. **53**(7): p. 2790-2799.

136. Zhao, Y., et al., *Density, viscosity, and performances of carbon dioxide capture in 16 absorbents of amine+ ionic liquid+ H2O, ionic liquid+ H2O, and amine+ H2O systems.* Journal of Chemical & Engineering Data, 2010. **55**(9): p. 3513-3519.

137. Xu, F., et al., *Solubility of CO 2 in aqueous mixtures of monoethanolamine and dicyanamide-based ionic liquids.* Fluid Phase Equilibria, 2014. **365**: p. 80-87.

138. Shahrom, M. and C. Wilfred, *Synthesis and Thermal Properties of Amino Acids Ionic Liquids (AAILS).* Journal of Applied Sciences, 2014. **14**(10): p. 1067.

139. Fukumoto, K., M. Yoshizawa, and H. Ohno, *Room temperature ionic liquids from 20 natural amino acids.* Journal of the American Chemical Society, 2005. **127**(8): p. 2398-2399.

140. Wang, C., et al., *Carbon Dioxide Capture by Superbase-Derived Protic Ionic Liquids.* Angewandte Chemie, 2010. **122**(34): p. 6114-6117.

141. Ma, C., et al., *Development of Low-Cost Deep Eutectic Solvents for CO 2 Capture.* Energy Procedia, 2017. **142**: p. 3320-3325.

142. Adeyemi, I., M.R. Abu-Zahra, and I. Alnashef, *Novel Green Solvents for CO2 Capture.* Energy Procedia, 2017. **114**: p. 2552-2560.

143. Arshad, M.W., *CO2 capture using Ionic Liquids*. 2009, Technical University of Denmark, DTU, DK-2800 Kgs. Lyngby, Denmark.

144. Sigma-Aldrich. 2016; Available from: https://www.sigmaaldrich.com/.

145. Hallett, J.P., *Tuning ionic liquids for low cost: applications in lignocellulose deconstruction*, in *"Tunable Solvents For Green Processing"*

International Symposium "InPROMPT 2016"2/3 June 2016 Berlin. 2016.

146. Chen, L., et al., *Inexpensive ionic liquids:[HSO 4]−-based solvent production at bulk scale.* Green Chemistry, 2014. **16**(6): p. 3098-3106.

147. Zhai, H. and E.S. Rubin, *Systems Analysis of Ionic Liquids for Post-combustion CO 2 Capture at Coal-fired Power Plants.* Energy Procedia, 2014. **63**: p. 1321-1328.

148. Wappel, D., et al., *Ionic liquids for post-combustion CO 2 absorption.* International Journal of Greenhouse Gas Control, 2010. **4**(3): p. 486-494.

149. Oliferenko, A.A., et al., *Prediction of gas solubilities in ionic liquids.* Physical Chemistry Chemical Physics, 2011. **13**(38): p. 17262-17272.

150. Mortazavi-Manesh, S., M.A. Satyro, and R.A. Marriott, *Screening ionic liquids as candidates for separation of acid gases: solubility of hydrogen sulfide, methane, and ethane.* AIChE Journal, 2013. **59**(8): p. 2993-3005.

151. Maiti, A., *Theoretical screening of ionic liquid solvents for carbon capture.* ChemSusChem, 2009. **2**(7): p. 628-631.

152. Sairi, N.A., et al., *Low pressure solubilities of CO 2 in guanidinium trifluoromethanesulfonate–MDEA systems.* Fluid Phase Equilibria, 2015. **385**: p. 79-91.

153. Ramdin, M., T.W. de Loos, and T.J.H. Vlugt, *State-of-the-Art of CO2 Capture with Ionic Liquids.* Industrial and Engineering Chemistry Research, 2012. **51**: p. 8149-8177.

154. Maia, F.M., et al., *Modeling of Ionic Liquid Systems: Phase Equilibria and Physical Properties*, in *Ionic Liquids-New Aspects for the Future*. 2013, InTech. p. 31-60.

155. Rebelo, L.P., et al., *On the critical temperature, normal boiling point, and vapor pressure of ionic liquids.* The Journal of Physical Chemistry B, 2005. **109**(13): p. 6040-6043.

156. Fredlake, C.P., et al., *Thermophysical properties of imidazolium-based ionic liquids.* Journal of Chemical & Engineering Data, 2004. **49**(4): p. 954-964.

157. Rogers, R.D. and K.R. Seddon, *Ionic liquids--solvents of the future?* Science, 2003. **302**(5646): p. 792-793.

158. Aghaie, M., N. Rezaei, and S. Zendehboudi, *A systematic review on CO2 capture with ionic liquids: Current status and future prospects.* Renewable and Sustainable Energy Reviews, 2018. **96**: p. 502-525.

159. Lei, Z., C. Dai, and B. Chen, *Gas solubility in ionic liquids.* Chemical reviews, 2013. **114**(2): p. 1289-1326.

160. Pomelli, C.S., et al., *Influence of the interaction between hydrogen sulfide and ionic liquids on solubility: experimental and theoretical investigation.* The Journal of Physical Chemistry B, 2007. **111**(45): p. 13014-13019.

161. Anthony, J.L., et al., *Anion effects on gas solubility in ionic liquids.* The Journal of Physical Chemistry B, 2005. **109**(13): p. 6366-6374.

162. Zakrzewska, M.E. and M. Nunes da Ponte, *Influence of Water on the Carbon Dioxide Solubility in [OTf]-and [eFAP]-Based Ionic Liquids.* Journal of Chemical & Engineering Data, 2017.

163. Almantariotis, D., et al., *Influence of Fluorination on the Solubilities of Carbon Dioxide, Ethane, and Nitrogen in 1-n-Fluoro-alkyl-3-methylimidazolium Bis (n-fluoroalkylsulfonyl) amide Ionic Liquids.* The Journal of Physical Chemistry B, 2017. **121**(2): p. 426-436.

164. Llovell, F., et al., *Solubility of greenhouse and acid gases on the [C4mim][MeSO4] ionic liquid for gas separation and CO2 conversion.* Catalysis Today, 2015. **255**: p. 87-96.

165. Pereira, L.M., et al., *High pressure solubility of CH4, N2O and N2 in 1-butyl-3-methylimidazolium dicyanamide: Solubilities, selectivities and soft-SAFT modeling.* The Journal of Supercritical Fluids, 2016. **110**: p. 56-64.

166. Shiflett, M.B. and E.J. Maginn, *The solubility of gases in ionic liquids.* AIChE Journal, 2017. **63**(11): p. 4722-4737.

167. Friedrich, M.F., et al., *Measuring Diffusion and Solubility of Slightly Soluble Gases in [C n MIM][NTf2] Ionic Liquids.* Journal of Chemical & Engineering Data, 2016. **61**(4): p. 1616-1624.

168. Zubeir, L.F., et al., *Effect of Oxygenation on Carbon Dioxide Absorption and Thermophysical Properties of Ionic Liquids: Experiments and Modeling Using Electrolyte PC-SAFT.* Industrial & Engineering Chemistry Research, 2016. **55**(32): p. 8869-8882.

169. Shariati, A. and C.J. Peters, *High-pressure phase behavior of systems with ionic liquids: Part III. The binary system carbon dioxide+ 1-hexyl-3-methylimidazolium hexafluorophosphate.* The Journal of supercritical fluids, 2004. **30**(2): p. 139-144.

170.	Kumełan, J., et al., *Solubility of CO 2 in the ionic liquid [hmim][Tf 2 N].* The Journal of Chemical Thermodynamics, 2006. **38**(11): p. 1396-1401.

171.	Zubeir, L.F., et al., *Carbon dioxide solubilities and diffusivities in 1-alkyl-3-methylimidazolium tricyanomethanide ionic liquids: an experimental and modeling study.* Journal of Chemical & Engineering Data, 2016. **61**(12): p. 4281-4295.

172.	Cameretti, L.F., G. Sadowski, and J.M. Mollerup, *Modeling of aqueous electrolyte solutions with perturbed-chain statistical associated fluid theory.* Industrial & engineering chemistry research, 2005. **44**(9): p. 3355-3362.

173.	Karakatsani, E.K. and I.G. Economou, *Perturbed chain-statistical associating fluid theory extended to dipolar and quadrupolar molecular fluids.* The Journal of Physical Chemistry B, 2006. **110**(18): p. 9252-9261.

174.	Shiflett, M.B. and A. Yokozeki, *Solubility of CO2 in room temperature ionic liquid [hmim][Tf2N].* The Journal of Physical Chemistry B, 2007. **111**(8): p. 2070-2074.

175.	Shin, E.-K. and B.-C. Lee, *High-pressure phase behavior of carbon dioxide with ionic liquids: 1-alkyl-3-methylimidazolium trifluoromethanesulfonate.* Journal of Chemical & Engineering Data, 2008. **53**(12): p. 2728-2734.

176.	Carvalho, P.J., et al., *High pressure phase behavior of carbon dioxide in 1-alkyl-3-methylimidazolium bis (trifluoromethylsulfonyl) imide ionic liquids.* The Journal of Supercritical Fluids, 2009. **48**(2): p. 99-107.

177.	Fu, D., et al., *Effect of water content on the solubility of CO2 in the ionic liquid [bmim][PF6].* Journal of Chemical & Engineering Data, 2006. **51**(2): p. 371-375.

178.	Firoozabadi, A., *Thermodynamics of hydrocarbon reservoirs.* 1999: McGraw-Hill New York.

179.	Wong, D.S.H. and S.I. Sandler, *A theoretically correct mixing rule for cubic equations of state.* AIChE Journal, 1992. **38**(5): p. 671-680.

180.	Álvarez, V.H. and M. Aznar, *Thermodynamic modeling of vapor–liquid equilibrium of binary systems ionic liquid+ supercritical {CO2 or CHF3} and ionic liquid+ hydrocarbons using Peng–Robinson equation of state.* Journal of the Chinese Institute of Chemical Engineers, 2008. **39**(4): p. 353-360.

181.	Gross, J. and G. Sadowski, *Perturbed-chain SAFT: An equation of state based on a perturbation theory for chain molecules.* Industrial & engineering chemistry research, 2001. **40**(4): p. 1244-1260.

182.	Wertheim, M., *Fluids with highly directional attractive forces. I. Statistical thermodynamics.* Journal of statistical physics, 1984. **35**(1-2): p. 19-34.

183.	Huang, S.H. and M. Radosz, *Equation of state for small, large, polydisperse, and associating molecules.* Industrial & Engineering Chemistry Research, 1990. **29**(11): p. 2284-2294.

184.	Chapman, W.G., et al., *New reference equation of state for associating liquids.* Industrial & Engineering Chemistry Research, 1990. **29**(8): p. 1709-1721.

185.	Oliveira, M.B., et al., *Evaluation of the CO2 behavior in binary mixtures with alkanes, alcohols, acids and esters using the Cubic-Plus-Association Equation of State.* The Journal of Supercritical Fluids, 2011. **55**(3): p. 876-892.

186.	Poling, B.E., et al., *The properties of gases and liquids.* Vol. 5. 2001: Mcgraw-hill New York.

187.	Ji, X., C. Held, and G. Sadowski, *Modeling imidazolium-based ionic liquids with ePC-SAFT.* Fluid Phase Equilibria, 2012. **335**: p. 64-73.

188.   Salgado, J., et al., *Density and viscosity of three (2, 2, 2-trifluoroethanol+ 1-butyl-3-methylimidazolium) ionic liquid binary systems.* The Journal of Chemical Thermodynamics, 2014. **70**: p. 101-110.

189.   Almeida, H.F., et al., *Densities and Viscosities of Mixtures of Two Ionic Liquids Containing a Common Cation.* Journal of Chemical & Engineering Data, 2016. **61**(8): p. 2828-2843.

190.   Esperança, J.M., et al., *Pressure− Density− Temperature (p− ρ− T) Surface of [C6mim][NTf2].* Journal of Chemical & Engineering Data, 2008. **53**(3): p. 867-870.

191.   Klomfar, J., M. Součková, and J. Pátek, *Low Temperature Densities from (218 to 364) K and up to 50 MPa in Pressure and Surface Tension for Trihexyl (tetradecyl) phosphonium Bis (trifluoromethylsulfonyl) imide and Dicyanamide and 1-Hexyl-3-methylimidazolium Hexafluorophosphate.* Journal of Chemical & Engineering Data, 2014. **59**(7): p. 2263-2274.

192.   Almantariotis, D., et al., *Absorption of Carbon Dioxide, Nitrous Oxide, Ethane and Nitrogen by 1-Alkyl-3-methylimidazolium (C n mim, n= 2, 4, 6) Tris (pentafluoroethyl) trifluorophosphate Ionic Liquids (eFAP).* The Journal of Physical Chemistry B, 2012. **116**(26): p. 7728-7738.

193.   Součková, M., J. Klomfar, and J. Pátek, *Temperature dependence of the surface tension and 0.1 MPa density for 1-C n-3-methylimidazolium tris (pentafluoroethyl) trifluorophosphate with n= 2, 4, and 6.* The Journal of Chemical Thermodynamics, 2012. **48**: p. 267-275.

194.   Canales, R.I., et al., *Predicting the Solubility of CO2 in Toluene+ Ionic Liquid Mixtures with PC-SAFT.* Industrial & Engineering Chemistry Research, 2017. **56**(35): p. 9885-9894.

195.   Britt, H. and R. Luecke, *The estimation of parameters in nonlinear, implicit models.* Technometrics, 1973. **15**(2): p. 233-247.

196.   Gómez, E., et al., *Thermal analysis and heat capacities of 1-alkyl-3-methylimidazolium ionic liquids with NTf2–, TFO–, and DCA–anions.* Industrial & Engineering Chemistry Research, 2013. **52**(5): p. 2103-2110.

197.   Paulechka, Y.U., et al., *Heat capacity of ionic liquids: experimental determination and correlations with molar volume.* Journal of Chemical & Engineering Data, 2010. **55**(8): p. 2719-2724.

198.   Safarov, J., et al., *Viscosity, Density, Heat Capacity, Speed of Sound and Other Derived Properties of 1-Butyl-3-Methylimidazolium tris (Pentafluoroethyl) Trifluorophosphate over a Wide Range of Temperature and at Atmospheric Pressure.* Journal of Chemical & Engineering Data, 2017. **62**(10): p. 3620-3631.

199.   Makino, T., et al., *Physical and CO 2-Absorption Properties of Imidazolium Ionic Liquids with Tetracyanoborate and Bis (trifluoromethanesulfonyl) amide Anions.* Journal of Solution Chemistry, 2014. **43**(9-10): p. 1601-1613.

200.   Kim, Y., et al., *Solubility measurement and prediction of carbon dioxide in ionic liquids.* Fluid Phase Equilibria, 2005. **228**: p. 439-445.

201.   Zhang, X., et al., *Absorption of CO2 in the Ionic Liquid 1-n-Hexyl-3-methylimidazolium Tris (pentafluoroethyl) trifluorophosphate ([hmim][FEP]): A Molecular View by Computer Simulations.* The Journal of Physical Chemistry B, 2009. **113**(21): p. 7591-7598.

202.   Muldoon, M.J., et al., *Improving carbon dioxide solubility in ionic liquids.* The Journal of Physical Chemistry B, 2007. **111**(30): p. 9001-9009.

203.   Freire, M.G., et al., *Mutual solubilities of water and the [C n mim][Tf2N] hydrophobic ionic liquids.* The Journal of Physical Chemistry B, 2008. **112**(6): p. 1604-1610.

204. Navia, P., J. Troncoso, and L. Romaní, *Viscosities for ionic liquid binary mixtures with a common ion.* Journal of Solution Chemistry, 2008. **37**(5): p. 677-688.

205. Katti, P. and M. Chaudhri, *Viscosities of Binary Mixtures of Benzyl Acetate with Dioxane, Aniline, and m-Cresol.* Journal of Chemical & Engineering Data, 1964. **9**(3): p. 442-443.

206. Grunberg, L. and A.H. Nissan, *Mixture law for viscosity.* Nature, 1949. **164**(4175): p. 799.

207. Seddon, K.R., A. Stark, and M.-J. Torres, *Influence of chloride, water, and organic solvents on the physical properties of ionic liquids.* Pure and Applied Chemistry, 2000. **72**(12): p. 2275-2287.

208. Wang, J., et al., *A volumetric and viscosity study for the mixtures of 1-n-butyl-3-methylimidazolium tetrafluoroborate ionic liquid with acetonitrile, dichloromethane, 2-butanone and N, N–dimethylformamide.* Green Chemistry, 2003. **5**(5): p. 618-622.

209. Zubeir, L.F., et al., *Solubility and diffusivity of CO2 in the ionic liquid 1-butyl-3-methylimidazolium tricyanomethanide within a large pressure range (0.01 MPa to 10 MPa).* Journal of Chemical & Engineering Data, 2015. **60**(6): p. 1544-1562.

210. Lay, E.N., V. Taghikhani, and C. Ghotbi, *Measurement and correlation of CO2 solubility in the systems of CO2+ toluene, CO2+ benzene, and CO2+ n-hexane at near-critical and supercritical conditions.* Journal of Chemical & Engineering Data, 2006. **51**(6): p. 2197-2200.

211. Canales, R.I. and J.F. Brennecke, *Liquid-liquid phase split in ionic liquid+ toluene mixtures induced by CO2.* AIChE Journal, 2015. **61**(9): p. 2968-2976.

212. Diamantonis, N.I. and I.G. Economou, *Evaluation of statistical associating fluid theory (SAFT) and perturbed chain-SAFT equations of state for the calculation of thermodynamic derivative properties of fluids related to carbon capture and sequestration.* Energy & Fuels, 2011. **25**(7): p. 3334-3343.

213. Rahmati-Rostami, M., et al., *Solubility of H 2 S in ionic liquids [hmim][PF 6],[hmim][BF 4], and [hmim][Tf 2 N].* The Journal of Chemical Thermodynamics, 2009. **41**(9): p. 1052-1055.

214. Kumełan, J., et al., *Solubility of H2 in the ionic liquid [hmim][Tf2N].* Journal of Chemical & Engineering Data, 2006. **51**(4): p. 1364-1367.

215. Zhang, X., et al., *Insight into the Performance of Acid Gas in Ionic Liquids by Molecular Simulation.* Industrial & Engineering Chemistry Research, 2018. **58**(3): p. 1443-1453.

216. Zhang, X., et al., *Insight into the Performance of Acid Gas in Ionic Liquids by Molecular Simulation.* 2018. **58**(3): p. 1443-1453.

217. Zhang, X., Z. Liu, and W.J.A.j. Wang, *Screening of ionic liquids to capture CO2 by COSMO-RS and experiments.* 2008. **54**(10): p. 2717-2728.

218. Aghaie, M., N. Rezaei, and S.J.J.o.M.L. Zendehboudi, *Assessment of carbon dioxide solubility in ionic liquid/toluene/water systems by extended PR and PC-SAFT EOSs: Carbon capture implication.* 2019. **275**: p. 323-337.

219. Huang, Y., et al., *Thermodynamic modeling and assessment of ionic liquid-based CO2 capture processes.* 2014. **53**(29): p. 11805-11817.

220. Aghaie, M., N. Rezaei, and S. Zendehboudi, *Assessment of carbon dioxide solubility in ionic liquid/toluene/water systems by extended PR and PC-SAFT EOSs: Carbon capture implication.* Journal of Molecular Liquids, 2019. **275**: p. 323-337.

221. Köddermann, T., D. Paschek, and R.J.C. Ludwig, *Molecular dynamic simulations of ionic liquids: A reliable description of structure, thermodynamics and dynamics.* 2007. **8**(17): p. 2464-2470.

222. Yan, T., et al., *Molecular dynamics simulation of ionic liquids: The effect of electronic polarizability.* 2004. **108**(32): p. 11877-11881.

223. Bhargava, B. and S.J.T.J.o.P.C.B. Balasubramanian, *Insights into the structure and dynamics of a room-temperature ionic liquid: Ab initio molecular dynamics simulation studies of 1-n-butyl-3-methylimidazolium hexafluorophosphate ([bmim][PF6]) and the [bmim][PF6]− CO2 mixture.* 2007. **111**(17): p. 4477-4487.

224. Köddermann, T., D. Paschek, and R. Ludwig, *Molecular dynamic simulations of ionic liquids: A reliable description of structure, thermodynamics and dynamics.* ChemPhysChem, 2007. **8**(17): p. 2464-2470.

225. Canongia Lopes, J.N., J. Deschamps, and A.A. Pádua, *Modeling ionic liquids using a systematic all-atom force field.* The journal of physical chemistry B, 2004. **108**(6): p. 2038-2047.

226. Cadena, C., et al., *Why is CO2 so soluble in imidazolium-based ionic liquids?* 2004. **126**(16): p. 5300-5308.

227. Perez-Blanco, M.E. and E.J.J.T.J.o.P.C.B. Maginn, *Molecular dynamics simulations of CO2 at an ionic liquid interface: Adsorption, ordering, and interfacial crossing.* 2010. **114**(36): p. 11827-11837.

228. Huang, X., et al., *Why is the partial molar volume of CO2 so small when dissolved in a room temperature ionic liquid? Structure and dynamics of CO2 dissolved in [Bmim+][PF6-].* 2005. **127**(50): p. 17842-17851.

229. Dommert, F., et al., *Force fields for studying the structure and dynamics of ionic liquids: a critical review of recent developments.* ChemPhysChem, 2012. **13**(7): p. 1625-1637.

230. Maginn, E.J., *Molecular simulation of ionic liquids: current status and future opportunities.* Journal of Physics: Condensed Matter, 2009. **21**(37): p. 373101.

231. Sambasivarao, S.V. and O. Acevedo, *Development of OPLS-AA force field parameters for 68 unique ionic liquids.* Journal of chemical theory and computation, 2009. **5**(4): p. 1038-1050.

232. Yan, T., et al., *Molecular dynamics simulation of ionic liquids: The effect of electronic polarizability.* The Journal of Physical Chemistry B, 2004. **108**(32): p. 11877-11881.

233. Bhargava, B. and S. Balasubramanian, *Insights into the structure and dynamics of a room-temperature ionic liquid: Ab initio molecular dynamics simulation studies of 1-n-butyl-3-methylimidazolium hexafluorophosphate ([bmim][PF6]) and the [bmim][PF6]− CO2 mixture.* The Journal of Physical Chemistry B, 2007. **111**(17): p. 4477-4487.

234. Perez-Blanco, M.E. and E.J. Maginn, *Molecular dynamics simulations of CO2 at an ionic liquid interface: Adsorption, ordering, and interfacial crossing.* The Journal of Physical Chemistry B, 2010. **114**(36): p. 11827-11837.

235. Perez-Blanco, M.E. and E.J. Maginn, *Molecular dynamics simulations of carbon dioxide and water at an ionic liquid interface.* The Journal of Physical Chemistry B, 2011. **115**(35): p. 10488-10499.

236. Zhang, X., et al., *Absorption of CO2 in the Ionic Liquid 1-n-Hexyl-3-methylimidazolium Tris (pentafluoroethyl) trifluorophosphate ([hmim][FEP]): A Molecular View by Computer Simulations.* 2009. **113**(21): p. 7591-7598.

237. Karplus, M. and J.A. McCammon, *Molecular dynamics simulations of biomolecules.* Nature Structural & Molecular Biology, 2002. **9**(9): p. 646.

238. Verlet, L.J.P.r., *Computer" experiments" on classical fluids. I. Thermodynamical properties of Lennard-Jones molecules.* 1967. **159**(1): p. 98.

239.   Jorgensen, W.L., D.S. Maxwell, and J. Tirado-Rives, *Development and testing of the OPLS all-atom force field on conformational energetics and properties of organic liquids.* Journal of the American Chemical Society, 1996. **118**(45): p. 11225-11236.

240.   Sambasivarao, S.V., O.J.J.o.c.t. Acevedo, and computation, *Development of OPLS-AA force field parameters for 68 unique ionic liquids.* 2009. **5**(4): p. 1038-1050.

241.   Green, M.S., *Markoff random processes and the statistical mechanics of time-dependent phenomena. II. Irreversible processes in fluids.* The Journal of Chemical Physics, 1954. **22**(3): p. 398-413.

242.   Kubo, R., *Statistical-mechanical theory of irreversible processes. I. General theory and simple applications to magnetic and conduction problems.* Journal of the Physical Society of Japan, 1957. **12**(6): p. 570-586.

243.   Frenkel, D. and B. Smit, *Understanding molecular simulation: from algorithms to applications*. Vol. 1. 2001: Elsevier.

244.   Allen, M., *Tildesley. DJ Computer simulation of liquids*. 1987, Oxford: Clarendon Press.

245.   Frisch, M.J., et al., *Gaussian 16 Rev. B.01*. 2016: Wallingford, CT.

246.   Zhang, Y. and E.J.J.T.J.o.P.C.B. Maginn, *A simple AIMD approach to derive atomic charges for condensed phase simulation of ionic liquids.* 2012. **116**(33): p. 10036-10048.

247.   Berendsen, H.J., D. van der Spoel, and R.J.C.p.c. van Drunen, *GROMACS: a message-passing parallel molecular dynamics implementation.* 1995. **91**(1-3): p. 43-56.

248.   Lindahl, E., B. Hess, and D.J.M.m.a. Van Der Spoel, *GROMACS 3.0: a package for molecular simulation and trajectory analysis.* 2001. **7**(8): p. 306-317.

249.   Evans, D.J. and B.L. Holian, *The nose–hoover thermostat.* The Journal of chemical physics, 1985. **83**(8): p. 4069-4074.

250.   Liou, M.-S., *An extended Lagrangian method.* Journal of Computational Physics, 1995. **118**(2): p. 294-309.

251.   Martínez, L., et al., *PACKMOL: a package for building initial configurations for molecular dynamics simulations.* Journal of computational chemistry, 2009. **30**(13): p. 2157-2164.

252.   Harris, K.R., M. Kanakubo, and L.A. Woolf, *Temperature and pressure dependence of the viscosity of the ionic liquid 1-butyl-3-methylimidazolium tetrafluoroborate: viscosity and density relationships in ionic liquids.* Journal of Chemical & Engineering Data, 2007. **52**(6): p. 2425-2430.

253.   Almeida, H.F., et al., *Thermophysical properties of five acetate-based ionic liquids.* Journal of Chemical & Engineering Data, 2012. **57**(11): p. 3005-3013.

254.   Johnston, K.P. and J.M. Penninger, *Supercritical fluid science and technology*. 1989: American Chemical Society.

255.   Shariati, A., C.J.J.C.O.i.S.S. Peters, and M. Science, *Recent developments in particle design using supercritical fluids.* 2003. **7**(4-5): p. 371-383.

256.   Wang, J., et al., *A volumetric and viscosity study for the mixtures of 1-n-butyl-3-methylimidazolium tetrafluoroborate ionic liquid with acetonitrile, dichloromethane, 2-butanone and N, N–dimethylformamide.* 2003. **5**(5): p. 618-622.

257.   Pinkert, A., et al., *Density, viscosity and electrical conductivity of protic alkanolammonium ionic liquids.* 2011. **13**(11): p. 5136-5143.

258.   Liu, H., C.M. Silva, and E.A. Macedo, *Unified approach to the self-diffusion coefficients of dense fluids over wide ranges of temperature and pressure—hard-sphere, square-well, Lennard–Jones and real substances.* Chemical engineering science, 1998. **53**(13): p. 2403-2422.

259. Ma'mun, S., et al., *Selection of new absorbents for carbon dioxide capture.* Energy Conversion and Management, 2007. **48**(1): p. 251-258.

260. Neumann, M., *Dielectric relaxation in water. Computer simulations with the TIP4P potential.* The Journal of chemical physics, 1986. **85**(3): p. 1567-1580.

261. Solomon, S., et al., *Irreversible climate change due to carbon dioxide emissions.* Proceedings of the national academy of sciences, 2009. **106**(6): p. 1704-1709.

262. Astaria, G., D.W. Savage, and A. Bisio, *Gas treating with chemical solvents.* 1983.

263. Boden, T., R. Andres, and G. Marland, *Global, regional, and national fossil-fuel co2 emissions (1751-2014)(v. 2017).* 2017, Carbon Dioxide Information Analysis Center (CDIAC), Oak Ridge National ….

264. Freire, M.G., et al., *Surface tensions of imidazolium based ionic liquids: Anion, cation, temperature and water effect.* Journal of Colloid and Interface Science, 2007. **314**(2): p. 621-630.

265. Jiang, W., Y. Wang, and G.A. Voth, *Molecular dynamics simulation of nanostructural organization in ionic liquid/water mixtures.* The Journal of Physical Chemistry B, 2007. **111**(18): p. 4812-4818.

266. Widegren, J.A., A. Laesecke, and J.W. Magee, *The effect of dissolved water on the viscosities of hydrophobic room-temperature ionic liquids.* Chemical communications, 2005(12): p. 1610-1612.

267. Goodrich, B.F., et al., *Effect of water and temperature on absorption of CO2 by amine-functionalized anion-tethered ionic liquids.* The Journal of Physical Chemistry B, 2011. **115**(29): p. 9140-9150.

268. Stevanovic, S.p., et al., *Effect of water on the carbon dioxide absorption by 1-alkyl-3-methylimidazolium acetate ionic liquids.* The Journal of Physical Chemistry B, 2012. **116**(49): p. 14416-14425.

269. Fendt, S., et al., *Viscosities of acetate or chloride-based ionic liquids and some of their mixtures with water or other common solvents.* Journal of Chemical & Engineering Data, 2011. **56**(1): p. 31-34.

270. Moreno, M., et al., *Interaction of water with the model ionic liquid [bmim][BF4]: Molecular dynamics simulations and comparison with NMR data.* The Journal of Physical Chemistry B, 2008. **112**(26): p. 7826-7836.

271. Hanke, C. and R. Lynden-Bell, *A simulation study of water− dialkylimidazolium ionic liquid mixtures.* The Journal of Physical Chemistry B, 2003. **107**(39): p. 10873-10878.

272. Shi, W., et al., *Theoretical and experimental studies of water interaction in acetate based ionic liquids.* Physical Chemistry Chemical Physics, 2012. **14**(45): p. 15897-15908.

273. Romanos, G.E., et al., *Enhanced CO2 capture in binary mixtures of 1-alkyl-3-methylimidazolium tricyanomethanide ionic liquids with water.* The Journal of Physical Chemistry B, 2013. **117**(40): p. 12234-12251.

274. Yuan, S., et al., *Experimental study of CO2 absorption in aqueous cholinium-based ionic liquids.* Fluid Phase Equilibria, 2017. **445**: p. 14-24.

275. Raghavachari, K., *Perspective on "Density functional thermochemistry. III. The role of exact exchange".* Theoretical Chemistry Accounts, 2000. **103**(3-4): p. 361-363.

276. Essmann, U., et al., *A smooth particle mesh Ewald method.* The Journal of chemical physics, 1995. **103**(19): p. 8577-8593.

277. de la Parra, C.J., et al., *Influence of water concentration in the viscosities and densities of cellulose dissolving ionic liquids. Correlation of viscosity data.* The Journal of Chemical Thermodynamics, 2015. **91**: p. 8-16.

278. Alvarez, V.H., et al., *Thermophysical properties of binary mixtures of {ionic liquid 2-hydroxy ethylammonium acetate+(water, methanol, or ethanol)}.* The Journal of Chemical Thermodynamics, 2011. **43**(7): p. 997-1010.

279. González, E.J., Á. Domínguez, and E.A. Macedo, *Physical and excess properties of eight binary mixtures containing water and ionic liquids.* Journal of Chemical & Engineering Data, 2012. **57**(8): p. 2165-2176.

280. Waseda, Y., *The structure of liquids, amorphous solids and solid fast ion conductors.* Progress in Materials Science, 1981. **26**(1): p. 1-122.

281. Haughney, M., M. Ferrario, and I.R. McDonald, *Molecular-dynamics simulation of liquid methanol.* Journal of Physical Chemistry, 1987. **91**(19): p. 4934-4940.

282. Feng, S. and G.A. Voth, *Molecular dynamics simulations of imidazolium-based ionic liquid/water mixtures: Alkyl side chain length and anion effects.* Fluid phase equilibria, 2010. **294**(1-2): p. 148-156.

283. Jeffrey, G.A. and W. Saenger, *Hydrogen bonding in biological structures.* 2012: Springer Science & Business Media.

284. Kazarian, S.G., B.J. Briscoe, and T. Welton, *Combining ionic liquids and supercritical fluids: in situ ATR-IR study of CO2 dissolved in two ionic liquids at high pressuresElectronic supplementary information (ESI) available: schematic view of the miniature high-pressure flow cell. See http://www. rsc. org/suppdata/cc/b0/b005514j.* Chemical Communications, 2000(20): p. 2047-2048.

285. Menjoge, A., et al., *Influence of water on diffusion in imidazolium-based ionic liquids: a pulsed field gradient NMR study.* The Journal of Physical Chemistry B, 2009. **113**(18): p. 6353-6359.

286. Harris, K.R. and L.A. Woolf, *Pressure and temperature dependence of the self diffusion coefficient of water and oxygen-18 water.* Journal of the Chemical Society, Faraday Transactions 1: Physical Chemistry in Condensed Phases, 1980. **76**: p. 377-385.

287. Tanaka, K., *Self-diffusion coefficients of water in pure water and in aqueous solutions of several electrolytes with 18 O and 2 H as tracers.* Journal of the Chemical Society, Faraday Transactions 1: Physical Chemistry in Condensed Phases, 1978. **74**: p. 1879-1881.

288. Kelkar, M.S., W. Shi, and E.J. Maginn, *Determining the accuracy of classical force fields for ionic liquids: atomistic simulation of the thermodynamic and transport properties of 1-ethyl-3-methylimidazolium ethylsulfate ([emim][EtSO4]) and its mixtures with water.* Industrial & Engineering Chemistry Research, 2008. **47**(23): p. 9115-9126.

289. Leung, D.Y., G. Caramanna, and M.M. Maroto-Valer, *An overview of current status of carbon dioxide capture and storage technologies.* Renewable and Sustainable Energy Reviews, 2014. **39**: p. 426-443.

290. Wang, M., et al., *Post-combustion CO2 capture with chemical absorption: a state-of-the-art review.* Chemical engineering research and design, 2011. **89**(9): p. 1609-1624.

291. Brennecke, J.F. and B.E. Gurkan, *Ionic liquids for CO2 capture and emission reduction.* The Journal of Physical Chemistry Letters, 2010. **1**(24): p. 3459-3464.

292. Gurkan, B., et al., *Molecular design of high capacity, low viscosity, chemically tunable ionic liquids for CO2 capture.* The Journal of Physical Chemistry Letters, 2010. **1**(24): p. 3494-3499.

293.	Weingärtner, H., *Understanding ionic liquids at the molecular level: facts, problems, and controversies.* Angewandte Chemie International Edition, 2008. **47**(4): p. 654-670.

294.	Izadiyan, P., M. Fatemi, and M. Izadiyan, *Elicitation of the most important structural properties of ionic liquids affecting ecotoxicity in limnic green algae; a QSAR approach.* Ecotoxicology and environmental safety, 2013. **87**: p. 42-48.

295.	Péneloux, A., E. Rauzy, and R. Fréze, *A consistent correction for Redlich-Kwong-Soave volumes.* Fluid phase equilibria, 1982. **8**(1): p. 7-23.

296.	Chapman, W.G., et al., *SAFT: Equation-of-state solution model for associating fluids.* Fluid Phase Equilibria, 1989. **52**: p. 31-38.

297.	Svetnik, V., et al., *Random forest: a classification and regression tool for compound classification and QSAR modeling.* Journal of chemical information and computer sciences, 2003. **43**(6): p. 1947-1958.

298.	Baghban, A., M.A. Ahmadi, and B.H. Shahraki, *Prediction carbon dioxide solubility in presence of various ionic liquids using computational intelligence approaches.* The Journal of supercritical fluids, 2015. **98**: p. 50-64.

299.	Wang, J. and T. Hou, *Recent advances on aqueous solubility prediction.* Combinatorial chemistry & high throughput screening, 2011. **14**(5): p. 328-338.

300.	Himmelblau, D.M., *Applications of artificial neural networks in chemical engineering.* Korean journal of chemical engineering, 2000. **17**(4): p. 373-392.

301.	Curilem, M., et al., *Neural networks and support vector machine models applied to energy consumption optimization in semiautogeneous grinding.* Chemical Engineering Transactions, 2011. **25**: p. 761-766.

302.	Guo, X., et al., *A novel LS-SVMs hyper-parameter selection based on particle swarm optimization.* Neurocomputing, 2008. **71**(16-18): p. 3211-3215.

303.	Friedl, M.A. and C.E. Brodley, *Decision tree classification of land cover from remotely sensed data.* Remote sensing of environment, 1997. **61**(3): p. 399-409.

304.	Liaw, A. and M. Wiener, *Classification and regression by randomForest.* R news, 2002. **2**(3): p. 18-22.

305.	Ferreira, C., *Gene expression programming in problem solving*, in *Soft computing and industry*. 2002, Springer. p. 635-653.

306.	Schölkopf, B., A.J. Smola, and F. Bach, *Learning with kernels: support vector machines, regularization, optimization, and beyond*. 2002: MIT press.

307.	Zendehboudi, S., N. Rezaei, and A. Lohi, *Applications of hybrid models in chemical, petroleum, and energy systems: A systematic review.* Applied energy, 2018. **228**: p. 2539-2566.

308.	Karelson, M., *Molecular descriptors in QSAR/QSPR*. Vol. 230. 2000: Wiley-Interscience New York.

309.	Karelson, M., V.S. Lobanov, and A.R. Katritzky, *Quantum-chemical descriptors in QSAR/QSPR studies.* Chemical reviews, 1996. **96**(3): p. 1027-1044.

310.	Eslamimanesh, A., et al., *Artificial neural network modeling of solubility of supercritical carbon dioxide in 24 commonly used ionic liquids.* Chemical engineering science, 2011. **66**(13): p. 3039-3044.

311.	Haghbakhsh, R., H. Soleymani, and S. Raeissi, *A simple correlation to predict high pressure solubility of carbon dioxide in 27 commonly used ionic liquids.* The Journal of Supercritical Fluids, 2013. **77**: p. 158-166.

312. Ghaslani, D., et al., *Descriptive and predictive models for Henry's law constant of CO2 in ionic liquids: a QSPR study.* Chemical Engineering Research and Design, 2017. **120**: p. 15-25.

313. Todeschini, R. and V. Consonni, *Handbook of molecular descriptors*. Vol. 11. 2008: John Wiley & Sons.

314. Crocker, G.H., *THE FRANK J. SEILER RESEARCH LABORATORY*. 1967, FRANK J SEILER RESEARCH LAB UNITED STATES AIR FORCE ACADEMY COLO.

315. Ahmad, S. and M.M. Gromiha, *Design and training of a neural network for predicting the solvent accessibility of proteins.* Journal of computational chemistry, 2003. **24**(11): p. 1313-1320.

316. Depczynski, U., V. Frost, and K. Molt, *Genetic algorithms applied to the selection of factors in principal component regression.* Analytica Chimica Acta, 2000. **420**(2): p. 217-227.

317. Theil, H., *Principles of econometrics*. 1971.

318. Wehenkel, L., D. Ernst, and P. Geurts, *Ensembles of extremely randomized trees and some generic applications.* Proceedings of Robust Methods for Power System State Estimation and Load Forecasting, 2006.

319. Xu, M., et al., *Decision tree regression for soft classification of remote sensing data.* Remote Sensing of Environment, 2005. **97**(3): p. 322-336.

320. Breiman, L., *Classification and regression trees*. 2017: Routledge.

321. Breiman, L., *Random forests.* Machine learning, 2001. **45**(1): p. 5-32.

322. Rodriguez-Galiano, V.F., et al., *An assessment of the effectiveness of a random forest classifier for land-cover classification.* ISPRS Journal of Photogrammetry and Remote Sensing, 2012. **67**: p. 93-104.

323. Vapnik, V., *The nature of statistical learning theory*. 2013: Springer science & business media.

324. Smola, A.J. and B. Schölkopf, *A tutorial on support vector regression.* Statistics and computing, 2004. **14**(3): p. 199-222.

325. Vapnik, V.N., *T he Nature of Statistical L earning T heory.* New York: Springer2V erlag, 1995.

326. Zhao, Y., et al., *Toxicity of ionic liquids: database and prediction via quantitative structure–activity relationship method.* Journal of hazardous materials, 2014. **278**: p. 320-329.

327. AK, S.J., *Least squares support vector machines*. 2002: World Scientific.

328. Suykens, J.A. and J. Vandewalle, *Least squares support vector machine classifiers.* Neural processing letters, 1999. **9**(3): p. 293-300.

329. Liu, H., et al., *Accurate quantitative structure− property relationship model to predict the solubility of C60 in various solvents based on a novel approach using a least-squares support vector machine.* The Journal of Physical Chemistry B, 2005. **109**(43): p. 20565-20571.

330. Tetko, I.V., et al., *Development of dimethyl sulfoxide solubility models using 163 000 molecules: using a domain applicability metric to select more reliable predictions.* Journal of chemical information and modeling, 2013. **53**(8): p. 1990-2000.

331. Schwaighofer, A., et al., *Accurate solubility prediction with error bars for electrolytes: A machine learning approach.* Journal of chemical information and modeling, 2007. **47**(2): p. 407-424.

332.   Mauri, A., et al., *Dragon software: An easy approach to molecular descriptor calculations.* Match, 2006. **56**(2): p. 237-248.

333.   Shariati, A., K. Gutkowski, and C.J. Peters, *Comparison of the phase behavior of some selected binary systems with ionic liquids.* AIChE Journal, 2005. **51**(5): p. 1532-1540.

334.   Tomida, D., et al., *Viscosity of ionic liquid mixtures of 1-alkyl-3-methylimidazolium hexafluorophosphate+ CO2.* Fluid Phase Equilibria, 2011. **307**(2): p. 185-189.

335.   Costantini, M., et al., *High-pressure phase behavior of systems with ionic liquids: Part IV. Binary system carbon dioxide+ 1-hexyl-3-methylimidazolium tetrafluoroborate.* Journal of Chemical & Engineering Data, 2005. **50**(1): p. 52-55.

336.   Kumełan, J., et al., *Solubility of CO2 in the ionic liquids [bmim][CH3SO4] and [bmim][PF6].* Journal of Chemical & Engineering Data, 2006. **51**(5): p. 1802-1807.

337.   Bahadur, I., et al., *Solubilities of carbon dioxide and oxygen in the ionic liquids methyl trioctyl ammonium bis (trifluoromethylsulfonyl) imide, 1-butyl-3-methyl imidazolium bis (trifluoromethylsulfonyl) imide, and 1-butyl-3-methyl imidazolium methyl sulfate.* The Journal of Physical Chemistry B, 2015. **119**(4): p. 1503-1514.

338.   Haghtalab, A. and A. Kheiri, *High pressure measurement and CPA equation of state for solubility of carbon dioxide and hydrogen sulfide in 1-butyl-3-methylimidazolium acetate.* The Journal of Chemical Thermodynamics, 2015. **89**: p. 41-50.

339.   Carvalho, P.J., et al., *Specific solvation interactions of CO2 on acetate and trifluoroacetate imidazolium based ionic liquids at high pressures.* The Journal of Physical Chemistry B, 2009. **113**(19): p. 6803-6812.

340.   Kim, J.E., J.W. Kang, and J.S. Lim, *Measurement of CO 2 solubility in cyanide anion based ionic liquids;[c 4 mim][SCN],[c 4 mim][N (CN) 2],[c 4 mim][C (CN) 3].* Korean Journal of Chemical Engineering, 2015. **32**(8): p. 1678-1687.

341.   Schilderman, A.M., S. Raeissi, and C.J. Peters, *Solubility of carbon dioxide in the ionic liquid 1-ethyl-3-methylimidazolium bis (trifluoromethylsulfonyl) imide.* Fluid Phase Equilibria, 2007. **260**(1): p. 19-22.

342.   Soriano, A.N., B.T. Doma Jr, and M.-H. Li, *Carbon dioxide solubility in 1-ethyl-3-methylimidazolium trifluoromethanesulfonate.* The Journal of Chemical Thermodynamics, 2009. **41**(4): p. 525-529.

343.   Nam, S.G. and B.-C. Lee, *Solubility of carbon dioxide in ammonium-based ionic liquids: Butyltrimethylammonium bis (trifluoromethylsulfonyl) imide and methyltrioctylammonium bis (trifluoromethylsulfonyl) imide.* Korean Journal of Chemical Engineering, 2013. **30**(2): p. 474-481.

344.   Ramdin, M., et al., *High pressure solubility of CO2 in non-fluorinated phosphonium-based ionic liquids.* The Journal of Supercritical Fluids, 2013. **82**: p. 41-49.

345.   Zhang, S., et al., *Solubility of CO2 in sulfonate ionic liquids at high pressure.* Journal of Chemical & Engineering Data, 2005. **50**(1): p. 230-233.

346.   Stevanovic, S. and M.C. Gomes, *Solubility of carbon dioxide, nitrous oxide, ethane, and nitrogen in 1-butyl-1-methylpyrrolidinium and trihexyl (tetradecyl) phosphonium tris (pentafluoroethyl) trifluorophosphate (eFAP) ionic liquids.* The Journal of Chemical Thermodynamics, 2013. **59**: p. 65-71.

347.   Lee, B.-C. and S.G. Nam, *High-pressure solubility of carbon dioxide in pyrrolidinium-based ionic liquids:[bmpyr][dca] and [bmpyr][Tf 2 N].* Korean Journal of Chemical Engineering, 2015. **32**(3): p. 521-533.

348.   Yuan, X., et al., *Solubilities of CO2 in hydroxyl ammonium ionic liquids at elevated pressures.* Fluid Phase Equilibria, 2007. **257**(2): p. 195-200.

349.   Kurnia, K., et al., *Thermodynamic properties of CO2 absorption in hydroxyl ammonium ionic liquids at pressures of (100–1600) kPa.* The Journal of Chemical Thermodynamics, 2009. **41**(10): p. 1069-1073.

350.   Shiflett, M.B., et al., *Phase behavior of N 2 O and CO 2 in room-temperature ionic liquids [bmim][Tf 2 N],[bmim][BF 4],[bmim][N (CN) 2],[bmim][Ac],[eam][NO 3], and [bmim][SCN].* International Journal of Thermophysics, 2012. **33**(3): p. 412-436.

351.   Zoubeik, M. and A. Henni, *Experimental and thermodynamic study of CO2 solubility in promising [TF2N and DCN] ionic liquids.* Fluid Phase Equilibria, 2014. **376**: p. 22-30.

352.   Makino, T., M. Kanakubo, and T. Umecky, *CO2 solubilities in ammonium bis (trifluoromethanesulfonyl) amide ionic liquids: effects of ester and ether groups.* Journal of Chemical & Engineering Data, 2014. **59**(5): p. 1435-1440.

353.   Tagiuri, A., K.Z. Sumon, and A. Henni, *Solubility of carbon dioxide in three [Tf2N] ionic liquids.* Fluid Phase Equilibria, 2014. **380**: p. 39-47.

354.   Zhang, S., et al., *Solubilities of CO2 in 1-butyl-3-methylimidazolium hexafluorophosphate and 1, 1, 3, 3-tetramethylguanidium lactate at elevated pressures.* Journal of Chemical & Engineering Data, 2005. **50**(5): p. 1582-1585.

355.   Ayad, A., A. Negadi, and F. Mutelet, *Carbon dioxide solubilities in tricyanomethanide-based ionic liquids: Measurements and PC-SAFT modeling.* Fluid Phase Equilibria, 2018. **469**: p. 48-55.

356.   Makino, T., et al., *Pressure–volume–temperature–composition relations for carbon dioxide+ pyrrolidinium-based ionic liquid binary systems.* Fluid Phase Equilibria, 2013. **360**: p. 253-259.

357.   Tagiuri, A., et al., *Effect of cation on the solubility of carbon dioxide in three bis (fluorosulfonyl) imide low viscosity ([FSI]) ionic liquids.* Fluid Phase Equilibria, 2014. **375**: p. 324-331.

358.   Kim, M., et al., *High pressure phase behaviour of carbon dioxide and two ionic liquids based on a benzyl functionalized cation.* The Journal of Chemical Thermodynamics, 2018. **121**: p. 91-96.

359.   Zoubeik, M., M. Mohamedali, and A. Henni, *Experimental solubility and thermodynamic modeling of CO2 in four new imidazolium and pyridinium-based ionic liquids.* Fluid Phase Equilibria, 2016. **419**: p. 67-74.

360.   Makino, T., et al., *CO2 solubility and physical properties of N-(2-hydroxyethyl) pyridinium bis (trifluoromethanesulfonyl) amide.* Fluid Phase Equilibria, 2013. **357**: p. 64-70.

361.   Zeng, S., et al., *Highly selective capture of CO2 by ether-functionalized pyridinium ionic liquids with low viscosity.* Energy & Fuels, 2015. **29**(9): p. 6039-6048.

362.   Pinto, A.M., et al., *Combined physical and chemical absorption of carbon dioxide in a mixture of ionic liquids.* The Journal of Chemical Thermodynamics, 2014. **77**: p. 197-205.

363.   Althuluth, M., et al., *Solubility of carbon dioxide in the ionic liquid 1-ethyl-3-methylimidazolium tris (pentafluoroethyl) trifluorophosphate.* Journal of Chemical & Engineering Data, 2012. **57**(12): p. 3422-3425.

364.   Kim, J.E., H.J. Kim, and J.S. Lim, *Solubility of CO2 in ionic liquids containing cyanide anions:[c2mim][SCN],[c2mim][N (CN) 2],[c2mim][C (CN) 3].* Fluid Phase Equilibria, 2014. **367**: p. 151-158.

365. Soriano, A.N., B.T. Doma Jr, and M.-H. Li, *Solubility of carbon dioxide in 1-ethyl-3-methylimidazolium tetrafluoroborate.* Journal of Chemical & Engineering Data, 2008. **53**(11): p. 2550-2555.

366. Raeissi, S., L. Florusse, and C. Peters, *Scott–van Konynenburg phase diagram of carbon dioxide+ alkylimidazolium-based ionic liquids.* The Journal of Supercritical Fluids, 2010. **55**(2): p. 825-832.

367. Mirzaei, M., et al., *Solubility of carbon dioxide and methane in 1-hexyl-3-methylimidazolium nitrate ionic liquid, experimental and thermodynamic modeling.* The Journal of Chemical Thermodynamics, 2018. **122**: p. 31-37.

368. Safavi, M., et al., *Study of the solubility of CO2, H2S and their mixture in the ionic liquid 1-octyl-3-methylimidazolium hexafluorophosphate: experimental and modelling.* The Journal of Chemical Thermodynamics, 2013. **65**: p. 220-232.